Etude des modes de résonance d'une torche à plasma d'arc associée à une injection synchrone pour la réalisation de dépôts par voie liquide

Joanna Krowka

UNIVERSITÉ DE LIMOGES

Ecole Doctorale Sciences et Ingénierie en Matériaux, Mécanique, Energétique et Aéronautique

Laboratoire Science des Procédés Céramiques et Traitements de Surface

Année : 2014 Thèse N X

Thèse

pour obtenir le grade de

DOCTEUR DE L'UNIVERSITÉ DE LIMOGES

Discipline : Matériaux Céramiques et Traitements de Surface

présentée et soutenue par

Joanna Krowka

le 14 novembre 2014

Etude des modes de résonance d'une torche à plasma d'arc associée à une injection synchrone pour la réalisation de dépôts par voie liquide

Thése dirigée par Vincent Rat

JURY :

Président du Jury:	
Jean-François Coudert	Professeur, Université de Limoges
Rapporteurs:	
Alain Gleizes	Directeur de recherche CNRS, Université Paul Sabatier de Toulouse
Marie-Pierre Planche	Maître de Conférence, HDR, UTBM, Belfort
Examinateurs:	
Christelle Dublanche-Tixier	Professeur, Ecole Nationale Supérieure d'Ingénieur de Limoges
Erick Meillot	Ingénieur CEA, CEA Le Ripault, Monts
Vincent Rat	Chargé de Recherche CNRS, HDR, Université de Limoges
Invité:	
Christophe Chazelas	Maître de Conférence, Ecole Nationale Supérieure d'Ingénieur de Limoges

"The good thing about science is that it's true whether or not you believe in it."

Neil deGrasse Tyson

A mes parents...

Remerciements

Ce travail a été mené au sein du laboratoire Science des Procédés Céramiques et de Traitements de Surface (SPCTS UMR CNRS 7315). Je tiens à remercier Monsieur Thierry CHARTIER de m'y avoir accueilli. Je voudrais remercier également la région Limousin pour le support financier apporté à cette thèse.

J'exprime ma très sincère reconnaissance à mes encadrants, Monsieur Vincent Rat, Chargé de Recherche CNRS HDR à l'Université de Limoges, et Monsieur Jean-François Coudert, Professeur à l'Université de Limoges, pour m'avoir donné l'opportunité de travailler pendant 3 ans sur ce sujet passionnant. Je les remercie tous deux pour leurs précieux conseils, leur disponibilité, leur aide ainsi que pour la confiance qu'ils ont su m'accorder. Je tiens également à remercier Monsieur Jean-François Coudert pour avoir accepté de présider le jury de cette thèse.

Je remercie vivement Madame Marie-Pierre Planche, Maître de Conférence HDR à l'UTBM de Belfort, et Monsieur Alain Gleizes, Directeur de recherche CNRS à l'Université Paul Sabatier de Toulouse, d'avoir accepté d'être les rapporteurs de cette thèse. Je leur exprime toute ma gratitude pour l'intérêt qu'ils ont manifesté à l'égard de ce travail.

Je voudrais remercier Messieurs Simon Goutier, Maître de Conférence à l'Université de Limoge, Alain Grimaud, Geoffroy Rivaud et Nicolas Lory pour leur aide précieuse, tous les conseils scientifiques et pragmatiques qui m'ont beaucoup apportés.

Je tiens également à remercier Messieurs Lech Pawlowski, Professeur à l'Université de Limoges, Stefan Kozerki, Docteur, et Leszek Latka, Docteur de l'Ecole Polytechnique de Wroclaw, pour partager avec moi leurs vastes connaissances sur la méthode de projection par plasma.

Je remercie à mes collègues de bureau: Rafika Zaabi, Vanessa Orozco, Michael Gaudin qui m'ont permis de travailler dans une très bonne ambiance.

Je tiens également à remercier plus largement tous les collègues: Fabrice Mavier, Guillaume Bidron, Alice Ravaux, Matthias de Sousa, Andrés Gonzalez Hernandez, William Duarte, Yohann Scaringella, Diane Dupuy, Claudia Palacio Espinosa, Inès Hidouri du l'axe 2 avec qui j'ai partagé ces trois années.

Merci à tous mes amis de m'avoir supporté. Jayanth Channagiri, Aleena Laganapan, Kasia Krupa, Ola Malachowska, Pawel Sokolowski, Andrea Cattini, Alberto Cambra, Quitterie Monegier du Sorbier, Gosia Piechowiak, Olivier Noguera, Laura Molina, Jess Gambe, vous avez rendu ces trois années passées à Limoges très agréables grâce à votre compagnie. Je tiens à remercier tout particulièrement à Jayanth (for our la firenza time, all bus-discussions and amazing surprise for my defence day), Aleena et Kasia (girls thank you for your support, friendship and all those amazing and crazy moments spent together).

Merci à ma famille (mes parents, mes sœurs) de m'avoir soutenue malgré la distance pendant ces trois années. Je tiens à remercier tout particulièrement à mon pére qui m'inspire toujours par son amour de la science.

Merci à mon compagnon, Pablo, sans qui je n'aurais pas été jusque là. Merci pour tout ton amour et ton soutien.

Enfin merci à vous lecteurs de vous intéresser à mes travaux, en vous souhaitant bonne lecture.

Etude des modes de résonance d'une torche à plasma d'arc associée à une injection synchrone pour la réalisation de dépôts par voie liquide

Resumé: La projection par plasma d'arc de suspension permet d'obtenir des revêtements finement structurés à gradients de propriétés qui répondent aux besoins, par exemple, des applications photocatalytiques, les piles à combustible à oxyde solide ou les revêtements de barrière thermique. Cependant, les torches à plasma, même alimentées par des sources de courant continu régulé, génèrent des jets de plasma fortement fluctuants. Ces instabilités causent des variations importantes dans les transferts thermiques et dynamiques des particules, ce qui diminue la fiabilité et la reproductibilité de la méthode. Par conséquent, des efforts particuliers doivent être faits pour améliorer la projection par plasma d'arc de suspension et, ainsi, les propriétés des revêtements. Depuis de nombreuses années, la recherche s'est concentrée sur l'amélioration des transferts de chaleur et de quantité de mouvement entre la matière et le plasma au moyen de la mise au point de nouvelles torches et la réduction des instabilités de l'arc. Cette thèse présente une nouvelle approche pour la projection par plasma d'arc de suspension. L'étude approfondie des instabilités du plasma sont réalisées ce qui conduit à la production du jet laminaire de plasma pulsé caractérisé par une forte modulation de l'enthalpie spécifique. Ces oscillations régulières de plasma sont associées à l'injection de la suspension synchronisée, ce qui est réalisé à l'aide de l'impression à jet d'encre déclenchée par le signal de tension d'arc. Les résultats sont évalués par le système d'imagerie résolue en temps et la spectroscopie d'émission optique résolue en temps. Cette nouvelle méthode offre la possibilité de contrôler les transferts de chaleur et de quantité de mouvement entre les particules et le plasma.

Mots clés : la projection par plasma d'arc de suspension, les instabilités du plasma, l'impression à jet d'encre, plasma d'arc pulsé, les matériaux nanostructurés.

Study of the plasma torch resonant modes associated with the synchronous injection for coating elaboration.

Abstract: Suspension plasma spraying permits to elaborate finely structured coatings with graded properties which address the needs, for example, in the photocatalytic applications, the solid oxide fuels or the thermal barrier coatings. However, the plasma torches, even powered by dc regulated sources, generate highly fluctuating plasma jets. These instabilities result in large variations in dynamic and heat transfers to particles, what decreases the reproducibility and reliability of the method. Consequently, the special efforts have to be devoted to ameliorate the suspension plasma spraying method and, thus, the properties of the coatings. In recent years, the research has been focused on the improvement of heat and momentum transfers between material and plasma by means of the development of new non-conventional torches and the reduction of arc instabilities. The following dissertation presents a new approach to the suspension plasma spraying. The profound studies of the plasma instabilities are performed, what leads to the production of the pulsed laminar plasma jet characterized by high modulation of the specific enthalpy. These regular plasma oscillations are combined with phased injection of suspension, what is achieved by using the ink-jet printer triggered by the arc voltage signal. The results are evaluated by time-resolved imaging system and the time-resolved emission optical spectroscopy. This new method presents the possibility to control heat and momentum transfers between the particles and the plasma.

Keywords: suspension plasma spraying, plasma instabilities, ink-jet printing, pulsed arc plasma, nanostructured materials.

SPCTS UMR CNRS n 7315
12, rue Atlantis - 87068 LIMOGES CEDEX

Contents

List of Figures

List of Tables

Introduction

The coating is a covering which is applied to the surface of the object to improve its functional performance, extend the components life by reducing wear due to e.g. erosion, and, therefore, decrease the cost of the object. The coatings deposition methods can be roughly divided into thin- and thick- film technologies. Thin films, with the thickness of less than 1 μm can be produced by the processes like Chemical Vapor Deposition (CVD) or Physical Vapor Deposition (PVD). Thick films have a thickness over 20 μm and can be several millimetres thick. They are obtained by e.g. chemical/electro-chemical plating, brazing, thermal spraying. The thermal spraying processes are characterized by a wide variety of materials that can be used to produce coatings, layers fabrication without significant heat input to the substrate, therefore, without changing its properties and a relatively low cost. Consequently, the following dissertation will be focused on one of the thermal spraying methods, the plasma spraying process.

The plasma spraying method is the technique where the material in the form of the powder is introduced to the plasma jet produced by the plasma torch. It results in the coatings presented micrometer-sized features. However, for several years, the researchers have been more interested in developing and studying the plasma-sprayed coatings with nano-sized features. As Gell has highlighted changing the structure scale to nanometer allows to increase e.g. coatings strength, toughness and coefficient of thermal expansion [1]. Therefore, in the field of plasma sprayed coatings technology, the use of the suspension of fine particles as material injected, so-called suspension plasma spraying method, is becoming a well-established process. It allows obtaining the finely structured and dense coatings with graded properties. The coatings produced by suspension plasma spraying can be used in wear-resistant applications as well as in more complex integrated devices, such as solid oxide fuel cells, thermal barrier coatings, photo catalytic coatings.

However, in more complex applications, the researchers face still many problems, such as obtaining the appropriate crystallographic structure of materials, e.g. perovskite structure of cathode in SOFC or anatase phase in TiO_2 coatings [2, 3]. These difficulties are mainly caused by the power fluctuations of the plasma torch due to the electric instabilities, which result in large variations in dynamic and heat transfers to particles. Consequently, the special efforts have to be made to ameliorate the suspension plasma spraying method and the properties of the coatings.

In recent years the research has been focused on the improvement of heat and momentum transfers between material and plasma produced by the plasma torch by means of the reduction of arc instabilities. One of the found solution is the development of a new non-conventional plasma torch. The numerous designs have been implemented, e.g. multi-electrode plasma torches which can be found in Triplex (Sulzer Metco, Switzerland)

or Axial III (Northwest Mettech Corp., Canada).

The following studies propose an improved suspension plasma spraying process. The principle is to produce a pulsed laminar plasma jet combined with synchronized injection of liquid droplets, what is expected to control heat and momentum transfers from plasma to materials and, therefore, increase the reproducibility and reliability of the process. The pulsed plasma is obtained by the particular design of the plasma torch that works at moderate power and following a resonant mode obtained by coupling the different modes of the instabilities which will be studied in this thesis, i.e. so-called Helmholtz and restrike modes. To accomplish the purpose of this thesis the origin of arc instabilities must be understood. Therefore, the following studies are divided into two parts. The first part is focused on the examination of plasma instabilities in dc torch, presenting a similar configuration as the commonly used Sultzer Metco F4 gun. This torch in the following thesis will be called the conventional. In the second part, a newly designed dc plasma torch which allows obtaining the pulsed arc jet is presented.

The studies presented above are described in three chapters. The form of the following dissertation differs from the traditional thesis. In order to facilitate the comprehension of the obtained results and due to the use of two various systems, the description of each experimental setup has been included in the particular chapter specifying the obtained results.

The first chapter gives the general context of the plasma spraying process. It explains the principles of this method, e.g. the properties of the plasma forming gases, the operation of the dc plasma torch. Then, it presents the coatings formation process from the material feedstock preparation to the different material injection systems, the suspension droplet-plasma interactions and the coatings build-up process. To better understand the fundamentals of the suspension plasma spraying process this part of the chapter has been divided into three phases: "Plasma production", "Suspension injection and penetration into the plasma jet" and "Material deposition". At the end of this part of the dissertation the problems encountered in the method have been highlighted. The description of the present research on the plasma instabilities gives the grounds to the studies presented in chapter 2.

The second chapter introduces the studies of plasma instabilities in conventional dc torch, presenting a similar configuration as the commercial Sultzer Metco F4 gun. The first part gives the detailed description of the time-resolved measurements and the data processing methods which have been applied to the arc voltage signal. The obtained results have highlighted the appearance of the resonant mode in the torch, so-called Helmholtz mode. The chapter shows the profound studies of these Helmholtz

oscillations. Moreover, the investigation of the restrike mode, following the model found in the literature and described in chapter 1, has been presented. The studies have leaded to determine the key parameters influencing these modes and to show the possibility to couple them together in a newly designed dc plasma torch. It results in a very repeatable saw-tooth shape arc voltage signal which produces the pulsed plasma jet. The last part of this chapter describes this original resonant mode, a new design of the torch and the characteristics of the plasma produced by this system.

The third chapter presents a new, developed in this thesis, system which may be described as the improvement of suspension plasma spraying method. The principle is to activate the suspension emission at the chosen moment of the obtained periodic plasma jet, following the requirements for the thermal treatment of the particular material. The chapter presents the optimization of the system which plays the key role of this new method. The experimental setup, together with the results have been divided into three parts: the time-resolved imaging system, synchronized suspension injection and time-resolved spectroscopy. The last part, the spectral measurements, has not been included in the initial objective of this thesis. Therefore, the first experiments of the plasma temperature measurements and the investigation of the plasma species have been presented. The results obtained by this new system have highlighted the possibility to control the heat and momentum transfers between the suspension and plasma. Moreover, the first attempts of the coatings deposition have been performed and presented in the end of this chapter.

The following thesis has been realized in the laboratory SPCTS - UMR CNRS 7315 of the University of Limoges. This work has been partly conducted in frame of a research program entitled PLASMAT sponsored by the French National Research Agency (ANR).

Chapter 1 :

Literature review

1.1 Introduction

Plasma spraying is the part of thermal spraying, which according to the definition given by American Society of Materials (ASM) is a group of processes in which finely divided metallic and non-metallic surfacing materials are deposited in a molten or semi-molten condition on a substrate to form a spray deposit [4]. The thermal spraying techniques can be classified according to the energy source and the conditions of the process, what is presented in Figure 1.1.

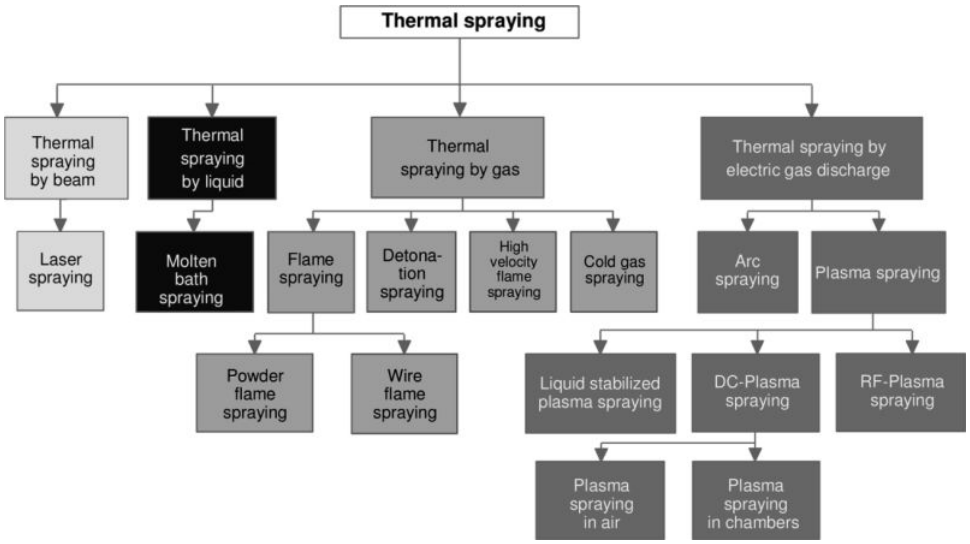

Figure 1.1: Overview of the different thermal-spray processes. [4]

This work focuses on the plasma spraying process with the material injected into a direct current (dc) plasma jet at atmospheric pressure (plasma spraying in air in Figure 1.1). Due to feedstock material injected into the plasma jet the plasma spraying technique can be categorized into: atmospheric plasma spraying (APS), solution precursor plasma spraying (SPPS) and suspension plasma spraying (SPS) [5–7]. In the APS process, solid powder particles are injected into the plasma jet. The minimum thickness of the coatings is limited to about 10 μm [7]. They are mostly used to provide protection against high temperatures, corrosion, erosion and wear. The increasing interest in nanomaterials, which according to the definition given by US National Nanotechnology Initiative are the material structures with at least one dimension smaller than 100 nm, results in the development of new plasma spraying processes. The one of this method, described by Karthikeyan *et al.* [8], is the solution precursor plasma spraying, in which instead of the conventional powder feedstock, an aqueous solution precursor is injected into the plasma jet. This process allows obtaining the nano- and sub-micrometric microstructure of coatings. An alternative method is a relatively new suspension plasma spraying, which has been invented by the University of Sherbrooke in the mid-1990s [9]. The suspension

composed of submicron or nano-sized powder particles suspended in a liquid is used as the feedstock. The SPS process permits to produce finely structured nano-sized coatings, what allows expanding the application area of the plasma spraying method. They may be used as:

- Solid oxide fuel cell (SOFC)
  It is an electrochemical conversion device that produces electricity directly from oxidizing a fuel. It consists of four layers: anode, electrolyte, cathode and interconnect. The three first coatings are ceramic, not electrically and ionically active below about 600°C. Therefore, many efforts have been devoted to produce the coatings for these SOFC components by suspension plasma spraying method. The anode consists of the porous nickel-YSZ (yttria-stabilized zirconia) cermet coating. The electrolyte requires a dense and thin ($< 15\ \mu$m) YSZ coating. The porous perovskite, e.g. lanthanum ferro-cobaltite doped with strontium (LSCF) or lanthanum manganite doped with strontium (LSM) coating should be produced for the cathode.

- Thermal barrier coating (TBC)
  Thermal barrier coatings (TBCs) are advanced material systems applied to metallic surfaces, e.g. gas turbine or aero-engine parts, to help protect these components from the heat and thermal degradation. The TBC materials should be characterized by: high melting point, low thermal conductivity, thermal expansion match with the metallic substrate, good adherence to the metallic substrate and a low sintering rate of the porous microstructure. Therefore, the number of materials that can be used as TBCs is very limited. The ceramic coatings such as Al_2O_3, TiO_2, mullite, ZrO_2, YSZ, CeO_2, $La_2Zr_2O_7$ are applied as TBC materials, among which yttria-stabilized zirconia (YSZ) is the most widely studied [10–12].

- Photo-catalytic coatings
  In recent years the photo-catalysis process has been used in a broad range of applications, including especially environmental and energy-related fields, illustrated in the example of TiO_2 photo-catalysis in Figure 1.2.

  Several semiconductors (TiO_2, ZnO, Fe_2O_3, CdS, ZnS) can act as photocatalysts but TiO_2 has been most commonly studied due to its photocatalytic and hydrophilic properties and moreover, high reactivity, reduced toxicity, chemical stability and lower cost. The photo-catalytic properties of TiO_2 coating depend on its phase composition. The anatase TiO_2 presents a higher photocatalytic activity than its rutile phase. 65 vol.% of anatase is necessary to achieve an acceptable photo-catalytic performance.

However, in more complex applications the researchers face still many problems, such as obtaining the appropriate crystallographic structure of materials.

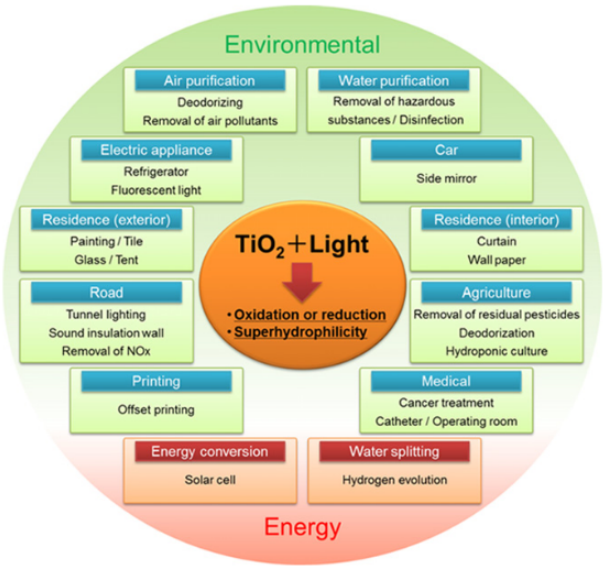

Figure 1.2: Applications of TiO_2 photo-catalysis [13].

As Henne has presented on the example of solid oxide fuel cells (SOFC), these more complex devices can be produced by other thermal spray methods, such as vacuum plasma spraying (VPS) [14]. However, the goal of technological development is the reduction of costs what can be achieved by suspension plasma spraying using dc torches at atmospheric pressure. Therefore, the following thesis is focused on the studies and the improvement of direct current plasma torch associated with the suspension injection.
In suspension plasma spraying method the material in the form of suspension is introduced into the plasma jet produced by a direct current (dc) plasma torch. This process can be divided into three important phases, indicated in Figure 1.3:

I Plasma production

II Suspension injection and penetration into the plasma jet

III Material deposition

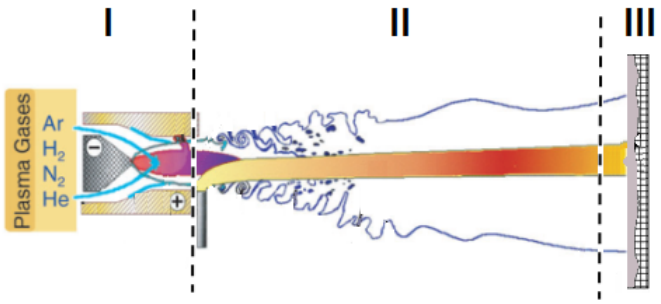

Figure 1.3: Schematic view of a plasma spraying method [15].

Therefore, the following paragraph has been divided into three parts.

1.2 Fundamentals of plasma spraying process

The plasma, often referred to a fourth state of matter, is a gas electrically conducting due to the presence of charged particles [16–18]. It can be defined as a collection of species: electrons, ions and neutral particles moving in random directions, schematically presented in Figure 1.4. The mass of the ions and neutrals, m_h, is much higher than the electron

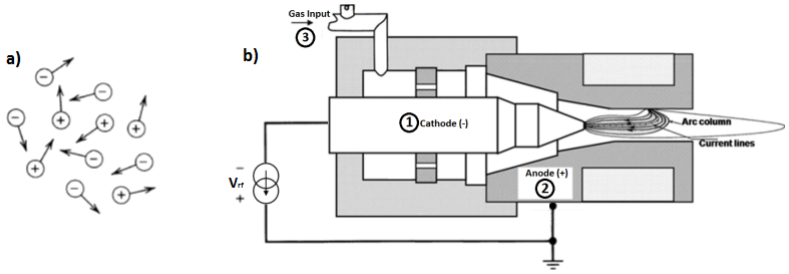

Figure 1.4: Schematic view of a) plasma; b) plasma formation by a direct current plasma torch.

mass, m_e, therefore, these species have been defined as heavy particles. The plasma is the result of the transformation of gas atoms to charged particles in consequence of the increasing temperature, what can be achieved by different methods, e.g. microwaves, RF discharges, laser. The following thesis is focused on the plasma spraying method. In this technique the plasma is produced by the electric discharge using the direct current (dc) plasma torch, what is presented in the following section.

1.2.1 Direct current plasma torch

As mentioned above, in the plasma spraying process the plasma jet is formed in the torch. According to the current terminology, defined by Zukov *et al.*, the term plasma torch indicates the apparatus designed for the production of low temperature plasma by heating the gas using the electric arc [19]. The first industrial dc plasma torches appeared in the 1960s [15]. Since that time, a large number of torch designs has been developed. The differences between the torches consist in various types of the cathode tips, the gas injection, the nozzle shapes and diameters. The basic concept of the plasma torch, shown in Figure 1.5, comprises a cathode, a plasma forming gas injector and an anode nozzle. The following section focuses on the detailed description of a direct current non-transferred plasma torch.

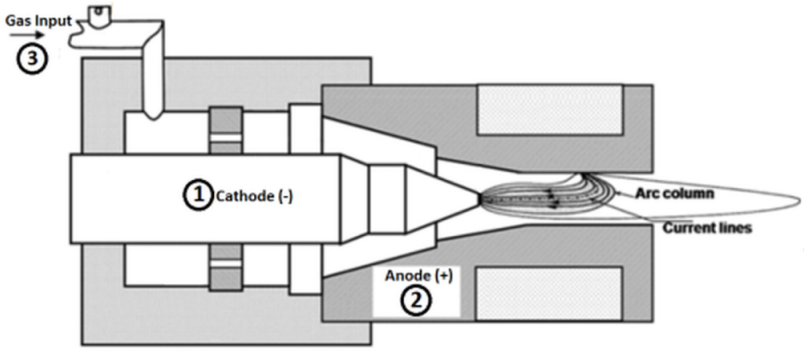

Figure 1.5: Schematic view of a direct current plasma torch.

- **Cathode**

It emits the electrons for maintaining the arc discharge. The parameters of the cathode differ according to the electrons emission mechanisms. In the case of the hot cathode (a, b in Figure 1.6) is the thermionic emission defined by Richardson-Dushman law:

$$J = A_G T^2 e^{\frac{-W}{kT}} \tag{1.1}$$

where:

J	is the emission current density [A.m^{-2}],
T	the temperature of the metal,
W	the work function of the metal,
k	the Boltzmann constant,
A_G	the constant defined by: $A_G = \frac{4\pi m k^2 e}{h^3} = 1.20173 \times 10^6$ [A.m^{-2}.K^{-2}].

This type of the cathode is commonly made of tungsten doped with $1-2$ wt% of ThO_2; 2 wt% of La_2O_3, Y_2O_3, CeO_2 [20, 21]. The role of the dopant is to lower the thermionic work function of tungsten and therefore, the operating temperature, to which generally the erosion of the cathode is related. Sadek *et al.* have investigated the erosion rates of different cathode materials in 150 A. The La_2O_3 doped tungsten electrode is characterized by the lowest operating temperature (2750 K comparing to 3600 K of ThO_2) and the lowest erosion rate [22].

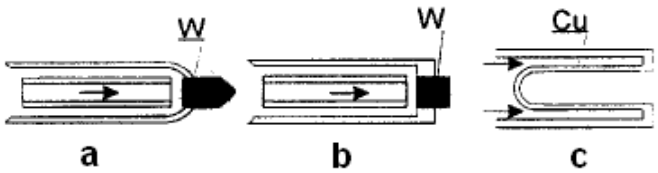

Figure 1.6: Schematic view of the cathode: a) stick-type; b) button-type; c) cold cathode [23].

As it is presented in Figure 1.6, two configurations of the hot cathode are commonly used: the stick-type and the button-type cathode. The power levels of torches using the stick-type cathode range between 10 and 150 kW, with arc currents below 1000 A. The button-type cathode is cylindrical and characterized by the diameter almost equals the length. This kind of cathode is inserted partially or completely in a water-cooled copper holder. It is used mainly in transferred arc configuration with the arc current until 3-6 kA. The cold cathode is commonly made of the copper, silver or alloy. It has a very simple cylindrical shape with the cylinder closed at the one side. The cold cathode torches work with the power levels from about 100 W to 10 MW and the arc current levels in the range 100-3000 A.

- **Anode**

The anode is a passive component used to collect the electrons to obtain the current flow from the electrical circuit to the plasma. The anode-nozzle, at which the localized heat flux can reach 160 $W.mm^{-2}$, should be water-cooled and made of high purity oxygen free copper, characterized by high thermal conductivity: 358 $W.m^{-1}.K^{-1}$ and thermal diffusivity: 114 x 10^{-6} $m^2.s^{-1}$ at 25°C, often with an insert of sintered tungsten. Typical nozzle diameters are between 6 and 10 mm for arc currents between 300 and 1000 A. The anode nozzle design can highlight different process parameters, as a high gas velocity, narrower or wider temperature profiles, different arc length and arc voltages. It has been shown that a smaller nozzle diameter results in shorter arcs, lower temperatures at the nozzle exit, but also higher velocities for the same current and mass flow rate [24]. The anode configuration can be separated into two groups: the anode surface perpendicular and parallel to the plasma jet axis. The first configuration is used in the case of transferred arcs. The anode surface parallel to the jet axis is commonly found in the plasma torches.

- **Gas injection**

Three types of the gas injection are used in the plasma spraying method: the axial, radial and swirl injection, presented in Figure 1.7.

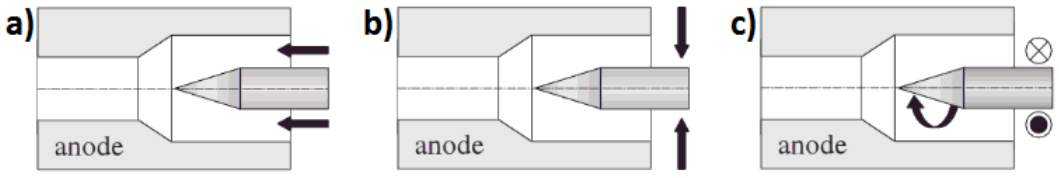

Figure 1.7: Schematic view of the gas injection: a) axial; b) radial; c) swirl [25].

In the axial injection the gas is injected parallel to the anode axis, Figure 1.7, and has the longitudinal velocity component. This type of the injection is mainly used in the torches with the stick-type cathode or the button-type for the high levels of the arc current (I > 1500A). In the case of the radial injection, the gas is injected perpendicular to the axis of the torch and presents strong radial component which afterwards is being reduced. In the swirl injection, the swirl flow creates the centrifugal forces, what pushes the cold gas towards the walls of the torch. The selection of the gas injection method has the influence on the arc current voltage, what was investigated in [26]. The use of the axial injector results in the longest arcs, the highest arc voltage, while the radial injection causes the shortest arc.

As has been mentioned, the plasma jet is produced by a torch in which the electrical arc is struck between a cathode, $\ominus$ in Figure 1.8, and an anode, $\oplus$. The arc column (3 in Figure 1.8) is developed from the cathode tip by pumping the part of the plasma forming gas (1), injected in the way described above.

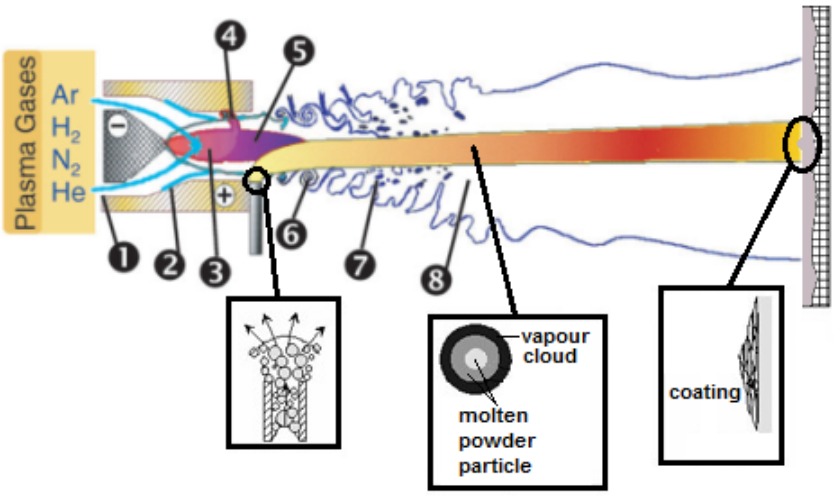

Figure 1.8: Schematic view of a plasma spraying method [15].

The arc column is characterized by a laminar flow which is limited by an isothermal envelope at $T = T_c$ (where T_c is the critical temperature, defined in the section of Stationary behavior of the torch). Outside this area no electrical conduction is possible, which appears as a boundary between the arc column and the "cold" sheath (2 in Figure 1.8). Therefore, this column is constructed from the tip of the cathode to point on the anode wall, presented as (4) in 1.8. This arc attachment to the nozzle wall is perpendicular to the anode surface and is in the form of a high-temperature, low-density gas column cutting through the cold gas boundary layer. The thickness of this layer depends strongly on the plasma process parameters: the arc current, nozzle internal diameter, injection of plasma forming gases. The studies of the arc attachment to the anode wall have shown

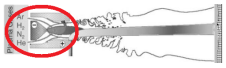

that it continuously fluctuates in length and position [27, 28]. This is due to the axial and rotational movements induced by the drag forces exerted by the cold flow in the boundary layer and the Lorentz forces. The rotational movement of the arc attachment is strongly favored by the swirl injection of the plasma forming gas. The axial displacement of the arc root gives the variation in the length of the arc column and, therefore, in enthalpy. The rotational displacement results in a nonsymmetry in the gas flow field and, consequently, inhomogeneity in the plasma jet. While the plasma jet, characterized by low density (approximately 1/30 of that of the cold gas) and a high speed (between 600 and 2200 m/s), exits the torch nozzle, it meets the surrounding atmosphere, what results in creating the swirl rings. They coalesce and cause large scale eddies (6 in Figure 1.8) which introduce cold surrounding gas bubbles (7).

1.2.1.1 Characteristic of the plasma jet

The plasma is a complex mixture of gases, chemically neutral in order to reduce the erosion of electrodes. Typical plasma forming gases are argon (Ar), hydrogen (H_2), helium (He) and nitrogen (N_2). The choice of the injected gas plays a significant role in the plasma spraying technique. It defines important plasma thermodynamic and transport properties. The following paragraph is focused on the determination of these characteristics by the choice of the plasma forming gas. Firstly, the plasma state and laws describing this state of matter are given.

1.2.1.1.1 Plasma state

The plasma in the plasma spraying method is obtained by the electric discharge produced by the direct current torch. The energy from the applied discharge is supplied to the plasma forming gas. If this energy is sufficiently high, it results in: the dissociation of molecules ($X_2 \longrightarrow 2X$) in case of molecular gases and the ionization of atoms ($X \longrightarrow X^+ + e$), where X symbolizes particular gas. Boulos *et al.* have summarized the energies of the main plasma forming gases, presented in Table 1.1.

Table 1.1: Ionization and dissociation energies of the plasma forming gases [17].

Species	Ar	He	H	N	H_2	N_2
Ionization energy(eV)	15.755	24.481	13.659	14.534	15.426	15.58
Dissociation energy(eV)	-	-	-	-	4.588	9.756

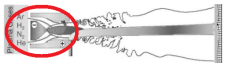

To sustain the plasma in thermal spray processes a relatively small degree of ionization of the gas is required (less than 1-3%). The degree of ionization is defined as follows:

$$\alpha = \frac{n_i}{n_n + n_i} \simeq \frac{n_i}{n_n} \tag{1.2}$$

where:

n_i is the number density of ionized atoms,

n_n the number density of neutral atoms.

In plasma systems, complete thermodynamic equilibrium (CTE) is related to uniform homogeneous plasma, in which kinetic and chemical equilibra are unambiguous functions of temperature. This temperature is supposed to be homogeneous and the same for all degrees of freedom, all the plasma system components, and all their possible reactions. Therefore, the following conditions should be fulfilled:

- The plasma is isotropic: the particles do not favor any direction of propagation. The velocity distribution functions for particles of every species must follow a Maxwell distribution as follows:

$$\frac{dn}{n} = \Big(\frac{m}{2\pi k_B T}\Big)^{3/2} exp\Big[-\frac{mv^2}{2k_B T}\Big] 4\pi v^2 dv \tag{1.3}$$

  where m is the mass of the particle and n the total number of particles.

- The population density of the excited states of every species follows a Boltzmann distribution:

$$\frac{n_j}{n} = \frac{g_j}{Q^{int}} exp\Big[-\frac{E_j}{k_B T}\Big] \tag{1.4}$$

  where:

  n_j, g_j, E_j are respectively the density of population, the statistical weight and energy associated with the level j,

  Q^{int} the partition function of the particular species, defined as follows: $Q^{int} = \sum_i g_i exp\Big[-\frac{E_i}{k_B T}\Big]$.

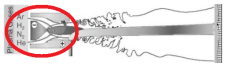

- The ionization equilibrium is described by the Saha equation:

$$\frac{n_e n_i}{n_0} = \frac{2{Q_i}^{int}}{{Q_0}^{int}}\left[\frac{2\pi k_B T m_e}{h^2}\right]^{3/2} exp\Big(-\frac{E_i - \Delta E}{k_B T}\Big) \tag{1.5}$$

where:

n_e, n_i, n_0	are the densities of electrons, the charged and neutral species,
${Q_i}^{int}, {Q_0}^{int}$	the partition functions of ionized atoms with the factor 2 corresponded to the statistical weight of the electron,
E_i	the ionization energy of the gas,
ΔE	the correction due to the decrease of E_i by electric-field effects.

Moreover, the law of mass action of Guldberg-Waage, describing the molecular dissociation, should be also introduced:

$$\frac{n_a n_b}{n_{ab}} = \frac{{Q_a}^{int}{Q_b}^{int}}{{Q_{ab}}^{int}}\left[\frac{2\pi k_B T M_a M_b}{(M_a + M_b)h^2}\right]^{3/2} exp\Big(-\frac{D_{ab}}{k_B T}\Big) \tag{1.6}$$

where:

n_a, n_b, n_{ab}	are respectively the densities of the species: a, b and ab,
D_{ab}	the dissociation energy of the molecule ab.

- The electromagnetic radiation field is that of blackbody radiation of intensity, what is given by the Planck function:

$${L_\lambda}^0(T) = \frac{2hc^2}{\lambda^5}\Big[exp\Big(\frac{hc}{\lambda k_B T}\Big) - 1\Big]^{-1} \tag{1.7}$$

However, the plasma in CTE conditions cannot be practically produced in the laboratory. Most plasmas are optically thin over a wide range of wavelengths and, therefore, the plasma radiation is much less than that of a blackbody. Consequently, the plasma produced by e.g. dc torch is considered in more realistic approximation, so-called local thermodynamic equilibrium (LTE).

According to the LTE approach, a thermal plasma is considered as optically thin and thus does not require a radiation field that corresponds to the blackbody radiation, what means that the Planck's law is no longer valid. However, the collisional processes are required to be locally in equilibrium. Therefore, the populations of all species and their excited levels are described by the presented above equations of Maxwell, Boltzmann, Saha and Guldberg-Waage, but with a temperature, which can differ from point to point in space and time.

Consequently, the plasma can be considered in the local thermodynamic equilibrium when the following conditions are fulfilled:

- The different species of the plasma have a Maxwellian distribution
- The plasma is in the kinetic equilibrium. The ratio E/p (where E is the energy that electron receives, p is the pressure) is sufficiently small that the temperatures of electrons, T_e, and heavy particles, T_h, approach each other $T_e = T_h$, what is presented in Figure 1.9.

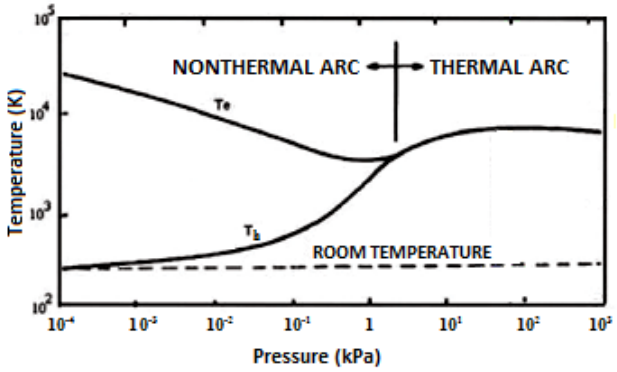

Figure 1.9: Evolution of electron temperature (T_e) and heavy particle temperature (T_h) in a mercury arc plasma [29].

- The collisions are the dominating mechanism for excitation (Boltzmann distribution) and ionization (Saha equilibrium).
- The spatial variations of the plasma properties are sufficiently small to give the chemical equilibrium.

However, it has been highlighted [17, 29, 30] that the equilibrium can be reached in the plasma core, not in the plasma boundaries, due to fast diffusion of electrons, and close to the walls or electrodes, where is a lower amount of the collisions.

1.2.1.1.2 Thermodynamic and transport properties

The choice of the injected gas plays a significant role in the plasma spraying technique. It defines important plasma thermodynamic and transport properties: the specific enthalpy, electrical conductivity, viscosity, thermal conductivity, which will be described in the following paragraph.

The total enthalpy of the gas for high-velocity flows, h_0, has two components: kinetic enthalpy and static enthalpy related to the internal energy. The specific enthalpy is determined by the following equation:

$$h_0 = h_g + \frac{v_g^2}{2} \tag{1.8}$$

where:

v_g is the gas velocity,
h_g the static enthalpy related to the internal energy, defined as following:

$$h_g - h_g^{ref} = \int_{T_{ref}}^{T} c_p(T)dT \tag{1.9}$$

where:

h_g^{ref} is the total enthalpy at the reference state: T = 0 K, p = 1 atm,
c_p the specific heat.

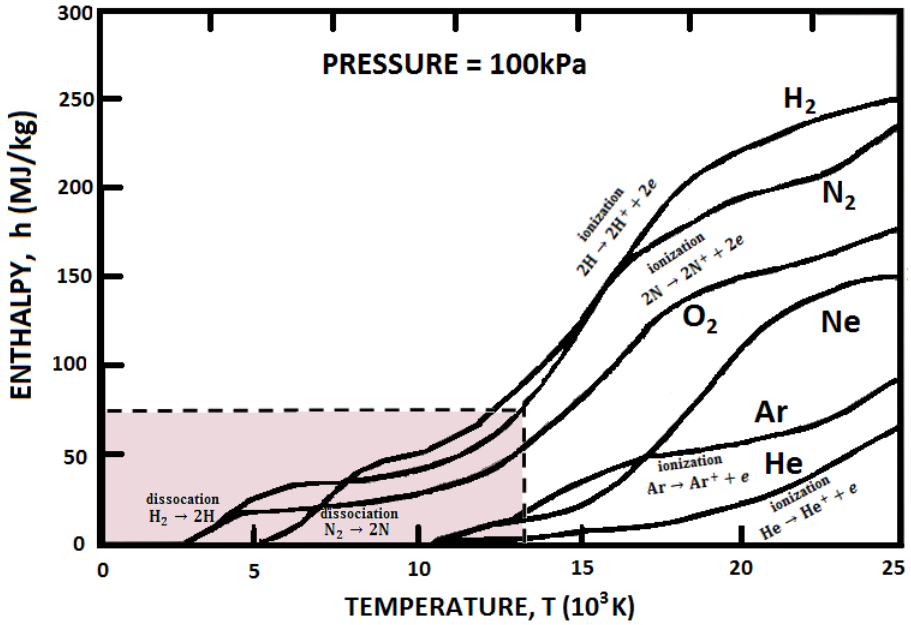

Figure 1.10: Specific enthalpy of various gases at atmospheric pressure with indicated region of interest [17].

Figure 1.10 shows the enthalpy of different plasma gases (N_2, H_2, Ar, He and O_2) as a function of temperature at atmospheric pressure. The plasma produced by dc plasma torch is characterized by the temperature up to 14 000 K, what has been indicated on the diagram. As can be noticed, the molecular gases have higher values of the enthalpy. The observed steep variations are caused by the heats of reaction (dissociation and ionization of the gas).

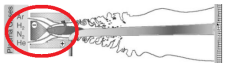

The use of argon provides high plasma temperature due to comparatively low enthalpy. The thermal expansion and thus high pressure lead to high plasma velocity. Adding helium further increases the velocity of the plasma. Therefore, argon/helium plasma is often referred to as cold and fast-moving whereas nitrogen/hydrogen is referred to as hot plasma.
In the plasma, the electrons and ions drift under the influence of an applied electric field, E, what gives rise to the density of the electric current, j, and can be presented by Ohm's law:

$$\vec{j} = \sigma_e \vec{E} \tag{1.10}$$

where:
σ_e is the electrical conductivity, which can be defined by the following equation after applying the simplifications for the ions ($n_i = n_e$ and $\mu_i \ll \mu_e$):

$$\sigma_e = e.n_e.\mu_e \tag{1.11}$$

where:

e	is the electron charge (1.6×10^{-19} C),
n_e	the electron density,
μ_e	the electron mobility.

As it is presented in Figure 1.11 the values of the electrical conductivity for Ar, H_2 and N_2 are close, within the temperature difference of 1000 K, what can be explained by the similar values of the ionization energies of these gases, noted in Table 1.1.

For helium the difference of the electrical conductivity is more significant. The temperature values are shifted by around 5000 K due to higher ionization energy.

The viscosity, μ, demonstrates the balance between the friction force in the direction of the plasma flow and the velocity gradient in the orthogonal direction. The dependence of μ on the temperature for different gases is presented in Figure 1.12. The drop of viscosity for temperatures above 10 000 K for Ar, H_2, N_2 and 17 000 K for He is due to ionization of the gas. When this process is significant the charged-species densities increase and their mobility decreases. Therefore, the molecular viscosity of thermal plasmas reaches its maximum when the volume fraction of the electrons reaches about 3%.

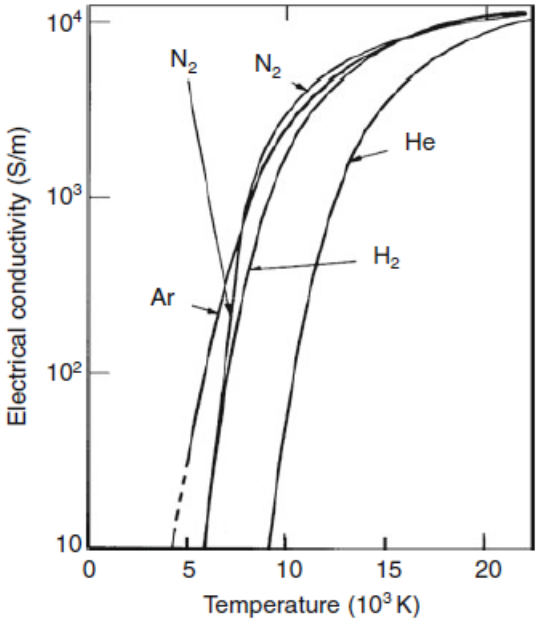

Figure 1.11: Dependence on the temperature of electrical conductivity of various gases [31].

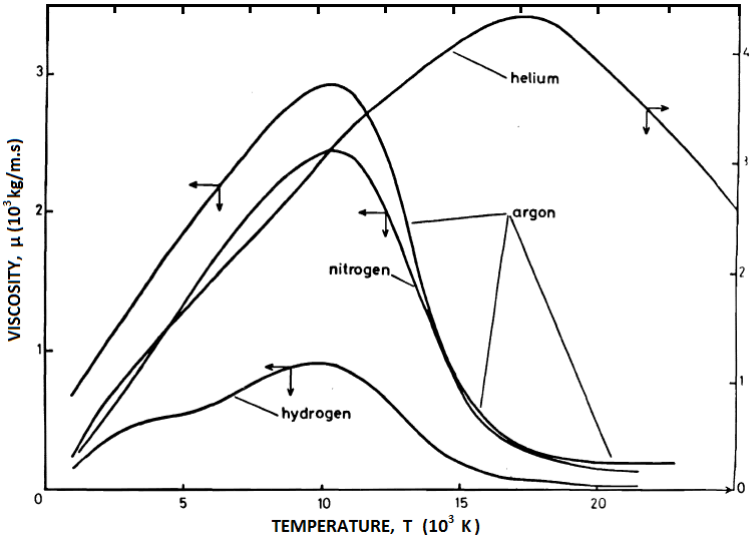

Figure 1.12: Temperature dependence of the viscosity of various gases (H_2, N_2, Ar, He) at atmospheric pressure [31].

As can be assumed from Figure 1.12 by adding helium to argon (He less than 60 vol.%) the viscosity keeps increasing up to 15 000 K instead of 10 000 K characteristic for argon. Then, it starts to decrease due to helium ionization. It permits to run slightly longer Ar-He jet than this obtained with Ar-H_2 mixture. Moreover, while mixing hydrogen with argon (H_2 less than 30 vol.%) the viscosity of argon is only slightly reduced as well as in case of N_2-H_2 mixture.

The thermal conductivity, κ, is one of the most important parameters of the thermal plasmas, which controls the energy losses in the arc as well as the heat transfer to sprayed particles. The thermal conductivity can be presented as the sum of three terms: $\kappa = \kappa_{tr} + \kappa_R + \kappa_{int}$, where κ_{tr} results from the translation of species and is divided into: κ_{tr}^h and κ_{tr}^e. The first element corresponds to the translational thermal conductivity of heavy species. The second, κ_{tr}^e, is the translational thermal conductivity of electrons, which becomes important above 8,000 K. κ_R, reactional thermal conductivity, results from the chemical reactions (dissociations, ionizations) and κ_{int}, internal thermal conductivity, from the internal degrees of freedom.
The temperature dependence of the thermal conductivity of the mixtures of argon with light gases is illustrated in Figure 1.13.

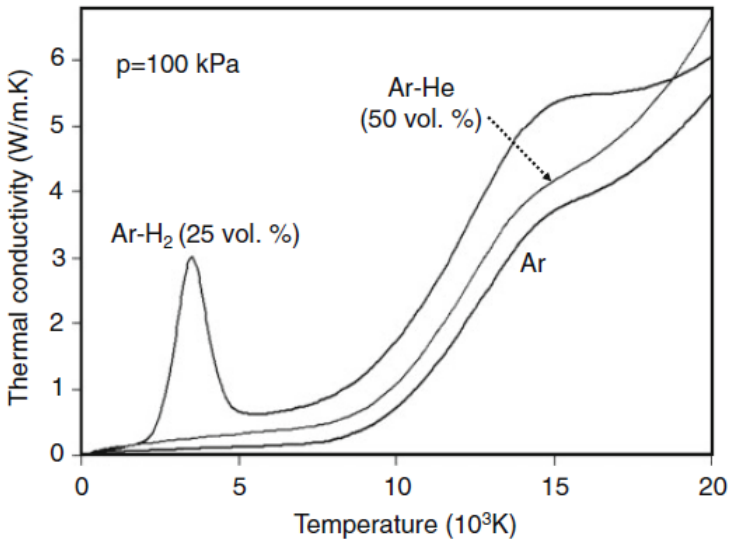

Figure 1.13: Temperature dependence of the thermal conductivity of the mixtures: Ar-H2 (25 vol.%), Ar-He (50 vol.%), and Ar at atmospheric pressure [17].

The mixture Ar-H_2 (25 vol.%) is characterized by the highest value of the thermal conductivity with the strong dissociation peak between about 2 500 and 5 000 K. The addition of helium to argon (He 50 vol.%) increases the thermal conductivity more regularly, what results in the values between these ones of argon and the argon-hydrogen mixture.
As has been presented, the plasma forming gases are characterized by different properties. Therefore, the mixtures of monatomic and molecular gases are often used in plasma spraying process [15, 23, 32].

1.2.2 Material injection

The plasma spraying is the method in which the molten material, by the plasma jet, is deposited on the substrate to form the coating. The previous part has presented the central part of this technique, the dc torch which converts the supplied energy into the stream of plasma. To obtain the coating the material has to be injected, heated and accelerated by the plasma jet toward a substrate. Therefore, the following section is focused on the material injection methods, what represents the second phase of the plasma spraying, indicated in Figure 1.3. Firstly, the technique used in the conventional APS method will be described. Than, the injection of the suspension droplets and the thermo-physical phenomena associated with this process will be presented.

1.2.2.1 Material injection in conventional plasma spraying

In the conventional plasma spraying method (APS) the powders with the diameters typically between 10 μm and 110 μm are injected to the plasma jet. The material injection is performed mainly by a straight tube with an internal diameter in the range of 1.5 - 2 mm. Powder particles are carried by the gas, e.g. argon, with the flow rate in the range of 3 to 10 slm. In the case of conventional dc plasma torches the material is introduced to the plasma jet radially. The axial injection is performed in new designs of the torch, e.g. Axial III which will be presented in next sections.

1.2.2.2 Suspension injection

As has been mentioned before, the following thesis is focused on the studies of dc plasma torch associated with the suspension injection. The suspension is formulated by the dispersion of fine powder particles within a solvent with the components which are added in order to improve the rheological properties, decreasing the agglomeration of fine solids and slowing down their sedimentation. The following section presents the suspension preparation process and different methods of the suspension injection.

1.2.2.2.1 Suspension preparation

The suspension suitable for SPS process generally consists of the solid submicron or nanosized powder, the solvent and chemical additives. The first mentioned component of the suspension is the powder. The chemical components, size of particles, technology used in production are very important factors in the powder fabrication. The powders are

mainly produced by the chemical precipitation processes, mechanical crushing, milling, thermal treatments. The choice of the solvent is very important for the liquid feedstock properties such as low viscosity and good stability. Table 1.2 presents the parameters of main liquids used in the suspension: water and ethanol.

Table 1.2: The parameters of the most common solvents for the suspension preparation [33].

Liquid	Surface tension	Viscosity	Specific heat	Latent heat of vaporization	Vaporization temperature
	σ_s ($J.m^{-2}$)	μ_s (Pa.s)	c_p ($J.kg^{-1}.\kappa^{-1}$)	L_V ($J.kg^{-1}$)	T_V (K)
Water	72×10^{-3}	10^{-3}	4.18×10^3	2.26×10^6	373
Ethanol	22×10^{-3}	1.06×10^{-3}	2.44×10^3	0.84×10^6	351

Comparing the properties of these two liquids it can be stated that water requires more energy than ethanol to get vaporized. In addition, ethanol is characterized by a lower surface tension. Nevertheless, it contains carbon which can pollute the coatings. Therefore, the mixture of the ethanol with water are commonly used.
A typical suspension preparation process is outlined in Figure 1.14.

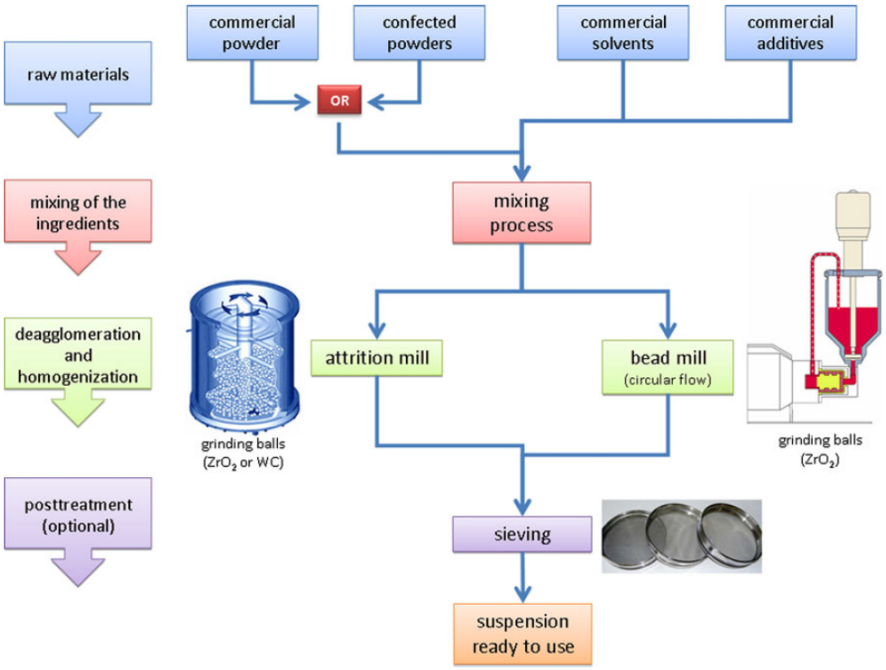

Figure 1.14: General preparation route for the suspension [34].

The most common way to produce the suspension is to make a simple slurry with powder particles and a solvent. To obtain good homogenization and deagglomeration of the suspension the slurry is treated by the attrition or bead milling. However, this process can be not sufficient for the nano-sized particles, especially of oxides which have the

tendency to agglomerate or aggregate. As shown in Figure 1.14 the dispersant is being added to the liquid feedstock to stabilize the powder within the solvent, e.g. a phosphate ester mixed with zirconia particles in [35]. It adsorbs on the particle surface and allows an effective dispersion of particles by electrostatic, steric, or electro-steric repulsions. By adding some supplements, e.g. ammonium polyacrylic acid (PAA) or polyvinyl alcohol (PVA), to the liquid feedstock is possible to modify the surface tension or the viscosity of the suspension. Good adjustment of these properties is important for the material injection and the treatment of the suspension droplets by the plasma, what is outlined in the following sections.

1.2.2.2.2 Suspension injection methods

In suspension plasma spraying the liquid material is injected to the plasma jet by an adequate method. In the conventional systems the injection is carried out mainly by the atomization and mechanical injection. The following chapter describes these conventional methods. Moreover, new techniques, which enable to control the injection moment, will be presented.

1.2.2.2.2.1 Spray atomization

This method uses an external energy, the atomizing gas, to break up the liquid into droplets. The low velocity liquid is injected inside a nozzle where is fragmented by a gas (mostly Ar because of a high mass density, presented in e.g. [36]) expanding within the body of the nozzle. Fauchais *et al.* have defined the types of break-up mechanisms due to the liquid viscosity, μ_l [37, 38]. The liquids with the viscosity between 0.1 and 50-60 mPa.s break-up into drops according to the Weber number, We, which is the ratio of the force exerted by the flow on the liquid to the surface tension force, defined as following:

$$We = \frac{\rho_g . v_r^2 . d_l}{\sigma_l} \tag{1.12}$$

where:

ρ_g	is the gas mass density,
v_r	the relative velocity between the gas and the liquid,
d_l	the diameter of the liquid droplet,
σ_l	the surface tension of the liquid.

For a fluid with higher viscosity the Ohnesorge number, Oh, has to be also considered. It relates the viscous forces to inertial and surface tension forces, according to the equation:

$$Oh = \frac{\mu_l}{\sqrt{\rho_g . d_l . \sigma_l}} \tag{1.13}$$

The typical sizes of atomized material droplets range between 2 and 100 μm, the corresponding velocities varying from 5 to 60 m/s.
There are many types of atomizers. One of the most widely used, the pneumatic droplets generator, is presented in Figure 1.15. It consists of a robust steel chamber, a nozzle at the bottom and a T-junction arrangement at the top.

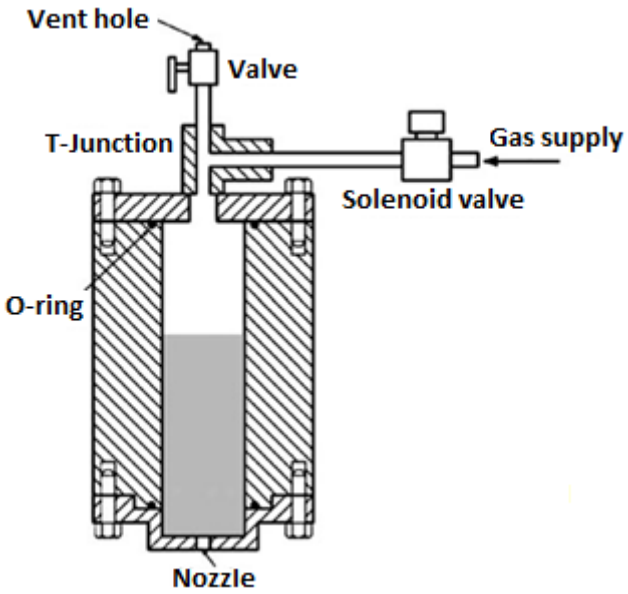

Figure 1.15: Schematic of a pneumatic droplet generator [39].

The functioning of pneumatic droplet generator based on applying pulses of a pressurized gas to the liquid contained in the chamber. The gas pulse forces out droplets through the nozzle in the bottom plate of the generator. A solenoid valve is rapidly opened and closed to create pressure pulses. In each pulse, one or more droplets emerge from the nozzle exit. The nozzle is a cylindrical synthetic sapphire nozzle of about 0,1 mm diameter. Due to this small size, droplets only may be ejected if a gas pressure pulse is applied. Droplet generation in this technique is controlled by the gas pulse duration (solenoid valve duration), the vent hole diameter and the gas supply pressure. In rotary atomizers centrifugal forces are used to further enhance the breakup process [40,41]. In this case the liquid is supplied to the centre of a spinning disk and liquid sheets or ligaments are thrown off the edges of the disk. Other types include vibratory and ultrasonic atomizers (or nebulizers), where the drops are formed by vibrating the injector nozzle at high frequencies and at large amplitudes to produce short-wave length disturbances to the liquid flow.

Ultrasonic atomizers are used in the applications where very fine sprays (submicron sizes) are required. The electrostatic atomizers can be also used for the generation of the droplets. In this type of atomizer the spray liquid is charged by applying a high-voltage drop across the nozzle. The dispersion of the spray drops is increased by exploiting electrical repulsive forces between the droplets.

1.2.2.2.2.2 Mechanical injection

In the mechanical injection, shown in Figure 1.16, the suspension is stored in the pressurized tank from where it is forced through a nozzle of specified internal diameter, d_n [33, 42–44]. Fazilleau *et al.* have used a calibrated nozzle hole with the diameter of 150 μm fabricated by the electro-erosion [43] and Etchart-Salas *et al.* have presented the results obtained by a laser-machined nozzle of diameter varying from 50 to 300 μm [33,44].

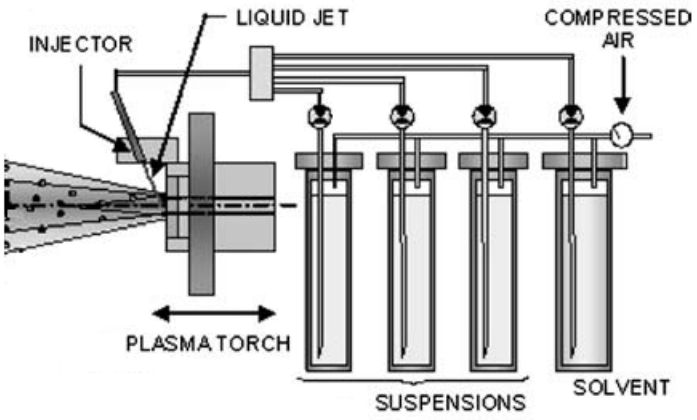

Figure 1.16: Schematic view of a mechanical injection [43].

The size of the droplets depends on the internal nozzle diameter following the relation: $d_l \simeq 1.9 \times d_n$ [45]. The suspension injection, in the mechanical method, is controlled by the pressure of the liquid in the reservoir. The mass flow rate, $\dot{m}_l$, is determined by the following equation:

$$\dot{m}_l = \rho_l . v_l . S_n \tag{1.14}$$

where:

ρ_l	represents the liquid specific mass,
v_l	the liquid average velocity at the nozzle exit,
S_n	the cross section area of the nozzle hole.

The gas pressure difference, Δp, between the pressure in the container and the surrounding atmosphere is depicted by the equation:

$$\Delta p = \frac{f.\rho_l.v_l^2}{2} \tag{1.15}$$

where:

f is the friction coefficient of the liquid in the injection nozzle which depends on nozzle

Fazilleau *et al.* have shown that the square of the liquid velocity varies linearly with the pressure of the reservoir. For example, injection velocities between 25 and 35 m/s were obtained with a tank pressure between 0.2 and 0.6 MPa.

1.2.2.2.2.3 Alternative suspension injection methods

New methods have been developed to control the properties of the liquid injection. Blazdell *et al.* have highlighted the possibility of continuous suspension injection by superimposing a modulation signal to piezoceramic material of dc jet printer head (Domino Inkjet, Japan), presented in Figure 1.17 [46]. The liquid was forced through a 50 μm diameter nozzle under pressure (up to 0.5 MPa), superimposed by a piezoelectric drive rod modulated with frequency of 64 kHz. Using this operating frequency permits to produce 64000 drops per second.

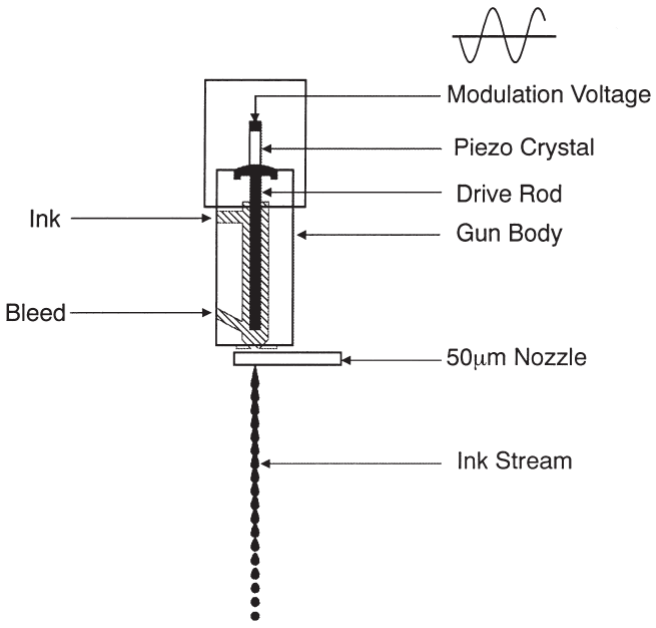

Figure 1.17: Schematic view of a jet printer head [46].

The drop diameter, d_l, depends on the factors, presented by the following equation:

$$d_l = \left[\frac{3d_n^2.v_l}{2f}\right]^{1/3} \tag{1.16}$$

where:

d_n	is the nozzle orifice diameter,
v_l	the stream velocity,
f	the frequency of piezoelectric modulation.

The equation above shows that the drop diameter is a function of the liquid flow velocity and therefore these two important parameters can not be controlled separately. Oberste Berghaus *et al.* have described the similar method using a magnetostrictive drive rod (Etrema AU-010, Ames, Iowa) [47]. The suspension was injected from the pressurized reservoir through the nozzle with diameters varied between 100 and 255 μm. A magnetostrictive drive rod, mounted at the nozzle, applied the pressure pulses at different frequencies up to 30 kHz. This new injection method allowed producing 400 μm drops with 10 μs delay between each and with a velocity of 20 m/s.
Both methods permit to control the droplet diameter, flow rate and velocity. By superimposing signal to the injection head the uniformly spaced, suspension droplets can be generated.

1.2.2.2.3 Thermo-physical phenomena of the droplets

The coatings obtained by the suspension plasma spraying method depend on the interaction between the plasma jet and the injected feedstock material. Therefore, understanding the movement and heating of the suspension droplets inside the plasma is the important part in the process. The study of the interactions between the liquid and the plasma jet should take into account the heat and momentum transfer to the particles, particle fragmentation and evaporation processes.

1.2.2.2.3.1 Suspension penetration into the plasma jet

While the suspension jet or drops are injected to the plasma jet they are progressively or rapidly fragmented into droplets. It results in the decrease of their volume, what causes that the injection force of the droplets and force imparted to them by the gas jet are being decreased. Therefore, the droplets do not penetrate any more into the plasma jet.

Fazilleau has presented the condition for good suspension penetration into the plasma jet [35]:

$$\rho_l {v_l}^2 \gg \rho_p {v_p}^2 \tag{1.17}$$

where:

ρ_l	is the liquid density,
ρ_p	the plasma mass density,
v_l	the liquid velocity,
v_p	the plasma velocity.

Once the suspension droplets are entrained into plasma jet, they undergo the fragmentation process due to a strong shear stress (generated by the plasma flow) and the liquid vaporization caused by high plasma heat flux. The fragmentation depends on the dimensionless Weber number defined as follows:

$$We = \frac{{v_r}^2 . d_l . \rho_p}{\sigma_l} \tag{1.18}$$

where:

v_r	is the relative velocity between the gas and the liquid,
d_l	the diameter of the droplet,
σ_l	the surface tension of the liquid.

Pilch and Erdman have determined the mechanisms of drop break-up according to We number, presented in Figure 1.18 [48].

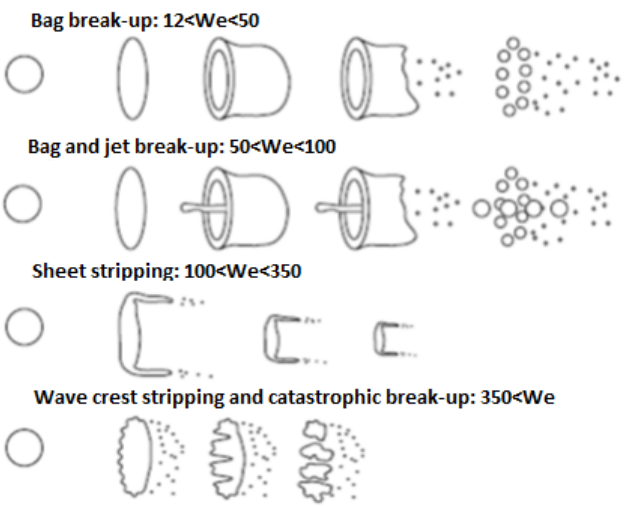

Figure 1.18: Droplet break-up mechanisms [48].

For $12 < We < 50$ and $50 < We < 100$ the fragmentation is called "bag break-up" and "bag and jet break-up" because it corresponds to the deformation of the drop as a bag-like structure. The droplet is stretched and swept off in the flow direction.
For $100 < We < 350$ the process is named "sheet stripping" fragmentation. Thin pieces of liquid are drawn from the periphery of the deforming droplets.
For $We > 350$ the fragmentation is called "wave crest stripping and catastrophic break-up" what corresponds to a multistage breaking process.
Moreover, the studies of the fragmentation process have shown that a Weber number of about 14 has been the critical value over which the droplet undergoes breakup. It has been highlighted by Basu *et al.* who have studied the phenomena associated with solution precursor plasma spray (SPPS) process [49, 50].
Once the suspension droplet is injected into the plasma it is exposed to the aerodynamic, F_a, and the surface tension, F_s, forces. The aerodynamic force of the plasma jet results in the break-up of the drop and the surface tension of the liquid opposes this force. To determine the minimum droplet diameter (d_f), when the fragmentation is completed, both forces are considered as following:

$$\frac{\pi}{8}.C_D.{d_f}^2.\rho.v^2 = \pi.d_f.\sigma \tag{1.19}$$

where:

C_D	is the flow drag coefficient,
ρ	the plasma specific mass ,
v	the relative velocity between flow and drop,
σ	the droplet surface tension.

The minimum droplet diameter is then given by:

$$d_f = \frac{8.\sigma}{C_D.\rho.v^2} \tag{1.20}$$

The droplet diameter (d_f), when the fragmentation is completed, depends strongly on the liquid and the plasma flow velocity, what is shown in Table 1.3. The calculations of d_f are presented for Ar-H_2 plasma jet.

Table 1.3: Calculation of fragmentation times for ethanol and water droplets for different plasma jet velocities [51].

	v (m/s)		
Calculation of d_f (μs)	500	1000	2000
Water	0.52	0.29	0.15
Ethanol	0.57	0.3	0.14

The important parameter of the fragmentation is the time duration of this process. Fazilleau *et al.* have shown that the fragmentation time, t_f, is given by [43]:

$$t_f = \frac{8\sigma(\frac{r_s}{r_d} - 1)}{C_D.\rho.v^3} \tag{1.21}$$

The model presented by Fazilleau considers that the radius of the initial droplet (r_s) is fragmented into n droplets of radius (r_d): $r_s{}^3 = n.r_d{}^3$.
All the droplets introduced into the plasma jet undergo heating resulting in solvent vaporization which is obtained by the energy balance equation:

$$4\pi.{r_s}^2.h_c(T - T_s) = L_V.\rho_s.\frac{dV_s}{dt} \tag{1.22}$$

where:

h_c	is the heat transfer coefficient, defined as follows: $h_c = \frac{\overline{\kappa}.Nu}{2r_s}$,
T	the plasma temperature,
T_s	the temperature at the surface of the liquid,
L_v	the latent heat of the liquid vaporization,
$\frac{dV_s}{dt}$	the volume variation of the droplet, determined as: $\frac{dV_s}{dt} = 4\pi {r_s}^2 \frac{dr_s}{dt}$.

Assuming that during the vaporization time, t_v, the drop radius varies from r_s to 0, t_v is defined by the equation:

$$t_v = \frac{L_V.\rho_s.{r_s}^2}{(T - T_s)\kappa.Nu} \tag{1.23}$$

Figure 1.19 presents the comparison between the fragmentation and the vaporization times of ethanol droplet in the plasma jet (Ar-H_2, 45-15 slm, 500 A, anode nozzle diameter 7 mm).

It highlights that the fragmentation time is at least two orders of magnitude lower than the vaporization time. This difference is increased when the buffer effect of the vapour cloud around droplets is taken into account.

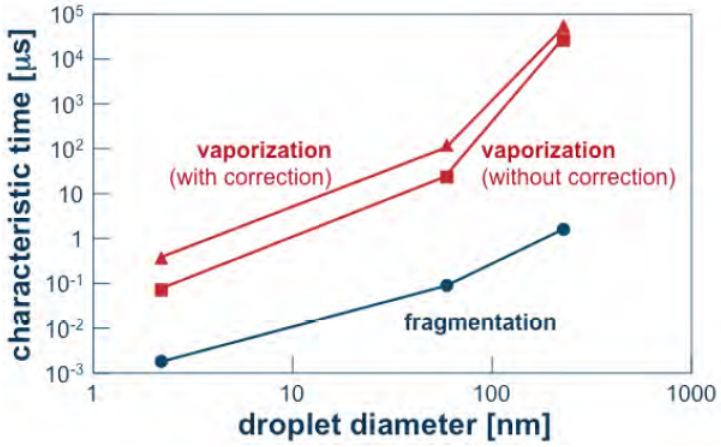

Figure 1.19: Variation of fragmentation and vaporization time of ethanol droplets inside Ar-H_2 plasma jet [43].

1.2.2.2.3.2 Behaviour of the particle in plasma jet

The mechanism of the heat transfer from the plasma to the particle and the particle to the surroundings is presented in Figure 1.20.

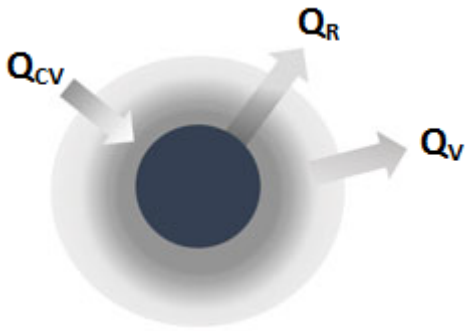

Figure 1.20: Schematic view of the heat transfer between the particle and the plasma [51].

The balance between conduction and convection heat (Q_{CV}) transfers from the hot gas to the particle and particle cooling due to radiative heat losses from the surface (Q_R) and losses from radiating vapour (Q_V) determines the net heat transfer to a particle (Q_{net}) by the following equation:

$$Q_{net} = Q_{CV} - Q_R - Q_V \tag{1.24}$$

The convection process has a major contribution to the heat transfer at the moment of the droplet injection to the plasma jet and at the end of particle flight if the gas become cooler and slower than the particle. The conduction is important when the relative velocity decreases, what corresponds to the middle of the particle flight. The radiative losses are significant when the temperature and size of the particles are relatively high.

Boulos *et al.* have shown that they affect the heat transfer in the case of pure argon plasmas when the heat transfer coefficient, h_c, is low [17].
The conduction and convection mechanisms are usually described by the Nusselt number:

$$Nu = \frac{h_c.d_l}{\kappa} = 2 + 0.6 \times Re^{0.5} \times Pr^{0.33} \tag{1.25}$$

where:

κ	is the thermal conductivity of the fluid,
d_l	the liquid particle diameter,
Re	Reynolds number,
Pr	Prandtl number.

The first term of the right-hand side of Equation (1.25) determines the conduction mechanism. It is dominant in the case of small values of Reynolds number, Re, defined as follows:

$$Re = \frac{v_r.d_l.\rho_g}{\eta_l} \tag{1.26}$$

where:

v_r	is the relative velocity between the gas and the liquid,
ρ_g	the gas mass density,
η_l	the liquid particle viscosity.

The conduction mechanism is principal when i.e. the particle has a velocity nearly equal to the velocity of the gas. Such a case occurs when a particle is in the middle of its flight. Otherwise, the second term, the Prandtl number, must be considered, defined as:

$$Pr = \frac{c_{p_g}\eta_p}{\kappa} \tag{1.27}$$

In the case of nanometer and sub-micrometer sized particles of the suspension the Knudsen effect, which reduces the heat transfer, should be also considered. It depends on the Knudsen number defined as follows:

$$Kn = \lambda/d_p \tag{1.28}$$

where λ defines the mean free path of the plasma molecules. It has been demonstrated that the Knudsen effect should be taken into account when the ratio of the plasma molecules mean free path, λ, to the particle diameter, d_p, is smaller than one ($0.1 < Kn < 1.0$) [17]. While the particle is moving in the plasma jet is exposed to a number of forces, which act

simultaneously on the particle and have varying influence on its trajectory and residence time in the plasma. The most important impact have inertia forces, F_i, and the viscous drag forces, F_D, defined as follows:

$$F_i = \frac{\pi {d_p}^3}{6}.\rho_p.\frac{dv_p}{dt} \tag{1.29}$$

$$F_D = \frac{\pi {d_p}^2}{4}.C_D.\frac{1}{2}.\rho_g.{v_r}^2 \tag{1.30}$$

As Pawlowski has presented, in most practical cases met in thermal spraying, only the drag force is taken into account and the force balance around a single particle in motion in a plasma flow can be written as: $F_i = F_D$ [42]. The drag coefficient, C_D, depends on the particle velocity relative to the flame velocity, what is determined by the Re number and presented in Table 1.4.

Table 1.4: Equations for C_D of a single sphere according to the Re number [42,51].

$C_D = \frac{24}{Re}$	$Re < 0.2$
$C_D = \frac{24}{Re}[1 + 0.187 \times Re]$	$0.2 \leq Re < 2$
$C_D = \frac{24}{Re}[1 + 0.11 \times Re^{0.81}]$	$2 \leq Re < 20$
$C_D = \frac{24}{Re}[1 + 0.189 \times Re^{0.62}]$	$20 \leq Re < 200$

In the case of the particles below 0.1 μm the thermophoresis force should be taken into account in the areas characterized by the steep temperature gradients. The small particles change their trajectories from the plasma core to the jet fringes characterized by lower gas temperature and velocity. Moreover, because of their low inertia, the particles can follow the hot gas trajectory which flows parallel to the substrate surface and never impact on it. It occurs when the particles velocity is below: $St < 1$. St, the Stokes number, characterizes the behaviour of particles suspended in a fluid flow, as follows:

$$St = \frac{\rho_p {d_p}^2 v_p}{\mu_g \iota_{BL}} \tag{1.31}$$

where:

ρ_p is the particle specific mass,
μ_g the gas viscosity,
ι_{BL} the thickness of the flow boundary layer, BL, in front of the substrate.

When $St > 1$, that is when particles velocity is high enough, particles can cross the boundary layer that develops at the substrate surface and impact on it.

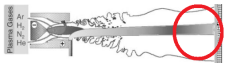

1.2.3 Coatings formation

The following section presents the last phase of the plasma spraying process- the material deposition.
Particles with given temperatures (above or close to their melting temperature) and velocities impact and flatten on the substrate, or previously deposited material, forming lamellae (splat). At impact with the substrate the particle flattens and the high pressure inside it forces melted material to flow laterally and ductile material to deform. The particle kinetic energy is transformed into work of viscous deformation and surface energy. The structure of the splat results from the spreading and solidification of the particles onto the substrate, what depends on the following parameters:

- the velocity and size of particle
- properties of the particle material in the liquid state, e.g. viscosity, surface tension
- ability of the wetting the substrate by liquid particles
- impact angle relative to the substrate
- surface roughness of substrate

The splat adhesion to the substrate depends strongly on the surface morphology of the base material. Therefore, the substrate has to be adequately prepared. The standard process is roughening of the surface by abrasive grit blasting. The substrate surface is blasted with compressed air jets carrying the abrasive grits, the angular particles of chilled cast iron or ceramic. In the plasma spraying process the stainless steel, aluminium or titanium substrates are commonly used. Therefore, the grits of 16-60 μm are generally applied. The preparation of the surface by abrasive grit blasting should answer the following purposes. Firstly, it should clean and activate the surface in order to avoid bonding defects in the interface between coating and base materials. The surface before this process can be treated by solvents, e.g. trichloroethylene, in order to remove the oil, grease or dirt. Secondly, grit blasting has to provide the right surface roughness to increase the effective surface area and to improve adhesive bonding of the sprayed deposit. The splat formation is presented in Figure 1.21. The flattening time is in the range of a few μs. The solidification process is longer though solidification starts before flattening is completed.

The time between two successive impacts is in the range of ten to a few tens of μs. Therefore, the next particle impacts on an already solidified splat.

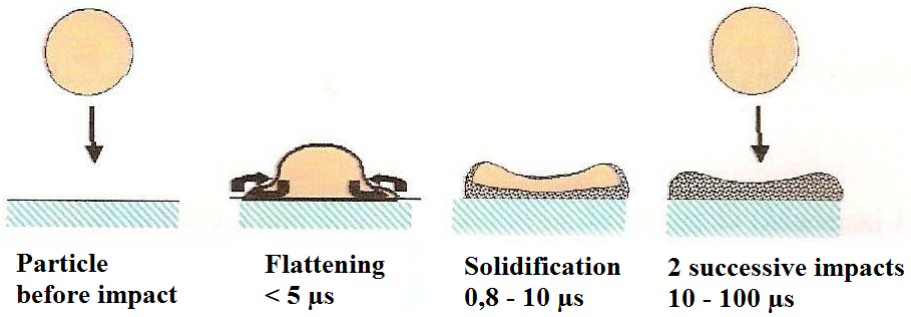

Figure 1.21: Characteristic time of lamallea formation in the conventional plasma spraying method [45].

The microstructure of the Al_2O_3 coating examined by a scanning electron microscopy (SEM) is presented in Figure 1.22. The suspension has been mechanically injected to the plasma jet produced by a stick-cathode dc plasma torch developed by Tingaud *et al.* [52, 53]. The torch has been operated with Ar-H_2 (45-15 slpm) plasma forming gas mixture and the arc current of 500 A.

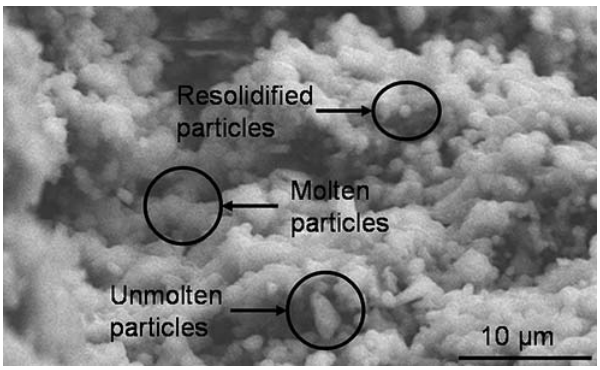

Figure 1.22: Al_2O_3 SPS coating architecture. Process parameters: Ar-H_2 45-15 slpm, I = 500 A, h = 14 MJkg^{-1}, mechanical suspension injection, feedstock d_{50} = 500 nm [53].

The examination of the coating has highlighted that it contains layered splats, unmolten particles (angular particles) and molten particles resoldified before their impact on the substrate (small spherical grains), what is highlighted in Figure 1.22.
To compare the results obtained by a stick-cathode dc plasma torch, the microstructure of the coating obtained by Triplex I plasma gun, described in the next section, is presented in Figure 1.23.

The coating microstructure consists of thin lamellas formed by single splats, which contain fine-grained, overspray particles (E) and re-solidified particles (C). The coating shows areas of good (A) and poor (B) inter-splat bonding. The splats have a columnar grain growth (D) with a grain thickness up to 0.1 μm. Moreover, the microstructure is characterized by inter-lamellar cracks (G), microcracks (H) and intrasplat cracks (F).

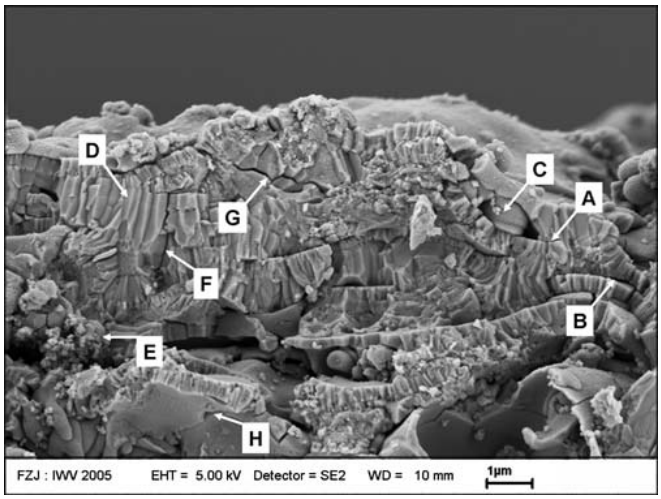

Figure 1.23: Main fracture features of 5YSZ SPS coating produced by Triplex I plasma gun [54].

Comparing both coatings microstructures, obtained by SPS method using the conventional torch and Triplex I plasma gun, it can be noticed that Triplex allows obtaining more and thinner lamellas formed by single splats. However, the similar features between two microstructures can be also found, e.g. the re-solidified or overspray particles. It can be assumed to the poorly controlled heat and momentum transfers between plasma and suspension, what is emphasized by the plasma fluctuations, presented in the following section.

1.3 Plasma instabilities

In the plasma spraying method most of the torches are supplied by a direct current (dc) power source. However, in spite of this fact, the plasma jet produced by a torch presents unsteady characteristics.

Etchart *et al.* has studied the suspension fragmentation process according to the arc voltage fluctuations, what is presented in Figure 1.24. The commercial dc plasma torch (PTF4 from Sultzer Metco) has been operated with Ar-H_2 (45-15 slpm) plasma forming gas mixture and the arc current of 503 A. The time-resolved imaging system permitted to observe the suspension penetration within chosen moments of the fluctuating plasma jet. Figure 1.24 shows the pictures taken for an instantaneous arc voltage of (a) 65 V and (b) 40 V. The differences in the droplets fragmentation and trajectory highlight the strong influence of the plasma jet fluctuations on the SPS method.
This time-fluctuating momentum of the plasma results in a poor reproducibility and reliability of the method, what causes the limited applications of suspension plasma spraying in advanced processing.

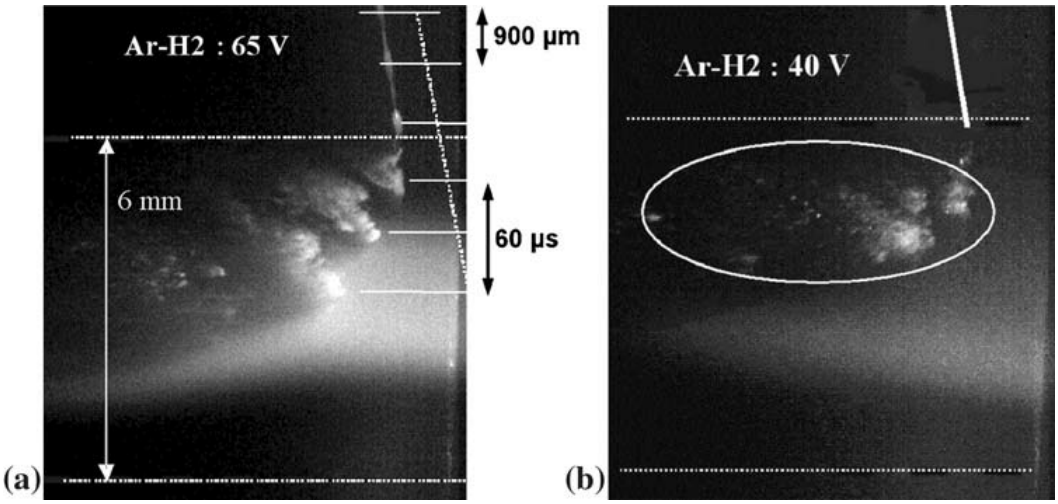

Figure 1.24: Plasma-suspension interaction at the triggering level of (a) 65 V and (b) 40 V [44].

Therefore, for many years, the special efforts have been devoted to understand the arc behavior in dc plasma torch, what is described in the following paragraphs.

1.3.1 Stationary behavior of the torch

To estimate the characteristics of the plasma jet and highlight the influence of experimental parameters on plasma jet velocity and pressure contributions, the simplified analytic model has been presented in [55]. The electrical conductivity and the heat potential have been presented in function of the specific enthalpy, what is highlighted in Figure 1.25.

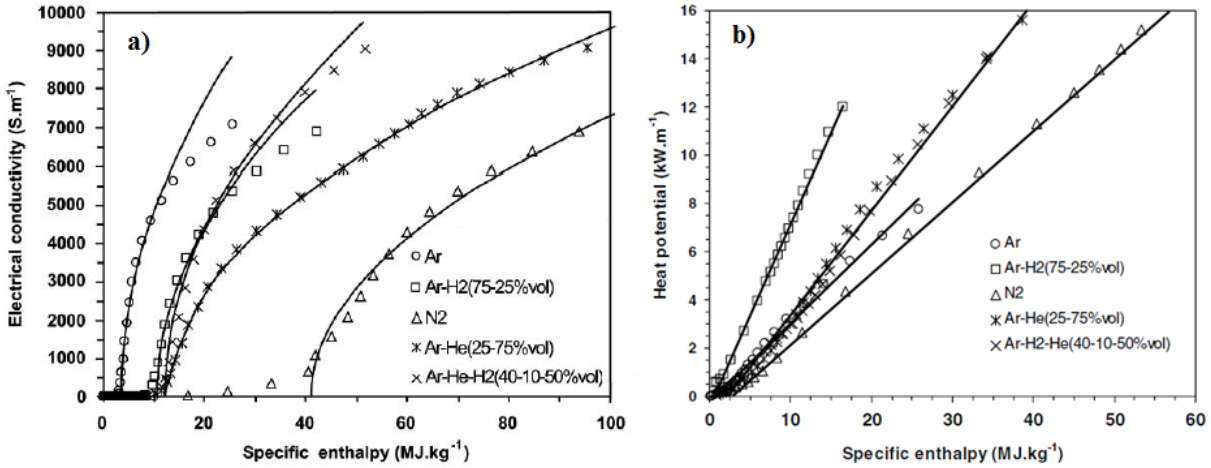

Figure 1.25: Dependence on specific enthalpy of: a) the electrical conductivity, b) the heat potential of various gases [55].

The representation of the electrical conductivity, given in Figure 1.25 a), allows defining the critical specific enthalpy, h_c given in Table 1.5, which represents the electrical conduction threshold, the enthalpy value above which the electrical conduction begins. To define the threshold of electrical conduction in nitrogen, the electrical conductivity has been fitted by a basic square root function:

$$\sigma(h) = \partial_\sigma (h - h_c)^{0.5} \tag{1.32}$$

for $h \geqslant h_c = h(T_c)$

Figure 1.25 b) highlights the linear dependence on the specific enthalpy of the heat potential, in the range of interest of spraying application, defined by the Kirchoff's equation as follows:

$$\kappa(T) = \frac{d\varphi}{dT} \tag{1.33}$$

where: κ and T are, respectively, the thermal conductivity and the temperature. If $\overrightarrow{q}$ is the heat flux, the heat potential can be written as: $\overrightarrow{q} = -\overrightarrow{\nabla}\varphi$.

Table 1.5: Critical enthalpy, h_c, at the electrical conduction threshold, linear coefficient between heat potential and specific enthalpy, a_φ, and coefficient used for electrical conduction as a function of specific enthalpy, ∂_σ, for different plasma forming gases [55].

Plasma gas	Ar	Ar-H_2 (75-25 vol%)	N_2	Ar-He (25-75 vol%)	Ar-H_2-He (40-10-50 vol%)
h_c ($MJ.kg^{-1}$)	3.70	10.40	41.10	13.20	12.14
a_φ ($10^{-4}kg.m^{-1}.s^{-1}$)	3.06	7.06	2.82	4.33	4.31
∂_σ ($C.V^{-1}.m^{-2}$)	1.89	1.42	0.95	1.03	1.56

The representation of the electrical conduction as the function of the specific enthalpy has leaded to estimate the plasma produced by a torch in the frame of a two-layer model, presented in Figure 1.26, if $h > h_c$ takes place.

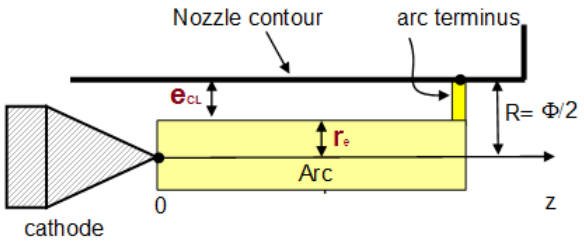

Figure 1.26: Schematic view of the two-layer model.

e_{CL} represents the thickness of the cold layer where the electrical conductivity is neglected, outside h_c surface. A mean radius, r_e, of the plasma is defined as follows: $h(r_e) = h_c$.

The main purpose of this model is to determine the enthalpy radius profiles to deduce the stationary characteristics of the plasma jet at the nozzle exit as function of easily measured experimental parameters (arc current, mean voltage, electrode thermal losses) and thermophysical properties of the plasma.
The specific enthalpy of the plasma results from the energy balance measurement of the electric power input, dissipated by Joule heating, and thermal losses due to radiation. The kinetic energy is negligible, therefore the energy equation is presented as follows:

$$\rho u \frac{\partial h}{\partial z} = \sigma E^2 + \nabla^2 \varphi - q_r \tag{1.34}$$

where z, ρ, σ, E, q_r are, respectively, the axial coordinate, the plasma density, the electrical conductivity, the electric field and the radiative losses. By assuming that the density of mass flux is constant, introducing the term s_h as the group of the convective specific enthalpy term, the Joule heating term and the radiative losses term, and by expressing the linearity between heat potential and specific enthalpy, the radial profile, h(r), at the nozzle exit can be deduced in the plasma ($0 \leq r \leq r_e$) and in e_{CL} ($r_e \leq r \leq R$):

$$\frac{1}{r}\frac{\partial}{\partial r}\left(r\frac{\partial h}{\partial r}\right) = \frac{s_h}{a_\varphi} \tag{1.35}$$

what allows determining the simple parabolic profile of the specific enthalpy within the plasma and a logarithmic one within e_{CL}, as follows:
For the arc column ($0 < (R/r_e)^2 < 1$):

$$h = h_c + \Delta h\left[1 - \left(\frac{R}{r_e}\right)^2\right] \tag{1.36}$$

For the cold sheath ($(R/r_e)^2 > 1$):

$$h = h_c - h_e\left[1 - \left(\frac{R}{r_e}\right)^2\right] - (\Delta h + h_e) ln\left(\left(\frac{R}{r_e}\right)^2\right) \tag{1.37}$$

where: $\Delta h = |s_h|.r_e^2/4a_\varphi$. Δh and r_e have been determined from two conditions: one concerning the overall thermal balance and the other one, the gas enthalpy at the anode wall whose temperature is sufficiently low so that: $h(R) = 0$. The integration of equation (1.35) by using (1.36) and (1.37), and reduced variables: $x = \overline{h}/h_c$, $y = (r_e/R)^2$ gives:

$$x ln(y) = \frac{1}{2}y - 1 \tag{1.38}$$

what defines the overall thermal balance as non-dimensional variables and is solved by using a Newton-Raphson method.

The derivation of the boundary condition, h(R) = 0, in terms of x and y variables, allows determining: $\Delta h = -\frac{h_c}{\ln(y)}$ and $r_e = R\sqrt{y}$.
The presented model permits, by introducing a mean isentropic coefficient, to calculate the axial velocity of the plasma jet at the nozzle exit. The plasma flow at the nozzle exit is assumed to be equivalent to an isentropic fictitious plasma flow presenting the same stagnation properties. Following basic consideration of compressible fluid mechanics, the energy conservation is applied along a streamline crossing the nozzle exit section at a distance r from the nozzle axis. Using the Barré de Saint-Venant relationship for an isentropic and compressible flow, it can be written as follows:

$$\frac{1}{2}u^2(r) + \frac{\gamma}{\gamma-1}\frac{P_a}{\rho(r)} = h(r) \tag{1.39}$$

By using $\dot{m} = \rho u S$, where S is the area of the nozzle cross section, equation (1.39) becomes:

$$u^2(r) + \frac{2\gamma P_a S}{(\gamma-1)\dot{m}}u(r) - 2h(r) = 0 \tag{1.40}$$

what leads to simple formula for the plasma velocity:

$$u(r) = v^*\left(\sqrt{1 + \frac{2h(r)}{v^{*2}}} - 1\right) \tag{1.41}$$

where:

$$v^* = \frac{\gamma}{\gamma-1}\frac{P_a S}{\dot{m}} \tag{1.42}$$

In general $v^{*2} >> 2h(r)$, therefore, the above equation is written as $u(r) \simeq h(r)/v^*$ within 10% of accuracy. This relationship can be used to define an averaged velocity, u_0, by using the measured specific enthalpy h_0 as follows:

$$u_0 = h_0\frac{\dot{m}(\gamma-1)}{P_a S\gamma} \tag{1.43}$$

where γ is the averaged isentropic exponent, directly linked to the plasma enthalpy or the ionization degree, what has been defined from an analysis of pressure contributions in the plasma flow, presented below. This obtained equation has been highlighted to be qualitatively in agreement with the relationship giving the maximum axial velocity of a nitrogen and an argon-hydrogen plasma jet deduced from measurements by Planche *et al.* as follows [24]:

$$u_{max} = K\frac{\dot{m}^{0.21}I^{0.44}}{R^{1.96}} \tag{1.44}$$

where K depends on the plasma gas chemical composition.

To find the pressure variations between the nozzle exit and a point located on the gas feeding line of the plasma torch, the total pressure has been measured as follows:

$$P_t = P_a + \Delta P_f + \Delta P_{is} + \Delta P_v + \Delta P_m \tag{1.45}$$

where:

P_a is the atmospheric pressure,

ΔP_f the overpressure due to the cold gas flow between the measurement point in the gas feeding line and the arc region,

ΔP_m the magnetic overpressure at the cathode tip due to the Maecker effect

ΔP_{is} the isentropic overpressure which is the driving pressure, defined as follows: $\Delta P_{is} = \dfrac{h_0 \dot{m}^2 (\gamma - 1)}{2\gamma S^2 P_a}$,

ΔP_v the overpressure due to the plasma viscosity within the nozzle, admitted to be proportional to the nozzle length ℓ, defined in two different ways:
1) as a linear loss pressure proportional to the nozzle length: $\Delta P_v = \dfrac{\alpha \ell}{2} \rho u^2$,
2) assuming a Poiseuille flow at the nozzle exit: $\Delta P_v = \dfrac{128 \overline{v} \dot{m} \ell}{\pi d^4}$.

The sum $(P_a + \Delta P_f)$ has been obtained as the results of the pressure measurements for the different mass flow rates and internal nozzle diameter without generating the plasma. If $\Delta \mathrm{P_p} = \mathrm{P_t} - (\mathrm{P_a} + \Delta \mathrm{P_f})$, $\Delta \mathrm{P_p}$ is defined as follows:

$$\Delta P_p = \Delta P_m + \left(\frac{\gamma - 1}{2\gamma}\right) \frac{\dot{m}^2 h_0}{S^2 P_a} (1 + \alpha \ell) \tag{1.46}$$

The equation leads to the linear relationship between the measured overpressure, $\Delta \mathrm{P_p}$, and the term $\dot{\mathrm{m}}^2 \mathrm{h_0}$ which is known from the experimental parameters, what is presented in Figure 1.27.

Figure 1.27 represents the dependence of the measured mean pressure on the term consisting of the mass flow rate of gases and the specific enthalpy, which is defined experimentally as follows: $\mathrm{h_0} = \dfrac{\mathrm{UI} - \mathrm{Q_{loss}}}{\dot{\mathrm{m}}}$, where U, I , and $\mathrm{Q_{loss}}$ are the measured mean values, respectively, of the arc voltage, of the arc current and of the torch thermal losses. Therefore, it can be assumed that these parameters influence $\Delta \mathrm{P_p}$, what has leaded to the studies presented in chapter 2.

To define the averaged isentropic exponent, γ, the Poiseuille flow is considered, and written as:

$$\Delta P_{is} = (\Delta P_p - \Delta P_m - \frac{128 \overline{v}}{\pi} \frac{\dot{m} \ell}{d^4}) = \left(\frac{\gamma - 1}{2\gamma}\right) \frac{16 h_0 \dot{m}^2}{P_a \pi^2 d^4} \tag{1.47}$$

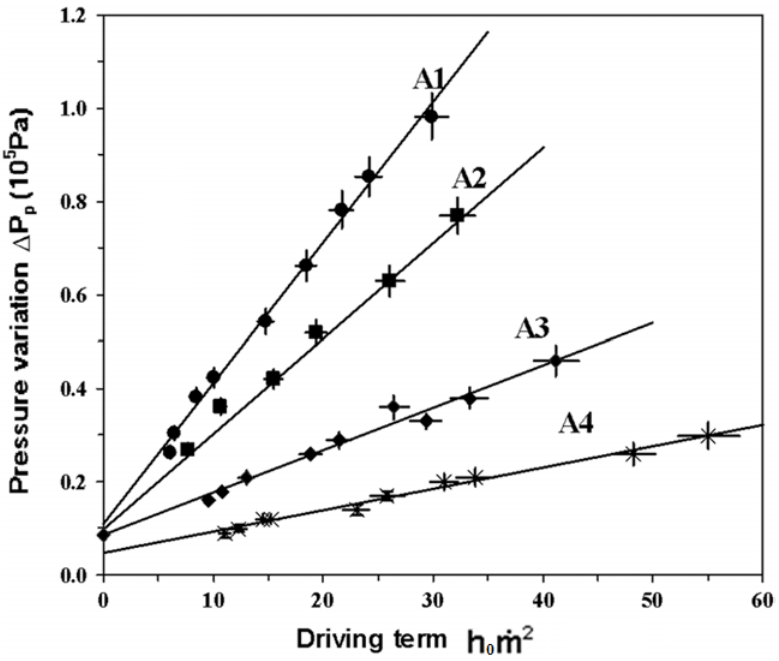

Figure 1.27: Pressure variation ΔP_p as function of $\dot{m}^2 h_0$ where $\dot{m}$ and h_0 are, respectively, the mass flow rates of gases and the specific enthalpy measured for the different anodes A1, A2, A3 and A4, the arc current from 350 to 600 A and plasma gas (Ar-H_2) mixtures: 30/10 45/15 60/30 (slm) [55].

Therefore, the isentropic component, γ, has been determined from the ratio $(\gamma - 1)/2\gamma$ defined as the slope of the evolution of ΔP_{is} as a function of $16 h_0 \dot{m}^2 / P_a \pi^2 d^4$ for the different experimental conditions, presented in Figure 1.28. As can be noticed the linear variation of the ratio $(\gamma - 1)/2\gamma$ has been obtained.

The presented results have been focused on the stationary behavior of the dc plasma torch. The plasma produced by a torch has been estimated in the frame of a two-layer model. It has permitted to determine the enthalpy radius profile to deduce the stationary characteristics of the plasma jet (at the torch exit) as a function of the measured parameters, e.g. arc current, mean voltage. It has leaded to calculate the axial velocity of the plasma jet at the nozzle exit and to evaluate the different pressure contributions. The determination of pressure as a function of the term $\dot{m}^2 h_0$ has shown the linear relationship between the mean pressure in the rear part of the plasma torch and the mean arc voltage, what has leaded to the studies of the pressure and the arc voltage presented later in this dissertation. The following paragraph will be focused on the studies of the arc instabilities and determination of different modes of these fluctuations.

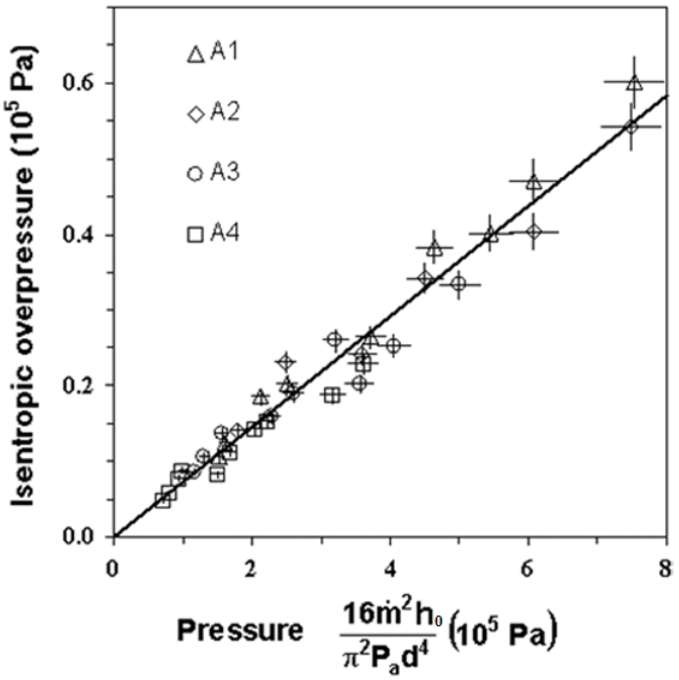

Figure 1.28: Dependence of isentropic pressure ΔP_{is} on experimental operating conditions [55].

1.3.2 Dynamic behavior of the torch: arc instabilities

The first experimental studies of the instabilities of electric arc with a superimposed flow of argon have been presented by Wutzke *et al.* [28]. The experiments have been performed in the arc tunnel by using a plane anode and the cathode positioned upstream, a double-anode configuration and a cylindrical anode. The results have identified three different modes of the arc instabilities: steady, takeover and restrike mode, presented in Figure 1.29. The numerical simulations, given by [27, 28, 56–58], have showed that the plasma instabilities have been mainly related to the elongation of electrical current paths due to the plasma flow and Lorentz forces. Duan and Heberlein have determined the mixed modes related to the combinations of the restrike and takeover modes or the takeover and steady modes [27]. The steady mode has been achieved with a high level of the arc current, 900 A, and a pure argon flow [27]. This mode corresponds to very small arc voltage fluctuations: $\Delta U_{arc} = \pm 0.5V$ due to the balance between the drag force of the plasma gas and the electromagnetic forces. The steady mode is characterized by a nearly fixed position of the anode attachment, what causes the rapid erosion of the anode.
The takeover mode appears mostly by using the monatomic plasma gases [25, 59]. It has been called takeover because a new attachment gradually "takes over" the role of the old attachment, instead of being created by the breakdown mechanism. The takeover mode is characterized by a periodic or quasi-periodic voltage fluctuations, shown in Figure 1.29.

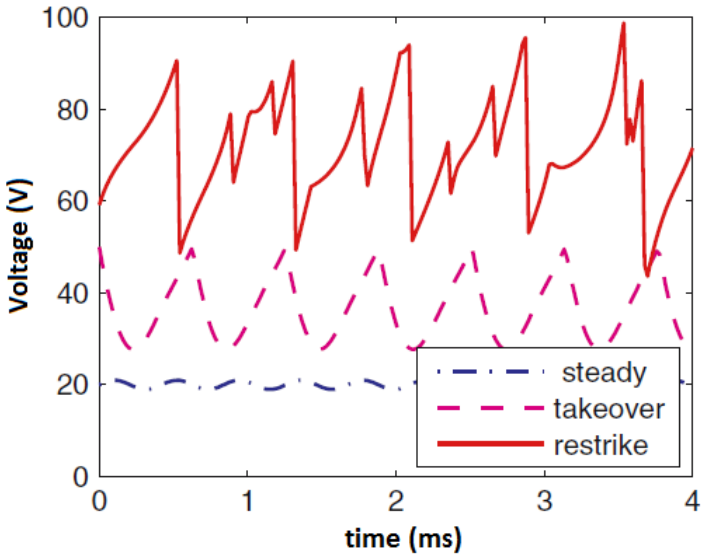

Figure 1.29: Arc voltage traces corresponding to different anode attachment modes in a dc torch [57].

The restrike mode is characterized by the highest voltage fluctuations and a sawtooth shape profile of the voltage trace. An arc operating in this mode is very unstable. It results in the increase of the arc voltage and sudden drop when a new current path is created by an electric breakdown (re-strike). This mode will be described in details in the following section.

Duan and Heberlein have determined the method to characterize the arc instabilities modes presented above [27]. It is based on the analysis of the voltage waveform, shown in Figure 1.30.

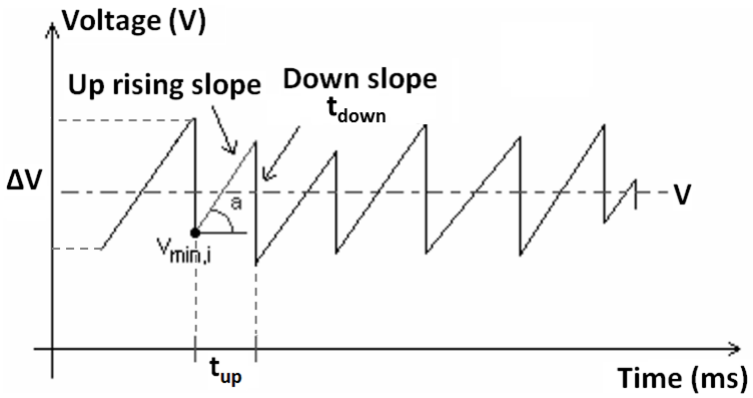

Figure 1.30: Arc voltage waveform used to distinguish the torch operation modes.

To separate the restrike mode from takeover mode, the shape of the voltage waveform,

characterized by a shape factor S, is determined by the following equation:

$$S = \frac{t_{up}}{t_{down}} \tag{1.48}$$

where:

t_{up} is the duration time of the waveform up-rising slope,
t_{down} the duration time of the down slope, highlighted in Figure 1.30.

The fluctuation amplitude is used to distinguish the takeover mode from the steady mode. The amplitude factor, A, is calculated as follows:

$$A = \frac{\Delta V}{V} \times 100\% \tag{1.49}$$

where:

ΔV is the amplitude of the arc voltage fluctuation,
V the mean arc voltage.

The arc mode is defined as running in restrike mode when A $\geq$ 10% and S $\geq$ 5. If A $\geq$ 10% and S $<$ 1.1, the arc is determined as running in takeover mode and for A $<$ 2% the arc is in a steady mode [27].
The origins of the arc instabilities should be divided into two sections according to the time scale. The presented modes of the fluctuations are associated with the short time scale evolution of the voltage.
Moreover, the drifting of the arc voltage can be explained by the erosion and wear of electrodes, what is shown in Figure 1.31 and belongs to the group of the long time evolution of voltage. Figure 1.31 presents the time dependence and corresponding power spectra of voltage fluctuations. The use of worn electrodes results in the increase of arc fluctuations.

The cathode erosion is due to the diffusion and evaporation of thoria. It results in a lower flow velocity of the plasma by the decrease of the current density of arc attachment at the cathode. The erosion of the anode is caused by the strong heat fluxes of arc attachment between the arc column and the anode surface. It is observed as a voltage drop which increases drastically after a few tens of hours working time and results in the ejection of tungsten or copper particles to the plasma jet, what is damaging the coating.

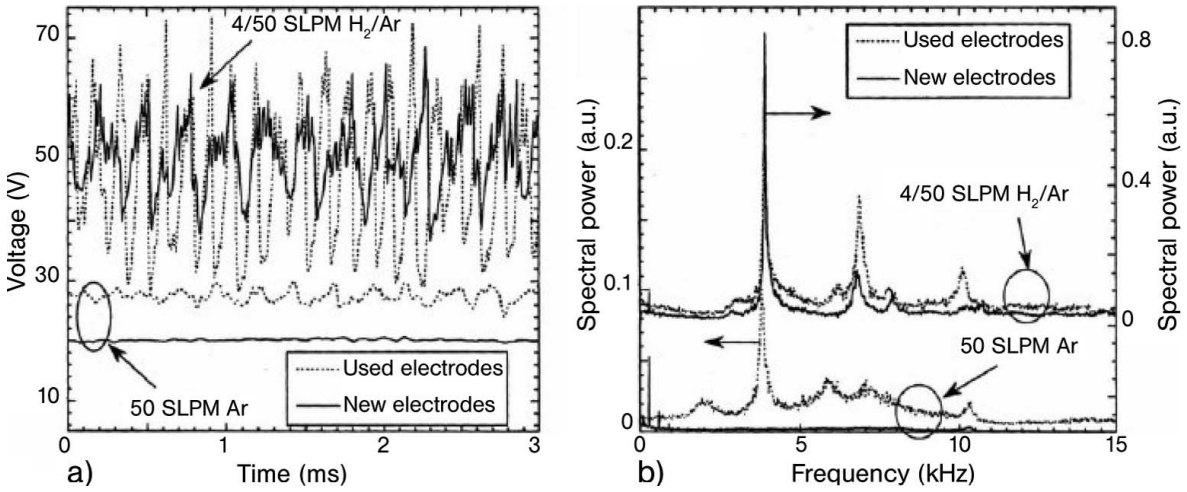

Figure 1.31: Time dependence (a) and corresponding power spectra (b) of the voltage fluctuations for new and used electrodes. Plasma parameters: 50 slpm Ar and 4/50 slpm H_2/Ar, 500A [60].

1.3.2.1 Restrike mode

As has been mentioned above, the arc column expands itself from the cathode tip and is surrounded by a cold gas boundary layer. Through this layer the electrical connection with the anode wall is carried out by an arc loop which is exposed to the drag and electromagnetic forces. The imbalance between these forces causes that the drag force, which is the result of the interaction of the incoming gas flow over the arc, induces the stretching and lengthening of the arc column, presented in Figure 1.32 a).

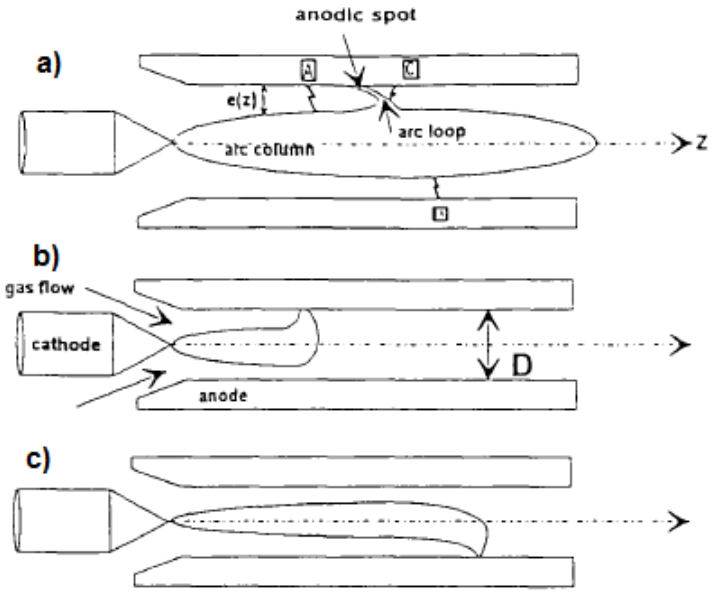

Figure 1.32: Schematic view of Restrike model: a) the arc column at the end of a lengthening process, b) after an upstream restrike, c) after a downstream restrike [61].

This process is accompanied by the rise of the arc voltage which corresponds to an increase of the electrical current path in the direction of the superimposed flow during $\tau_i = t_{i+1} - t_i$ in Figure 1.33.

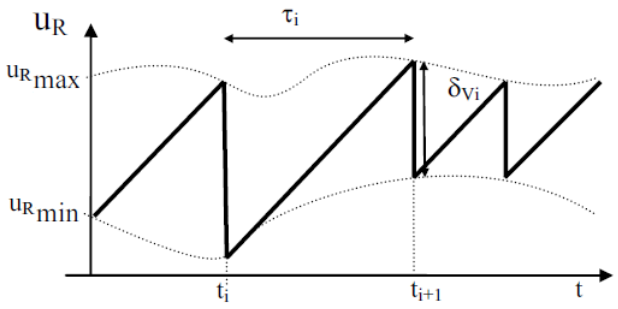

Figure 1.33: Temporal evolution of the arc voltage corresponding to restrike mode.

The lengthening process is followed by an electrical breakdown at t_{i+1} in Figure 1.33. It leads to the creation of new arc root, what corresponds to a minimum arc voltage U_{Rmin} and is identified with a voltage jump δ_{Vi}. Coudert *et al.* have highlighted that the voltage breakdown, defined as $V_b(Z)$, is related to the thickness of the cold gas boundary layer, $e(Z)$, as follows: $V_b(Z) = e(Z).E_b$, where E_b is the breakdown field [61], which has been determined up to now by Paschen's law. However, the results presented in Chapter 2 have highlighted that due to the magnitude of this field, it can not be attributed to Paschen's law but is divergently referred to the thermal instabilities [V. Nemchinsky private communication]. The restrike arc voltage is depicted as: $V_r(t) = U_a + U_c + V_c(Z_{i-1}) + V_l(t)$, for $t_{i-1} < t < t_i$, where U_a and U_c are respectively the anode and cathode falls, presented in Figure 1.34, $V_c(Z_{i-1})$ is the voltage drop along the arc column which depends on the arc root location, Z_{i-1}, $V_l(t)$ the voltage drop along the arc loop connecting the column to the anode wall. Assuming that just after the spot creation, at time $t_{i-1} + \varepsilon$, the arc voltage is defined by:

$$V(t_{i-1} + \varepsilon) = V_m(t_{i-1}) = V_c + V_a + V_c(Z_{i-1}) \tag{1.50}$$

and the voltage just before the further breakdown giving rise to a new arc root location, Z_i, at time $t_i - \varepsilon$, is determined by the equation:

$$V(t_i - \varepsilon) = V_c + V_a + V_c(Z_{i-1}) + V_l(t_i - \varepsilon) \tag{1.51}$$

the voltage jump, δ_{Vi}, occurring at t_i, is given by:

$$\delta_{Vi} = V(t_i - \varepsilon) - V(t_i + \varepsilon) = V_l(t_i - \varepsilon) + V_c(Z_{i-1}) - V_c(Z_i) \tag{1.52}$$

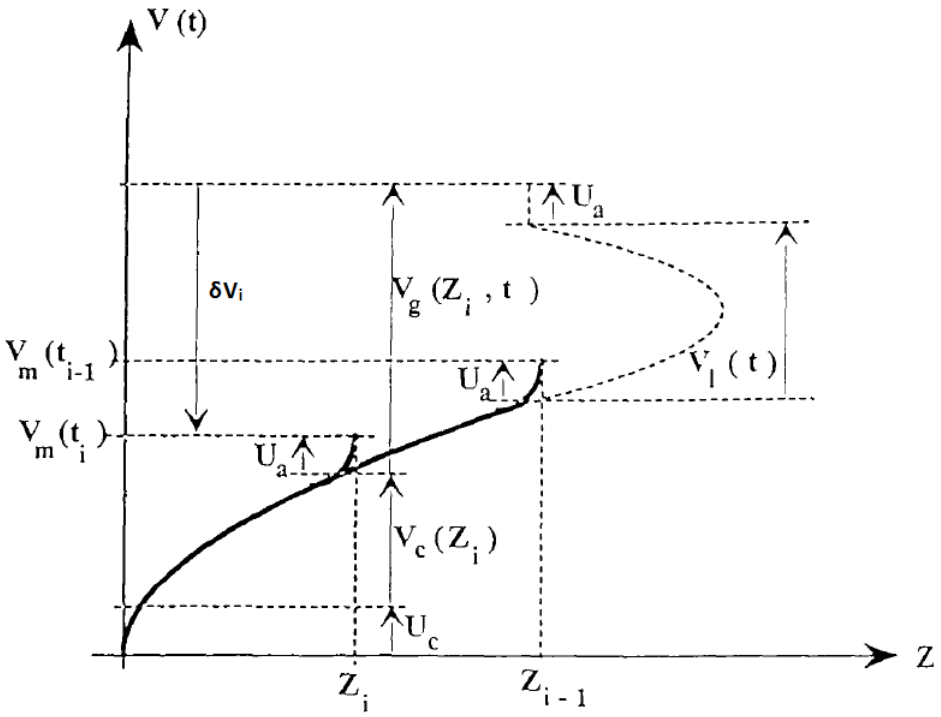

Figure 1.34: The arc voltage evolution [61].

1.3.2.2 Improvement of plasma spray process

For many years, the special efforts have been made to understand and improve the control of suspension plasma spray processes. In particular, the plasma unsteady characteristics which result in a poor reproducibility and reliability of the method. The following section focuses on the improvement methods of the plasma spray process concerning the plasma instabilities.

1.3.2.2.1 New designs of dc plasma torch

Development of new plasma torches is driven by the need to improve stability and to increase the range of powders to be used. A large number of the thermal plasma torches have been designed [19,62]. The following section describes the recently developed torches: Triplex and Axial III.

- **Triplex (Sulzer Metco, Switzerland)**
  In the mid-1990s Sulzer Metco developed a new plasma gun concept in the co-operation with the Universitat der Bundeswehr, Munich (University of the Federal Armed Forces). The result is the Triplex gun, a three-cathode plasma spray torch with cascading nozzle and anode end ring, presenting in Figure 1.35 [63,64].

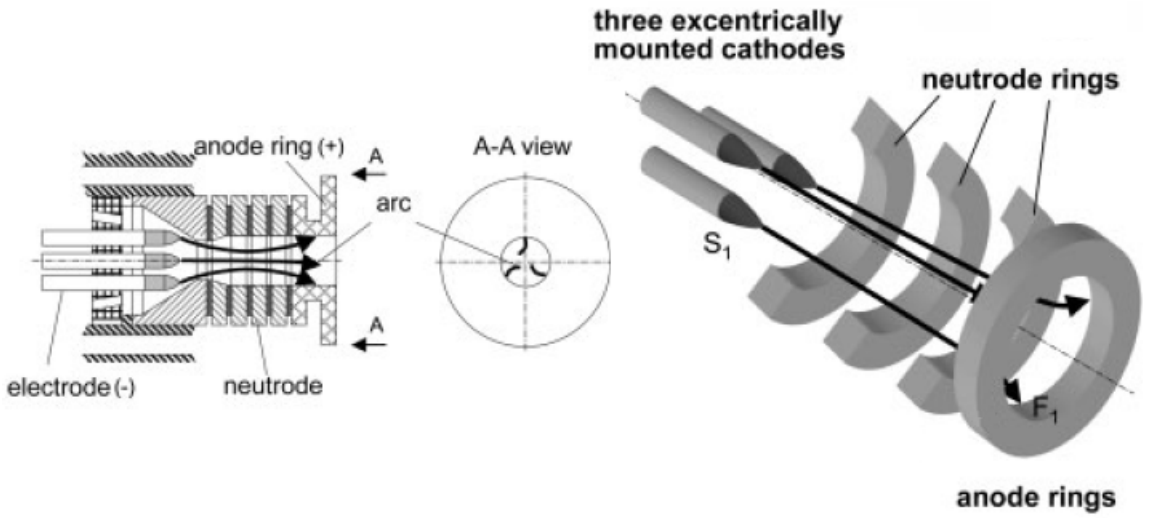

Figure 1.35: The schematic view of the Triplex torch [64].

It consists of three water cooled parallel cathodes insulated against each other and supplied by independent power sources. The electrical energy is distributed through three parallel arcs striking at a single anode with three separate anode attachments, what has solved the problem of increased anode erosion (the voltage loss equals to 1-5% over 90h working time). To prevent the instability of the anode attachments the nozzle is consisted of several rings electrically insulated, except of the last one which operates as an anode. Schein *et al.* have shown that the conventional dc torch, F4, produces a very unstable plasma jet with large variations in the jet length, presented in Figure 1.36 a). This characteristic Triplex construction results in the elongation of the arcs and a much more stable plasma jet, what is shown in Figure 1.36 b).

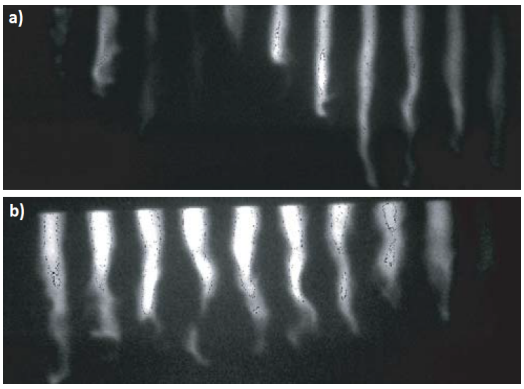

Figure 1.36: Pictures of the plasma jets obtained by: a) F4 (exposure time 5 ns, 6 mm nozzle, current: 540 A, plasma gas: 45 slpm Ar and 12 slpm N_2), b) Triplex (exposure time 3 ns, 9 mm nozzle, current: 350 A, plasma gas: 45 slpm Ar) [63].

Triplex torch allows obtaining higher arc voltage and enthalpy of the plasma jet. It is able to achieve the voltages of 80-120 V (with arc currents limited to 300 A and Ar-He plasma forming gases) compared to 40 V obtained by the conventional dc torch.

Another advantage of Triplex torch is the temperature distribution produced at the nozzle exit. As it can be observed in Figure 1.37 the plasma jets are constituted of three lobes, the zones with higher and lower gas viscosity.

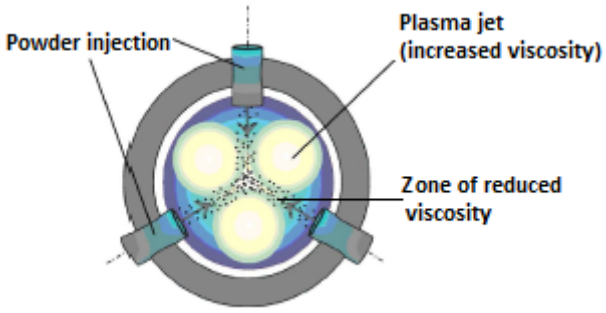

Figure 1.37: Schematic view of the powder injection into Triplex torch [51].

Thus the powder injection into the central region of the plasma jet (the zone with high viscosity) is more easily achieved along one of the canals where the gas viscosity is reduced (Figure 1.37). It allows obtaining a better interaction of the particles with the plasma flow what leads to improved coatings.

- **Axial III (Northwest Mettech Corp., Canada)**

Axial III consists of three cathodes and three anodes, arranged such that their axes are parallel, presented in Figure 1.38. They are operated by three power supplies (total power ranging from 50 to 150 kW) and generally they work with Ar-N_2-H_2 or Ar-N_2-He gas mixtures.

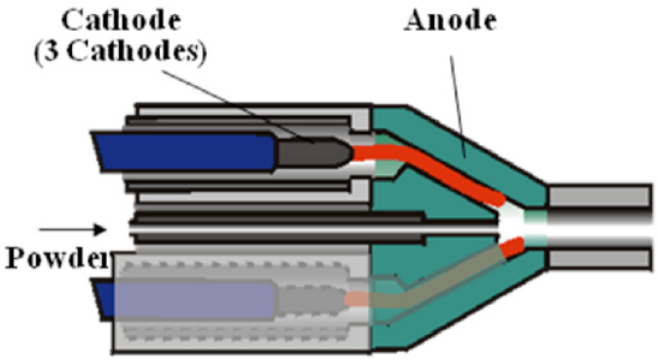

Figure 1.38: Schematic view of Axial III [65].

The AxialIII configuration allows producing three plasma jets which converge together in a common nozzle. The feedstock material is injected axially between these three plasma jets, what permits to obtain the particle trajectories more homogeneous and a longer residence time of the feedstock material in the plasma zone. Moreover, as these three plasma jets fluctuate independently, voltage fluctuations have lower effects on the axially injected feedstock material.

1.3.2.2.2 Reduction of plasma instabilities

The studies of the instabilities of the plasma jet have resulted in the methods to reduce these fluctuations.

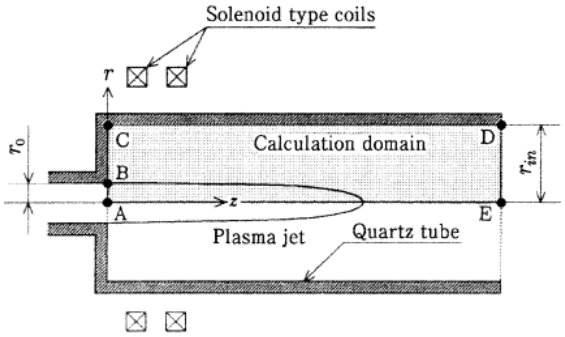

Figure 1.39: Schematic view of the plasma jet stabilized by magnetic field [66].

Nishiyama *et al.* have highlighted the possibility of the stabilization of unstable plasma jet behaviour by applying magnetic field [66, 67]. Figure 1.39 shows the schematic model of this method. The plasma jet has been issued into a quartz tube. Two solenoidal coils have been placed at the nozzle exit to produce a mirror type magnetic field. The maximum magnetic flux density, $B_{z_{max}}$, was equal to 0.44 T. The pure argon (20 slpm) plasma was tested supplied by the power of 8 kW. The temperature and velocity for each plasma species with and without magnetic field were measured, what is presented in Figure 1.40. By applying the magnetic field it is possible to increase the temperatures of all plasma

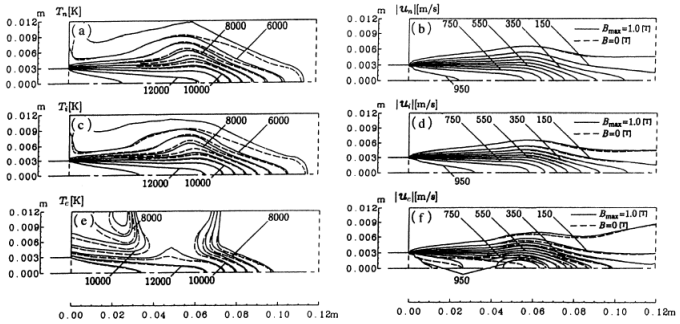

Figure 1.40: Isocontours of temperature and velocity of the heavy species (T_n, T_i and U_n, U_i) and of the electrons (T_e and U_e) with and without applied magnetic field [66].

species outer from the jet fringe. In addition the electron velocity is changed considerably in the central region by Lorentz force in the magnetic field. The results have shown that the application of magnetic field can control the electron velocity and the temperature in the plasma jet.

1.4 Conclusions

The relatively new method, suspension plasma spraying, allows producing finely structured nano-sized coatings, what expands its application area to e.g. thermal barrier coatings (TBCs), solid oxide fuel cell (SOFC), photo-catalytic coatings. However, the results of the examination of coatings microstructures by SEM or the studies of the suspension fragmentation according to the arc voltage fluctuations have highlighted the difficulties encountered in this method. The large discrepancies in the particles trajectories and the heat transfers, the plasma instabilities result in the insufficient reproducibility and reliability of the SPS method. Therefore, for many years the special efforts have been made to improve this process. One of the solutions is to develop new non-conventional plasma torch. However, as the coating microstructure has highlighted, the plasma produced by these torches still remain non-uniform resulting in non-homogeneous microstructure of the coatings. Consequently, the following dissertation will present a new approach to arc fluctuations by the increase of the instabilities in a controlled way to obtain a pulsed arc plasma jet with a synchronous injection of materials. This process requires an understanding of the origin of arc instabilities. Therefore, the next chapter will present the studies of the plasma fluctuations in the conventional dc torch.

Part I

Résumé du chapitre 1

Cette thèse présente le procédé de projection par plasma d'arc produit par une torche plasma à courant continu (dc en anglais) à la pression atmosphérique. Selon la matière injectée dans le jet de plasma, la technique de projection par plasma peut être classée dans plusieurs catégories: la projection dans l'air à pression atmosphérique (APS, Atmospheric Plasma Spraying en anglais) en utilisant la poudre comme la matière injectée, la projection de solution (SPPS) et de suspension (SPS). Dans le procédé APS, les particules de poudresont injectées dans le jet de plasma. L'épaisseur minimale des revêtements est limitée à environ 10 μm [7]. Ils sont principalement utilisés pour fournir une protection contre les températures élevées, la corrosion, l'érosion et l'usure. Le procédé SPPS, décrit par Karthikeyan *et al.* [8], est la méthode de projection de solution, dans lequel au lieu d'utiliser une poudre, un précurseur en solution aqueuse est injecté dans le jet de plasma. Ce procédé permet d'obtenir une microstructure des revêtements nano et micrométrique. Une méthode relativement nouvelle est la projection par plasma de suspension, qui a été inventée par l'Université de Sherbrooke au milieu des années 1990 [9]. La suspension est composée de particules de poudre micro- et nano-métriques dispersées dans un liquide. Le procédé SPS permet produire les revêtements finement structurées, voire de taille nanométrique, ce qui donne la possibilité d'étendre le domaine d'application des couches. Ils peuvent être utilisés en tant que:

- Pile à combustible à oxyde solide (SOFC en anglais)
- Barrières thermiques
- Dépôts catalytiques

Le plasma, appelé aussi le quatrième état de la matière, est un gaz électriquement conducteur en raison de la présence de particules chargées: les ions et les électrons. La thèse suivante décrit le plasma thermique produit par une décharge électrique à fort courant continu. Une torche à plasma transforme l'énergie électrique fournie par un générateur de courant en énergie thermique par effet Joule au sein d'un gaz plasmagène en contact avec un arc électrique. Cet arc électrique est créé entre une cathode, pôle négatif, et une anode, pôle positif, et soufflé par les gaz plasmagènes qui sont injectés en amont de la torche entre les deux électrodes.
La torche à plasma d'arc à courant continu comporte trois éléments essentiels: la cathode, l'anode et l'injecteur de gaz.

- **Cathode**
  Elle permet de fournir les électrons à l'arc électrique. Les paramètres de la cathode sont différents en fonction des mécanismes d'émission d'électrons. Dans le cas de la cathode chaude, les électrons sont fournis par l'émission thermoionique, suivant la loi de Richardson-Dushman, Equation 1.1. $1-2$ % en masse de ThO_2; 2 % en masse de

La_2O_3, Y_2O_3, CeO_2. Le rôle de dopant est d'abaisser la fonction de travail thermoionique de tungstène. Deux types de cathodes chaudes sont généralement utilisés: les électrodes tiges et les électrodes boutons.

- **Anode**
  L'anode a un rôle passif qui consiste à collecter les électrons. Elle est soumise à des flux thermiques très élevés (jusqu'à 160 $W.mm^{-2}$) au point d'accrochage de l'arc électrique. Par conséquent, elle doit être refroidi à l'eau et fabriquée en cuivre ultra-pur (OFHP Oxygen Free High Purity), caractérisé par une forte conductivité thermique: 358 $W.m^{-1}.K^{-1}$ et la diffusivité thermique: 1114 10^{-6} $m^2.s^{-1}$ à 25°C, avec parfois un gainage en tungstène.

- **Injecteur de gaz**
  Il existe trois méthodes principales d'injection: l'injection swirl, l'injection radiale et l'injection axiale. Dans l'injection axiale le gaz est injecté parallèlement à l'axe de l'anode et possède une composante de vitesse longitudinale. Dans le cas de l'injection radiale la bague d'injection est percée de trous perpendiculaires à l'axe de la torche. La vitesse des gaz présente donc une forte composante radiale qui diminue ensuite. Dans le cas de l'injection swirl, le gaz possède une composante de vitesse initiale axiale et radiale.. Les tourbillons formés créent des forces centrifuges, ce qui pousse le gaz froid vers les parois de la torche.

Le jet de plasma est produit par une torche dans laquelle l'arc électrique est établi entre une cathode et une anode. La colonne d'arc est développée à partir de la tête de cathode est caractérisée par un écoulement laminaire qui est délimité par une enveloppe isotherme ($T_c > 7500K$) à l'intérieur de laquelle la conductivité électrique des gaz est suffisamment élevée pour permettre le passage du courant. En dehors de cette zone, la conduction électrique est négligeable, ce qui apparaît comme la couche limite froide. L'épaisseur de cette couche dépend fortement des paramètres du procédé: le courant d'arc, le diamètre interne de la tuyère, l'injection de gaz formant le plasma. L'accrochage de l'arc à la paroi de la tuyère est perpendiculaire à la surface de l'anode et il est sous la forme d'une colonne de gaz à haute température et à basse densité traversant la couche limite de gaz froid. Les études sur le pied d'arc ont montré que ce point d'accrochage se déplace continuellement. Ceci est dû à des mouvements axiaux et de rotation induits par les forces dynamiques (force de traînée) liées à l'écoulement du gaz, les forces électromagnétiques de Lorentz dues à l'interaction entre le courant d'arc et le champ magnétique induit par ce courant, et les effets thermiques. Quand le jet de plasma, caractérisé par une faible densité et une vitesse élevée (entre 600 et 2200 m/s), sort de la tuyère de la torche, il se mélange avec l'atmosphère environnante. Cela entraîne donc des forces de cisaillement qui vont se traduire par la création d'anneaux tourbillonnaires.

Le plasma produit par la torche à courant continu est supposé à équilibre thermodynamique local (Local Thermal Equilibrium LTE en anglais). Le plasma thermique est considéré comme optiquement mince et donc le rayonnement ne correspond pas au rayonnement du corps noir. Cela signifie que la loi de Planck n'est pas valable dans LTE. Les processus de collision doivent être localement en équilibre. Par conséquent, les populations de toutes les espèces et leurs niveaux excités sont décrits par les équations de Maxwell, Boltzmann, Saha et Guldberg-Waage, présentés dans le chapitre 1, mais avec la température qui peut varier dans le temps et l'espace.
Les principaux gaz rencontrés en projection thermique sont l'argon (Ar), l'hydrogène (H_2), l'hélium (He) et l'azote (N_2). Le choix du gaz injecté joue un rôle important dans la technique, il définit les propriétés thermodynamiques et de transport importantes des plasmas: l'enthalpie, la conductivité électrique, la viscosité et la conductivité thermique.
Dans le procédé de projection conventionnelle (APS) les poudres avec des diamètres généralement entre 10 μm et 110 μm sont injectées au jet de plasma. L'injection de la matière est effectuée principalement par un tube de diamètre interne de 1.5 - 2 mm. Les particules de poudre sont transportées par le gaz, par exemple l'argon, à la vitesse d'écoulement entre 3 et 10 slm. Dans le cas des torches à plasma à courant continu classiques, le matériau est introduit dans le jet de plasma radialement. L'injection axiale est réalisée dans les nouvelles conceptions de la torche, par exemple Axial III. La thèse suivante se concentre sur les études de la torche plasma en courant continu associés à l'injection de suspension.
La suspension appropriée pour le procédé SPS se compose généralement: de poudres submicronique ou nanométriques, de solvant et d'additifs chimiques. Les poudres sont principalement produites par les procédés de précipitation chimique, de broyage mécanique, des traitements thermiques. Le choix du solvant est très important pour les propriétés de la suspension, par exemple pour avoir unefaible viscosité et une bonne stabilité. Les principaux solvants utilisés dans la production de la suspension sont l'eau et l'éthanol. En comparant les propriétés de ces deux liquides, on peut dire que l'eau nécessite plus d'énergie que l'éthanol pour vaporiser. En plus, l'éthanol est caractérisé par une tension de surface inférieure. Néanmoins, il contient du carbone qui peut polluer les revêtements. Par conséquent, le mélange de l'éthanol avec de l'eau sont couramment utilisés. Pour obtenir une bonne homogénéisation et désagglomération de la suspension une agent dispersant est généralement ajouté pour stabiliser la poudre dans le solvant, par exemple un ester de phosphate. En ajoutant par exemple de l'ammonium d'acide polyacrylique (PAA) ou de l'alcool polyvinylique (PVA), il est aussi possible de modifier la tension de surface ou la viscosité de la suspension.
Il existe deux grandes familles d'injection de suspensions: l'atomisation et l'injection mécanique.

Le principe de fonctionnement de l'atomiseur est basé sur l'application de pulse de gaz sous pression, contrôlée par l'action d'une électrovanne, sur le liquide contenu dans un réservoir. Le liquide est éjecté par la buse et forme un spray de gouttelettes. Il est à noter qu'un gaz d'atomisation peut être utilisé pour atomiser un jet de liquide en gouttelettes. Il a été montré que les liquides caractérisés par la viscosité comprise entre 0.1 et 50 à 60 mPa.s se fragmentent en gouttelettes en fonction du nombre de Weber, We, qui est le rapport entre la force exercée par l'écoulement du liquide à la force de tension de surface, définie par l'équation 1.12. Pour les liquides à viscosité élevée le nombre Ohnesorge, Oh, doit aussi être considéré. Il concerne les forces visqueuses et les forces de tension de surface et d'inertie, selon l'équation 1.13. Les dimensions typiques des gouttelettes atomisées de la matière sont comprises entre 2 et 100 μm, les vitesses correspondantes variant de 5 à 60 m/s.

Dans le cas de l'injection mécanique, la suspension est stockée dans un réservoir sous pression et injectée à travers une buse de diamètre interne spécifiée, d_n. Fazilleau *et al.* ont utilisé un diaphragme de buse calibrée au diamètre de 150 μm fabriqué par l'électro-érosion et Etchart-Salas *et al.* ont présenté des résultats obtenus par la buse d'un diamètre variant de 300 μm, usiné par laser. Les études ont montré que le carré de la vitesse du liquide varie de façon linéaire avec la pression du réservoir. Par exemple, les vitesses d'injection entre 25 et 35 m/s ont été obtenues avec une pression d'air comprise entre 0,2 et 0,6 MPa.

Lorsque le jet de la suspension ou les gouttes sont injectées dans le jet de plasma, ils sont progressivement ou rapidement fragmentés en gouttelettes. Ce processus de fragmentation conduit à la diminution de leur volume, ce qui entraîne que la diminution de leur quantité de mouvement. Fazilleau a présenté les conditions favorables pour une bonne pénétration de la suspension dans le jet de plasma définie par l'équation 1.17. Quand les gouttelettes de la suspension sont entraînées en jet de plasma, elles sont soumises à la fragmentation en raison d'une forte contrainte de cisaillement (générée par l'écoulement du plasma) et la vaporisation du liquide due à haut flux thermique du plasma. Il a été démontré que la fragmentation de la suspension dépend du nombre de Weber, We. Le nombre de Weber d'environ 14 est la valeur critique pour laquelle la goutte est fragmentée

Une goutte dans un écoulement de plasma est soumise à deux forces principales, la force aérodynamique et la force de tension de surface. La force aérodynamique du jet de plasma permet la désintégration de la goutte, et la tension de surface du liquide s'y oppose. En égalant ces deux forces, le diamètre minimum, d_f, de ces micro-gouttes, lorsque la fragmentation est terminée, peut être déterminé par la formule 1.20. Le paramètre important de la fragmentation est la durée de ce processus. Fazilleau *et al.* ont montré que le temps de fragmentation, t_f, est donnée par l'équation 1.21.

Le flux de chaleur du plasma transmis par convection à la goutte, permet l'évaporation

complète de celle-ci après un temps, t_v, défini par l'équation 1.23. Il est intéressant de comparer ce temps avec le temps de fragmentation de la goutte. Les résultats présentés sur la figure 1.19 montrent que le temps de vaporisation est deux ordres de grandeur plus élevé que celui de la fragmentation. Le phénomène de fragmentation se produit donc toujours avant la vaporisation complète du solvant.

L'équilibre entre la conduction et la convection thermique (Q_{CV}) du gaz chaud vers la particule et son refroidissement en raison des pertes de chaleur rayonnante de la surface (Q_R) et les pertes de rayonnement vapeur (Q_V) détermine le transfert de chaleur net à une particule (Q_{net}). Les mécanismes de conduction et de convection sont généralement décrits par le nombre de Nusselt, Nu, défini par 1.255. Dans le cas des particules de la suspension de dimensions nanométriques ou sub-micrométriques l'effet de Knudsen, qui réduit les transferts de chaleur, devrait être également pris en considération. Il dépend du nombre de Knudsen, Kn, déterminée par l'équation 1.28. Dans le cas des particules de moins de 0.1 μm, la force de thermophorèse doit être prise en compte dans les zones caractérisées par des gradients de température. Les petites particules changent leurs trajectoires du coeur du plasma à la périphérie du jet, caractérisée par des températures et des vitesses de gaz inférieures. En outre, en raison de leur faible inertie, les particules peuvent suivre la trajectoire de gaz chaud qui s'écoule parallèlement à la surface du substrat et ne jamais avoir un impact sur cette surface, ce qui se produit lorsque le nombre de Stokes St est inférieur à 1. Le nombre de Stokes caractérise le comportement des particules en suspension dans un écoulement de fluide et il est déterminé par l'équation 1.311.

Lorsque les particules sont caractérisées par St$>$ 1, elles peuvent traverser la couche limite qui se développe à la surface du substrat. Ces particules frappent et s'aplatissent sur le substrat, ou sur un matériau précédemment déposé, en formant des lamelles (splat). La structure de la lamelle résulte de l'étalement et de la solidification des particules sur le substrat, ce qui dépend des paramètres suivants: la vitesse et la taille de particule, les propriétés du matériau de la particule à l'état liquide, par exemple, la viscosité, la tension superficielle, la mouillabilité du substrat par des particules liquides, l'angle de l'incidence par rapport au substrat, la rugosité de surface du substrat.

Le temps d'étalement d'une lamelle est de l'ordre de quelques μm. Le procédé de solidification est plus longue et commence avant l'étalement est terminé. Le temps entre deux lamelles successives est de l'ordre de dix à quelques dizaines de μs. Par conséquent, la prochaine particule frappe sur une lamelle déjà solidifiée.

Comme mentionné ci-dessus, dans le procédé de projection par plasma la plupart des torches sont alimentées par une source d'alimentation en courant continu. Toutefois, le jet de plasma produit par une torche présente des caractéristiques instationnaires. Les études ont permis de vérifier que ces fluctuations du plasma ont une forte influence

sur les processus de la fragmentation et la vaporisation des gouttelettes, en particulier dans la technique récemment développée, la projection par plasma d'arc de suspension. Il en résulte une mauvaise reproductibilité et la fiabilité du procédé, ce qui cause des applications limitées de la projection par plasma. En analysant les variations de la tension d'arc modes suivants ont été identifiés:

- **Le mode stable ("steady mode")**
  Ce mode de fonctionnement est observé avec un haut niveau de courant d'arc, 900 A, et un argon pur (par exemple débit d'argon de 60 L/min). Le mode stable correspond à de très faibles variations de tension de l'arc: $\Delta U_{arc} = \pm 0.5V$ en raison de l'équilibre entre la force de traînée du gaz de plasma et les forces de Lorent. Le mode stable est caractérisé par une position fixe du pied d'arc, ce qui provoque l'érosion rapide de l'anode.

- **Le mode oscillant ("takeover mode")**
  Ce mode apparaît surtout en utilisant les gaz de plasma monoatomiques. Le mode "takeover" est caractérisé par les fluctuations périodiques ou quasi-périodiques de la tension. Ce mode a été appelé "takeover", car le nouveau pied d'arc naît pendant que l'ancien s'éteint progressivement.

- **Le mode claquage-réamorçage ("restrike mode")**
  Le mode claquage-réamorçage correspond aux fluctuations de tension plus élevées. Le signal de tension présente une forme caractéristique en dents de scie avec de fortes fluctuations de tension. Le déséquilibre entre la force de traînée et de force électromagnétique induit l'étirement et l'allongement de la colonne d'arc qui est accompagnée par l'augmentation de la tension d'arc. Le processus d'allongement est suivi par un claquage électrique au travers de la couche limite entre la colonne d'arc et la paroi anodique. Un nouveau point d'accrochage est créé en amont dans la tuyère, ce qui correspond à une tension d'arc minimale et est identifiée par un saut de tension.

Chapter 2 :

Study of plasma fluctuations in conventional torch

2.1 Introduction

The previous chapter has shown the coatings production by the suspension plasma spraying method and its advantages, i.e. the simplicity, low cost, wide range of the materials. However, there are still many difficulties encountered by the researchers working on this method. The problem with sufficient reproducibility and reliability, due to e.g. the plasma instabilities, is the reason why for many years the special efforts have been devoted to improve this method. This development process requires the profound studies of the plasma instabilities produced by a torch. Therefore, the purpose of the following chapter is to understand the origins of the arc fluctuations. The measurements will be performed by using the conventional dc plasma torch, which will be described in the following paragraph. The time-resolved measurements and the data processing methods will be presented. This kind of experimental procedure applied to the arc voltage signal has leaded to determine a mode due to Helmholtz resonance in the torch, what will be described and investigated in the following chapter. The presented profound studies of the resonance in the torch and described in the previous chapter restrike fluctuations will result in a new resonant mode in the dc plasma torch.

2.1.1 Plasma torch

All measurements have been carried out at atmospheric pressure using a home-made plasma torch, shown schematically in Figure 2.1. It presents a similar configuration as the commercial F4 gun (Sulzer Metco, Switzerland). The torch consists of the nozzle with the variable diameter, d, which in the performed experiments will be chosen between 6 mm and 8 mm. The swirl gas injection is obtained by the injection ring with 16 holes of diameter 1 mm. The geometrical parameters of the torch are indicated in Figure 2.1. The volume of the cathode cavity, V_g, corresponds to the space limited by the injection ring up to the cathode tip. V_g and the distance between the end of cathode and the nozzle exit, L_k, are variable, what is shown in Table 2.1.

It presents the configurations of V_g and L_k used in the experiments. It is possible to choose the cathode cavity volume between: V_g = 6 cm^3, which corresponds to the standard volume, V_g = 8.7 cm^3, obtained by removing the injection ring and V_g = 12.5 cm^3, volume of a cavity specially machined in the laboratory.

The torch is power supplied with a current regulated source (SNMI, type P130, open circuit voltage 180 V), that provides the current up to 1000 A with a maximum voltage of 100 V. The electrodes cooling system consists of the pump which can be operated at the pressure 1.6 MPa.

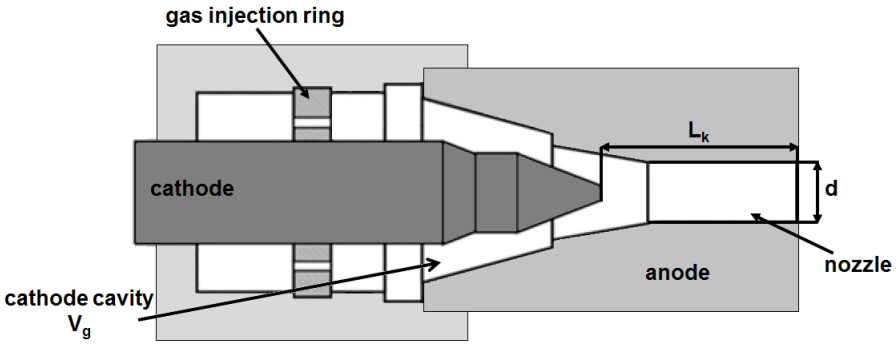

Figure 2.1: Schematic view of the torch.

Table 2.1: Configurations of the volume of cathode cavity and of the distance between cathode tip and the nozzle exit chosen in the experiments.

V_g	(cm^3)	6	8.7	12.5
L_k	(mm)	30	29.5	

The circulating water is delivered to the anode and cathode with an average flow rate of 17 l/min. The operation of the torch is characterized by mean values of the arc voltage ($\overline{V}$) and the arc current. The following paragraphs define the measurement methods of the process parameters.

2.1.1.1 Time-resolved measurements and data processing

The time-resolved measurements of the signals have been carried out using a data acquisition PCI 6132 computer card piloted by Labview software. This National Instruments card, which has 4 simultaneous recording channels (bandwidth 1.3 MHz, sampling rate 2.5 MS/s/channel, accuracy 14 bits), allows converting the signal from an analog to a digital form, by sampling and then digitizing it using an analog-to-digital converter (ADC). The sampling process is of critical importance in this kind of measurement. The resulting signal waveform is highly dependent on the sampling frequency. If this frequency is too low, aliasing occurs and the original analog signal is incorrectly reconstructed, what is presented in Figure 2.2 b).

To obtain the signal without aliasing, the Nyquist sampling criterion should be met. It shows that samples taken at a frequency, f_s, at least twice the highest frequency content of a signal, f_{max}, are sufficient for a correct reconstruction. In practice, f_s should be greater than f_{max} to obtain the original analog signal reconstructed exactly, what is presented as follows: $f_s > 2f_{max}$.

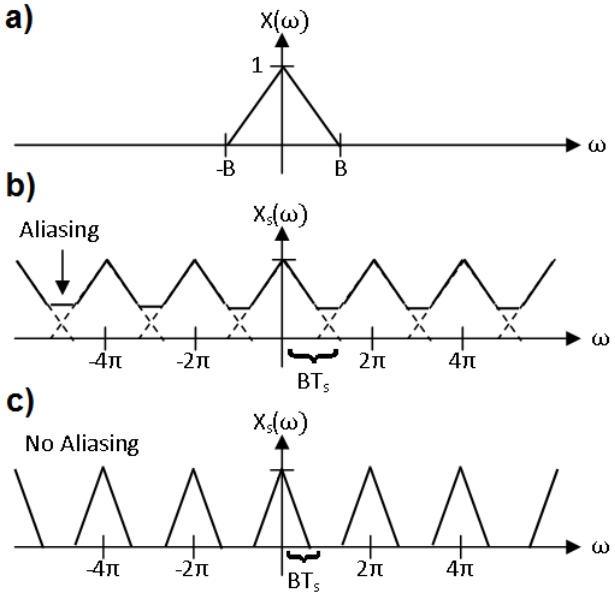

Figure 2.2: Results of the sampling frequency choice: a) original signal, b) sampling frequency below Nyquist frequency (resulting signal with aliasing), c) sampling above Nyquist frequency (no aliasing occurs) [68].

The signals have been recorded by LabView program for further data processing, e.g. the statistical analysis of the signals. To achieve the reliable values the results are the average of 10 measured signals.

The statistical analysis of the measured data gives the information about:

- Mean value

  Considering the recorded data as X the mean value is denoted by $\overline{X}$ and defined by the following formula:

$$\overline{X} = \frac{1}{n}\sum_{i=1}^{n} X_i \tag{2.1}$$

  where n = 6500 samples in the measurements performed in this work.

  To obtain the reliable values for each operating conditions the data contains 10 measurements. Therefore, the final mean value, $\overline{X}_f$, is presented as follows:

$$\overline{X}_f = \frac{1}{10}\sum_{i=1}^{10} \overline{X_i} \tag{2.2}$$

- Variance
  The variance of the data set X consisting of n samples is defined as $\langle s^2 \rangle$ and given by the equation:

$$\langle s^2 \rangle = \frac{1}{n-1} \sum_{i=1}^{n} \left[(x_i - \overline{X})^2 \right] \tag{2.3}$$

- Standard deviation
  The positive square root of the variance, $\langle s^2 \rangle$, is denoted by σ and presented as follows:

$$\sigma = \sqrt{\langle s^2 \rangle} \tag{2.4}$$

- RMS (Root Mean Square)
  The root mean square of a sequence X is determined as the positive square root of the mean of the square of the input sequence. The formula used to compute the RMS value is given by the equation:

$$RMS = \sqrt{\frac{1}{n} \sum_{i=0}^{n-1} {X_i}^2} \tag{2.5}$$

However, the analysis of the signal in the time domain is generally not sufficient. To study all information, which signal contains, it is necessary to transform this signal to the frequency domain, what can be done by the Fourier Transformation described in the following section.

2.1.1.1.1 FFT method

The strongly optimized algorithm, Fast Fourier Transformation, has been chosen because of its shorter time of computation. FFT reduces the number of calculations needed for N points to $N \cdot \log_2 N$ comparing to N^2 of the DFT (Discrete Fourier Transform). Therefore, the following paragraph presents the use of FFT method. According to Fourier theory any function f(x) with period 2π ($f(x) = x + 2\pi$) can be described in terms of an infinite sum of sines and cosines, as follows:

$$f(x) = \frac{a_0}{2} + \sum_{m=1}^{\infty} (a_m cosmx + b_m sinmx) \tag{2.6}$$

Where a_0, a_m and b_m are the Fourier coefficients defined by:

$$a_m = \frac{1}{\pi}\int_{-\pi}^{\pi} f(x)cosmxdx \tag{2.7}$$

$$b_m = \frac{1}{\pi}\int_{-\pi}^{\pi} f(x)sinmxdx \tag{2.8}$$

$$a_0 = \frac{1}{\pi}\int_{-\pi}^{\pi} f(x)dx \tag{2.9}$$

The result of the FFT analysis is an array of complex numbers, amplitudes and phases, corresponding to elementary harmonic oscillations into which the signal may be decomposed. The amplitudes correspond to the power spectrum, which shows the amount of power in a given frequency band or in a given line. The frequency spectrum can be used as a tool to distinguish different regimes of periodicity, chaos and noise.
In the frame of this thesis, Fast Fourier Transform has been applied under LabView platform. It provides a complete set of tools to perform Fourier and spectral analysis.

2.1.1.1.2 Application to arc voltage

The measurement of the arc voltage signal has been carried out using a data acquisition PCI 6132 computer card piloted by Labview software, as has been presented above. This PCI 6132 card consists of 4 simultaneously sampled analog inputs limited by the level voltage of ±10 V. Therefore, to make the measurements of the arc voltage the bridge circuit has to be implemented. The resistors R_1 and R_2 are respectively 2.16 kΩ and 48.93 kΩ, what gives the value of divider equals 23.65, obtained by using the following equation:

$$U_{out} = \frac{R_1}{R_1 + R_2}U_{in} \tag{2.10}$$

The measurement of the circuit has given the value of divider equals 22.86. The difference between the calculated value of divider and the measured one is caused by the heat dissipation of the resistors, what results in differential resistances.
As has been presented above, the sampling process is crucial in the time-resolved measurements. Because of fast variations of re-arcing phenomena in the plasma torch (up to 50 μm) the sample rate of 320 kS/s during 0.2 s has been chosen. It gives a sampling frequency of 160 kHz which meets the Nyquist sampling criterion and the frequency resolution equals to approximately 5 Hz.

	A(X)	B(Y)	C(Y)	D(Y)	E(Y)	F(Y)	G(Y)	H(Y)	I(Y)	J(Y)	K(Y)	L(Y)	M(Y)
Long Name	Time	V(t)	Vh(t)	Va(t)	Vr(t)	Frequency	FFT(V)	FFT(Vh)	FFT(Va)	FFT(Vr)	Frequency filter	Fh	Fa
Units	s	V				Hz							
Comments													
Sparklines													
1	0	-4,52395	-9,08004	2,60496	1,95113	0	8,51898E-32	1,56212E-34	2,68678E-36	7,71369E-32	0	0,04282	0,00562
2	3,1E-6	-9,99507	-8,61457	2,35585	-3,73635	4,96278	0,00464	8,5493E-6	1,46703E-7	0,0042	4,96278	0,04292	0,00562
3	6,2E-6	-13,92578	-8,11813	2,04925	-7,85691	9,92556	0,01046	1,93508E-5	3,31279E-7	0,00947	9,92556	0,04301	0,00563
4	9,3E-6	-15,59899	-7,59213	1,69476	-9,70162	14,88834	0,00526	9,7783E-6	1,67012E-7	0,00476	14,88834	0,04311	0,00563
5	1,24E-5	-15,86458	-7,03887	1,30252	-10,12823	19,85112	0,01107	2,0662E-5	3,52079E-7	0,01001	19,85112	0,04321	0,00564
6	1,55E-5	-15,75834	-6,4612	0,88311	-10,18025	24,8139	0,01036	1,9432E-5	3,30345E-7	0,00937	24,8139	0,0433	0,00565
7	1,86E-5	-15,43964	-5,86225	0,44738	-10,02477	29,77668	0,0042	7,91678E-6	1,34271E-7	0,0038	29,77668	0,0434	0,00565
8	2,17E-5	-14,64287	-5,24528	0,00626	-9,40385	34,73945	0,01084	2,05124E-5	3,4708E-7	0,0098	34,73945	0,04349	0,00566
9	2,48E-5	-13,60708	-4,61377	-0,42954	-8,56376	39,70223	0,00328	6,23241E-6	1,05208E-7	0,00297	39,70223	0,04359	0,00566
10	2,79E-5	-12,70408	-3,97127	-0,84974	-7,88306	44,66501	0,00354	6,74968E-6	1,13671E-7	0,00319	44,66501	0,04369	0,00567
11	3,1E-5	-11,66828	-3,32129	-1,24465	-7,10234	49,62779	0,01817	3,48358E-5	5,85284E-7	0,01641	49,62779	0,04379	0,00568
12	3,41E-5	-10,76528	-2,66728	-1,60537	-6,49263	54,59057	0,01147	2,20857E-5	3,7019E-7	0,01036	54,59057	0,04389	0,00568
13	3,72E-5	-10,02163	-2,01258	-1,92396	-6,08509	59,55335	0,00253	4,9042E-6	8,20074E-8	0,00229	59,55335	0,04399	0,00569
14	4,03E-5	-9,17175	-1,36035	-2,19358	-5,61782	64,51613	0,00572	1,11147E-5	1,85418E-7	0,00516	64,51613	0,04408	0,00569
15	4,34E-5	-9,35766	-0,71359	-2,4086	-6,23547	69,47891	0,01215	2,37167E-5	3,94707E-7	0,01097	69,47891	0,04419	0,0057
16	4,65E-5	-10,26066	-0,07483	-2,56458	-7,62125	74,44169	0,00372	7,28773E-6	1,20998E-7	0,00335	74,44169	0,04428	0,00571
17	4,96E-5	-11,00431	0,55378	-2,65837	-8,89972	79,40447	0,02389	4,70579E-5	7,79439E-7	0,02155	79,40447	0,04439	0,00571
18	5,27E-5	-10,89807	1,17016	-2,68839	-9,37985	84,36725	0,01938	3,83571E-5	6,33805E-7	0,01749	84,36725	0,04448	0,00572
19	5,58E-5	-10,26066	1,77211	-2,65475	-9,37803	89,33003	0,00205	4,07648E-6	6,71979E-8	0,00185	89,33003	0,04459	0,00572
20	5,89E-5	-9,38422	2,35731	-2,55922	-9,1823	94,2928	0,0029	5,79446E-6	9,52886E-8	0,00262	94,2928	0,04469	0,00573
21	6,2E-5	-8,32187	2,92344	-2,40513	-8,84018	99,25558	0,02472	4,9584E-5	8,1344E-7	0,02228	99,25558	0,04479	0,00574
22	6,51E-5	-6,78145	3,46821	-2,19719	-8,05247	104,21836	0,0171	3,4466E-5	5,64064E-7	0,01542	104,21836	0,04489	0,00574
23	6,82E-5	-5,00201	3,98928	-1,94145	-7,04984	109,18114	0,00328	6,64001E-6	1,08408E-7	0,00296	109,18114	0,04499	0,00575
24	7,13E-5	-2,95698	4,48434	-1,64504	-5,79628	114,14392	0,00773	1,57267E-5	2,5614E-7	0,00697	114,14392	0,0451	0,00575
25	7,44E-5	-0,83227	4,95109	-1,31596	-4,4674	119,1067	0,02899	5,92148E-5	9,621E-7	0,02611	119,1067	0,0452	0,00576
26	7,75E-5	1,39867	5,38738	-0,96287	-3,02585	124,06948	0,01558	3,19721E-5	5,18211E-7	0,01403	124,06948	0,0453	0,00577
27	8,06E-5	3,65617	5,79118	-0,59475	-1,54025	129,03226	0,00192	3,95307E-6	6,39169E-8	0,00173	129,03226	0,04541	0,00577
28	8,37E-5	6,09958	6,16061	-0,22076	0,15973	133,99504	0,0254	5,26123E-5	8,48616E-7	0,02287	133,99504	0,04551	0,00578
29	8,68E-5	8,78203	6,49396	0,1501	2,13796	138,95782	0,02483	5,16659E-5	8,31321E-7	0,02235	138,95782	0,04561	0,00579
30	8,99E-5	11,59726	6,78968	0,50914	4,29844	143,9206	0,01589	3,32146E-5	5,3313E-7	0,0143	143,9206	0,04572	0,00579
31	9,3E-5	14,46562	7,04645	0,84826	6,5709	148,88338	0,02811	5,9015E-5	9,44938E-7	0,02528	148,88338	0,04582	0,0058
32	9,61E-5	10,42867	7,26353	1,1604	2,00474	153,84615	0,00944	1,99195E-5	3,18166E-7	0,00849	153,84615	0,04593	0,0058
33	9,92E-5	1,13308	7,44264	1,44066	-7,75023	158,80893	0,00114	2,41367E-6	3,84581E-8	0,00102	158,80893	0,04603	0,00581
34	1,02E-4	-3,22257	7,58722	1,68599	-12,49578	163,77171	0,00691	1,47196E-5	2,33958E-7	0,00622	163,77171	0,04614	0,00582
35	1,05E-4	-3,78031	7,69949	1,89332	-13,37311	168,73449	1,15E-4	2,46416E-7	3,90696E-9	1,04E-4	168,73449	0,04625	0,00582

Figure 2.3: Example of the structure of the recorded data.

The example of the data structure of the arc voltage signal, recorded at 400 A for Ar-H_2 (45-10 slm) plasma by the torch with a standard configuration of the cathode cavity: V_g = 6 cm^3, is shown in Figure 2.3. The measured and calculated results have been processed by the Origin Pro software to present the temporal evolution of the fluctuating component of the arc voltage signal $\upsilon(t)$, what is given in Figure 2.4. These variations have been obtained from the instantaneous voltage, V(t), which is considered as the sum of the mean voltage, $\overline{V}$, and of the fluctuating component, $\upsilon(t)$.

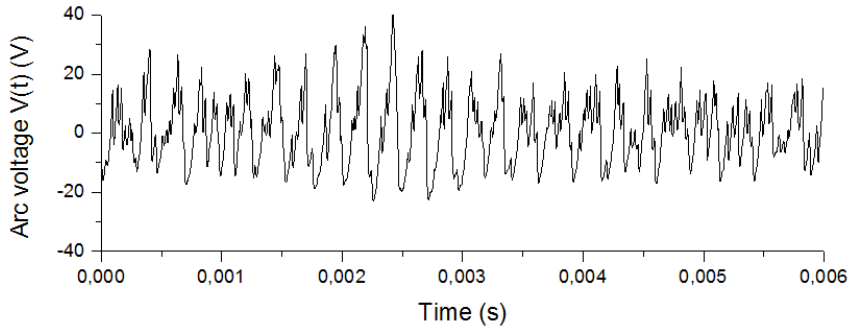

Figure 2.4: Time evolution of the fluctuating component of the arc voltage signal.

The statistical analysis of this signal, performed by Labview program, is indicated in Table 2.2.

Table 2.2: Statistical analysis of the signal presented in Figure 2.4.

$\overline{V}$ (V)	σ (V)	$\langle \upsilon^2 \rangle$ (V)	RMS (V)
62	13.1	171.7	62.5

The mean value, standard variation, variance and RMS of the signal have been calculated.

The obtained temporal evolution of the arc voltage signal shows the characteristic features related to the restrike mode but they are superimposed on more regular oscillations, pseudo sine wave with the period of about 200 μs. Therefore, to complete the analysis of the measured arc voltage Fast Fourier Transformation has been performed.
To compare computed power spectra of the signals measured under different experimental conditions, presented in the further paragraphs, each spectrum has been normalized with respect to the variance of the voltage. As has been presented above, the instantaneous voltage, V(t), is the sum of the mean voltage, $\overline{\mathrm{V}}$, and of the fluctuating component, v(t). The average squared quantities are obtained as follows:

$$\langle V^2 \rangle = \overline{V}^2 + \langle v^2 \rangle \tag{2.11}$$

where $\langle v^2 \rangle$ is the variance of the voltage, presented in Table 2.2.
The power spectrum, ϕ(f), of the voltage fluctuating component, v(t), which is the squared amplitude of its Fourier components, is then given by:

$$\int_0^{f_{max}} \phi(f)df = \langle v^2 \rangle \tag{2.12}$$

Figure 2.5 presents the computation of the voltage power spectrum of the signal given in Figure 2.4.

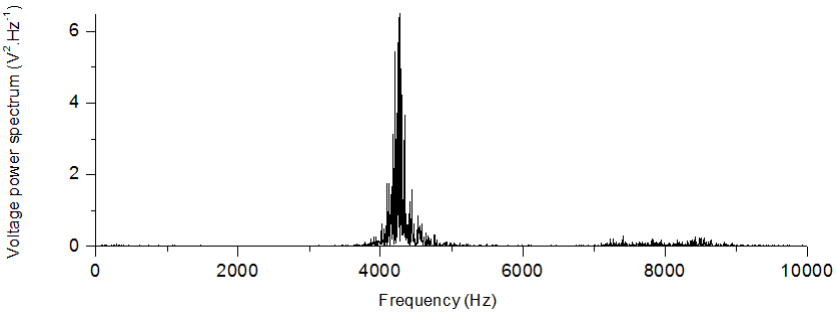

Figure 2.5: Voltage power spectrum of the arc voltage signal presented in Figure 2.4.

2.1.1.1.3 Resonance in dc plasma torch

The power spectrum, presented in Figure 2.5, highlights the presence of a sharp peak at ~4.3 kHz, what cannot correspond to mentioned in chapter 1 restrike fluctuations, which are characterized by non-reproducible spectral components. This spectral peak matches, approximately, to the reverse of the period of the above-mentioned sine wave in Figure 2.4. The obtained results suggest that in dc plasma torch is another phenomenon superimposed on the restrike mode.

One of the explanation of this phenomenon could be the existence of the acoustic wave in the nozzle in which resonance could take place, provided the length of the channel is an integer multiple of the half wavelength. However, the length of the nozzle torch should be of about 0.6 m instead of around 30 mm, given in Table 2.1. Therefore, acoustic longitudinal stationary waves cannot occur at this frequency in this nozzle channel.

In the description of the plasma instabilities presented in chapter 1 the linear dependence of the mean measured pressure on the specific enthalpy and, therefore, the mean voltage has been highlighted (see Figure 1.27). It has leaded to the idea to consider the coupling between the arc and pressure variations in the cathode cavity. These variations of the pressure can be generated by the oscillation of the plasma into the nozzle channel, what shows that the cathode cavity together with the nozzle channel can appear to be a Helmholtz resonator.
Delair *et al.* has first suggested that Helmholtz oscillations in the arc chamber can be the reason for high frequency fluctuations of the arc voltage [69]. This hypothesis has been referred to the field of combustion systems where it has been discovered that the burners behave like Helmholtz resonators [70, 71].
The Helmholtz oscillation is a very basic phenomenon studied in the framework of vibration theory. The resonator is a simple acoustic system, presented in Figure 2.21, which consists of a rigid-walled cavity of volume V, filled with air, with a neck of section S and the length L.

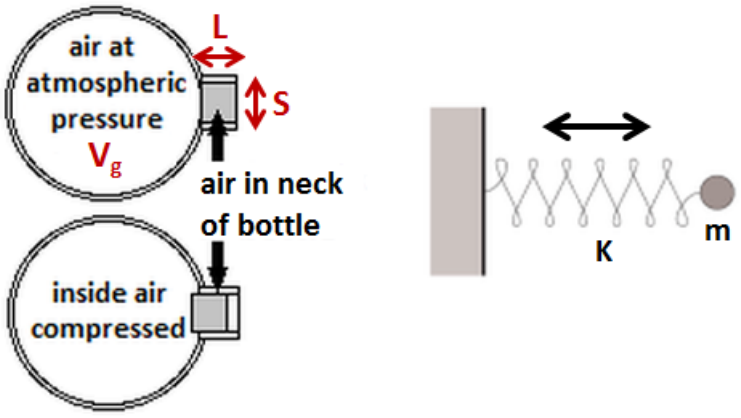

Figure 2.6: Helmholtz resonator as mass-spring system.

The air filling the system is under the atmospheric pressure. After a proper short exterior pressure excitation, the air in the neck is starting to move back and forth damping out in time. The Helmholtz resonator is commonly compared to the mass-spring system. The air filling the cavity, submitted to condensations and rarefactions, acts like a spring. The air located in the neck plays the role of an incompressible mass moving back and forth along the neck.

The mass of the air in the neck can be presented by the equation:

$$m = \rho.S.L \tag{2.13}$$

where:

ρ is the density of air.

If this mass descends a small distance x into the neck, it compresses the air in the cavity so that the air that previously occupied the volume V now has the volume: V − S.x. Consequently, the pressure of the air rises from atmospheric pressure, P_0, to the value: $P_0 + p$.
Assuming the oscillations to be adiabatic, the pressure change p/P_0 produced by this small volume change, ΔV, is equal to:

$$\frac{p}{P_0} = -\gamma\frac{\Delta V}{V} = -\gamma\frac{Sx}{V} \tag{2.14}$$

This mass of the air, m, is moved by the difference in pressure between the top and bottom of the neck, what can be presented by Newton law for the acceleration:

$$m\frac{d^2x}{dt^2} = F \tag{2.15}$$

assuming that F is a net force presented by F = pS and introducing m determined by Equation (2.13), it gives:

$$\frac{d^2x}{dt^2} = \frac{p.S}{\rho.S.L} = -\frac{\gamma SP_0}{\rho.V.L}x \tag{2.16}$$

It shows that restoring force is proportional to the displacement. This is the condition for simple harmonic motion, which has a frequency $1/2\pi$ times the square root of the constant of proportionality, as follows:

$$f = \frac{1}{2\pi}\sqrt{\frac{\gamma SP_0}{\rho.V.L}} \tag{2.17}$$

While determining the speed of sound in air, c, by the density, the pressure and ratio of specific heats, the resonant frequency is given by the equation:

$$f = \frac{c}{2\pi}\sqrt{\frac{S}{V.L}} \tag{2.18}$$

The cold gas in the cathode cavity, characterized by the volume V_g, presented in Figure 2.7, is analogous to the air in the cavity of the Helmholtz resonator, described above, and to the spring in the mass-spring system.

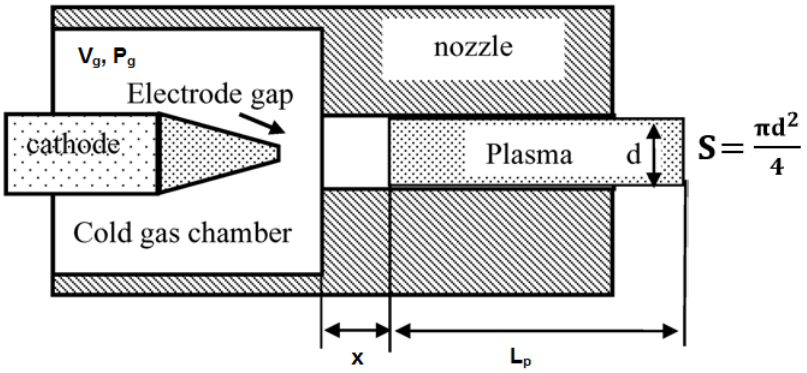

Figure 2.7: Schematic view of the plasma Helmholtz oscillations.

This cathode cavity is connected to the nozzle channel which contains the oscillating plasma (compared to the mass in the mass-spring system). The oscillating plasma induces the pressure drop due to the friction resistance and turbulence, which added to the viscous effects in the channel, is a source of non-reversible phenomena. Then, the pressure perturbation in the cathode cavity is given by the equation:

$$\frac{d^2p}{dt^2} + \frac{\omega_H}{Q}\frac{dp}{dt} + {\omega_H}^2 p = {\omega_H}^2 p_{ext} \tag{2.19}$$

where:

p_{ext} is the excitation source of the resonator coupled with the arc voltage,
Q the quality factor due to dissipative effects.

This Q factor is linked to the band pass of the resonator, Δf, and to the damping factor, ξ, as follows:

$$Q = \frac{f_H}{\Delta f} = \frac{1}{2\xi} \tag{2.20}$$

By applying similar assumptions to the plasma mass as has been presented above, for a Helmholtz resonator, a Helmholtz frequency of plasma mass motion in the torch nozzle can be defined as:

$$f_H = \frac{1}{2\pi}\sqrt{\frac{\gamma_g P_g}{\rho_p}}\sqrt{\frac{S}{L_p V_g}} \tag{2.21}$$

where:

γ_g is the isentropic coefficient of the cold gas,
P_g the mean pressure in the cathode cavity,
ρ_p the plasma density,
S the cross section area of the torch nozzle, presented in Figure 2.7,
L_p the length of the nozzle channel,
V_g the volume of the cathode cavity.

The equation (2.21) highlights the dependence of the Helmholtz mode on the thermophysical properties, γ_g and ρ_p, related, respectively, to the cold gas and to the plasma, the torch configuration, $\sqrt{S/L_p.V_g}$ and the pressure in the cathode cavity, what is the function of the working conditions and of the thermodynamic properties of the gas.

Consequently, the investigation of Helmholtz mode of plasma oscillations requires the simultaneous measurements of the arc voltage and the pressure inside the cathode cavity. The time-resolved total pressure has been measured using a piezoresistive sensor ENDEVCO 8510C (Meggitt's Endevco, Irvine, USA). It is a miniature and high sensitivity piezoresistive transducer for measuring dynamic pressure (in ranges from 15 to 100 psi). A small size, 4 mm in diameter, enables to mount this sensor in the cathode cavity of the torch. The simultaneous measurements of the arc voltage and the pressure signals have been performed using a data acquisition PCI 6132 computer card piloted by Labview software, what has been highlighted in the previous paragraphs.

2.2 Investigation of the plasma instabilities

The theoretical model of Helmholtz mode has highlighted the dependencies of Helmholtz fluctuations on the geometrical parameters of the torch and the thermophysical properties related to the cold gas and to the plasma. Therefore, the purpose of the presented studies is to confirm this model by the experimental measurements. The influence of different operating conditions will be examined by measuring the arc voltage signals and the pressure inside the cathode cavity.
Moreover, the previous work of the laboratory has highlighted the existence of other fluctuation modes due to acoustic waves propagation and reflection inside the torch [72, 73]. These modes, so-called acoustic modes, occur at higher frequencies, presented as a divergent peak at ∼8.5 kHz in the voltage power spectrum in Figure 2.5. Therefore, the following sections will give the investigation results of the Helmholtz and acoustic modes. Moreover, the arc voltage signal presents more randomly distributed short events which correspond to the restrike mode, what will be also studied in this work.
To examine the Helmholtz, acoustic and restrike modes of the plasma instabilities, the signals of these modes have to be isolated from the measured arc voltage and pressure by applying the filtering methods, what is described in the following section.

2.2.1 Filtering method

The fluctuating component, υ(t), obtained from the measured arc voltage signal, V(t), where υ(t) = V(t) - $\overline{\text{V}}$, can be presented as the sum of the instability modes of plasma jet: Helmholtz (H), restrike (R) or acoustics (a), as follows:

$$\upsilon(t) = \upsilon_H(t) + \upsilon_R(t) + \upsilon_a(t) \tag{2.22}$$

The time-resolved measurement of the pressure can be also predicted as the superposition of the modes of the plasma fluctuations. The signal of the arc voltage or the pressure which contains several components can be written as:

$$s(t) = \sum_i s_i(t) \tag{2.23}$$

where the subscript, i, is associated with the modes of the instability.
To observe the influence of these modes on the operating conditions they have been isolated from the signal by using numerical Wiener filter programmed under LabView platform. The purpose is to separate each component, s_i(t), by using a Wiener filter, F_i(f), which is obtained by a minimization method (minimization of the Euclidean distance between the ideal s_i(t) function and the one obtained by filtering, S_i(f)) as follows:

$$\frac{\partial}{\partial F_i} = \left\{ \int \parallel s_i(t) - FT^{-1}\{F_i(f) \times S(f)\} \parallel^2 dt \right\} = 0 \tag{2.24}$$

where:

TF^{-1} is the reciprocal Fourier transform,
S(f) the Fourier transform of the recorded signal, s(t), defined as S(f) = FT{s(t)} where $S(f) = \sum_i S_i(f)$.

By applying the Plancherel-Parseval theorem, the above equation can be written as:

$$\frac{\partial}{\partial F_i} = \left\{ \int_0^{f_{max}} \parallel S_i(f) - \{F_i(f) \times S(f)\} \parallel^2 dt \right\} = 0 \tag{2.25}$$

what gives the following formula:

$$\int_0^{f_{max}} \frac{\partial}{\partial F_i} \parallel S_i - F_i \times S \parallel^2 df = \int_0^{f_{max}} \{2F_i \times SS^* - (SS_i^* + S^*S_i)\} df = 0 \tag{2.26}$$

where:

$*$ stands for the complex conjugate.

The expansion of S gives cross products, such as $S_iS_j^*$. Assuming that the instability modes are uncorrelated either because the frequency domains of i and j components are disconnected or by phase mixing if the restrike mode is implied, the optimum Wiener filter, F_i, is given by:

$$F_i(f) = \frac{\Phi_{ii}}{\Phi_{HH} + \Phi_{RR} + \Phi_{aa}} \tag{2.27}$$

where Φ_{HH} and Φ_{aa} are obtained by fitting a Lorentzian function to each peak of the recorded spectrum, as follows:

$$\Phi_{ii}(f) = \frac{A_i}{1 + 4{Q_i}^2(f - f_i)^2} \tag{2.28}$$

Figure 2.8 presents the filters F_H and F_a determined from the arc voltage spectrum, from Figure 2.5, recorded for a plasma torch operated at 400 A and Ar-H_2 (45-10 slm) gas mixture, what was indicated in Figure 2.4. Figure 2.8 highlights that the calculated filter is a real function of frequency and does not produce phase shifts.

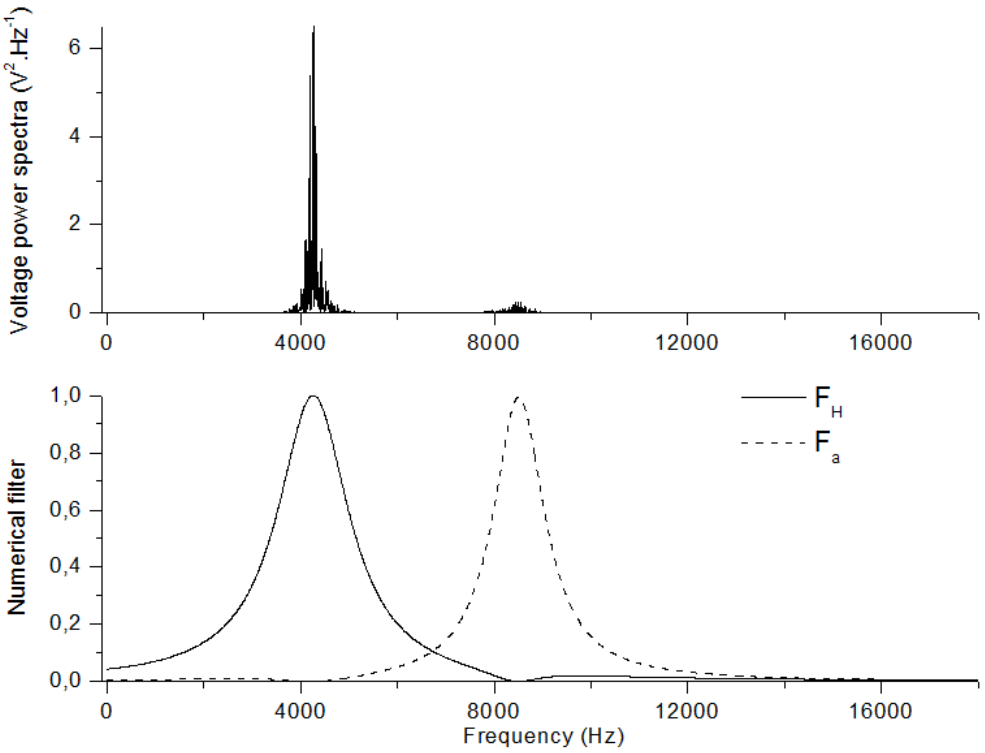

Figure 2.8: Calculated filters F_H and F_a applied to the power spectrum, presented in Figure 2.5, of the arc voltage generated for the conditions from Figure 2.4.

The determination of the filters: F_H and F_a allows obtaining Helmholtz and acoustic modes components by the following equation:

$$s_i(t) = FT^{-1}\{F_i(f) \times S(f)\} \tag{2.29}$$

Then, the restrike component can be deduced as follows:

$$s_R(t) = s(t) - [s_H(t) + s_a(t)] \tag{2.30}$$

Figure 2.9 presents the example of the filtering from a raw arc voltage signal its components: the restrike, Helmholtz and acoustic modes of instabilities. It shows that the Helmholtz component has the most important contribution to the arc voltage together with the restrike mode. A modulation of the signal envelopes in Helmholtz and acoustic components is observed (beating phenomena).

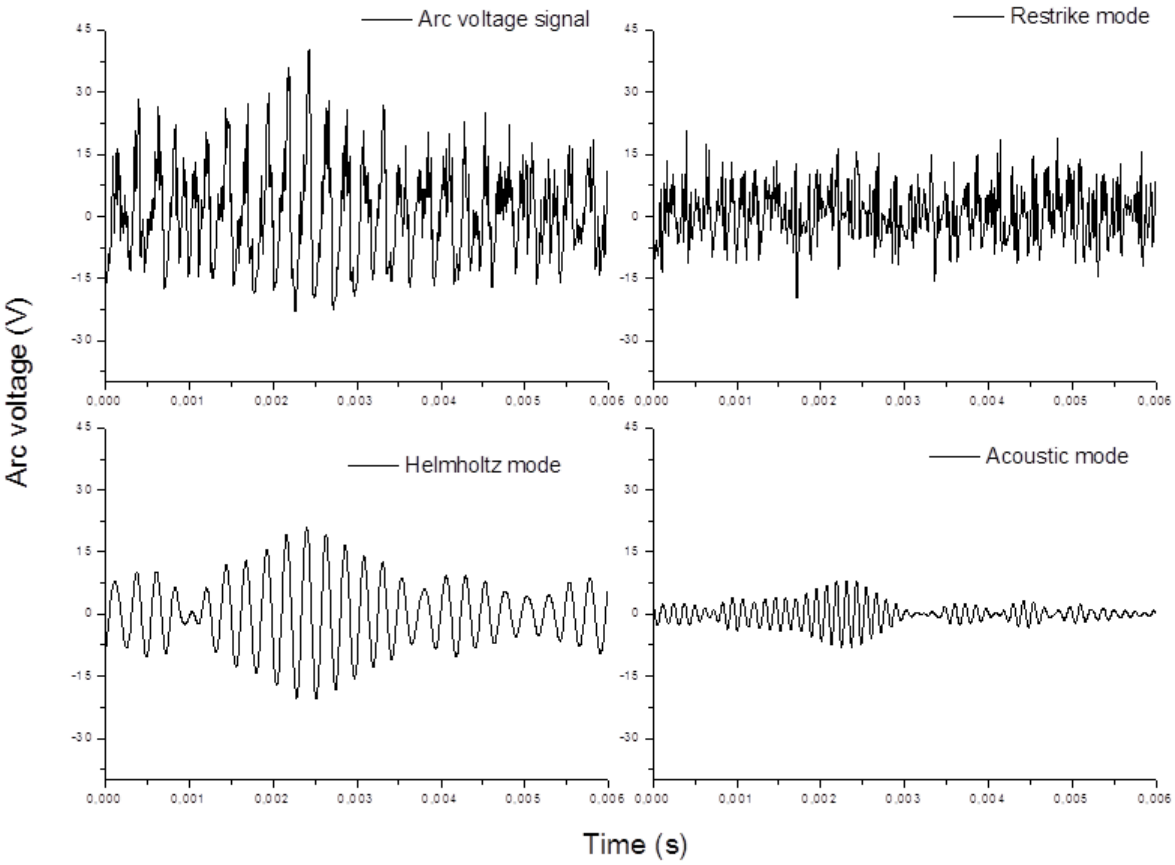

Figure 2.9: Raw arc voltage signal, from Figure 2.4, and its filtered components: Helmholtz, restrike and acoustic.

Similar behavior has been observed for the fluctuating component of pressure.

2.2.2 Helmholtz and acoustic modes

The following section will highlight experimentally the dependence of the Helmholtz and acoustic modes on the geometrical parameters of the torch: the volume of the cavity and the position of the cathode. Moreover, the influence of the composition of plasma forming gases will be shown.

2.2.2.1 Configuration of the cathode cavity

This paragraph gives the investigation results of the effect of different configurations of the cathode cavity on the Helmholtz and acoustic modes. By removing the injection ring, Figure 2.10 (b), and using the specially machined cathode cavity, 2.10 (c), three different configurations have been obtained characterized by the volumes: (a) V_g = 12.5 cm^3, (b) V_g = 8.7 cm^3 and (c) V_g = 6 cm^3.

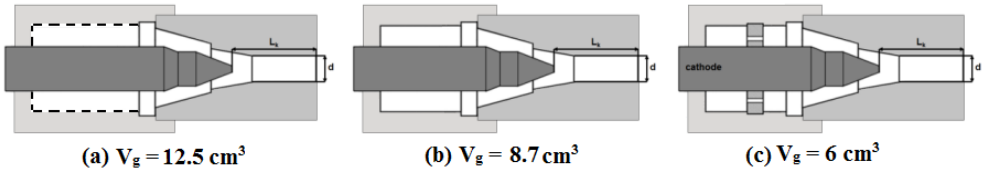

Figure 2.10: Configurations of the cathode cavity.

Figures 2.11 and 2.12 present the voltage and pressure power spectra of Helmholtz (H) and acoustic (A) components, filtered and computed from the arc voltage and pressure signals. They have been recorded for each configuration of the cathode cavity, for the same operating conditions: L_k = 30 mm, I = 500 A, Ar-H_2 (45-10 slm).

The results presented in Figures 2.11 and 2.12 show a very good matching between the Helmholtz and acoustic modes of the voltage and pressure. These results confirm the coupling between the pressure in the cathode cavity and the arc voltage, what proves that the main plasma oscillations follow the Helmholtz resonator. To analyze the evaluation of Helmholtz and acoustic modes their parameters have been established from the power spectra presented in Figures 2.11 and 2.12 and summarized in Table 2.3.
The standard deviation, defined as follows: $\sigma_i = \sqrt{\langle s_i{}^2 \rangle}$, where s_i are the signals of voltage or pressure associated with the Helmholtz, acoustic or restrike modes, has been calculated from the filtered spectra by LabView program. The Q factor has been established from Equation (2.20), as follows: $Q = f_i/\Delta f$, where Δf has been measured as the full-width at half-maximum of the Helmholtz or acoustic modes line in voltage and pressure power spectra.

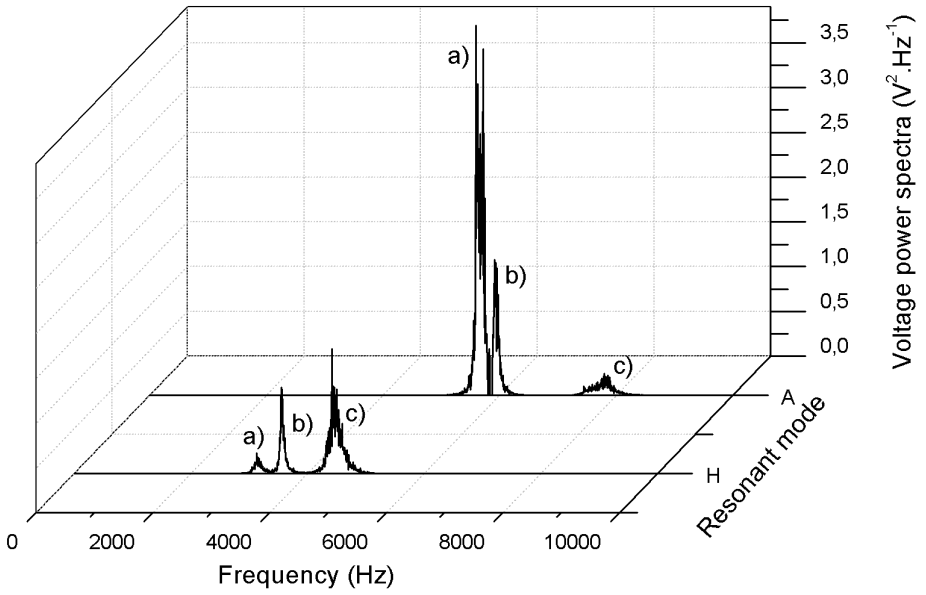

Figure 2.11: Voltage power spectra of filtered voltage fluctuations of H-Helmholtz and A-acoustic modes for: (a) V_g = 12.5 cm^3, (b) V_g = 8.7 cm^3 and (c) V_g = 6 cm^3. Operating parameters: L_k = 30 mm, I = 500 A, Ar-H_2 (45-10 slm) [74].

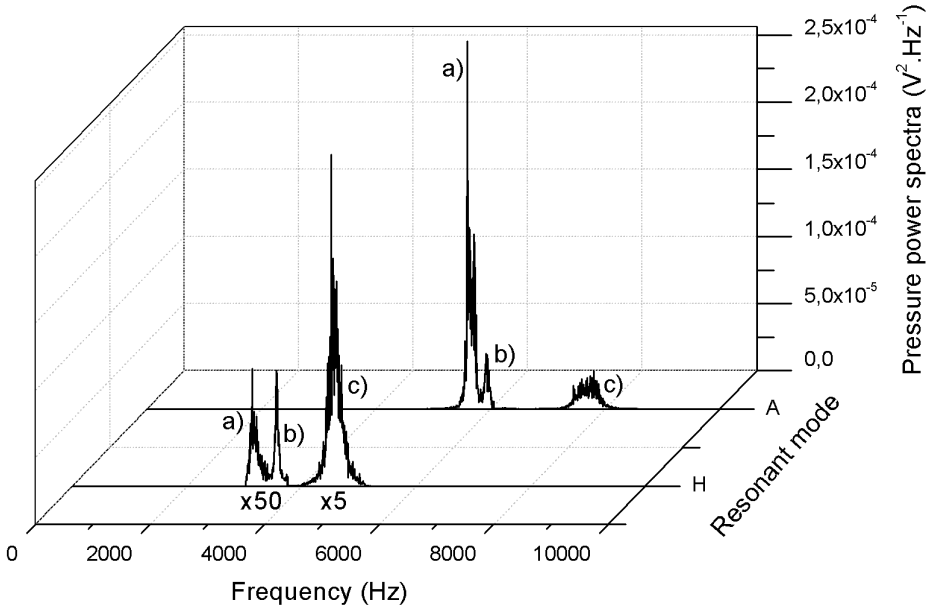

Figure 2.12: Pressure power spectra of filtered arc fluctuations of H-Helmholtz and A-acoustic modes for: (a) V_g = 12.5 cm^3, (b) V_g = 8.7 cm^3 and (c) V_g = 6 cm^3 [74].

Table 2.3: The frequency, standard deviation (σ) and Q factor of voltage and pressure power spectra presented in Figure 2.11 and 2.12, where: (a) V_g = 12.5 cm^3, (b) V_g = 8.7 cm^3 and (c) V_g = 6 cm^3.

		Arc voltage			Pressure		
		f (Hz)	σ (V)	Q	f (Hz)	σ (mbar)	Q
Helmholtz mode	(a)	3100	3.3	19	3170	3	14.5
	(b)	3600	5.5	30	3550	6	32
	(c)	4500	9	30.5	4500	53	30.5
Acoustic mode	(a)	5700	13.4	36.5	5700	90	35.5
	(b)	5950	8	43	5950	40	43
	(c)	7850	5	17	7800	56	17

The values of Helmholtz frequency of the voltage and pressure power spectra, given in Table 2.3, highlight the shift of f_H peaks to lower values due to the increase of the cathode cavity volume, e.g. from 4500 Hz obtained for the case (c) to 3100 Hz for (a). It has to be mentioned that the frequency peaks in the pressure power spectra have similar values. By following the theoretical model for Helmholtz mode, given by Equation (2.21), the modification of f_H in the function of the cathode cavity configuration can be presented as follows:

$$\left(\frac{f_1}{f_2}\right)^2 = \frac{V_2}{V_1} \tag{2.31}$$

where the subscripts 1 and 2 stands for the different cases: (a), (b) and (c) given in Table 2.3.

The calculations presented in Table 2.4 highlight a good agreement between the experimental results and the model of Helmholtz mode described in the previous section.

Table 2.4: Calculations of the Helmholtz frequency modifications due to different configurations of cathode cavity.

	Ar-H_2 (45-10 slm)				Ar-N_2 (40-6 slm)	Ar-N_2 (40-16 slm)
cavities		(a)/(b)	(b)/(c)	(a)/(c)	(a)/(c)	(a)/(c)
$(f_1/f_2)^2$	V	1.35	1.55	2.1	1.7	1.6
	P	1.25	1.6	2.02	1.7	1.6
(V_2/V_1)		1.44	1.45	2.05	2.05	2.05

The computed standard deviations of Helmholtz and acoustic modes show that with the increase of the volume of the cathode cavity, not only the Helmholtz frequencies are shifted to lower values but also a major part of the signal power turns to acoustic modes. This phenomenon is more obviously presented in Figure 2.13.

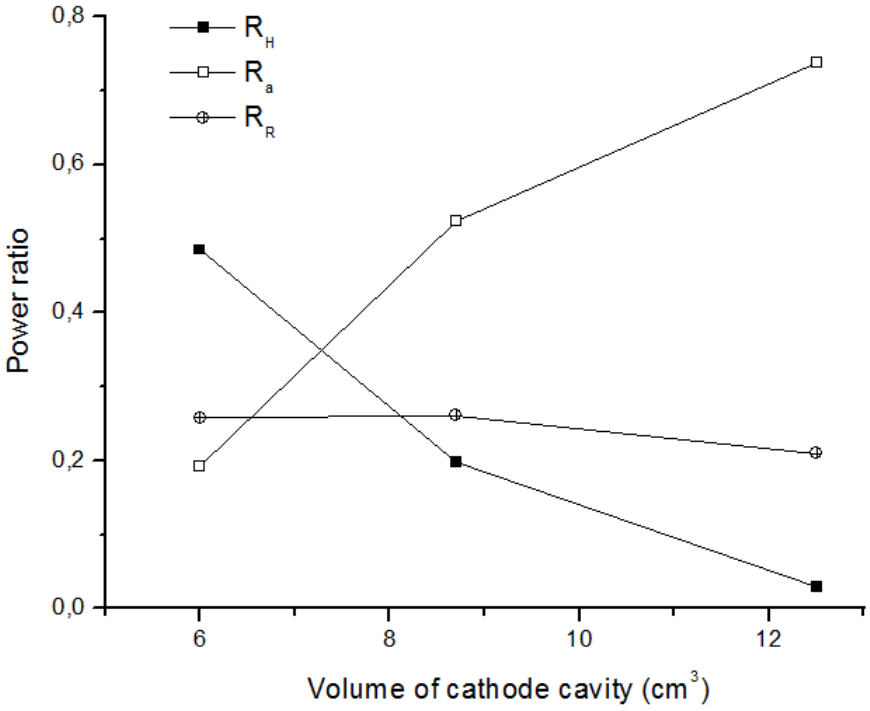

Figure 2.13: Influence of the volume of cathode cavity (cases: (a), (b), (c)) on power ratio for voltage components: H-Helmholtz, a-acoustic and R-restrike.

The power ratio, R_i, for each mode has been calculated as follows: $R_i = \sigma_i{}^2/\sigma^2$. It characterizes the power contained in each mode in relation to the raw arc voltage signal. These dimensionless power ratios have been plotted as a function of the volume of cathode cavity. For the case (c), where V_g = 12.5 cm^3, most of fluctuating power is contained in the acoustic mode oppositely to the case (a).
Moreover, the Q factors of Helmholtz resonance for the arc voltage also decrease from 30.5 to 19 when V_g varies from 6 to 12.5 cm^3. This indicates that the Helmholtz resonance energy is transferred to acoustic modes.
The presented results lead to the assumption of the model for the acoustic resonances in the conventional torch. The cathode cavity can be assumed to be of cylindrical geometry and have an annular tube shape with the length: L = 38 mm, the inner radius a = 7 mm and the outer diameter b = 10.5 mm. Defining the acoustic pressure, p, as follows: $p(\overrightarrow{r}, t) = p(\overrightarrow{r})\exp(-j\omega t)$, the acoustic modes in the cathode cavity can be determined from the solution of the homogeneous Helmholtz equation for an ideal gas obtained from the acoustic propagation equation, i.e. $\Delta p(\overrightarrow{r}, t) + k^2 p(\overrightarrow{r}, t) = 0$, where k is the wave number linked to the speed of sound, a_g, as follows: $k.a_g = 2\pi f$. The obtained resonance modes are due to a combination of the axial modes and those of radial and azimuthal modes, defined as: $k^2 = k_r{}^2 + k_z{}^2$. The cathode cavity is assumed to be an annular tube which is closed at the injection ring and supposed to be opened at the cathode tip. It can

be shown that the acoustic pressure can be written as:

$$p(r,\theta,z) = (AJ_n(k_r r) + BY_n(k_r r))cos(n\theta)cos\Big(\frac{\ell\pi}{2L}z\Big) \tag{2.32}$$

where:

r, θ, z	are the cylindrical coordinates,
J_n, Y_n	the Bessel's functions, respectively, of first and second kind of nth order,
ℓ	the integer number,
A, B	constant numbers,
L	the cathode axial length.

Since the r-component of acoustic velocity is zero at r = a and r = b, what gives $\partial p(r = a \text{ and } b, \theta, z)/\partial r = 0$, the resonance modes are obtained from the solution of the following relationship:

$$J_n'(K_r)Y_n'(\lambda K_r) - J_n'(\lambda K_r).Y_n'(K_r) \tag{2.33}$$

where:
$K_r = ak_r$,
$\lambda = b/a$,
the symbol $'$ stands for the derivation.
The resonance frequencies are: $f_{nm} = a_g K_{nm}/2\pi a$, where $K_r = K_{nm}$ are the solutions of equation (2.33), in which m gives the mth roots of equation. The resulting resonance modes have frequencies defined by:

$$f_0 = ({f_{nm}}^2 + {f_\ell}^2)^{0.5} \tag{2.34}$$

where f_ℓ corresponds to acoustic longitudinal modes and is defined as follows: $f_\ell = \ell a_g/4L$. The calculation of modes shows that most of them have frequencies above 10 kHz except the mode (n, m , ℓ) = (1, 1, 1), which defines:
the first longitudinal mode $f_\ell = 2368$ Hz and $f_{11} = 6589$ Hz, what gives the frequency $f_0 =$ 7000 Hz. This value shows a good agreement of presented model with the acoustic mode frequency obtained in the power spectra presented in Figures 2.14 and 2.15. Moreover, when the volume of the cathode cavity, V_g, increases, L presented in the model (2.32) increases, what gives the decrease of the acoustic frequency. The experimental results, listed in Table 2.3 and 2.5, show the same dependency.

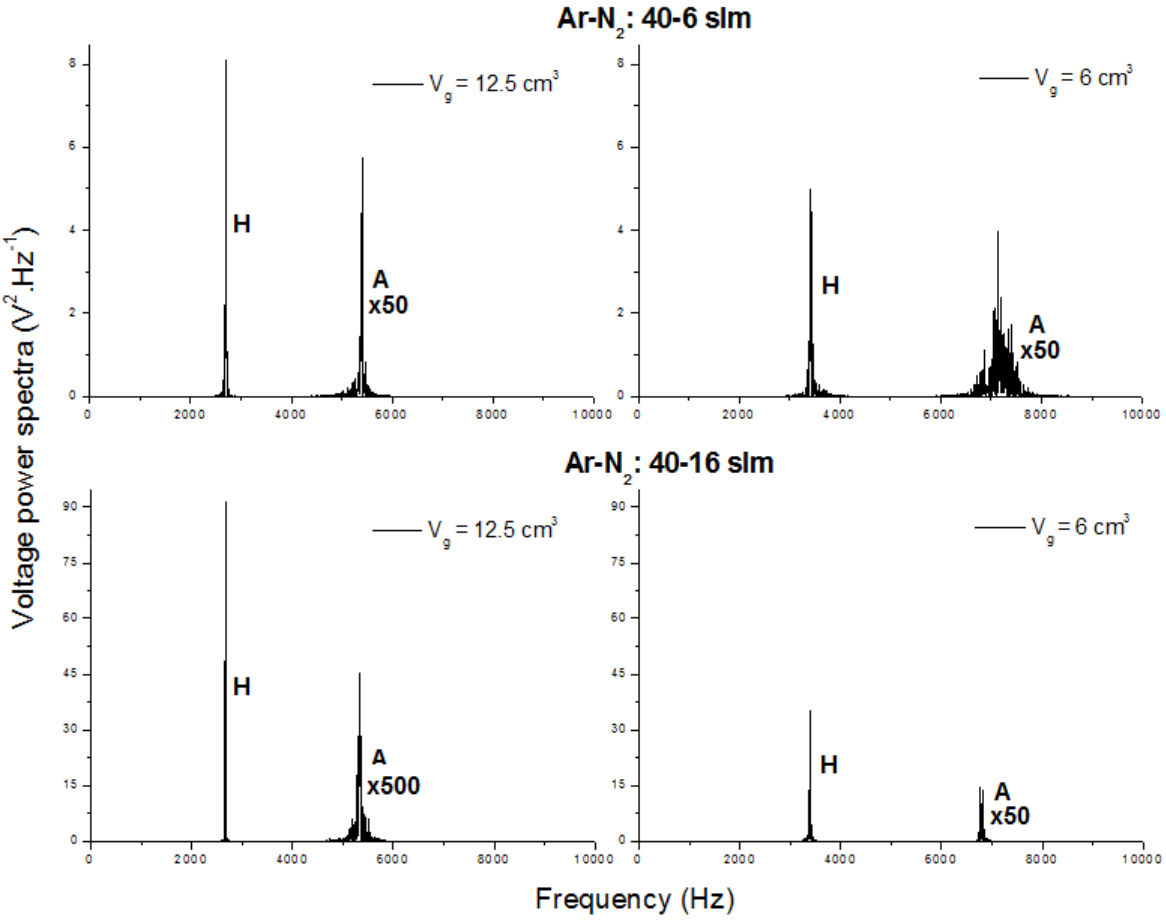

Figure 2.14: Voltage power spectra of filtered voltage fluctuations of H-Helmholtz and A-acoustic modes obtained for two configurations of cathode cavity: (a) V_g = 12.5 cm^3, (c) V_g = 6 cm^3 and for the Ar-N_2 compositions: 40-6 and 40-16 slm.

The influence of the configurations of the cathode cavity on the resonance modes has been also examined for the Ar-N_2 plasma forming gases mixtures: 40-6 and 40-16 slm. The arc voltage and pressure signals have been obtained for two configurations of the cathode cavity: (a) V_g = 12.5 cm^3 and (c) V_g = 6 cm^3 at 500 A. Figures 2.14 and 2.15 present the arc voltage and pressure power spectra computed for the signals recorded for Ar-N_2: 40-6 and 40-16 slm. The values of Helmholtz frequency, defined from the power spectra and given in Table 2.5, highlight the shift of f_H peaks to lower values, as has been expected from the model for Helmholtz mode, (2.21).

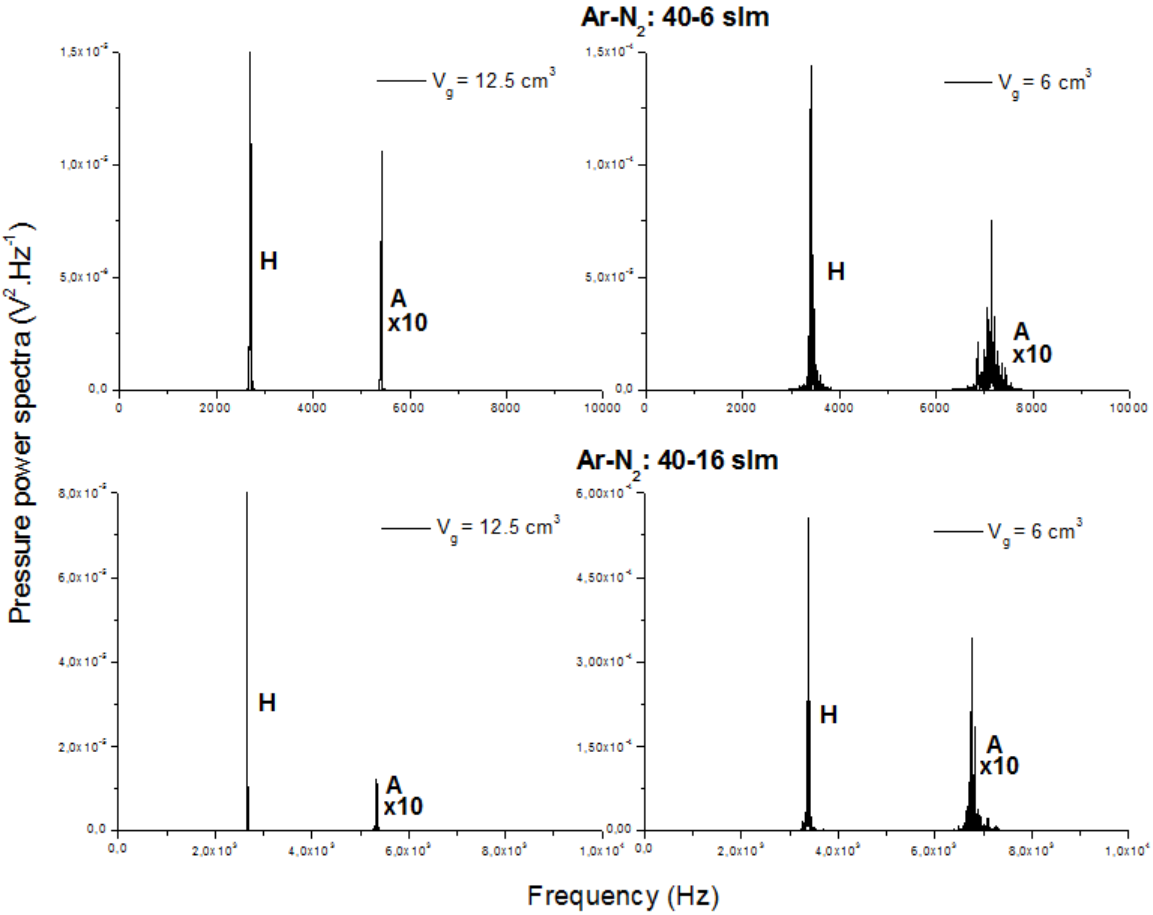

Figure 2.15: Pressure power spectra of filtered arc fluctuations of H-Helmholtz and A-acoustic modes for: (a) V_g = 12.5 cm^3 and (c) V_g = 6 cm^3.

However, the significant difference between f_H obtained for the Ar-N_2 plasma forming gases and f_H computed for Ar-H_2 has been observed, e.g. for the same configuration of cathode cavity: V_g = 6 cm^3 and the arc current = 400 A, the Helmholtz frequency, f_H, equals 3450 Hz compared to 4450 Hz of the signal measured for Ar-H_2.
Moreover, the calculated standard deviations of Helmholtz and acoustic modes show notable differences in comparison to the results obtained for the same configurations of the cathode cavity for Ar-H_2. While the volume V_g increases, particularly in the case of Ar-N_2 (40-16 slm), the Helmholtz mode of the instabilities seems to dominate, what is more clearly presented in Figure 2.16.

The power ratios for the Helmholtz, R_H, and acoustic modes, R_a, have been calculated from the filtered voltage power spectra and plotted as a function of the volume of cathode cavity. To compare the results obtained for Ar-N_2: 40-6 and 40-16 slm, the power ratios computed from signal for Ar-H_2: 45-10 slm have been indicated. All signals have been measured at the arc current of 400 A and for the configuration of cathode cavity: (a) V_g = 12.5 cm^3 and (c) V_g = 6 cm^3.

Table 2.5: The frequency, standard deviation (σ) and Q factor of voltage and pressure power spectra presented in Figure 2.14 and 2.15, for: (a) V_g = 12.5 cm^3 and (c) V_g = 6 cm^3.

		Arc voltage			Pressure		
		f (Hz)	σ (V)	Q	f (Hz)	σ (mbar)	Q
Ar-N_2 (40-6 slm)							
Helmholtz mode	(a)	2700	7.5	55	2700	11	55
	(c)	3450	9	90	3450	50	91
Acoustic mode	(a)	4650	13.4	9	4300	6	7
	(c)	7150	1.5	14	7150	19	20
Ar-N_2 (40-16 slm)							
Helmholtz mode	(a)	2700	16.5	90	2700	15	85
	(c)	3400	17	97	3400	70	97
Acoustic mode	(a)	4700	0.5	7	4300	3	5
	(c)	6800	2.5	33	6800	30	41

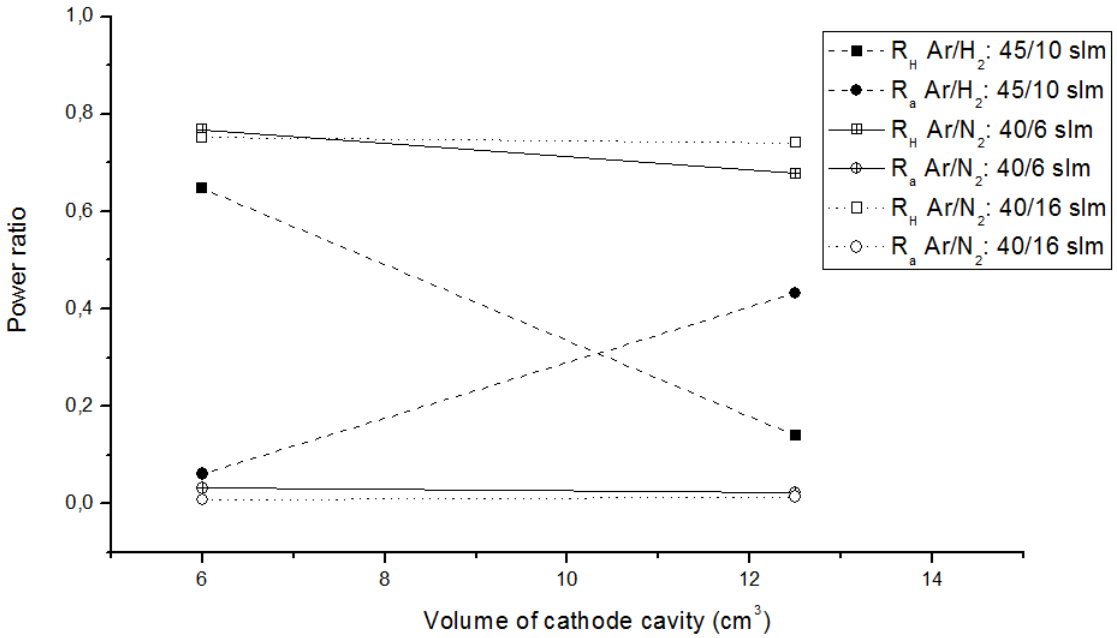

Figure 2.16: Influence of the volume of cathode cavity, for the cases: (a), (c), on power ratio for voltage components: H-Helmholtz and a-acoustic, obtained for Ar-N_2: 40-6 and 40-16 slm . To compare: the results of the power ratio computed from signal for Ar-H_2: 45-10 slm.

The obtained results show that in the case of Ar-N_2 most of fluctuating power is contained in the Helmholtz mode for both volumes V_g, what presents the different behavior than in the case of the signals obtained for Ar-H_2. This phenomenon will be more studied in the following paragraph.

2.2.2.2 Composition of plasma forming gases

In the previous studies performed in the laboratory the measurements of the arc voltage and pressure signals, obtained for argon-hydrogen mixtures as plasma forming gases, have been highlighted. The experiments have been carried out using the same home-made plasma torch, presenting a similar configuration as the commercial Sultzer Metco F4 gun. The arc voltage and pressure in the cathode cavity have been obtained at 600 A, for the constant argon flow rate at 45 slm and the hydrogen flow rate varying between 2 and 10 slm.

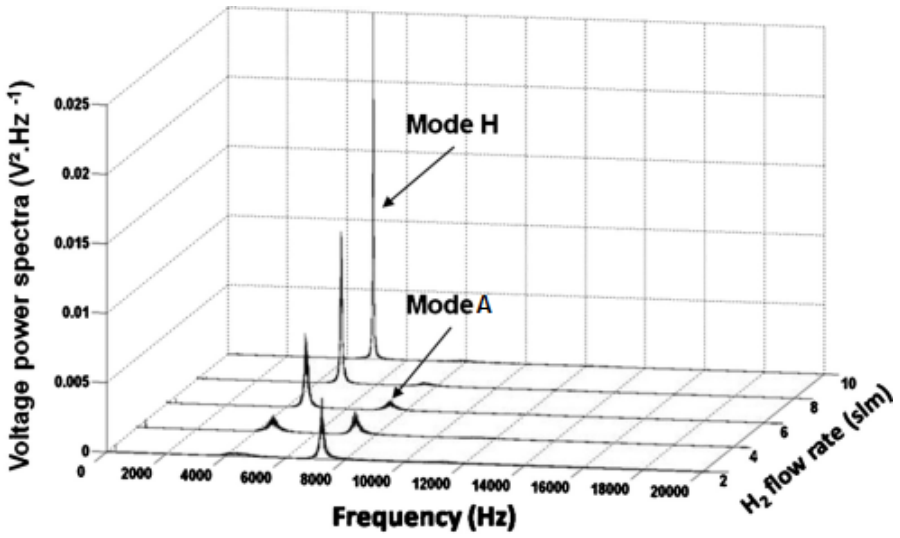

Figure 2.17: Power spectra of arc voltage calculated from signals generated at 600 A for an Ar-H_2 plasma. The mass flow rate of hydrogen varies between 2 and 10 slm [72].

The voltage power spectra, presented in Figure 2.17, show that the chemical composition of plasma forming gases strongly influences the Helmholtz resonance, especially when hydrogen content is increased in binary mixture such as Ar-H_2. Moreover, the hydrogen flow rate needs to reach a certain threshold, about 5 slm, to sustain Helmholtz oscillations. In the following paragraph, the results of the use of Ar-H_2 and Ar-N_2 as the plasma forming gases is highlighted. The results have been obtained for the following gas compositions:

- Ar-H_2 (45-5 slm)
- Ar-H_2 (45-10 slm)
- Ar-N_2 (40-6 slm)
- Ar-N_2 (40-16 slm)

The measurements of the arc voltage and pressure in the cathode cavity have been obtained at 400 A for a standard configuration of cathode cavity: case (a) $V_g = 6$ cm^3 and for the distance between cathode tip and the nozzle exit: $L_k = 30$ mm.

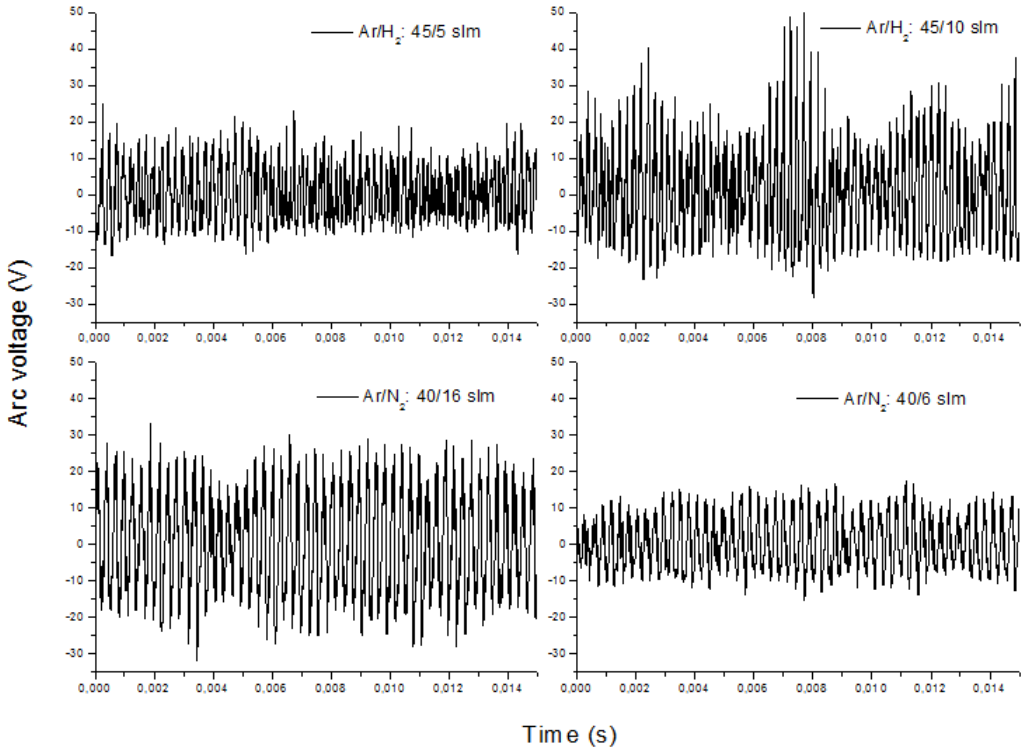

Figure 2.18: Temporal evolution of the fluctuating components of the arc voltage for argon-nitrogen and argon-hydrogen plasma.

Figure 2.18 depicts time-resolved fluctuating components of the arc voltage measured for argon-nitrogen and argon-hydrogen plasma. The calculations of the mean voltage, presented in Table 2.6, show the similar values for Ar-H_2 (45-5 slm) and Ar-N_2 (40-6 slm)- around 50 V and Ar-H_2 (45-10 slm), Ar-N_2 (40-16 slm)- around 60 V. The results obtained for Ar-H_2 mixtures have verified the experiments presented at the beginning of this paragraph, where the increase of the hydrogen content has strongly influenced the Helmholtz resonance. The voltage and pressure power spectra of the signals, in Figure 2.19 and 2.20, exhibit the same dependence. The computed standard deviations of voltage and pressure increase from 8.5 to 14.5 V and 47 to 65 mbar, what shows that a major part of signal turns to Helmholtz mode while the content of H_2 increases.

Comparing the oscillations patterns of the arc voltage obtained with an Ar-H_2 (45-10 slm) mixture to the signals measured for argon-nitrogen plasma, a significant beating component producing successive groups of peaks of high and low amplitudes is exhibited in the case of Ar-H_2 mixture.

Table 2.6: Statistical analysis of the arc voltage signals presented in Figure 2.18.

	Ar-H_2 (45-5 slm)	Ar-H_2 (45-10 slm)	Ar-N_2 (40-6 slm)	Ar-N_2 (40-16 slm)
$\overline{V}$ (V)	52	62	47	61
σ (V)	8	13	7	14
$\langle v^2 \rangle$ (V)	63	172	54	186
RMS (V)	53	63	47	62

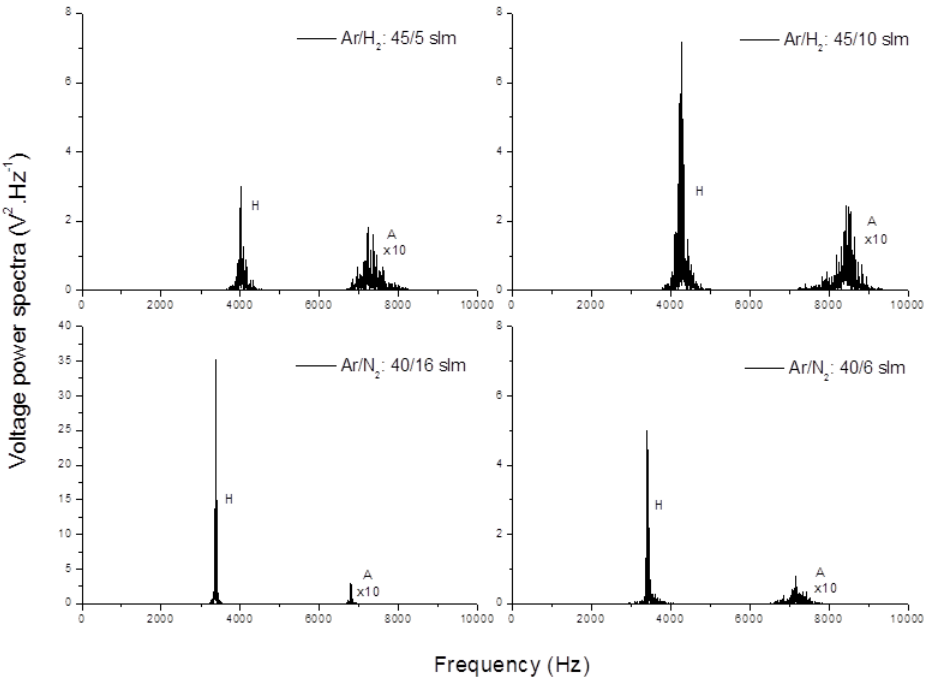

Figure 2.19: Voltage power spectra of Helmholtz and acoustic modes obtained by the filtering of the arc voltage signals presented in Figure 2.18.

The analysis of the voltage power spectra obtained with Ar-N_2 mixtures, shown in Figure 2.19, and the data given in Table 2.7 highlight that the arc voltage signals contain Helmholtz resonance without any acoustic mode influence.

Therefore, the beating phenomenon found in the temporal evolution of the fluctuating component of the voltage signal measured for Ar-H_2 (45-10 slm) mixture can be ascribed to a coupling between Helmholtz and acoustics modes.
The results shown in the previous paragraph and presented in the power spectra calculated from the arc voltage (Figure 2.19) and the pressure (Figure 2.20) signals highlight the shift of the Helmholtz frequency peaks towards the lower values for argon-nitrogen plasma. The frequency equals 3.4 kHz for Ar-N_2 (40-16 slm) plasma and 4.45 kHz for Ar-H_2 (45-10 slm). Analysing the model for Helmholtz frequency given in (2.21) this frequency drop is due to the following parameters of Ar-N_2 plasma: lower isentropic coefficient, γ, and higher density, ρ, compared to Ar-H_2 plasma.

Table 2.7: The frequency, standard deviation (σ) and Q factor of voltage and pressure power spectra, presented in Figure 2.19 and 2.20, for Ar-H_2 (45-10 slm) and Ar-N_2 mixtures.

		Arc voltage			Pressure		
		f (Hz)	σ (V)	Q	f (Hz)	σ (mbar)	Q
Ar-H_2 (45-10 slm)	H mode	4450	14	30.5	4300	72	30
	A mode	7850	3.5	17	7500	35	17.5
Ar-N_2 (40-6 slm)	H mode	3450	9	90	3450	49	91
	A mode	7150	1.5	14	7150	19	20
Ar-N_2 (40-16 slm)	H mode	3400	17	97	3400	68	97
	A mode	6800	2.5	33	6800	30	41

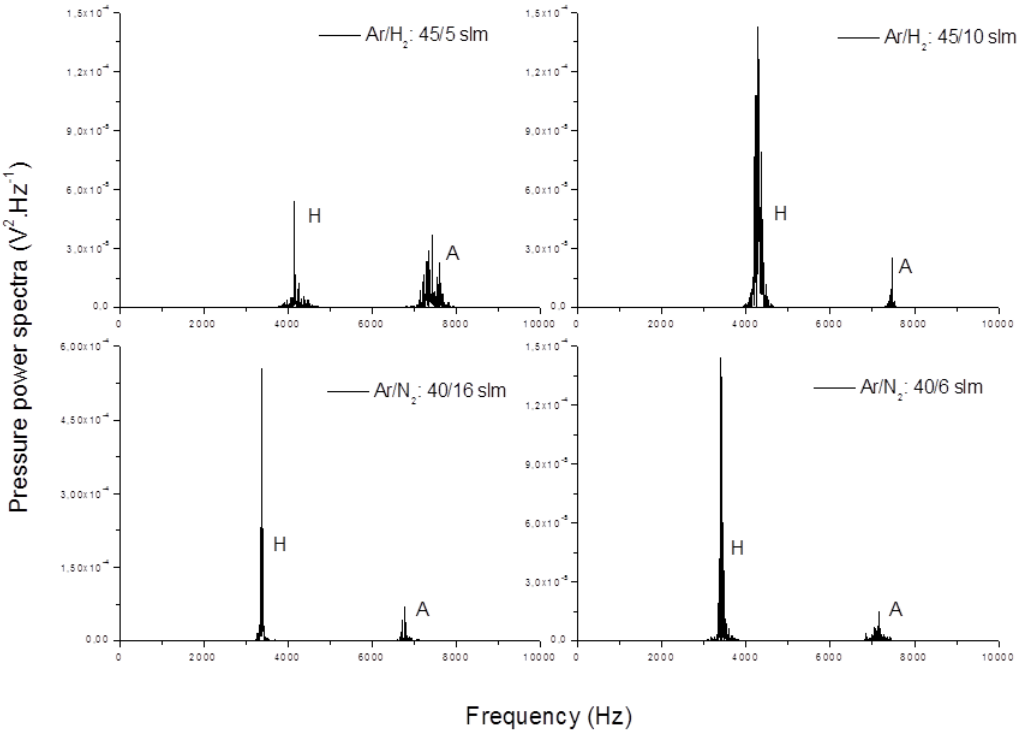

Figure 2.20: Pressure power spectra of filtered arc fluctuations of Helmholtz and acoustic modes for argon-nitrogen and argon-hydrogen plasma.

Moreover, Q factors calculated from voltage power spectra for Ar-H_2 (45-10 slm) and Ar-N_2 (40-16 slm) plasma are, respectively, 30.5 and 97 which highlights stronger Helmholtz resonance when using argon-nitrogen as plasma forming gases mixture. It is confirmed by the results obtained from the pressure power spectra. The standard deviation for Ar-N_2 (40-16 slm) is equal to 68 mbar, which is smaller than the value obtained for Ar-H_2 (45-10 slm), equals 72 mbar. This discrepancy in pressure amplitude can be also explained by a weaker compressibility of plasma forming gases containing nitrogen. In the frame of the mass-spring system model for the Helmholtz resonance, during adiabatic oscillations, the

pressure variation, δp, due to the longitudinal displacement, δx, is given as follows:

$$\delta p = -\gamma_g S P_g \delta x / V_g \tag{2.35}$$

Therefore for the same, δx, smaller pressure amplitude is given by gases with lower isentropic exponent, in this case by Ar-N_2 mixture.

2.2.2.3 Position of the cathode

The model of Helmholtz mode of the instabilities, (2.21), shows that these arc voltage fluctuations are also responsive for the length of the nozzle channel. Therefore, this paragraph presents the examination of the influence of distance between the cathode tip and nozzle exit, L_k, on the resonance of the conventional torch.
The length of the nozzle channel has been varied as presented in Figure 2.21.

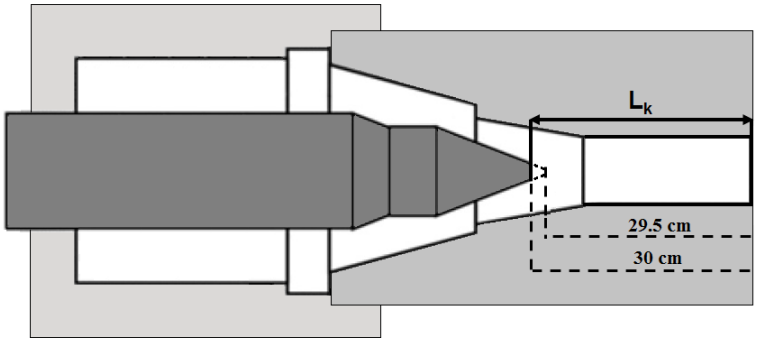

Figure 2.21: Configuration of the torch with identified distance between the cathode tip and nozzle exit, L_k, equals 30 mm and 29.5 mm.

The measurements of the arc voltage and pressure signals have been performed at 400 A for argon-hydrogen (45-10 slm) plasma forming gases mixture by using the torch with the configuration of cathode cavity: (b) V_g = 8.7 cm^3. The signals have been recorded for different L_k, equal to 30 mm and 29.5 mm. The arc voltage and pressure power spectra of the filtered Helmholtz mode computed from the measurements are presented in Figure 2.22 and 2.23.

Table 2.8: The frequency, standard deviation (σ) and Q factor of voltage and pressure power spectra presented in Figure 2.22 and 2.23, for: L_k = 30 mm and 29.5 mm.

	Arc voltage			Pressure		
	f (Hz)	σ (V)	Q	f (Hz)	σ (mbar)	Q
L_k = 30 mm	3500	10	44	3500	13	44
L_k = 29.5 mm	3500	7.5	34.5	3500	9	35

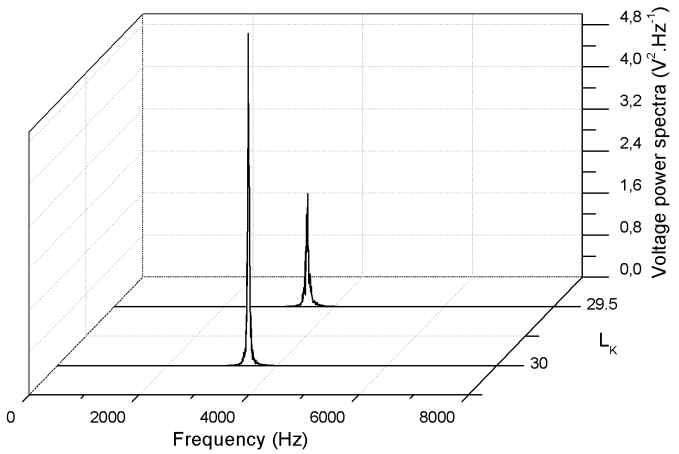

Figure 2.22: Voltage power spectra of filtered Helmholtz mode for L_k: 30 and 29.5 mm [74].

The power spectra and data computed and mentioned in Table 2.8 show that the change of the cathode position does not modify the Helmholtz frequency peak which is approximately 3.5 kHz for both configurations.

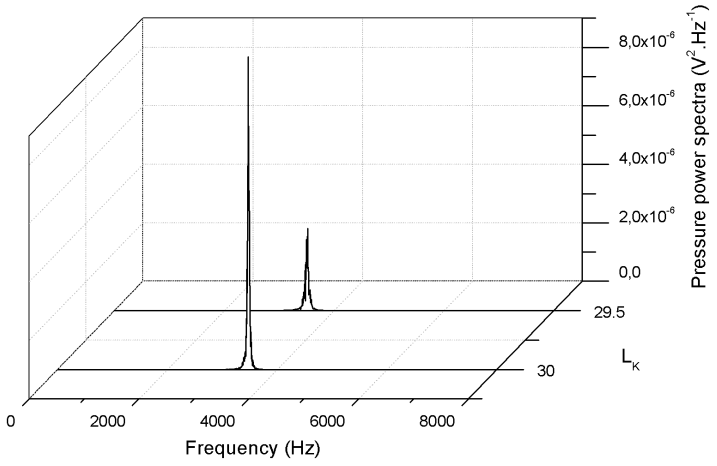

Figure 2.23: Pressure power spectra of filtered Helmholtz mode for L_k: 30 and 29.5 mm [74].

However, a slight decrease of the distance between the cathode tip and nozzle exit,ΔL_k = 0.5 mm, substantially influences the standard deviation calculated from the arc voltage, 10 V and 7.5 V, respectively, for L_k = 30 mm and L_k = 29.5 mm.

Moreover, the Q factor of the Helmholtz resonance is changed from 44 for L_k = 30 mm to 34.5 for L_k = 29.5 mm. Accordingly the cathode position directly affects the Helmholtz resonance, keeping unchanged the mean plasma properties. The cathode position should

influence the turbulence pattern at the entrance of the nozzle and so, by changing the importance of dissipative effects, acts as an adjustable damping parameter.

2.2.2.4 External resonator

To confirm the theory about Helmholtz resonator in the dc plasma torch the external resonator mounted on the cathode cavity has been used. This type of installation allows modifying the pressure waves in the plasma torch, what means that the modification of the pressure inside the cathode cavity leading to the change of arc voltage signal can demonstrate the resonance phenomenon in the torch.

The resonator, presented in Figure 2.24, is composed of a cylindrical cavity (the diameter ϕ_1, in Figure 2.24, equals to 10 ± 0.1mm) and a cylindrical neck (the diameter $\phi_2 = 5 \pm 0.1$mm and the height h $= 6 \pm 0.5$mm) which is connected with the torch cathode cavity.

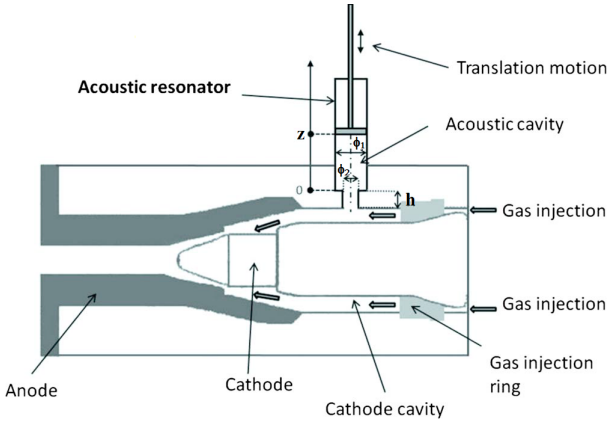

Figure 2.24: Scheme of dc plasma torch with the acoustic resonator [73].

The depth of the resonator cavity is modified using the adjustable position of a piston (referenced with z coordinate). The example of the use of the external resonator is shown in Figure 2.25. The voltage power spectra have been computed from the arc voltage signal obtained for 400 A, for a standard configuration of cathode cavity: case (a) $V_g = 6$ cm^3 and for Ar-N_2 (40-16 slm) plasma forming gases mixture.

The position of a piston z has been changing from 0 mm, which corresponds to closed resonator, to $z_1 = 6$ mm and $z_2 = 8.7$ mm. For z equals 0 mm the power spectrum of the arc voltage signal presents the major peak around 3400 Hz. Comparing the voltage power spectra obtained for different positions of the piston and the standard deviations listed in Table 2.9, the decrease of σ of Helmholtz mode is observed.

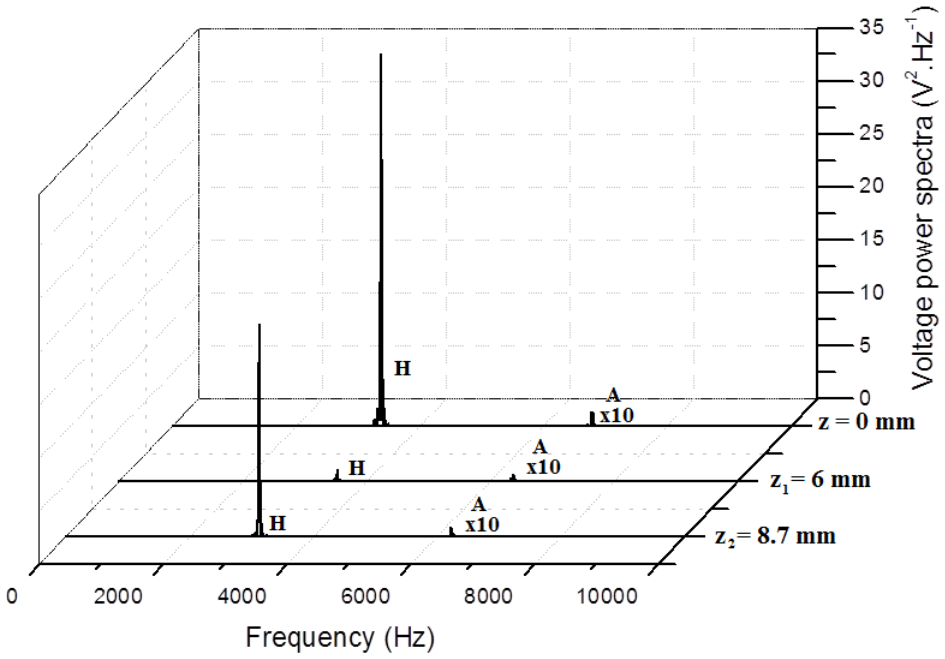

Figure 2.25: Power spectra of arc voltage for different z values obtained for Ar-N_2 (40-16 slm) mixture.

Table 2.9: The frequency, standard deviation (σ) and Q factor of voltage power spectra, presented in Figure 2.25, for z of 0, 6 and 8.7 mm.

		f (Hz)	σ (V)	Q
z = 0 mm	H mode	3400	17	97
	A mode	6800	2.5	33
z = 6 mm	H mode	~3400	3.8	22
	A mode	~6400	1.4	22
z = 8.7 mm	H mode	~3400	11.5	58
	A mode	~6300	1.3	32

For z = 0 mm the standard deviation and Q factor are, respectively, 17 V and 97, what means that the Helmholtz resonance imposes to the arc a strong oscillatory motion. While increasing the z coordinate σ of Helmholtz peak is decreasing. As it is presented in Figure 2.25 the most effective results are obtained for z_1 = 6 mm. The Helmholtz peak and Q factor are significantly reduced what means that the resonance phenomenon is damped. The influence of the external resonator has been also examined for the arc voltage signal recorded at 400 A for Ar-H_2 (45-10 slm) plasma. Figure 2.26 presents the time-resolved voltage obtained for z_1 = 5.57 mm. To compare the temporal evolution of the signal, from Figure 2.9, measured for the same operating conditions but for the closed resonator, z = 0 mm, is introduced.

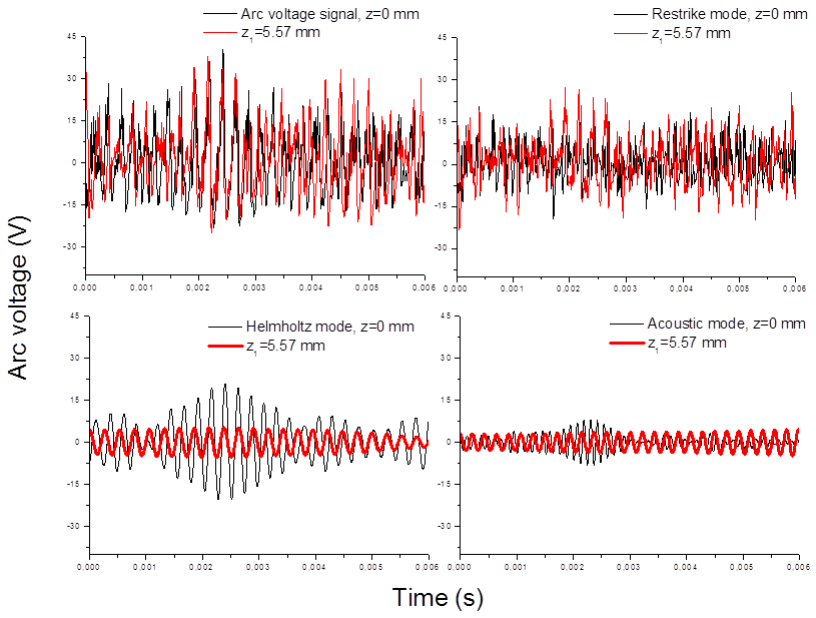

Figure 2.26: Comparison between the arc voltage signal and its filtered components: restrike, Helmholtz and acoustic, measured for closed resonator, z = 0 mm, from Figure 2.9, and the signals obtained for z_1 = 5.57 mm.

The comparison between the results obtained for z = 0 mm and z_1 = 5.57 mm highlights that the amplitude of Helmholtz mode is significantly reduced. Moreover, the resonator has a slight influence on the acoustic and restrike modes.

As the obtained results have shown the use of the external resonator significantly has reduced the arc voltage variations. It is the evidence of a strong coupling between the pressure inside the cathode cavity and the voltage signal. It can be confirmed that the torch nozzle together with the cathode cavity appears to be a Helmholtz resonator. Moreover, the use of the external resonator can be a good method to reduce the plasma instabilities. As the power spectra and the temporal evolution of the fluctuating component of the arc voltage have highlighted typical Helmholtz oscillations can be significantly damped.

In this part of the plasma instabilities studies the Helmholtz and acoustic modes have been investigated. The obtained results have highlighted the the dc plasma torch can behave like the Helmholtz resonator and the frequency of the Helmholtz mode of the plasma oscillations follows the equation:

$$f_H = \frac{1}{2\pi}\sqrt{\frac{\gamma_g P_g}{\rho_p}}\sqrt{\frac{S}{L_p V_g}} \tag{2.36}$$

The measurements of the arc voltage signal and the pressure variations in the cathode cavity have shown the coupling between them what has been confirmed by the use of the

external resonator. Moreover, the results have highlighted the parameters influencing the Helmholtz and acoustic modes. The increase of the cathode cavity volume has noticeably influenced the Helmholtz mode by reducing its frequency. The use of the nitrogen as plasma forming gas has reinforced the Helmholtz mode and dominated the acoustic modes.

2.2.3 Restrike mode

Analysing the temporal evolution of the arc voltage fluctuating component, in Figure 2.27, the regular oscillations with the period of a few hundred μs can be observed, what has been determined as Helmholtz oscillations and studied in the previous paragraphs.

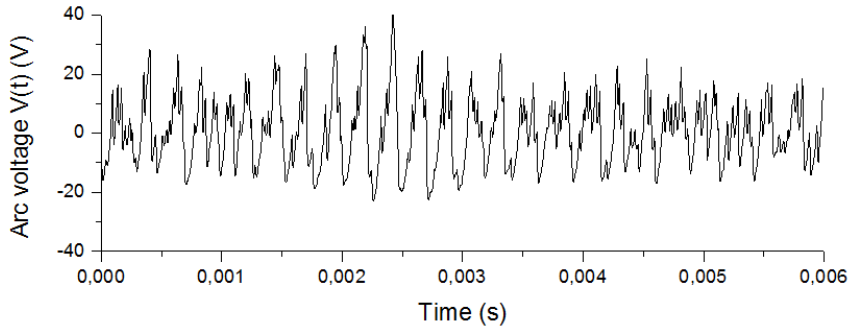

Figure 2.27: Time evolution of the fluctuating component of the arc voltage signal.

Figure 2.27 highlights that to Helmholtz oscillations are superimposed more randomly distributed short events with sharp peaks and sudden falls. The filtering method, Figure 2.9, has underlined that these features, with a mean characteristic time of a few tens of μs, correspond to the restrike mode, i.e. a repetition of the elongation-re-arcing sequences. The model of restrike mode, given in [61], has been presented in chapter 1. It has been determined from the arc voltage signal characterized by pure restrike mode (without the influence of Helmholtz or acoustic modes which depend on the plasma torch geometry). The following section is focused on the examination of the restrike mode in the signal superimposed with the Helmholtz oscillations. The analysis of the restrike fluctuating component, $u_R(t)$, is possible due to the use of the filtering method. The purpose of the following studies is to verify if the restrike component, $u_R(t)$, follows the model presented in chapter 1 [61]. Moreover, the following examinations will be focused on the operating parameters influencing the restrike mode.

As has been presented in Chapter 1, the restrike fluctuations are caused by the elongation of electrical current paths of the arc due to the gas flow until re-arcing phenomena occur through the cold boundary layer, what is presented in Figure 2.28.

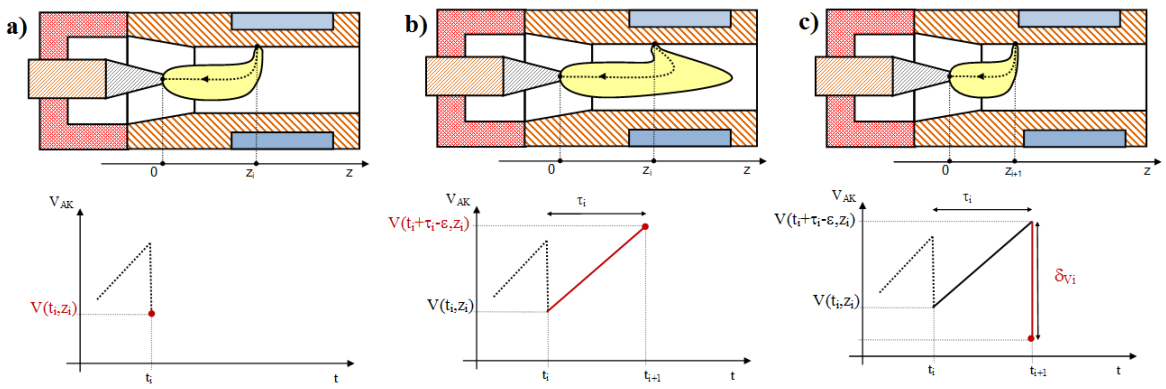

Figure 2.28: Schematic view of restrike model: starting at $t = t_i$ the electrical current path of the arc elongates due to the gas flow, to which corresponds the increase of arc voltage from $V(t_i, z_i)$ to $V(t_i + \tau_i - \varepsilon, z_i)$ (b) during $\tau_i = t_{i+1} - t_i$. Then, a sudden re-arcing occurs at t_{i+1} (c). A new arc is created corresponding to a minimum arc voltage and associated with a voltage jump, δV_i.

The re-arcing occurs from a location of the arc column when the arc voltage, between the arc periphery and the anode wall, exceeds the breakdown threshold, $V_b(z)$, what has been defined in Chapter 1. The voltage drop across the cold layer, $u_{CL}(z,t)$, can also be assumed from Figure 2.29 as follows:

$$u_{CL}(z,t) = u_R(z,t) - u_C(z) \tag{2.37}$$

where $u_C(z) = E_0 z$. E_0 is the electric field through the arc column which is assumed to be constant. The cathode and anode falls are assumed to be also constant during the arc motion and therefore, do not belong to fluctuating component of the signals.

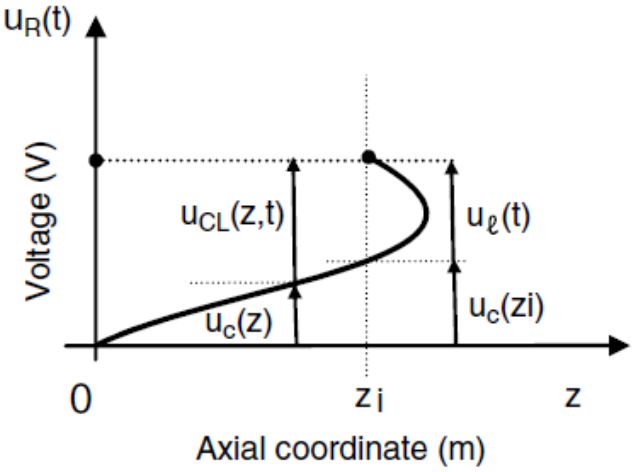

Figure 2.29: Components of restrike arc voltage $u_R(t)$: the voltage drop along the arc column $u_C(z_i)$ which depends on the arc root location, z_i, and the voltage drop along the arc loop, $u_\ell(t)$, which connects the column to the anode wall. The arc voltage presented just after the creation of a new arc root at z_i and at time $t_i + \varepsilon$, $u_\ell(t_i + \varepsilon) = 0$.

When $u_{CL}(z,t) \geq V_b(z)$, a new arc root is created at $z = z_{i+1}$. As has been presented in Chapter 1 and [61] $V_b(z)$ is linked to the thickness of the cold layer, $e_{CL}(z)$. Figure 2.30 shows the evolution of $e_{CL}(z)$.

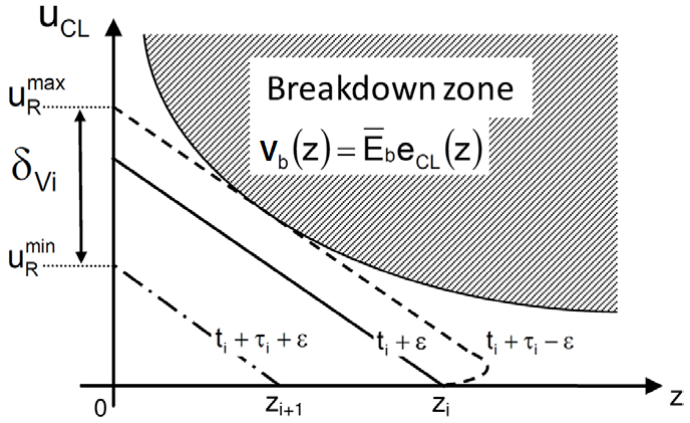

Figure 2.30: Evolution of the voltage drop through the cold layer between the arc column and the anode wall.

At time $t_i + \varepsilon$ just after the formation of an arc root, the arc spot is located at $z = z_i$. The arc current path is elongated by plasma flow during τ_i, u_{CL} increases, and at time $t_i + \tau_i - \varepsilon$, just before re-arcing, u_{CL} reaches the breakdown voltage at $z = z_{i+1}$. Re-arcing occurs and a new arc root is created at a new location, at $z = z_{i+1}$, at time $t_i + \tau_i + \varepsilon$. Therefore, the voltage jump, δV_i, can be defined as follows:

$$\delta V_i(t_i+\tau_i) = u_{CL}(z_i, t_i+\tau_i-\varepsilon) = {u_R}^{max}(t_i+\tau_i-\varepsilon) - {u_R}^{min}(t_i+\tau_i+\varepsilon) = V_b(z_{i+1}) \quad (2.38)$$

If the breakdown zone would be considered as steady, these voltage jumps, δV_i, should be equal. However the turbulences and the instabilities, to which the arc is submitted, have to be taken into account. Therefore, the restrike mode will be considered as a probabilistic process and δV_i will be studied from a statistical point of view, what will be presented below.

The highest values of voltage jumps are obtained for re-arcing occurring close to the cathode. Consequently, for each signal, $u_R(t)$, obtained by the filtering from the raw arc voltage signal, the voltage jumps, $\delta V_i(t_i + \tau_i)$, and their corresponding voltage minima, ${u_R}^{min}(t_i + \tau_i + \varepsilon)$, have been measured. The statistical analysis, which will be presented in the following section, has been obtained from the arc voltage signals measured and shown in the previous paragraphs considering Helmholtz fluctuations but in this section the fluctuating component of the restrike mode obtained by the filtering method will be analyzed.

Figure 2.31 gives the voltage jumps as a function of their corresponding minima for the arc voltage signal obtained at a) 400 A and b) 600 A, for Ar-H_2 (45-10 slm) mixture and the internal nozzle diameter of 6 mm.

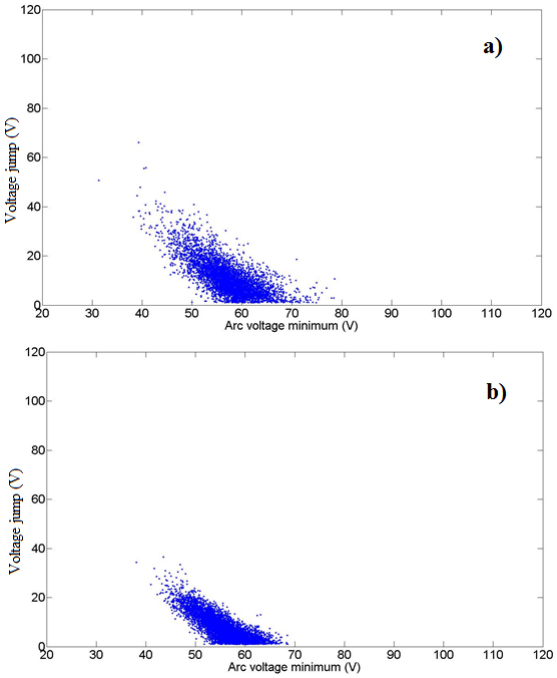

Figure 2.31: Voltage jumps of the fluctuating component as a function of their corresponding minima for the arc voltage signal obtained at a) 400 A and b) 600 A for an internal nozzle diameter of 6 mm, Ar-H_2 (45-10 slm). The mean voltage, $\bar{u}$ = 64.4 V, has been added to ${u_R}^{min}(t_{i+1})$.

The analysis of these data highlights that with the increase of the arc current, the amplitudes of the voltage jumps and the dispersion of the voltage minimum decrease, what is more obviously presented in Figure 2.32. It shows the probability density of voltage jumps calculated for the same measurements as those in Figure 2.31. The number of low amplitude voltage jumps increases as the arc current increases, what is detrimental to the highest amplitude voltage jumps.

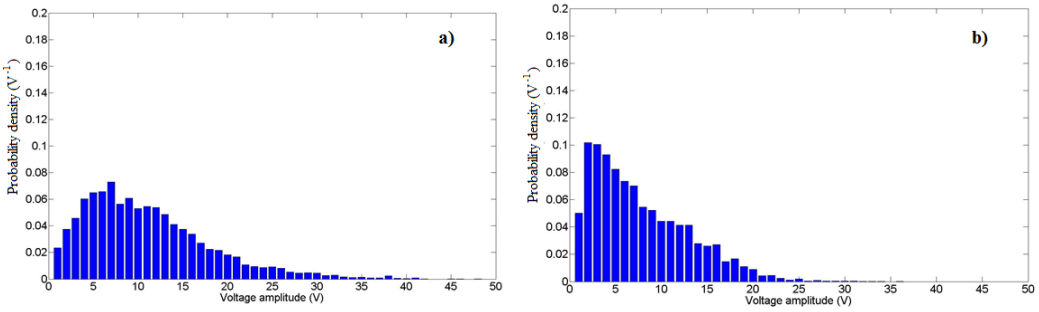

Figure 2.32: Probability density of voltage jump for the arc voltage signal obtained at a) 400 A and b) 600 A for an internal nozzle diameter of 6 mm, Ar-H_2 (45-10 slm).

Figure 2.33 presents the comparison between the voltage jumps computed for the signal measured for the a) Ar-H_2 45-5 slm mixture and b) 45-10 slm. It can be observed that, for a lower H_2 content, the distribution of measurements is shifted to lower values of voltage minima and the dispersion of them is smaller. Moreover, the number of high-amplitude voltage jumps increases as the hydrogen content increases.

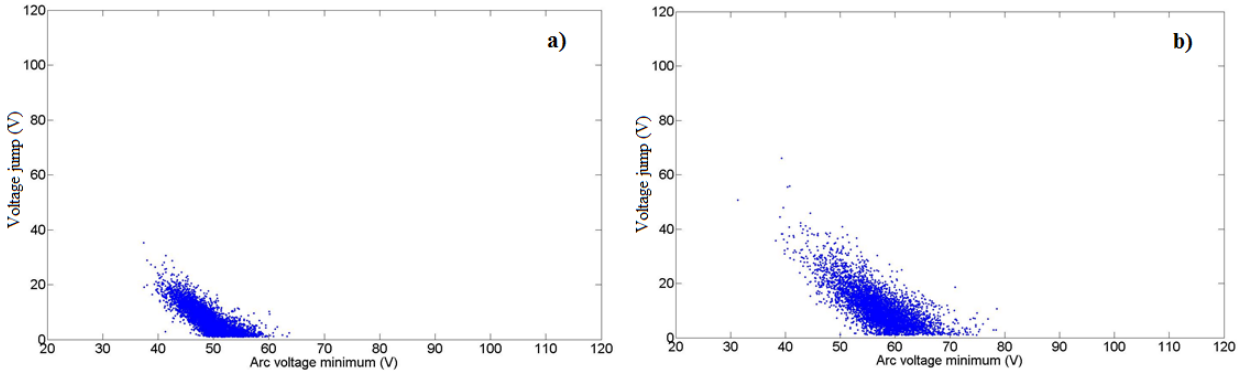

Figure 2.33: Voltage jumps as a function of their corresponding minima for the arc voltage signal obtained at 400 A for Ar-H_2 a) 45-5 slm and b)45-10 slm . The mean voltage has been added to $u_R{}^{min}(t_{i+1})$.

Figure 2.34 presents the mean values of voltage jumps determined from the probability densities of δV_i obtained from the signals measured for different experimental parameters: Ar-H_2 mixtures: 45-5, 45-10 and 45-15 slm and two anode nozzle diameters, 6 and 8 mm, in the function of the arc current.

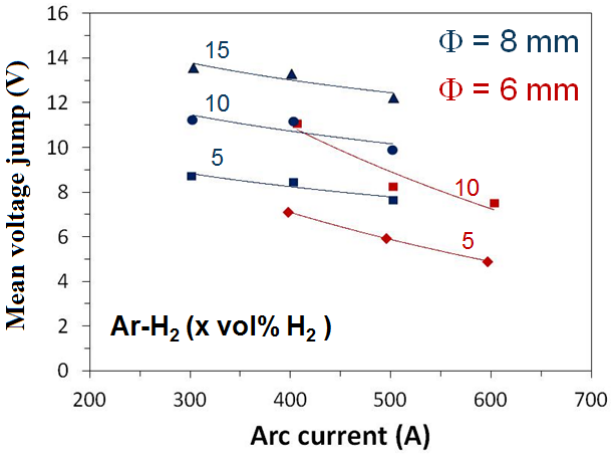

Figure 2.34: Mean voltage jump as function of the arc current for different hydrogen contents in Ar-H_2 mixture x = 5, 10 and 15 slm, and two anode nozzle diameters, 6 and 8 mm.

Figure 2.34 highlights the decrease of mean voltage jumps while the arc current is increasing. Considering the assumptions presented above and taking into account a two-layer model of a stationary axisymmetric arc column in a plasma torch presented in chapter 1, the dependence of mean voltage jumps on operating parameters can be

interpreted in terms of mean thickness of the cold layer, $\bar{e}_{CL}(z)$ and also determine the mean electrical arc radius $\bar{r}_e$. Consequently, as Figure 2.34 highlights the increase of the arc current decreases the mean voltage jumps, what results in the reduction of the thickness of the cold layer, $\bar{e}_{CL}(z)$, and the increase of $\bar{r}_e$. When the hydrogen content is increased from 5 slm to 15 slm, the radial thermal conduction losses are increased, what leads to the decrease of $\bar{r}_e$ and consequently the increase of e_{CL}. Finally, when the internal nozzle diameter increases, e_{CL} also increases. In this case higher voltage jumps are observed, what is due to the decrease of the probability of re-arcing [75].

Figure 2.35 presents the dependence of the mean voltage jumps on the mean cold layer thicknesses for different operating parameters indicated above.

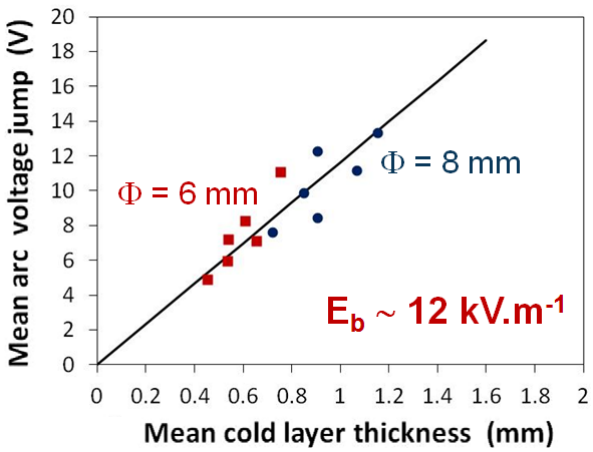

Figure 2.35: Mean voltage jump as function of mean cold layer thickness for different operating parameters: the arc current of 400, 500, 600 A, H_2 content: 5, 10 and 15 slm, and two anode nozzle diameters: 6 and 8 mm [75].

The mean cold layer thickness, $\bar{e}_{CL}$, has been evaluated from the two-layer model presented in chapter 1. The presented quasi-linear dependence allows determining an estimation of the mean breakdown electric field, $\overline{E}_b$, following the restrike model given in chapter 1. $\overline{E}_b$ obtained from the presented experiments is around 12 kVm^{-1}. Up to now, $\overline{E}_b$ has been determined by Paschen's law, which would give the value of $\overline{E}_b$ about two orders of magnitude bigger for the same operating parameters. Therefore, $\overline{E}_b$ may be attributed to the thermal instabilities, what requires more profound studies.

The presented results have verified by the statistical studies that the filtered restrike fluctuating component, $u_R(t)$, follows the model for pure restrike instabilities, given in [61]. It highlights that restrike and Helmholtz modes are relatively separated, what is confirmed by the different times at which they appear: Helmholtz mode at a few hundreds of μs and restrike a few tens of μs. However, the following section will present the different approach to these modes of the instabilities.

2.3 Coupling Helmholtz and restrike modes- "Mosquito mode"

The previous paragraphs have been focused on the studies of the plasma instabilities. As has been presented, the Helmholtz mode appears at the frequency of a few kHz. These oscillations are mainly driven by a cold gas in the cathode cavity, what has been verified by the use of the external resonator mounted on the torch. The frequency of the Helmholtz oscillations, f_H, is defined as follows:

$$f_H = \frac{1}{2\pi}\sqrt{\frac{\gamma_g P_g}{\rho_p}}\sqrt{\frac{S}{L_p V_g}} \tag{2.39}$$

The presented studies of the arc voltage and the pressure signals have highlighted that the increase of the cathode cavity volume can influence the Helmholtz mode by reducing its frequency. Moreover, the use of the nitrogen as plasma forming gas reinforces the Helmholtz mode and dominates the acoustic modes, which, as has been shown, are due to the acoustic waves propagation and reflection inside the torch and occur at higher frequencies ($\sim$ 10 kHz).

The experimental results of the restrike mode can provide the assumption for the mean occurrence frequency of restrike events, f_R, which depends on the probability of re-arcing and on the rate of increase of the arc voltage, as follows:

$$f_R \simeq \frac{1}{\overline{\delta V_i}}\overline{\frac{du_R}{dt}} \tag{2.40}$$

where the rate of increase of the arc voltage, $\overline{\frac{du_R}{dt}}$, presented in Figure 2.28, is proportional to the electric field in the column, E_0, and to the plasma speed, $\overline{v}_p$. The plasma speed has been approximated in the frame of the two-layer model, presented in chapter 1, by the formula:

$$\overline{v}_p = \frac{(\gamma - 1)}{\gamma}\frac{\eta \overline{u} I}{P_a S} \tag{2.41}$$

where S is the nozzle cross section, $\overline{u}$, I and η are respectively measured mean value of the arc voltage, of the arc current and the thermal torch efficiency computed from the energy balance measurements. The presented results of the statistical approach to restrike mode have highlighted the dependence of these fluctuations on the arc current, torch nozzle diameter and flow rate of the plasma forming gas.

As the experimental results have highlighted, the difference between the frequencies of Helmholtz and restrike modes is significant. The Helmholtz mode appears at the time of a few hundreds of μs and the time of the restrike mode equals a few tens of μs, what shows that they are relatively decoupled. However, as the studies of these instabilities have shown, by adjusting the appropriate operating parameters it is possible to influence these two modes.

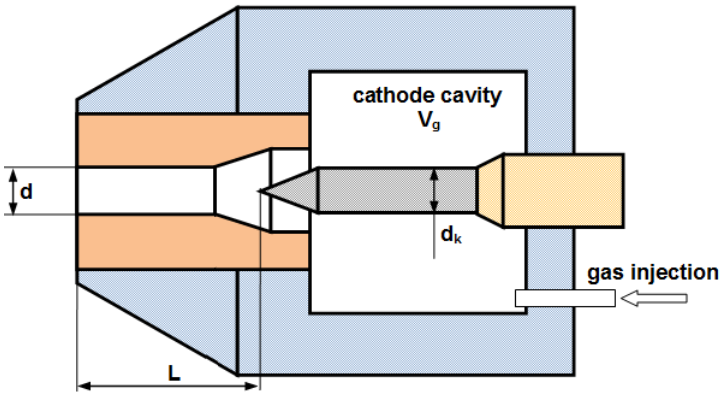

Figure 2.36: Schematic view of a newly designed torch called Mosquitorch.

By increasing the cathode cavity volume, it is possible to noticeably decrease the Helmholtz frequency. Therefore, the obtained results have leaded to the design of a new dc torch with a larger cathode cavity (V_g = 17.8 cm^3), compared to the commercial plasma torches, what is presented in Figure 2.36.

The increase of the cathode cavity has permitted to reinforce the Q factor and to decrease the specific frequency of the Helmholtz mode. Moreover, the longitudinal dimensions of the torch have been shortened to reject the acoustic modes to a higher frequency region. The geometric parameters of the torch as the cathode diameter, d_K, the channel length, L, and the diameter of channel, d, are variable, what is presented in Table 2.10.

Table 2.10: Geometric parameters of a new torch.

Parameter	Value
Cathode diameter d_K (mm)	2.5, 3.5, 4
Channel diameter d (mm)	2.5, 3, 3.5, 4
Channel length L (mm)	10-20

Taking into consideration the parameters influencing and decreasing the frequency of restrike events, the coupling between Helmholtz and restrike modes have been searched experimentally, what is presented in the following paragraph.

2.3.1 Time-resolved measurements of arc voltage

The purpose of these studies is to find the operating parameters which define the most regular temporal variations of the arc voltage. Figure 2.37 presents the arc voltage signals obtained for different experimental conditions. The nitrogen has been used as plasma forming gas due to the possibility to reinforce the Helmholtz mode and dominate the acoustic modes, what has been experimentally presented in the previous paragraphs. The experiments performed above have shown that the frequency of the restrike events depends on the arc current, the diameters of the torch nozzle and the gas flow rate. Therefore, the following studies are focused on the adjustment of these operating parameters.

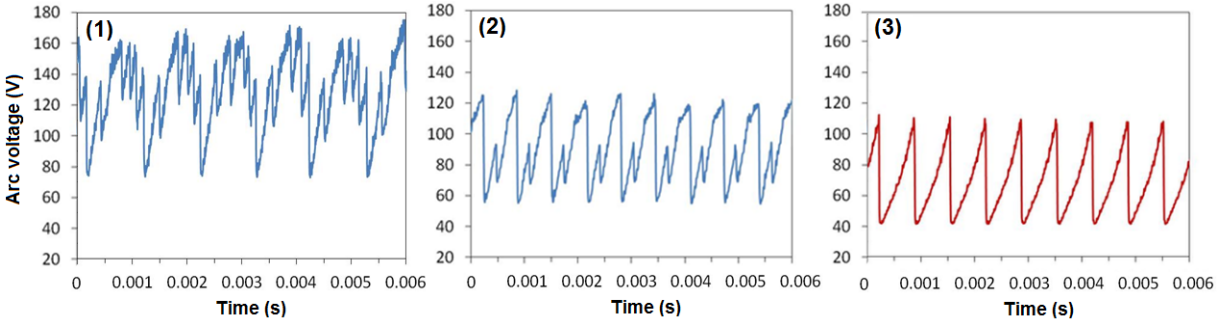

Figure 2.37: Arc voltage signals for different experimental conditions: (1) d_{nozzle} = 3.5 mm, I = 25 A, 2.7 slm N_2, $\overline{V}$ = 129 V, f = 970 Hz; (2) d_{nozzle} = 3.5 mm, I = 10 A, 2.25 slm N_2, $\overline{V}$ = 118 V, f = 1540 Hz; (3) Mosquito mode: d_{nozzle} = 4 mm, I = 15 A, 2 slm N_2, $\overline{V}$ = 73.7 V, f = 1410 Hz [74].

The different nozzles have been tested with the diameters, d, of 3.5 and 4 mm. The torch has been power supplied by the source with regulated arc currents between 8 and 35 A. In Figure 2.37 (1) a typical arc voltage signal, similar to that observed in the conventional plasma torches, has been obtained choosing the nozzle diameter of 3.5 mm, 2.7 slm pure nitrogen and the arc current of 25 A. As can be noticed, this signal is dominated by Helmholtz mode at a frequency close to 1 kHz, shown in Figure 2.38 (1), on which restrike components are superimposed at higher frequencies.

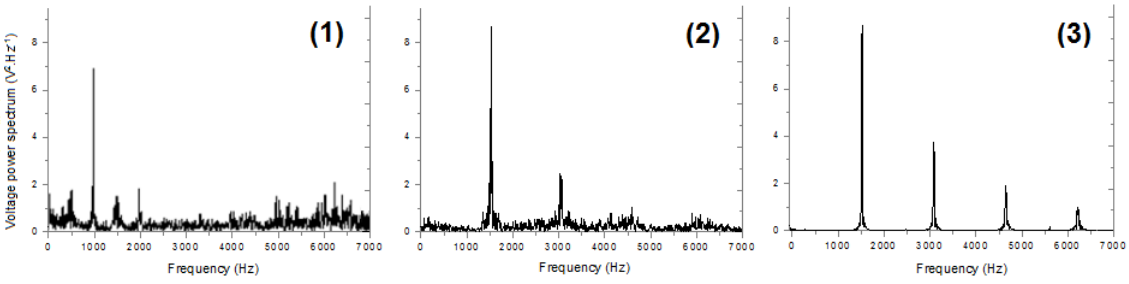

Figure 2.38: Power spectra of the arc voltage signals presented in Figure 2.37.

The decrease of the frequency characteristic for Helmholtz mode is due to the enlargement of the cathode cavity volume and the use of pure nitrogen as plasma forming gas, as has been mentioned above.
The idea is to lower the restrike frequency to approximate this one of Helmholtz and couple these two modes. To define the evolution of the restrike frequency by the operating parameters used in the experiment, the rate of increase in the arc voltage, $(\overline{\mathrm{dV/dt}})$, has been established. To determine $(\overline{\mathrm{dV/dt}})$ the mean slope of the voltage has been measured by the diagnosis of maxima and minima of signals and the calculation of histograms giving the density probability, $\mathrm{p_i}$, of slopes, as follows:

$$(\overline{dV/dt}) = \sum_i (dV/dt)_i p_i \tag{2.42}$$

Figure 2.37 (2) has been obtained by the reduction of the arc current to 10 A and the nitrogen flow rate to 2.25 slm. The nozzle diameter has not been changed and equals 3.5 mm. It is possible to observe a significant decrease of restrike events, which is presented as two patterns per main period ($\sim$ 650 μs).
The excepted coupling between the Helmholtz and restrike modes is obtained in Figure 2.37 (3). A very repeatable saw-tooth shape signal has been achieved by increasing the nozzle diameter to 4 mm and the arc current to 15 A, while reducing N_2 mass flow rate to 2 slm. The arc voltage signal is characterized by large and stable amplitude ($67.7\mathrm{V} \pm 2.1\mathrm{V}$). The signal regularity is verified by a low standard deviation of $(\overline{\mathrm{dV/dt}})$, presented in Table 2.11, which gives the mean rate of increases of the arc voltage, $(\overline{\mathrm{dV/dt}})$, and their standard deviations, σ, of all signals: (1), (2) and (3).

Table 2.11: Mean slope of the arc voltage ramps of the signals presented in Figure 2.37.

Figure 2.37	$(\overline{\mathrm{dV/dt}})$ $(10^5\mathrm{Vs}^{-1})$	σ $(10^5\mathrm{Vs}^{-1})$
(1)	2.8594	1.3644
(2)	1.8905	0.3442
(3)	1.0204	0.0411

In case of the arc voltage signal presented in Figure 2.37 (1) the filtering procedure has been used to obtain the separated modes because Helmholtz and restrike are still disconnected. The rate of increase in the arc voltage, $(\overline{\mathrm{dV/dt}})$, what is coupled with restrike frequency, decreases when the nozzle diameter increases, or with the decrease of the arc current either the mass flow rate.

The frequency, 1.4 kHz, of the resonant mode should be the same as that of the Helmholtz mode, which can be written as: $f_H = K_H.\sqrt{\gamma_g P/\rho_p}$ following the model for Helmholtz oscillations. K_H defines the geometric parameters: $\sqrt{S/L_p V_g}$ determined in the equation (2.21). $(\gamma_g P/\rho_p)$ has been calculated as a function of the measured specific enthalpy, h_0, using the database TTWinner [76].

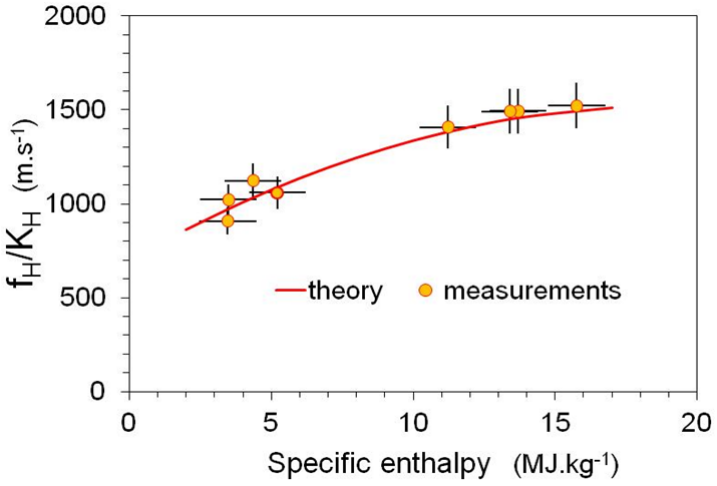

Figure 2.39: Dependence of Helmholtz frequency f_H/K_H on the measured mean specific enthalpy h_0.

Figure 2.39 presents the determination of f_H/K_H as a function of h_0. For a different values of the torch nozzle diameter, d, the arc current, I, and the gas flow rate, q, the frequency f_H has been measured in the range of 1-1.6 kHz with K_H between 0.97 and 1.29 m^{-1}. As Figure 2.39 highlights the obtained results are grouped on a single curve, what shows very good agreement between the experimental and the theoretical values. It confirms that the Helmholtz oscialltions drive the voltage signal in this new regular mode.
When the torch works in this particular mode it emits a stable, sharp and loud sound which resembles the sound produced by a mosquito. Therefore, the term "mosquito mode" has been used to describe the phase locking between Helmholtz and restrike modes.

2.3.2 Enthalpy modulation

To define the stationary characteristics of this periodic plasma jet the energy balance measurements have been carried out. The following section presents the measuring procedures of the mean values of the voltage across the torch (V_{torch} in Figure 2.40), of the arc current (I_{arc}) and the difference of water temperature (ΔT). The obtained results enable to obtain the average specific enthalpy of the plasma jet (h_0), the thermal torch efficiency (η) and the thermal losses at the electrodes in the cooling circuit ($\dot{Q}_{loss}$).

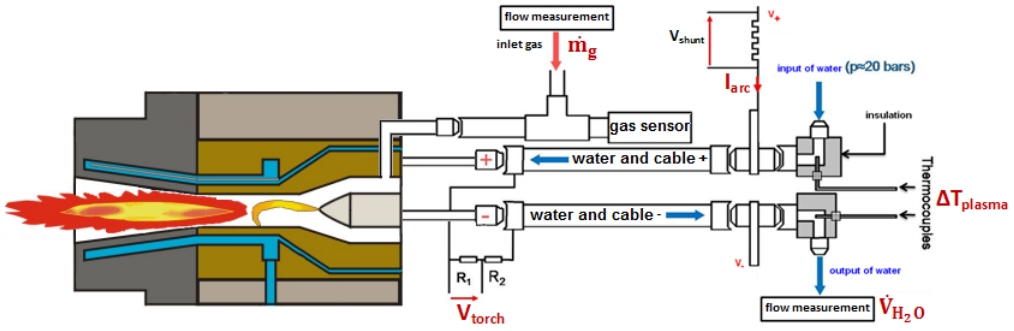

Figure 2.40: Simplified scheme of the energy balance measurements of the torch.

The temperature difference has been measured by two thermocouples type J mounted between the input and the output of the cooling circuit of torch, shown in Figure 2.40. The type J, made by iron-constantan, has been chosen because of its high sensitivity of about 50 μV/°C. The arc current signal is obtained from the voltage drop across the shunt resistor, which is equal to 10^{-3} Ω. The use of shunt resistor allows the measurement of current values too large to be directly measured by the ammeters. In this case the shunt, a manganin resistor of accurately known resistance equals 10^{-3} Ω, is placed in series with the load so that all of the current to be measured will flow through it, shown in Figure 2.40. To make the measurements of the arc voltage the bridge circuit has been implemented, presented in Figure 2.40, with the divider equal to 38.506. Moreover, a new torch uses lower flow rates of the plasma forming gases than in the conventional systems. Therefore, a more accurate measurement of the gas flow has been required. The flow rates have been monitored by a Brooks Instrument SLA5850 mass flow controller (Hatfield, PA, USA) which allows measuring the gas in the range from 0.003 to 30 slpm with the accuracy equals ±1.0% of the rate.

The measurement of ΔT has enabled to determine the thermal losses at the electrodes in the cooling circuit according to the following equation:

$$\dot{Q}_{loss} = \dot{V}.\rho_{water}.C_p.\Delta T \tag{2.43}$$

where:

$\dot{V}$	is the volume flow rate of water circulate in the torch,
ρ_{water}	the density of water,
C_p	the specific heat of water,
ΔT	the temperature difference of water, defined as: $\Delta T = T_{out_{H_2O}} - T_{in_{H_2O}}$

The thermal torch efficiency, η, has been calculated by using the equation:

$$\eta = 1 - \frac{\dot{Q}_{loss}}{V.I} \tag{2.44}$$

where:

V is a measured value of the mean voltage,
I a measured value of the mean arc current.

The electrical power supplied to the torch after removing the heat losses in the cooling circuit is supposed to be converted into enthalpy flux. Neglecting the kinetic energy of the plasma flow, which represents a few per cent of total energy in these conditions, the specific enthalpy can be defined as follows:

$$h_0 = \frac{\eta VI}{\dot{m}_g} \tag{2.45}$$

where:

$\dot{m}_g$ is the total plasma forming gas mass flow rate.

The obtained results of the measurements, performed for the plasma: (1), (2) and (3) in Figure 2.37, are presented in Table 2.12. First of all, it can be noticed that the obtained values of the specific enthalpy are similar to these ones in conventional torches. Moreover, these measurements highlight the use of much lower flow rates of the plasma forming gas comparing to the conventional systems (e.g. Ar-H_2 (45-10 slm) used in the experiments presented in this chapter).

Table 2.12: Energy balance measurements for the case (1), (2) and (3) presented in Figure 2.37.

	d (mm)	I (A)	N_2 (slm)	$\dot{m}$ ($kg.s^{-1}$)	$\overline{U}_{arc}$ (V)	f (Hz)	Q_{loss} (W)	h_0 ($MJkg^{-1}$)
(1)	3.5	25	2.7	5.6×10^{-5}	129	970	854	42
(2)	3.5	10	2.25	4.7×10^{-5}	118	1540	364.5	17.4
(3)	4	15	2	4.2×10^{-5}	73.7	1410	537	13.34

It has been found experimentally that $\dot{Q}_{loss}$ varies almost linearly with the arc current and slightly depends on the nozzle diameter and the gas flow [77, 78]. Therefore, the following part presents the estimation of the specific enthalpy modulation assuming that the thermal losses are constant. This hypothesis permits to determine the equivalent "thermal" voltage, V_{th}, given by: $V_{th} = \dot{Q}_{loss}/I$, where the mean value of the arc current and the thermal losses have been determined above.

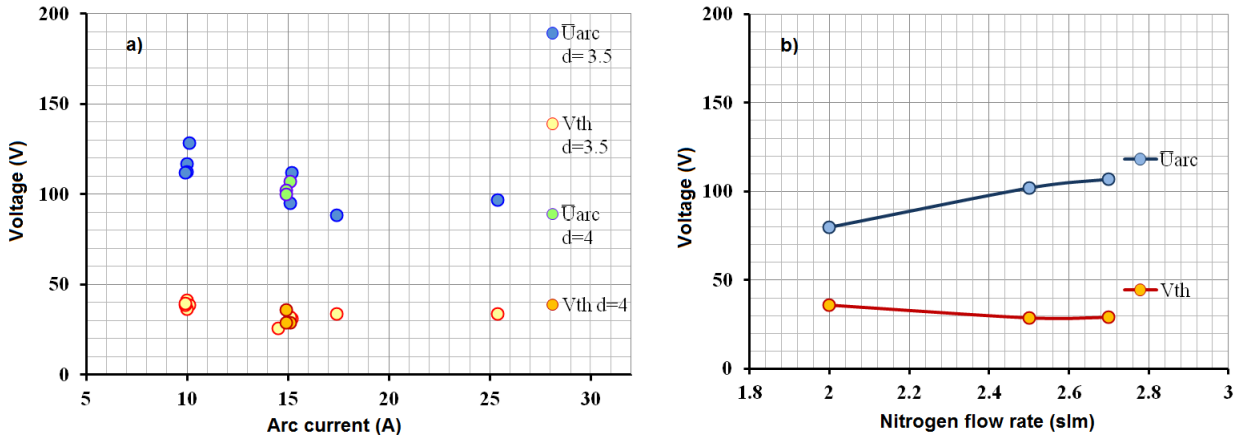

Figure 2.41: Dependence of mean arc voltage and thermal voltage on (a) arc current and (b) nitrogen mass flow rate (b) for different anode nozzle diameters d (mm).

Figure 2.41 presents the measurements of the mean arc voltage, $\overline{U}_{arc}$, and thermal voltage, V_{th}, of the plasma obtained by a new torch. Figure 2.41 a) shows the dependence of $\overline{U}_{arc}$ and V_{th} on the arc current. The measurements have been carried out for two diameters of the torch nozzle: 3.5 and 4 mm. The dispersion of the measurements is related to the fact that for each arc current value different gas flows have been studied. Figure 2.41 b) presents the dependence of $\overline{U}_{arc}$ and V_{th} on the gas flow rates. The results show that the thermal voltage is weakly dependent on the nozzle diameter and gas flow rates.
In case of the plasma jet related to "Mosquito" mode, presented in Figure 2.37 (3) and Table 2.12 (3), the equivalent thermal voltage, V_{th}, can be considered as constant due to high thermal inertia of the heat transfer process through the copper nozzle in comparison with the time variations of arc voltage. V_{th}, calculated from the data listed in Table 2.12 (3), is equal to $\sim$ 36 V. This assumption permits to determine the efficient voltage, which is useful for the conversion of electric power into enthalpy, given as follows:

$$V_{eff} = U(t) - V_{th} \tag{2.46}$$

where U(t) is the arc voltage, presented in Figure 2.37 (3), with U_{min} equals around 40 V and U_{max} around 110 V. Therefore, V_{eff} fluctuates between 4 V and 74 V.
As a consequence, it can be shown that the power supplied to the gas: $P_{el} = V_{eff} \times I$ is modulated in the range 60-1110 W. The variations of the specific enthalpy associated with the efficient voltage fluctuations are given by the following equation:

$$h = \frac{(U(t) - V_{th}).I}{\dot{m}} \tag{2.47}$$

Therefore, the assumed variation of h ranges between 1.4 and 26 $MJkg^{-1}$, what gives the proportion of the enthalpy modulation: $h_{max}/h_{min} \simeq 18$ with a mean value of around 13.3 $MJkg^{-1}$, given by the energy balance measurements (Table 2.12) [74]. Consequently, the temporal variation of temperature, corresponding to given range of enthalpy, should be between 1500 and 7100 K (according to the thermodynamic data found in [17]).

2.4 Conclusions

As has been presented in Chapter 1, the uncontrolled arc plasma instabilities in suspension plasma spraying cause non-homogeneous plasma treatments of material during their flight and also during coatings formation. Therefore, in the framework of this thesis, the modes of plasma fluctuations have been studied in common mono-cathode dc plasma torch. Firstly, the parameters influencing the Helmholtz and acoustic modes have been examined. The presented model of Helmholtz resonance has highlighted that the pressure oscillations in the cathode cavity govern the arc motion. Therefore, the arc voltage signal have been measured simultaneously with the cathode cavity pressure. The obtained results have shown that the Helmholtz resonance strongly depends on the volume of cathode cavity. Moreover, the use of nitrogen as plasma forming gas reinforces the Helmholtz oscillations which dominates the acoustic modes. The studies presented in this part of the chapter have validated experimentally the Helmholtz model and leaded to the assumption of the acoustic resonances representation. Moreover, the investigation of the arc voltage fluctuations have highlighted that the arc motion in dc plasma torch originates, in addition to Helmholtz mode, in the restrike mode. Therefore, the dependence of re-arcing phenomenon on experimental parameters has been highlighted by the statistical measurements. These studies have shown that filtered restrike fluctuations measured from the arc voltage signal coupled with Helmholtz mode follow the model given in [61] for pure restrike fluctuations, which depends on the properties of the cold boundary layer around the arc column. It has highlighted that both modes, Helmholtz and restrike are relatively decoupled. However, the understanding of Helmholtz and restrike phenomena has leaded to a new mode of the arc instabilities. By changing the parameters influencing the Helmholtz and restrike fluctuations, it is possible to couple them together in a newly designed dc plasma torch. Torch working in this new mode emits sharp and stable sound which resembles the sound of the mosquito. Therefore, this mode has been called "Mosquito mode". The energy balance measurements have highlighted that the plasma produced in this new mode is characterized by the enthalpy highly modulated. The properties of this obtained periodic plasma will be used in the following chapter to achieve the suspension injection synchronized with this plasma.

Part II

Résumé du chapitre 2

L'objectif de ce travail est de comprendre les origines des fluctuations de l'arc dans une torche à plasma d'arc conventionnele à courant continu. Les mesures se sont concentrées sur le mode de réamorçage, décrite dans le chapitre 1, et sur le mode Helmholtz récemment mis en évidence. Le but est d'examiner les paramètres de fonctionnement qui influencent ces deux modes. Toutes les mesures ont été réalisées à la pression atmosphérique en utilisant une torche à plasma conçue au laboratoire qui présente une configuration similaire à une torche commerciale F4 (Sulzer Metco, Suisse). La torche est constituée d'une tuyère de diamètre, d, égale 7 mm et la bague d'injection percée de 16 trous de diamètre 1 mm. Le volume de la cavité cathodique, V_g, et la distance entre la pointe de cathode et la sortie de tuyère, L_k, sont variables. Le volume de la cavité cathodique peut être choisi entre: $V_g = 6cm^3$, ce qui correspond au volume standard, $V_g = 8.7cm^3$, obtenue en enlevant la bague d'injection et $V_g = 12.5cm^3$, le volume d'une cavité usinée spécialement dans le laboratoire. L'alimentation de la torche est assurée par une source à thyristors régulée en courant (SNMI, de type P130) qui fournit le courant jusqu'à 1000 A avec une tension maximale de 100 V.

Les mesures résolues en temps des signaux ont été effectuées en utilisant une carte d'acquisition de données (PCI 6132), pilotée par logiciel LabView. Cette carte de National Instruments permet de convertir le signal analogique au format numérique, par échantillonnage et numérisation à l'aide d'un convertisseur analogique-numérique (ADC analog-to-digital converter en anglais). Pour obtenir le signal sans aliasing, le critère d'échantillonnage de Nyquist doit être respecté. Il montre que les échantillons prélevés à une fréquence f_s, doit être supérieure à f_{max} pour obtenir le signal analogique d'origine reconstruit exactement, ce qui est présenté comme suit: $f_s > 2f_{max}$.

Les signaux ont été enregistrés par le programme LabView pour un traitement ultérieur de données, par exemple l'analyse statistique des signaux. Pour atteindre les valeurs fiables, les résultats sont des moyennes de 10 signaux mesurés.

Cependant, l'analyse du signal dans le domaine temporel n'est généralement pas suffisante. Pour étudier toutes les informations que le signal, il est nécessaire de transformer ce signal pour le domaine des fréquences, ce qui peut être fait par la transformation de Fourier FFT. Le résultat de l'analyse FFT est une matrice de nombres complexes, les amplitudes et les phases, ce qui correspond à des oscillations harmoniques élémentaires dans lesquelles le signal peut être décomposé. Les amplitudes correspondent au spectre de puissance, qui indique la quantité d'énergie dans une bande de fréquence donnée ou dans une ligne donnée. Le spectre de fréquence peut être utilisé comme un outil pour distinguer les différents régimes de périodicité et le bruit. Dans le cadre de cette thèse, la transformation de Fourier rapide a été appliquée sous plate-forme LabView.

Les mesures résolues en temps et le traitement des données ont été appliquées au signal de tension d'arc. L'estimation du signal de tension d'arc a été réalisée en utilisant une

carte PCI 6132 d'ordinateur d'acquisition de données, piloté par logiciel Labview, comme cela a été présenté ci-dessus. Cette carte PCI 6132 se compose de 4 entrées analogiques échantillonnées simultanément limitées par la tension au niveau de ±10 V. Par conséquent, pour effectuer les mesures de la tension d'arc un pont diviseur (construit à l'aide de résistances) d'un facteur 22.86 a été implémenté. Comme cela a été présenté ci-dessus, le processus d'échantillonnage est essentiel dans la mesure en temps résolu. En raison de variations rapides des phénomènes re-amorçage dans la torche à plasma (jusqu'à 50 μs), le taux d'échantillonnage de 320 kS/s en 0.2 s a été choisi. Il donne une fréquence d'échantillonnage de 160 kHz, qui répond au critère d'échantillonnage de Nyquist et la résolution de fréquence est égal à environ 5 Hz.
L'évolution temporelle obtenue du signal de tension de d'arc a montré les caractéristiques liées au mode de réamorçage mais superposées à des oscillations plus régulières, pseudo-sinusoidales avec une période d'environ 200 μs. De plus, le spectre de puissance, présenté dans la figure ref FFT2, a mis en évidence la présence d'un pic à ∼4.3 kHz, ce qui ne peut pas correspondre aux fluctuations de restrike, caractérisés par des composantes spectrales non-reproductibles. Les résultats obtenus suggèrent que, dans la torche à plasma à courant continu le mode de réamorçage est superposé sur un autre phénomène. Delair *et al.* ont d'abord suggéré que des oscillations de Helmholtz dans la chambre d'arc pouvaient être la cause des fluctuations de la tension d'arc à hautes fréquences [69]. Cette hypothèse a été proposée car certains systèmes de combustion se comportent comme des résonateurs de Helmholtz [70, 71].
Les variations de la pression dans la cavité cathodique sont générées par l'oscillation du plasma dans le canal de la tuyère, ce qui montre que la cavité de la cathode ainsi que le canal de la tuyère peuvent apparaître comme un résonateur de Helmholtz. L'oscillation de Helmholtz est un phénomène très étudié dans la théorie des vibrations est peut être décrit par analogie par un système masse-ressort.
Le gaz froid dans la cavité cathodique, caractérisée par le volume V_g, est analogue au au ressort, la cavité cathodique constituant alors la cavité du résonateur de Helmholtz.
Cette cavité est connectée au canal de tuyère qui contient le plasma oscillant, analogue à la masse du système masse-ressort. Le plasma oscillant induit une perte de charge due aux frottement et à la turbulence, ce qui ajoute des effets visqueux dans le canal, source de phénomènes non-réversibles. Ensuite, la perturbation de pression dans la cavité de cathode est donnée par l'équation (2.19), où le facteur de qualité, Q, est lié à la bande passante du résonateur, Δf, et au facteur d'amortissement. Par conséquent, la fréquence de Helmholtz liée au mouvement de la masse du plasma dans la tuyère est définie comme:

$$f_H = \frac{1}{2\pi}\sqrt{\frac{\gamma_g P_g}{\rho_p}}\sqrt{\frac{S}{L_p V_g}} \tag{2.48}$$

où: γ_g est le coefficient isentropique du gaz froid, P_g la pression moyenne dans la cavité cathodique, ρ_p la densité du plasma, S est l'aire de la section de la tuyère de la torche, L_p la longueur du canal de buse, V_g le volume de la cavité cathodique. L'équation met en évidence la dépendance du mode de Helmholtz sur les propriétés thermophysiques, γ_g et ρ_p, liées, respectivement, au gaz froid et au plasma, la configuration de la torche, $\sqrt{\mathrm{S/L_p.V_g}}$, et la pression dans la cavité cathodique, ce qui fonction des conditions opératoires et des propriétés thermodynamiques du gaz.
Par conséquent, les études du mode de Helmholtz des oscillations de plasma nécessitent des mesures simultanées de la tension de l'arc et de la pression à l'intérieur de la cavité cathodique.
La pression totale a été mesurée à l'aide d'un capteur piézo-résistif de petite taille (diamètre 4 mm) ENDEVCO 8510C (Meggitt's Endevco, Irvine, Etats-Unis). Le capteur est installé dans la cavité cathodique de la torche. Les mesures simultanées des signaux de la tension de l'arc et de la pression ont été effectuées à l'aide d'une carte d'acquisition de données PCI 6132 pilotée par le logiciel Labview.
L'influence de différentes conditions de fonctionnement sur les oscillations de Helmholtz a été examinée par la mesure des signaux de tension d'arc et la pression à l'intérieur de la cavité cathodique. En outre, les travaux antérieurs du laboratoire ont mis en évidence l'existence d'autres modes de fluctuation due à la propagation des ondes acoustiques [72, 73]. Ces modes, appelés les modes acoustiques, se produisent à des fréquences plus élevées, ∼8.5 kHz. Par conséquent, les expériences présentées ont donné les résultats du mode Helmholtz et des modes acoustiques et du mode de réamorçage (restrike). Pour examiner les oscillations de Helmholtz, acoustique et de réamorçage du plasma, les signaux de ces modes doivent être isolés à partir de la tension d'arc mesurée et de la pression.
La tension d'arc mesurée et la pression peuvent être présentées sous la forme de la somme des modes d'instabilité de jet de plasma: Helmholtz (H), réamorçage (R) ou acoustique (a). Pour observer l'influence de ces modes sur les conditions de fonctionnement, ils ont été isolés à partir du signal, en utilisant le filtre de Wiener numérique programmé sous LabView, définie par la formule 2.27.
Premièrement, les études sur les modes de Helmholtz et acoustique ont été présentées. L'effet de différentes configurations de la cavité cathodique sur ces modes a été examiné. En enlevant l'anneau d'injection, la figure 2.10 (b), et en utilisant la cavité de cathode spécialement usiné, 2.10 (c), trois configurations différentes ont été obtenus avec les volumes : (a)$\mathrm{V_g}$ = 12.5 $\mathrm{cm^3}$, (b) $\mathrm{V_g}$ = 8.7 $\mathrm{cm^3}$ et (c)$\mathrm{V_g}$ = 6 $\mathrm{cm^3}$. Les figures 2.11 et 2.12 présentent les spectres de puissance de la tension et de la pression les composantes des modes Helmholtz (H) et acoustiques (A), filtrées et calculées à partir de la tension d'arc et de pression. Ils ont été enregistrés pour chaque configuration de la cavité de la cathode, pour les mêmes conditions de fonctionnement: $\mathrm{L_k}$ = 30 mm, I = 500 A, Ar-$\mathrm{H_2}$

(45-10 slm). Les résultats présentés dans les figures 2.11 et 2.12 montrent une bonne correspondance entre les modes Helmholtz et acoustiques, et, en outre, entre la tension et la pression. Pour analyser l'évaluation de ces modes les paramètres ont été établis à partir des spectres de puissance et résumées dans le tableau 2.3.
Les écart-types, défini par: $\sigma_i = \sqrt{\langle s_i{}^2 \rangle}$, où s_i sont les signaux de tension ou de pression associés aux modes Helmholtz ou acoustiques, ont été calculés à partir des spectres filtrés par le programme développé sous LabView. Le facteur Q a été établi par l'équation, comme suit: $Q = f_i/\Delta f$, où Δf est la largeur à mi-hauteur mesurée sur les raies Helmholtz ou acoustique dans le spectre de puissance de la tension et de la pression.
Les valeurs de la fréquence de Helmholtz définis à partir des spectres de puissance de la tension et de pression, donnée dans le tableau 22.3, mettent en évidence le décalage des pics f_H à des valeurs plus faibles en raison de l'augmentation du volume de la cavité de cathode, par exemple, de 4500 Hz obtenue pour le cas (c) à 3100 Hz pour (a). Les calculs présentés dans le tableau 2.4 mettent en évidence une bonne compatibilité entre les résultats expérimentaux et le modèle du mode de Helmholtz. Les écarts-types calculées de Helmholtz et modes acoustiques montrent qu'avec l'augmentation du volume de la cavité de cathode, non seulement les fréquences de Helmholtz sont décalées vers des valeurs plus faibles, mais aussi une grande partie de la puissance du signal passe en mode acoustique. Ce phénomène est plus évidemment présenté dans la figure 2.13. Le rapport de puissance, R_i, pour chaque mode de fonctionnement est calculé à partir de la puissance des spectres de tension filtré en programme LabView et tracé en fonction du volume de la cavité de la cathode. Pour le cas (c), où $V_g = 12.5$ cm^3, plus de puissance fluctuante est contenue dans le mode acoustique à l'opposé du cas (a).
En outre, les facteurs Q de résonance de Helmholtz pour la tension de l'arc diminuent également de 30.5 à 19 quand V_g varie de 6 à 12.5 cm^3. Ceci indique que l'énergie de résonance de Helmholtz est transférée à des modes acoustiques.
Les résultats présentés conduisent à rechercher analytiquement les modes acoustiques dans la cavité cathodique en tenant compte des modes radiaux et azimutaux, en plus des modes longitudinaux. La cavité de la cathode peut être supposée être de géométrie cylindrique avec une forme annulaire de longueur L = 38 mm, le rayon intérieur a = 7 mm et le diamètre extérieur b = 10.5 mm. Cette approche analytique compte tenu dans la section "Configuration of the cathode cavity", ont fourni l'équation de modes de résonance des fréquences défini par:

$$f_0 = ({f_{nm}}^2 + {f_\ell}^2)^{0.5} \tag{2.49}$$

où f_ℓ correspond à l'acoustique modes longitudinaux. Le calcul montre que la plupart d'entre eux ont des fréquences supérieures à 10 kHz, sauf le mode (n, m , ℓ) = (1, 1, 1), qui définit:

f_ℓ = 2368 Hz et f_{11} = 6589 Hz, ce qui donne la fréquence f_0 = 7000 Hz. Cette valeur est cohérente avec avec celles mesurées dans les spectres de puissance présentée dans les figures 2.14 et 2.15. En outre, lorsque le volume de la cavité cathodique, V_g, augmente, L présenté dans le modèle (2.32) augmente, ce qui donne la diminution de la fréquence acoustique. Les résultats expérimentaux, énumérés dans le tableau 2.3 et 2.5, montrent la même dépendance.

Dans les études précédentes, présentées dans [72], les mesures des signaux de la tension d'arc et de la pression, obtenues pour des mélanges argon-hydrogène ont été mises en évidence. Les expériences ont été effectuées en utilisant la même torche à plasma. La tension d'arc et la pression dans la cavité cathodique ont été obtenus à 600 A, pour le débit constant d'argon à 45 slm et le débit d'hydrogène variant entre 2 et 10 slm. Les spectres de puissance de tension, présenté sur la figure 2.17 montrent que la composition chimique des gaz plasmagènes influe fortement sur la résonance de Helmholtz, en particulier lorsque le contenu de l'hydrogène est augmentée à mélange binaire comme Ar-H_2. De plus, le débit d'hydrogène doit atteindre un certain seuil, d'environ 5 slm, pour maintenir des oscillations de Helmholtz. Dans la partie suivante, les résultats de l'utilisation de Ar-H_2 et Ar-N_2 sont mis en évidence. Ils ont été obtenus pour les compositions des gaz suivants:

- Ar-H_2 (45-5 slm)
- Ar-H_2 (45-10 slm)
- Ar-N_2 (40-6 slm)
- Ar-N_2 (40-16 slm)

Les mesures de la tension d'arc et de la pression dans la cavité cathodique ont été obtenues à 400 A pour une configuration standard de la cavité: cas (a)$V_g = 6$ cm^3 et pour la distance entre la pointe de cathode et la sortie de la tuyère: L_k = 30 mm. En comparant les motifs des oscillations de la tension d'arc, présentés sur la figure 2.18, obtenue avec le mélange Ar-H_2 (45-10 slm), avec les signaux mesurés pour le plasma argon-azote, un phénomène de battement est observé qui produit des groupes successifs de pics d'amplitudes hautes et basses dans le cas de Ar-H_2 mixture. L'analyse des spectres de puissance de la tension obtenue avec Ar-N_2, représentés sur la figure 2.19, et les données indiquées dans le tableau 2.7 montre que les signaux de tension d'arc contiennent la résonance de Helmholtz sans aucune influence du mode acoustique. Par conséquent, ce phénomène de battement trouvé dans l'évolution temporelle du signal de tension mesurée pour Ar-H_2 (45-10 slm) pourrait être attribuée à un couplage entre les modes de Helmholtz et acoustique. De plus, le spectre de puissance calculé à partir de la tension d'arc (figure 2.19) et la pression de signaux (figure 2.20) mettent en évidence le décalage des pics de fréquence de Helmholtz vers les valeurs inférieures pour plasma argon-azote. La fréquence est égale à 3.4 kHz

pour Ar-N_2 (40-16 slm) plasma et 4.45 kHz pour Ar-H_2 (45-10 slm). L'analyse du modèle de la fréquence de Helmholtz donné dans ((2.21)) montre que cette baisse de la fréquence est dû aux paramètres suivants du plasma Ar-N_2: faible coefficient isentropique, γ, et une densité plus élevée, ρ, comparativement au plasma Ar-H_2.
Le modèle du mode de Helmholtz des instabilités ((2.21)) montre que ces fluctuations de la tension d'arc sont aussi sensibles à la longueur du canal de tuyère. Par conséquent, cette partie présente l'examen de l'influence de la distance entre la pointe de la cathode et de sortie de la buse, L_k, à la résonance de la torche conventionnelle. La longueur du canal de tuyère a été modifiée comme indiqué à la figure 2.21. Les mesures des signaux de tension d'arc et de pression ont été effectuées à 400 A pour le mélange argon-hydrogène (45-10 slm) en utilisant la torche de cavité cathodique: (b) $V_g = 8.7$ cm^3. Les signaux ont été enregistrés pour différentes L_k, égal à 30 mm et 29.5 mm. Les spectres de puissance de tension d'arc et de pression du mode de Helmholtz filtré et calculé à partir des mesures sont présentés sur les figures 2.22 et 2.23. Les spectres de puissance et les données calculées et mentionnées dans le tableau 2.8 montrent que la variation de la position de la cathode ne modifie pas la fréquence de Helmholtz qui est d'environ 3.5 kHz, pour les deux configurations. Toutefois, une légère diminution de la distance entre la pointe de la cathode et de sortie de tuyère, $\Delta L_k = 0.5$ mm, influence sensiblement l'écart-type calculée à partir de la tension d'arc, 10 V et 7.5 V, respectivement, pour L_k = 30 mm et L_k = 29.5 mm.
Pour confirmer la théorie de résonateur de Helmholtz dans une torche plasma à courant continu, un résonateur acoustique externe monté sur la cavité cathodique a été utilisé. Ce type d'installation permet de modifier les ondes de pression dans la torche à plasma, ce qui signifie que la modification de la pression à l'intérieur de la cavité cathodique qui conduit à la modification du signal de tension d'arc peut démontrer le phénomène de résonance dans la torche.
Le résonateur externe est composé d'une cavité cylindrique (le diamètre ϕ_1, illustré sur la figure 2.24, est égal à 110 ± 0.1mm) et un col cylindrique (le diamètre $\phi_2 = 5 \pm 0.1$mm et la hauteur h $= 6 \pm 0.5$mm) qui est relié à la cavité cathodique de la torche. La profondeur de la cavité de résonateur est modifié en utilisant la position d'un piston réglable (référencé avec coordonnée z). L'exemple de l'utilisation du résonateur externe est représenté sur la Figure 2.25. Les spectres de puissance de tension ont été calculés à partir du signal de tension de l'arc obtenu pour 400 A, pour une configuration standard de la cavité de la cathode: cas (a) $V_g = 6$ cm^3 et pour le mélange des gaz Ar-N_2 (40-16 slm).
La position d'un piston z a changé de 0 mm, ce qui correspond à résonateur fermé, par z_1 = 6 mm à $z_2 = 8.7$ mm. Pour z égal à 0 mm, le spectre du signal de tension d'arc électrique présente un pic majeur autour de 3400 Hz. En comparant les spectres de puissance de tension obtenus pour différentes positions du piston et les écarts-types mentionnés dans

le tableau 2.9, une diminution de l'écart type de mode de Helmholtz est observée. Pour z = 0 mm, σ est 17 V, ce qui signifie que la résonance de Helmholtz impose à l'arc une forte oscillation. En augmentant la coordonnée z, σ des fluctuations de Helmholtz diminue. Comme il est présenté sur la figure 2.25, les résultats les plus efficaces sont obtenus pour $z_1 = 6$ mm. Le pic de Helmholtz est considérablement réduit, ce qui signifie que le phénomène de résonance est amorti. Les résultats obtenus ont montré l'utilisation du résonateur externe a considérablement réduit les variations de tension d'arc. C'est la preuve d'un couplage fort entre la pression à l'intérieur de la cavité cathodique et le signal de tension. En outre, l'utilisation du résonateur externe peut être une bonne méthode au réduire les instabilités du plasma puisque les fluctuations de tension peuvent être réduites de façon significative.

La section suivante se concentre sur l'examen du mode de réamorçage superposé aux oscillations de Helmholtz. L'analyse de la composante fluctuante de réamorçage, $u_R(t)$, est possible grâce à l'utilisation de la méthode de filtrage. Le but de ces études suivantes est de vérifier si le composant de réamorçage, $u_R(t)$, suit le modèle présenté dans le chapitre 1 [61]. En outre, les examens suivants seront axés sur les paramètres de fonctionnement qui influencent le mode de réamorçage.

Comme cela a été présenté dans le chapitre 1, les fluctuations de réamorçage sont causées par l'augmentation de la tension d'arc en raison de l'écoulement du gaz. Le processus d'allongement est suivi par un claquage électrique de la couche limite du gaz froid entre la colonne d'arc et la paroi anodique. Un nouveau point d'accrochage est créé en amont de la tuyère, qui correspond à une tension d'arc minimale et qui est identifiée par un saut de tension, ce qui est présenté dans la figure 2.28. La ré-amorçage d'arc se produit à partir de la colonne d'arc lorsque la tension de l'arc, entre la périphérie de l'arc et la paroi de l'anode, est supérieure au seuil de rupture, $V_b(z)$, ce qui a été défini dans la Chapitre 1. La chute de la tension aux bornes de la couche froide, $u_{CL}(z,t)$, peut aussi déduire de la figure 2.29 comme suit:

$$u_{CL}(z,t) = u_R(z,t) - u_C(z) \tag{2.50}$$

où $u_C(z) = E_0 z$. E_0 est le champ électrique à travers la colonne d'arc, qui est supposée être constante. Lorsque $u_{CL}(z,t) \geq V_b(z)$, un nouveau pied d'arc est créé à $z = z_{i+1}$. Comme cela a été présenté dans le chapitre 1, $V_b(z)$ est liée à l'épaisseur de la couche froide, $e_{CL}(z)$ [61]. Figure 2.30 montre l'évolution de $e_{CL}(z)$. Au moment de $t_i + \varepsilon$ juste après la formation du pied d'arc, le spot anodique est situé à $z = z_i$. Le chemin du courant d'arc est allongé par le plasma lors de τ_i, la tension u_{CL} augmente, et au temps $t_i + \tau_i - \varepsilon$, juste avant de re-amorçage, u_{CL} atteint la tension de claquage à $z = z_{i+1}$. Une nouveau pied d'arc est créé dans un nouveau lieu, à $z = z_{i+1}$, au temps $t_i + \tau_i + \varepsilon$. Par conséquent, le saut de tension, δV_i, peut être défini par l'équation (2.38). Cependant, dans ce modèle, les

turbulences et les instabilités de l'arc, doivent être prises en compte. Par conséquent, les arguments ci-dessus doivent être considérés d'un point de vue statistique. Cette analyse statistique a été obtenue à partir des signaux de tension d'arc, le même que dans le cas de l'étude des variations de Helmholtz mais dans ce cas, les études de la composante fluctuante de la mode de réamorçage obtenues par le procédé de filtrage sont présentés.
L'analyse des données a montré que l'augmentation du courant d'arc cause la diminution de l'amplitude des sauts de tension et la diminution de la tension minimum. De plus, pour un plus faible H_2 contenu, la distribution des mesures est décalée vers des valeurs de plus faible de tension. Le nombre desauts de tension à haute amplitude augmente lorsque le contenu de hydrogène augmente. Les résultats présentés sur la figure 2.34 ont montré des valeurs moyennes de sauts de tension déterminées à partir des densités de probabilité de δV_i obtenues à partir des signaux mesurés pour différents paramètres expérimentaux: Ar-H_2 mélanges: 45-5, 45-10 et 45-15 slm et deux diamètres de la tuyère, 6 et 8 mm, en fonction du courant d'arc. Figure 2.34 a mis en évidence la diminution des sauts de tension moyenne tandis que le courant d'arc augmente. Compte tenu d'un modèle à deux couches d'une colonne d'arc stationnaire, axisymétrique dans une torche à plasma présenté dans le chapitre 1, la dépendance des sauts de tension moyenne des paramètres de fonctionnement peut être interprétée en terme d'épaisseur moyenne de la couche froide, $\bar{e}_{CL}(z)$. Le rayon moyen de l'arc électrique $\bar{r}_e$ peut aussi être déterminé. Par conséquent, comme Figure 2.34 met en évidence que l'augmentation du courant d'arc diminue les sauts de tension moyens, ce qui résulte en la réduction de l'épaisseur de la couche froide,$\bar{e}_{CL}(z)$, et l'augmentation de $\bar{r}_e$. Lorsque le débit d'hydrogène est augmenté de 5 slm à 15 slm, les pertes de conduction thermique radiale sont augmentées, ce qui conduit à la diminution de $\bar{r}_e$ et par conséquent l'augmentation de $\bar{e}_{CL}(z)$. Enfin, lorsque le diamètre de la tuyère augmente, $\bar{e}_{CL}(z)$ augmente également. Dans ce cas, les sauts plus élevés de la tension sont observés, ce qui est dû à la diminution de la probabilité de reamorçage [75]. Les résultats présentés ont été vérifiés par les études statistiques que la composante fluctuante filtrée du réamorçage, $u_R(t)$, suit le modèle des instabilités pures du réamorçage, donnés dans [61]. Ils soulignent que le réamorçage et modes de Helmholtz sont relativement séparés, ce qui est confirmé par les différents temps caractéristiques: le mode de Helmholtz à quelques centaines de μs et réamorçage quelques dizaines μs.
En augmentant le volume de la cavité cathodique, il est possible de diminuer notablement la fréquence de Helmholtz. Par conséquent, une nouvelle torche à courant continu a été conçu avec une cavité cathodique plus grande (V_g = 17.8 cm^3), par rapport aux torches à plasma commerciales. L'augmentation de la cavité cathodique a permis de renforcer le facteur Q et de diminuer la fréquence spécifique du mode de Helmholtz. En outre, les dimensions longitudinales de la torche ont été raccourcies pour rejeter les modes acoustiques vers les régions de plus hautes fréquences. En tenant compte des paramètres

d'influence et en diminuant la fréquence des événements de réamorçage, le couplage entre mode Helmholtz et de réamorçage a été recherché expérimentalement. L'azote a été utilisé comme le gaz plasmagène en raison de la possibilité de renforcer le mode de Helmholtz et dominer les modes acoustiques. En outre, la fréquence des événements de réamorçage dépend du courant d'arc, le diamètre de la buse de la torche et de la vitesse d'écoulement du gaz. Par conséquent, les études ont été concentrées sur le réglage de ces paramètres de fonctionnement. Différentes tuyères ont été testées avec un diamètre, d, variant de 3.5 et 4 mm. Le courant d'arc a été modifié de 25 A à 15 A. Le débit d'azote a été choisi de 2.7 slm à 2 slm. Le couplage entre les modes de Helmholtz et réamorçage a été obtenu pour le courant d'arc de 15 A, le diamètre diamètre de tuyèrede 4 mm et le débit d'azote de 2 slm, présenté sur la figure 2.37 (3). Le signal de tension d'arc obtenue dans ce nouveau mode est très reproductible en forme de dents de scie, caractérisée par une amplitude importante et stable ($67.7\text{V} \pm 2.1\text{V}$), à la fréquence de 1.4 kHz. Lorsque la torche fonctionne dans ce mode particulier, il émet un son stable, fort et bruyant qui ressemble au son produit par un moustique. Par conséquent, le terme "mosquito mode" a été utilisé pour décrire ce nouveau mode de couplage entre les modes de Helmholtz et réamorçage. Les mesures de bilans d'énergie ont permis de définir l'enthalpie spécifique, h, du plasma produit dans ce nouveau mode. Les variations de h ont été obtenues, comprise entre 1.4 et 26 MJkg^{-1} en considérant constantes les pertes thermiques aux électrodes. Il donne la proportion de la modulation d'enthalpie: $h_{max}/h_{min} \simeq 18$ avec une valeur moyenne d'environ 13.3 MJkg^{-1}. Par conséquent, la variation temporelle de la température, ce qui correspond à l'enthalpie modulée, doit être comprise entre 1500 et 7100 K (d'après les données thermodynamiques trouvés dans [17]).

Chapter 3 :

Suspension phased injection in pulsed arc jet

Introduction

The following chapter focuses on the improvement of suspension plasma spraying method. The principle is to inject the suspension droplets at the right moment in the cycle of the periodic plasma jet oscillations.
The previous chapter has shown the possibility to obtain very regular plasma oscillations. A new dc torch has been designed with a larger cathode cavity ($V_g = 17.8\ cm^3$) to reinforce the Q factor and to decrease the specific frequency of the Helmholtz mode. Moreover, the use of nitrogen as plasma forming gas has allowed to reinforce the Helmholtz and dominate the acoustic modes. The presented experiments have highlighted the possibility of coupling the Helmholtz with restrike oscillations into a new resonant mode, which has been called "mosquito" mode. The arc voltage signal, produced in this "mosquito" mode, is a very repeatable saw-tooth shape signal. Moreover, the thermal losses determination has allowed to define the local specific enthalpy of different moments of this periodic plasma oscillations. The calculations have highlighted that the obtained plasma is characterized by the enthalpy modulated with a ratio $h_{max}/h_{min} \simeq 18$.
The following chapter will present the application of these regular plasma oscillations to the suspension treatment and coatings deposition process. As has been highlighted in the previous chapters, the conventional SPS method demonstrates the difficulties due to e.g. the discrepancies in the particles trajectories and the heat transfers, what makes the control of coatings properties more difficult to achieve. The purpose of this work is to develop a new system which may allow to increase the reproducibility and reliability of the process by the use of the regular plasma oscillations synchronized with the suspension injection. The activation of the suspension droplet emission at the chosen moment of the periodic plasma, following the requirements for the thermal treatment of the particular material, may be able to increase the control of the heat and momentum transfers between plasma and materials, thus, of the coatings properties. Therefore, it is important to optimize the system which will allow to synchronize the suspension injection with the arc voltage signal. Moreover, the different kinds of the time-resolved and synchronized diagnostic methods are required to study the thermal and dynamic treatments of the material in the periodic plasma. Consequently, the system schematically presented in Figure 3.1 has been developed in the framework of this thesis to work with this periodic plasma produced in "Mosquito" mode.

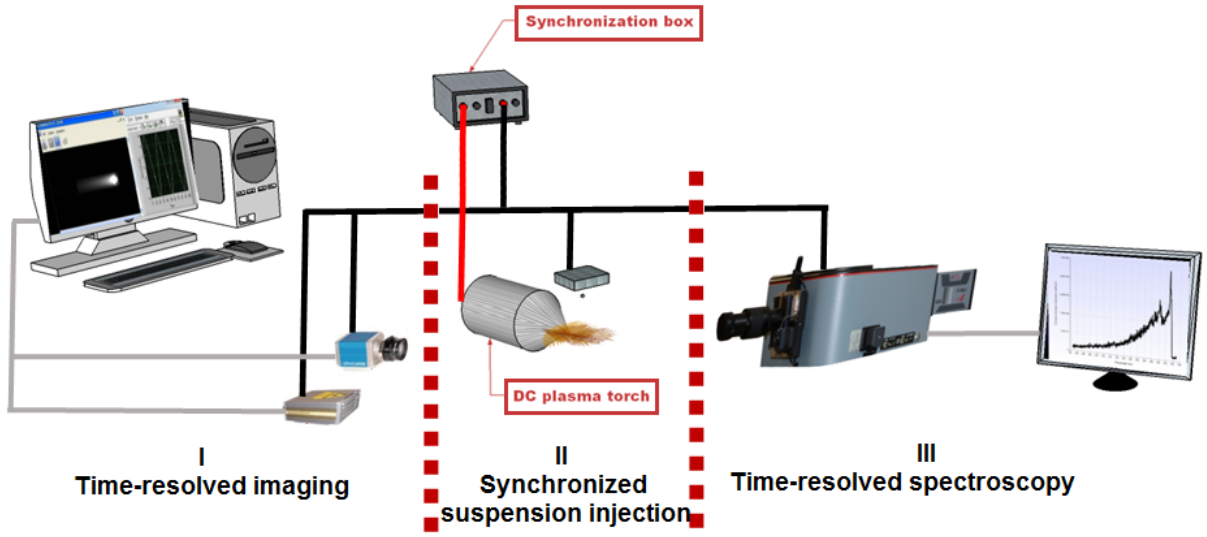

Figure 3.1: Schematic view of the experimental setup.

It consists of three important parts:

I Time-resolved imaging system

It consists of the camera and the laser. This part of the system requires the choice of the devices suitable to observe and register the oscillating plasma with the periods of around 700 μs. Moreover, the experiments have to be performed to obtain the synchronization of the camera with the laser.

II Synchronized suspension injection

The periodic plasma oscillations allow to obtain a new approach to the injection of reactive material in the arc jet. The suspension droplet can be inserted at the chosen moment of this regular plasma jet, what may lead to the control of dynamic and thermal interaction between the plasma and the material. However, it requires the injection system capable to control the moment of material introduction to the plasma. This requirement has been found in the piezoelectric-based DOD (Drop-On-Demand) ink-jet printer provided by Ceradrop Company (Limoges, France). In the paragraph devoted to this part of the system a new injector will be described. Moreover, the observation of the suspension droplets without the plasma and inside the plasma jet will be presented.

III Time-resolved spectroscopy

Chapter 2 has highlighted that the plasma produced in "Mosquito" mode is characterized by the enthalpy highly modulated. To experimentally determine this estimation the time-resolved optical emission spectroscopy has been implemented in the system. This method has been used to make the measurements of the plasma temperature and to determine the plasma species. However, this technique requires

careful calibration methods, what will be presented with the first spectroscopic measurements of the periodic plasma.

The principle of this new system is to inject the suspension droplet at the right moment of the periodic plasma jet. Therefore, the emission of the feeding material has to be synchronized with the arc voltage signal. Moreover, to observe the modulated plasma and the interaction between the plasma and the injected suspension the time-resolved imaging system and time-resolved optical emission spectroscopy have to be also synchronized with the plasma.
Consequently, the synchronization system has been implemented in the framework of this thesis, what will be described in the following paragraphs.
All assumptions and characterization given above have been used to construct a new system which may be an alternative method to the conventional suspension plasma spraying method. To determine the possibilities of this new technique the first attempts of the material deposition have been performed, what will be presented in the final part of this chapter.

I Time-resolved imaging system

To observe the periodic plasma oscillations obtained in "mosquito" mode the time-resolved and synchronous imaging system has been implemented. The study of the oscillating plasma with the periods of around 700 μs is possible by the choice of the fast shutter camera.

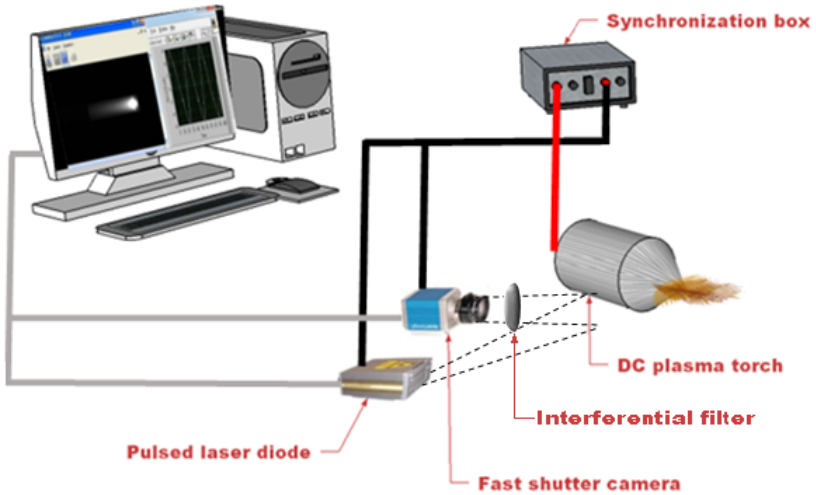

Figure 3.2: Schematic view of the experimental setup of time-resolved imaging system.

The time-resolved imaging system is presented in Figure 3.2. It consists of a fast shutter camera, high-power laser diode and an interferential filter (801 nm). The laser and the filter have been combined with the fast shutter camera to permit the observation of the suspension treatment within the plasma jet. The principle is to observe the suspension penetration within the plasma jet by illuminating droplets using the laser shots. The interferential filter (801 nm) centered on the laser wavelength permits to eliminate on the image the light coming from the pure nitrogen plasma.

I.1 Camera

Fast shutter camera Pixelfly (PCO, Germany) can be applied in many scientific areas, e.g. luminescence spectroscopy, particle image velocimetry (PIV), high resolution microscopy. The camera is equipped with the CCD matrix with the high resolution of 1392 x 1040 pixels, what enables to observe the details of the suspension droplet. Pixelfly camera can work in three operation modes: async (asynchronous) mode, double/shutter mode, video mode. In order to synchronize the camera with the laser the async mode has been used, which enables to control the CCD matrix exposure time in the range from 5 μs to 65 ms. The functioning of CCD can be divided into two phases: exposure and readout. During the first phase (CCD-Exposure in Figure 3.3) the CCD collects passively incoming photons and stores electrons in its cells. After the exposure time, the cells are read out one line at a time (CCD-Readout in Figure 3.3) and are shifted down the entire area of the CCD matrix.

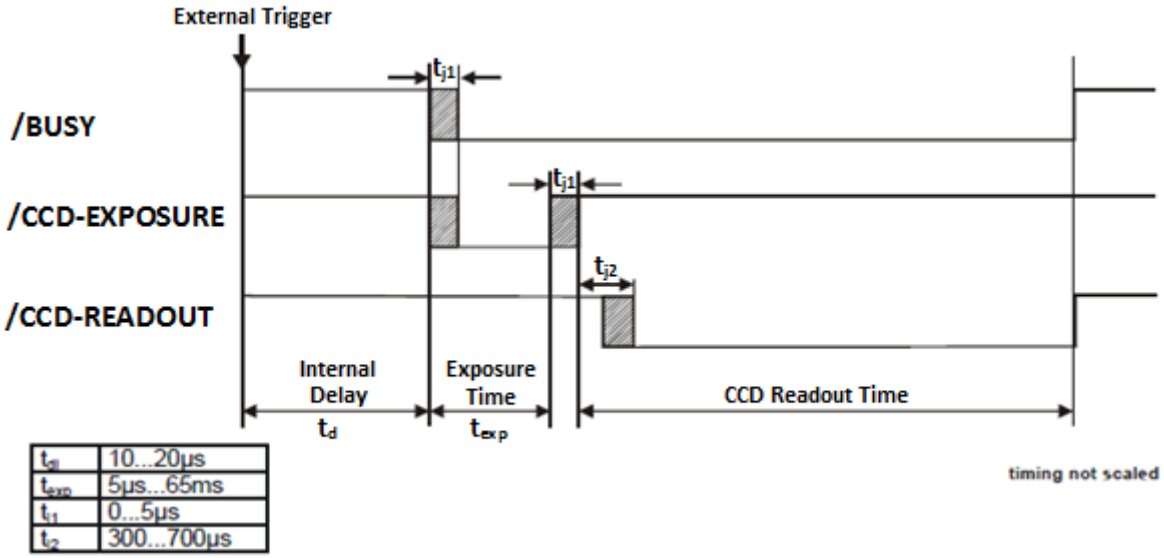

Figure 3.3: Timing diagram of the async mode.

Camera Pixelfly is connected via USB 2.0 connector to computer and controlled by program Camware. This software allows to trigger the camera by the internal or external signal. In the case of the time-resolved imaging the second option has been chosen. Camware enables also to record images, save one image which is displayed in the active window or save the sequence of 75 images which is useful in the observation of the plasma jet.
To study the plasma with higher resolution, e.g. to record the treatment of suspension droplets inside the plasma jet, the Infinimax long-distance microscope system (Infinity, Boulder, USA) has been used. It consists of the objective and large format amplifier which can be additionally mounted. The use of the objective results in the increase of magnification up to 2.9x. The optional amplifier extends the magnification, what is highlighted in Figure 3.4.

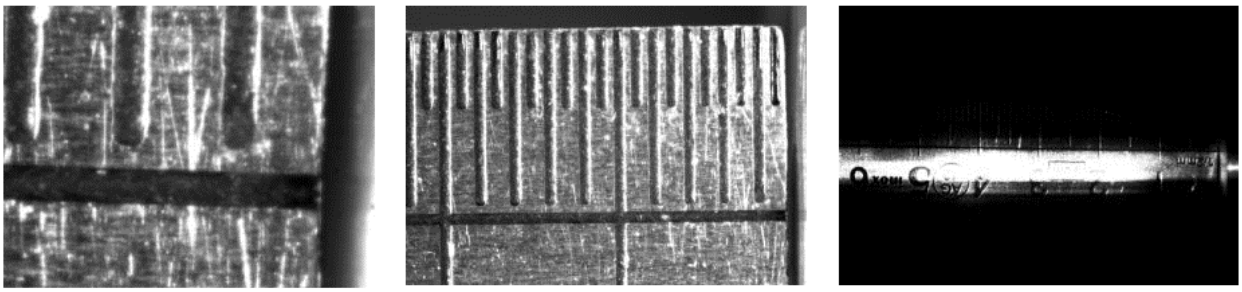

Figure 3.4: Pictures taken by Pixelfly camera at different magnifications with mounted a) Infinimax and the amplifier, b) Infinimax objective, c) Pixelfly camera synchronized with the laser sheet.

Figure 3.4 a) has been taken by the camera Pixelfly with the mounted Infinimax and the amplifier. It is possible to observe a magnified object at the distance of 3 mm from the torch nozzle. In Figure 3.4 b) the result of using the camera with Infinimax objective is shown where the magnification decreases. The distance from the torch equals 22 mm. The last figure, 3.4 c), presents the picture taken by the camera Pixelfly. The magnification decreases 2.9 times compared to the figure b). Figure 3.4 c) presents also the use of the laser synchronized with the camera.

I.2 Laser

High power laser diode (HiWatch, Oseir, Finland) is designed for demanding illumination applications. The parameters of this laser unit are presented in Table 3.1.

Table 3.1: Parameters of a laser diode.

Parameter	Value
Emission wavelength	801 ± 2 nm
Output geometry	8 x 1 mm
Emission power	50 W
Single pulse length	0.025-1 μs
Max. pulse frequency	20 MHz
Time delay	36 ns

The emission wavelength of the laser is in the range of 801 ± 2 nm which corresponds to the infra-red (IR) spectral region. The response time of the laser diode is negligible and equals 36 ns. The HiWatch laser is controlled by a driver module, presented in Figure 3.5.

The diode is energized when the MOSFET transistor is turned on by the signal sent to the gate input. The current flows from the energy storage capacitor, through the laser diode, current limiting resistor, MOSFET and the current sense resistor, back to the energy storage capacitor. The output pulse width and frequency follow the signal which is directed to input gate. The driver provides variable output current from 5A to 50A with pulse widths up to 1 μs and frequencies up to 1MHz.

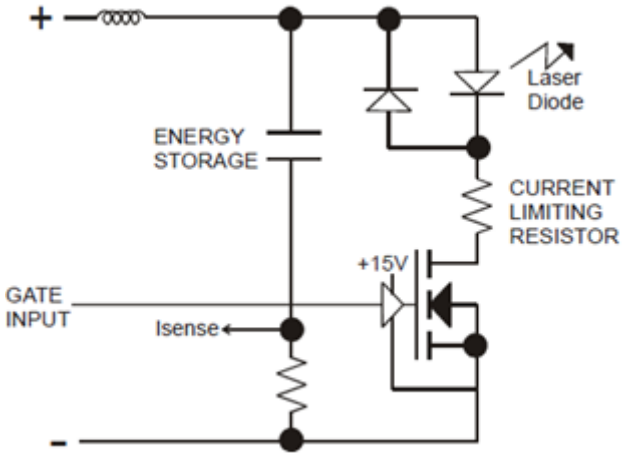

Figure 3.5: Diagram of power supply module of the laser diode.

The width of the pulse emitted by the laser depends mainly on the width of signal put to the input gate. It is possible to obtain 50 ns laser pulse by providing 50 ns input to the driver module. The width of pulse transmitted to the input gate should be smaller than

1 μs due to recharging of the energy storage capacitor (Figure 3.5). It is also possible to input any binary waveform which will be replicated in the emission. In this case, it is important to take into consideration the dependence presented in Figure 3.6.

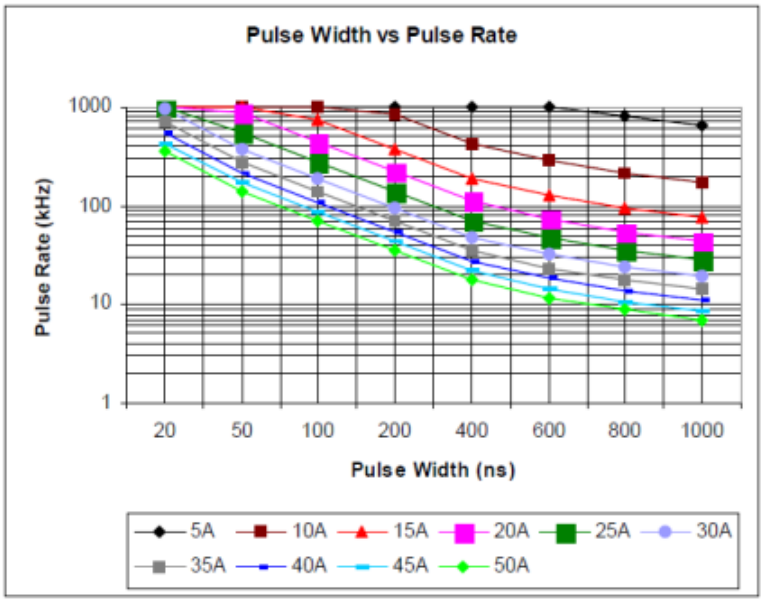

Figure 3.6: Dependence of the pulse width, pulse rate and current.

The pulse width, frequency and the driver output current (therefore the power emitted by the laser diode) are the dependent parameters, related to the available charge of the drivers energy storage network. This dependence shows that in the time-revolved imaging method, it is important to choose an appropriate value of the pulse rate for the synchronization of the camera and the laser.

I.3 Synchronization procedure of time-resolved imaging system

To observe different moments of the periodic plasma oscillations the time-resolved imaging should be synchronized with the arc voltage signal. Moreover, the suspension droplets should be illuminated by the laser shot during the registration by the camera. Therefore, the laser and the camera should be also synchronized.

To make the synchronization of the laser diode with the fast shutter camera the accurate time delay, t_d, of each device has to be determined. t_d is defined as the time between sending the external trigger signal to the instrument and the response of this instrument. The time delay of the laser has been determined by the producer and equal to 36 ns. However, the t_d of the camera has been given in the range between 10 μs and 20 μs. The laser pulse duration equals up to 1 μs. Therefore, it can be noticed that the precise time of the camera delay is the important parameter in the synchronization procedure.

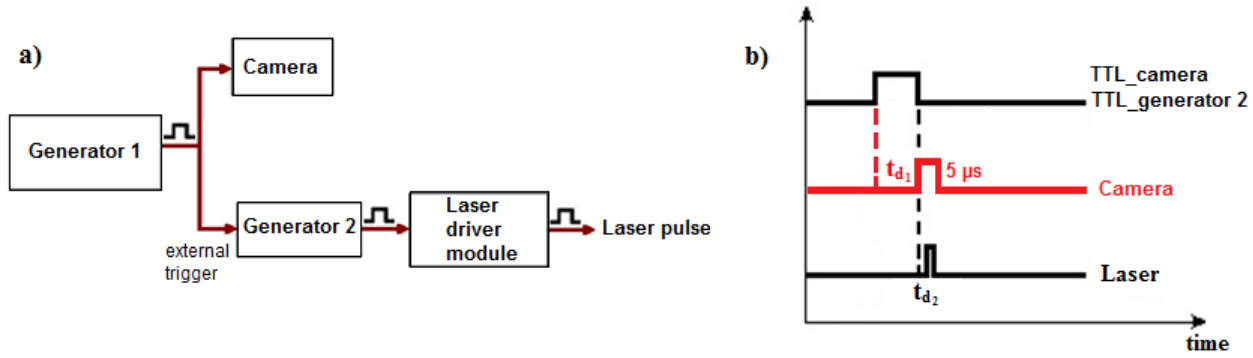

Figure 3.7: Investigation method of the camera delay time: a) the experimental setup, b) the timing diagram.

Figure 3.7 presents the investigation procedure to determine the delay time of the camera, t_{d1}. The principle is to synchronize the camera with the laser by using two generators. Generator ♯1, Figure 3.7, sends the triggering signal to the camera and the generator ♯2. The pulse reaches both devices at the same time, what is measured by the oscilloscope. The camera is triggered by a rising edge of the signal and the generator ♯2 by a falling edge. The generator ♯2 inputs the pulse to TRIG connector of the laser diode driver module, what results in the emission of the laser shot. t_{d2} is the laser time delay equals 36 ns. It has to be mentioned that the camera is controlled by Camware software and the option of the external trigger of the camera has been chosen.

The exposure time of the camera is regulated to minimal value of 5 μs. The width of the trigger pulse sent by the generator ♯1 simulates the time delay of the camera. The camera has been recording the image for different widths of the signal in the range of 10 to 20 μs. The width of the trigger pulse for which the image of the laser beam has been obtained using camera is 14 μs, what is in the range of camera delay time given by the producer.

As has been mentioned, the time-resolved imaging system has to be synchronized with the arc voltage. To obtain this synchronization the TTL signal has to be formed from the arc voltage, which is measured by the bridge circuit connected between the cathode of the torch and the ground.

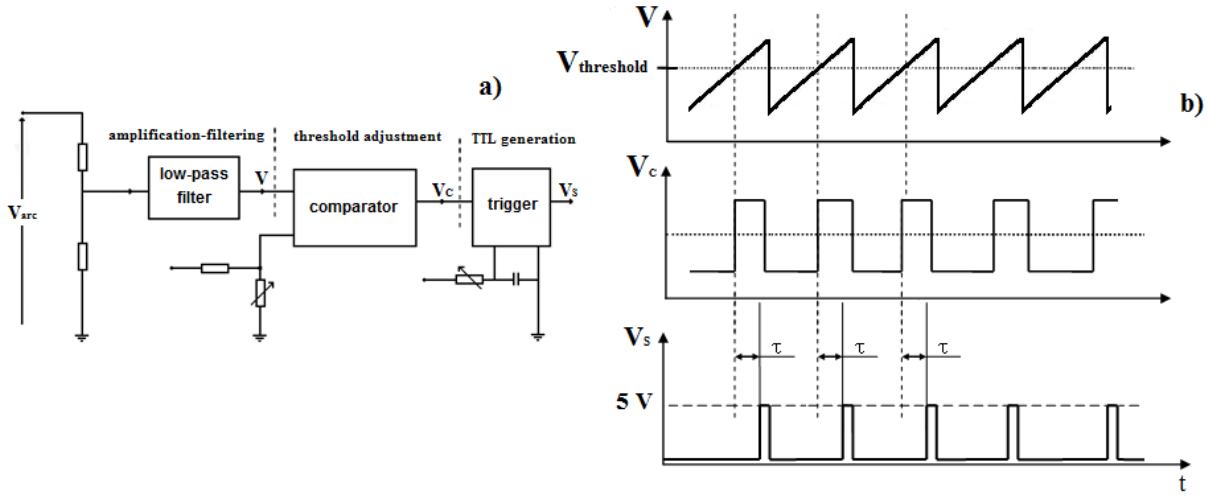

Figure 3.8: The principle of the synchronization device: a) the schematic view, b) the functioning of the system.

To generate the initial TTL signal the synchronization device has been designed, which is presented in Figure 3.8, and composed of:

- the amplification-filtering unit to isolate the Helmholtz mode component from the raw signal, V_{arc},
- the threshold adjustment unit which consists of the comparator to set the trigger level, $V_{threshold}$,
- the generation of the pulse at the fundamental frequency, f_H, unit which produces a TTL pulse V_s (5 V, 10 μs). It permits to generate the signal with an adjustable delay, τ, relative to the threshold

TTL signal, generated by this synchronization box by the adjustment of the threshold level and the time delay, is then sent to the control panel (Ceradrop, France), Console Ceradrop presented in Figure 3.9.

The Ceradrop console can generate two trigger signals (Output ♯1 to activate the camera and Output ♯2 connected to the laser in 3.9) with the adjustable pulse width. The console permits to change the time delay relative to Triggering signal, in Figure 3.9, formed from the arc voltage by using the synchronization box. Moreover, it is possible to choose the time delay between two triggering signals from output 1 and output 2 to synchronize the camera with the laser sheet. The results of the experiments have shown that the delay between these two devices equals 14 μs. Therefore, the time between the triggering signals of output 1 and output 2 is regulated to this value. The developed synchronization system permits to select the moment of the periodic arc voltage signal by changing the threshold level and the time delay.

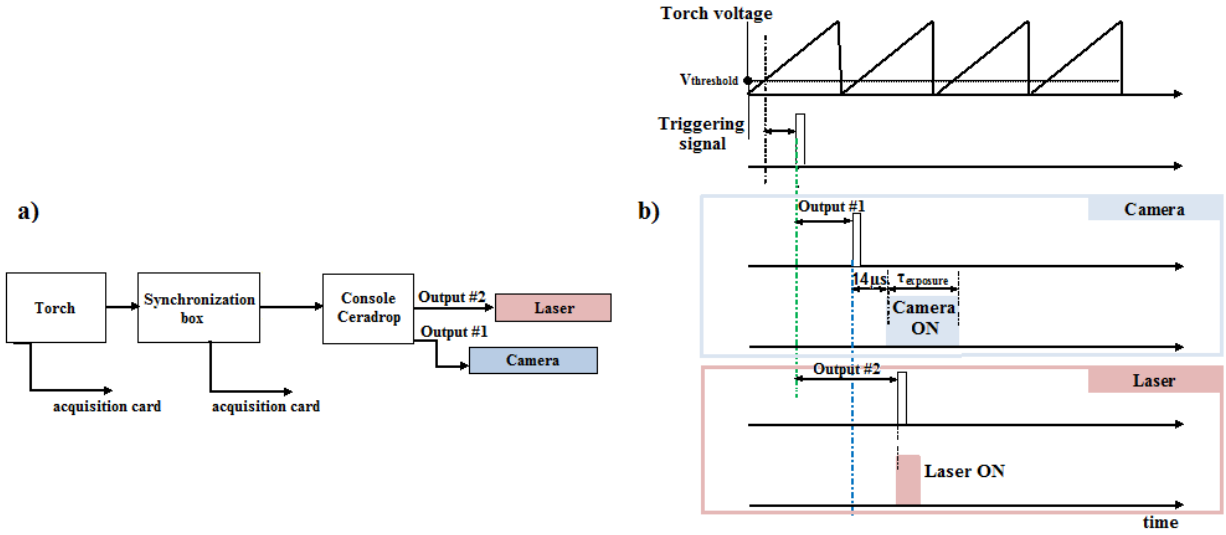

Figure 3.9: Schematic view of the synchronous time-resolved imaging procedure: a) the experimental setup, b) the timing diagram.

The obtained TTL signal triggers the Ceradrop console which after 14 μs activates the camera and the laser.

I.4 Pulsed and laminar plasma jet

The time-resolved imaging system synchronized with the arc voltage signal allows to observe the different moments of the periodic plasma oscillations. As has been presented, Helmholtz and restrike modes locked together oscillate at the frequency of 1.4 kHz. Therefore, one period of the plasma oscillation is around 700 μs, what can be observed in Figure 3.10. It presents time-resolved imaging of this periodic plasma obtained in "mosquito" mode.

As can be noticed this very regular arc voltage signal obtained by coupling Helmholtz and restrike modes together, presented in Figure 2.37 c), results in the pulsed plasma jet. The different pulses of this periodic plasma are able to be observed by the camera triggered at a given moment of this periodic arc voltage signal. Figure 3.10 presents the voltage signal obtained in "mosquito" mode with indicated TTL pulses sent to the camera. The aperture time of the camera is regulated at 60 μs and 75 pictures are recorded in each situation: from a) to e) in Figure 3.10. The picture a) corresponds to a trigger of 70 μs after a falling front of the voltage. The moments b) to e) have been taken with respective time delays: 210, 310, 520 and 770 μs, which corresponds to 70 μs in the next period, taking into account that one period of the pulsed plasma jet is around 700 μs. Figure 3.10 a) presents the moment after re-arcing and shows an extinguishing plasma ball. The arc is very short and located in the rear part of the nozzle.

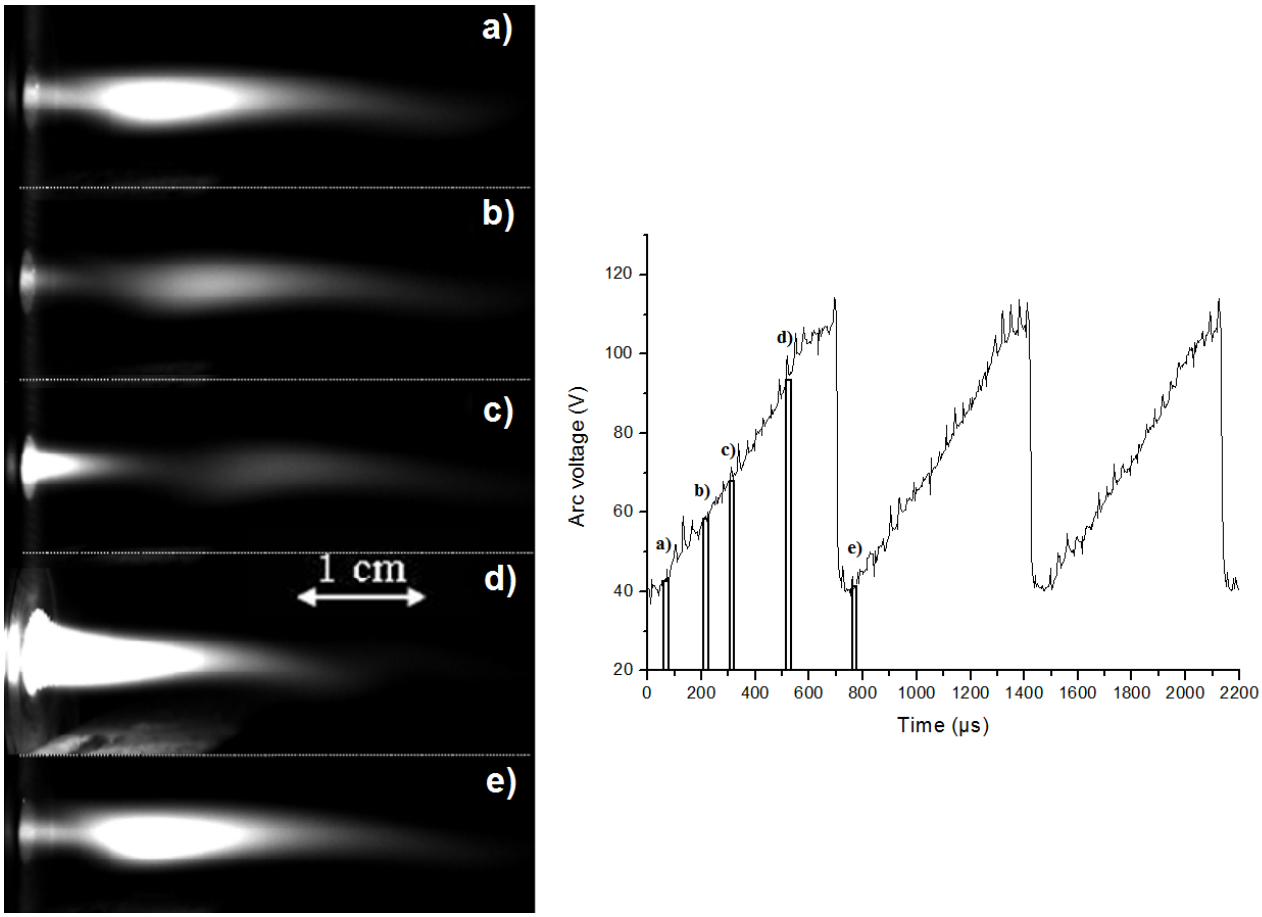

Figure 3.10: Time-resolved imaging (camera exposure time: 60 μs) of pulsed arc jets for different trigger time delays indicated in the temporal evolution of the arc voltage signal: (a) 70 μs, (b) 210 μs, (c) 310 μs, (d) 520 μs and (e) 70 μs in the next period, 700 μs after (a) [79].

Pictures b) - d) demonstrate the progressive development of the arc and Figure 3.10 e) represents a situation similar to a) but for the following cycle. This sequence testifies the strong modulation of the plasma, which from high luminescence appears to be almost lighted off. The examination of the series of 75 pictures has shown a very regular evolution of the plasma in each cycle.

Figure 3.11 is obtained by a standard camera with an exposure time of 10^{-2} s, what results in the superposition of 13 cycles presented in Figure 3.10. It shows the laminar feature of the plasma flow, what can be experimentally verified by the Reynolds number, defined for the plasma torch in [80], as follows:

$$Re = \frac{4\dot{m}}{\pi\eta d} \tag{3.1}$$

where η is the dynamic viscosity of the plasma equals around 1.7×10^{-4} kg.m^{-1}.s^{-1}, what has been defined from the energy balance measurements and data found in [17].

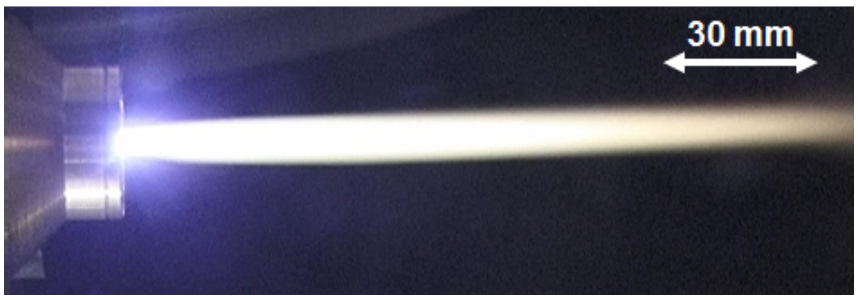

Figure 3.11: Laminar feature of pulsed arc jet. Operating parameters: d_{nozzle} = 4 mm, I = 15 A, N_2: 0.042 g.s^{-1}, $\overline{U}$ = 73.7 V, exposure time of camera = 10^{-2} s, the superposition of 13 cycles presented in Figure 3.10 [74].

Reynolds number allows defining different flow regimes, such as laminar or turbulent flow. The laminar flow occurs at low Reynolds numbers. The transition from laminar to turbulent flow starts at about Re $>$ 2100 and the flow is considered to become fully turbulent at Re $>$ 4000.
For plasma parameters, given in Table 2.12, Reynolds number is estimated to approximately 78, what defines the laminar flow of the plasma.

II Synchronized suspension injection

In the introduction to this chapter has been highlighted that the obtained periodic plasma oscillations require the appropriate injection method, capable to control the moment of material introduction to the plasma jet. The analysis of different injection techniques, presented in the literature review in chapter 1, has resulted in selecting the piezoelectric-based DOD ink-jet printer, provided by Ceradrop Company (Limoges, France), due to the possibility of the emission of each droplet triggered at the frequency of the pulsed plasma, i.e. 1.4 kHz. The following paragraph describes this new injector. Moreover, the idea of development of the plasma spraying method is to insert the material at the chosen moment of the pulsed plasma jet, presented above.

Therefore, the synchronization of the suspension injection with the arc voltage signal has to be implemented in this method. Figure 3.12 shows the schematic view of the developed system with added suspension injection. This experimental setup allows to obtain the synchronization of the material insertion to chosen moment of the plasma jet with the camera and the laser. It results in the possibility of the observation of the suspension-plasma interaction, what will be presented in the following paragraphs.

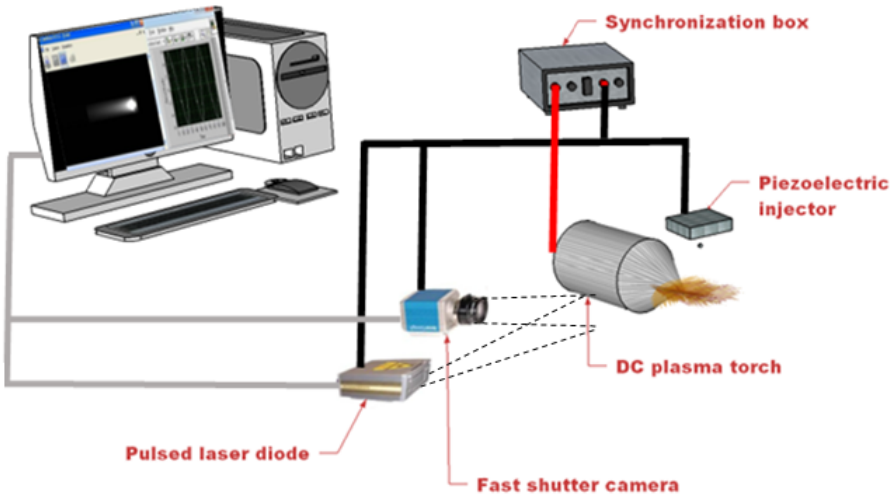

Figure 3.12: Schematic view of the experimental setup with added synchronized suspension injection.

II.1 Injection system

This ink-jet type technique, commonly applied in the printing devices, is now being used in a wide variety of industries for micro-droplet generation [81–83]. In the system developed in this thesis the injector prepared by Ceradrop Company (Limoges, France) has been used. Figure 3.13 schematically presents the injector based on drop-on-demand technique. The liquid is ejected out of small orifices (diameter equal to 50μm) to form pulsed jets due to the pressure generated by a voltage pulse driven piezoelectric actuator (voltage excitation equals 120 V).

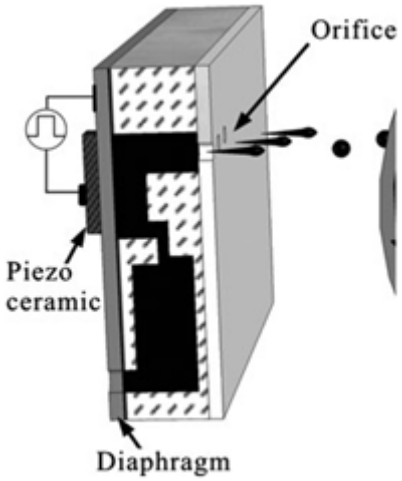

Figure 3.13: Schematic view of piezoelectric DOD printhead [39].

It has to be mentioned that voltage pulses are carefully shaped to avoid satellite droplets and to adjust the velocity of single calibrated droplet between 2 and 10 $m.s^{-1}$. The pulse shape must also be adapted to the rheological properties of the suspension, what will be presented in the following paragraphs. The piezoelectric injector can be triggered at frequencies up to 20 kHz and comprises a ramp of 128 individual micro-nozzles, disposed perpendicular to the plasma jet axis, with a step of 0.5 mm. The injection system is protected from heat flux coming from the plasma by a water-cooled copper screen, presented in Figure 3.14, in which a horizontal slit, 10 mm long and 1 mm wide, is machined.

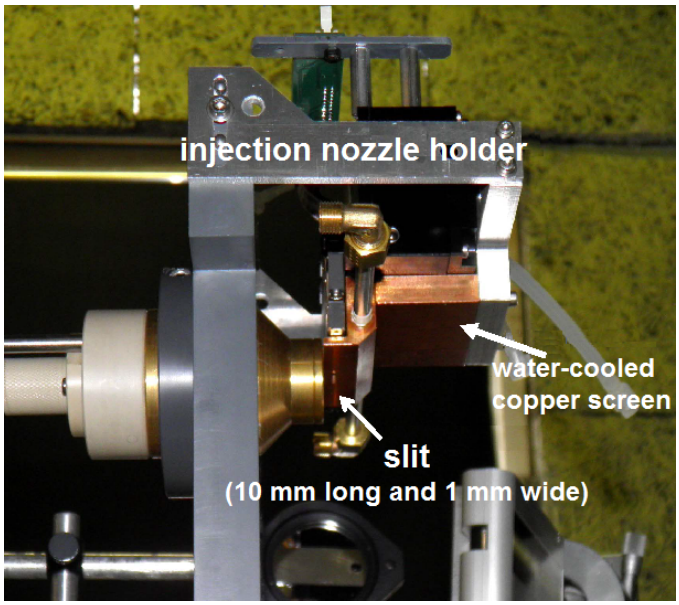

Figure 3.14: "Mosquitorch", a newly designed dc plasma torch, with a water-cooled copper screen.

II.2 Synchronization system

The principle of synchronous suspension injection is to inject the droplet of the feeding material at the right moment of the periodic plasma jet oscillations. This synchronization process is possible for the following postulate:

$$f_H = f_i \tag{3.2}$$

where:

f_H is the frequency of Helmholtz resonant mode equals the plasma frequency,
f_i the frequency of suspension injection.

Figure 3.15 presents the schematic view of the synchronous suspension injection system. The emission of the droplet is triggered by the TTL signal formed from the arc voltage by using the synchronization box. This triggering pulse is sent to Ceradrop console which activates the piezoelectric injector.

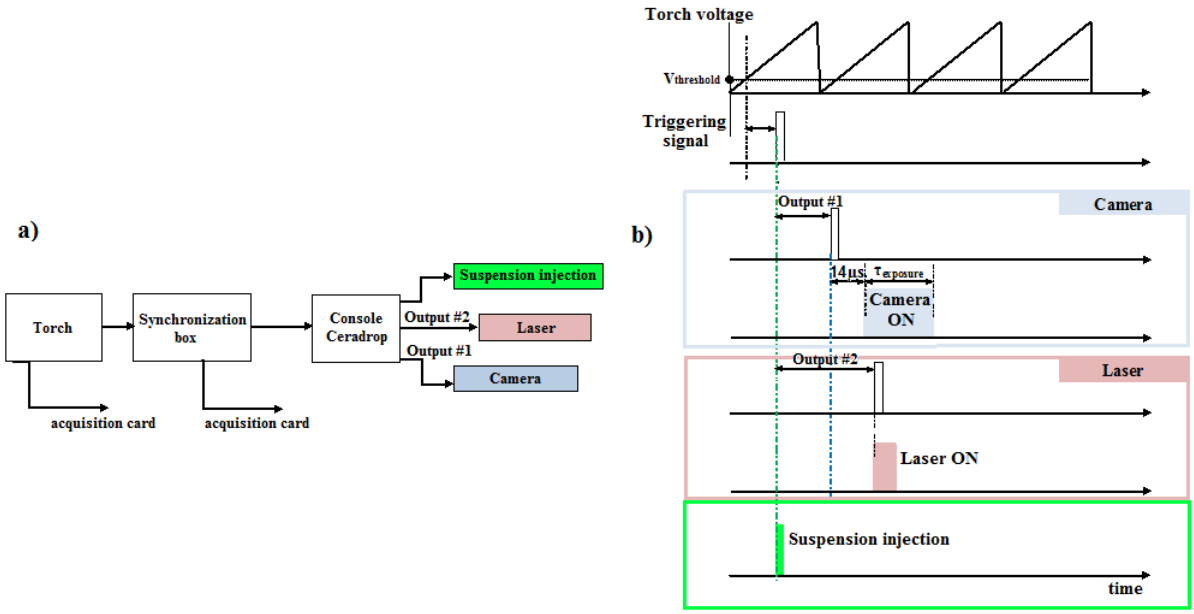

Figure 3.15: Schematic view of the synchronous injection procedure: a) the experimental setup, b) the timing diagram.

The system permits to select the moment at which the suspension droplet is injected to the pulsed plasma jet by using the function of the time delay in the synchronization box. It results in the suspension emission after an adjustable delay, $\tau_{droplet}$, counted after a falling front of the arc voltage signal, as follows:

$$\tau_{droplet} = nT + \tau_j \tag{3.3}$$

where T is the arc voltage period and τ_j is the time at which a droplet penetrates the plasma.

As presented in Figure 3.15 the triggering signal generated from the arc voltage activates all outputs of Ceradrop console, what permits to obtain the synchronization of the suspension injection with the camera and the laser shot. In the Ceradrop console it is possible to choose the time delay of the outputs 1 and 2 in relation to the triggering signal and the suspension injection as well. To observe the suspension-plasma interaction the delay time has been regulated to 0 s.

II.3 Observation of the suspension droplets without the plasma

II.3.1 Suspension properties and size distribution

The suspension used in the experiments, prepared by Ceradrop Company (Limoges, France), is composed of titanium dioxide (90% TiO_2 rutile phase) powder and it consists of 5 wt% of powder and 95 wt% of water. The properties of the suspension are specified in Table 3.2.

Table 3.2: Parameters of the suspension.

TiO_2 concentration	Conductivity	Viscosity	Surface tension	Density
vol%	$\mu S.cm^{-1}$	mPa.s	$mN.m^{-1}$	$g.cm^{-3}$
5	480	7.57	34.067	1.204

The particle size distribution of the injected feedstock material has to be adjusted with the diameter of the printing head nozzle, which equals 50 μm in Ceradrop injector. To avoid the clogging of the nozzle the particles sizes of the suspension have to be analyzed.

They have been determined by using Mastersizer 2000 (Malvern Instruments Ltd., UK) which is based on the technique of laser diffraction. The scattering pattern in this method depends on the ratio of particle diameter, D, and the wavelength of the incident light, λ. According to D/λ the scattering of particles is predicted by the Fraunhofer or Mie models. In Mastersizer 2000 the Mie model ($D/\lambda \simeq 1$) is applied for the particles smaller than 3 μm. Therefore, this model has been used to determine the particle size distribution of the suspension, presented in Figure 3.16.

The peak of the particle size distribution curve is centered on 66 nm (d_{50}). The dispersion size ($d_{90} - d_{10}$) is equal to 48 nm.

II.3.2 Trajectory of a single droplet

In the ink jet printers, the suspension formulation has to be optimized in order to avoid the sedimentation, clogging and to be compatible with the printing head. Moreover, the injection of a single calibrated droplet is the important parameter in this kind of method. To obtain the emission of a single droplet two conditions have to be fulfilled:

- the rheological properties of the suspension (e.g. viscosity, surface tension) have to be adjusted to obtain the ratio $Re/\sqrt{We}$ ranged between 1 and 10
- the voltage driven pulse sent to the piezoelectric injector has to be optimized

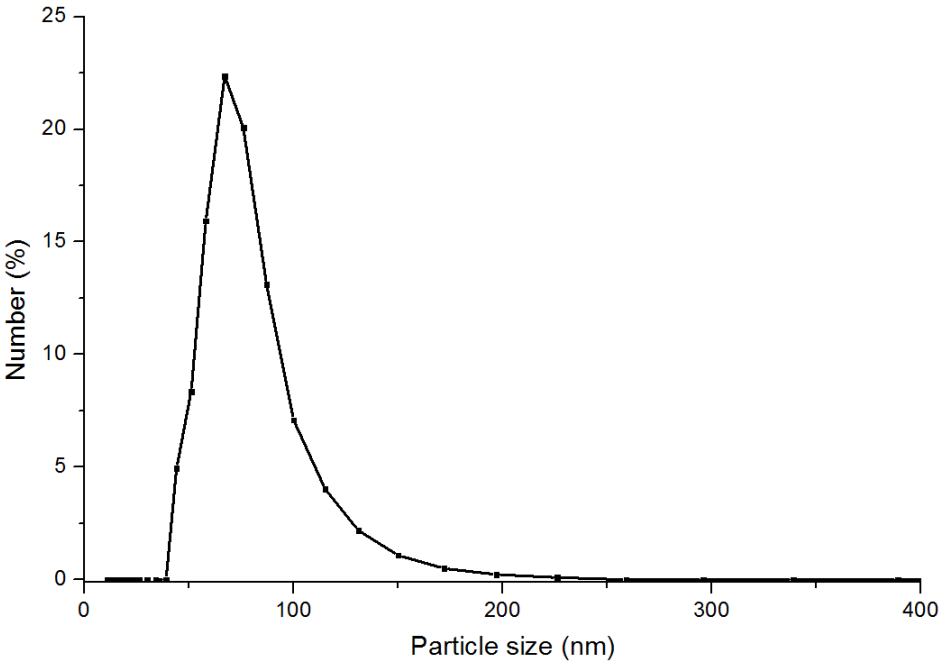

Figure 3.16: The particle size distribution of TiO_2 suspension.

The first condition requires the definition of the ratio $\mathrm{Re}/\sqrt{\mathrm{We}}$. It is the dimensionless number which enables to analyze the fluid flows. It consists of respectively Reynolds and Weber numbers, defined by the following equations:

$$Re = \frac{v.r.\rho}{\eta} \tag{3.4}$$

where:

v	is the suspension velocity,
r	the radius of the nozzle,
ρ	the suspension density,
η	the suspension viscosity.

and Weber number, obtained by:

$$We = \frac{v^2.r.\rho}{\sigma} \tag{3.5}$$

where:

σ	is the suspension surface tension.

Noguera *et al.* have shown the different cases of the suspension injection observed according to the value of ratio $\mathrm{Re}/\sqrt{\mathrm{We}}$, presented in Figure 3.17.

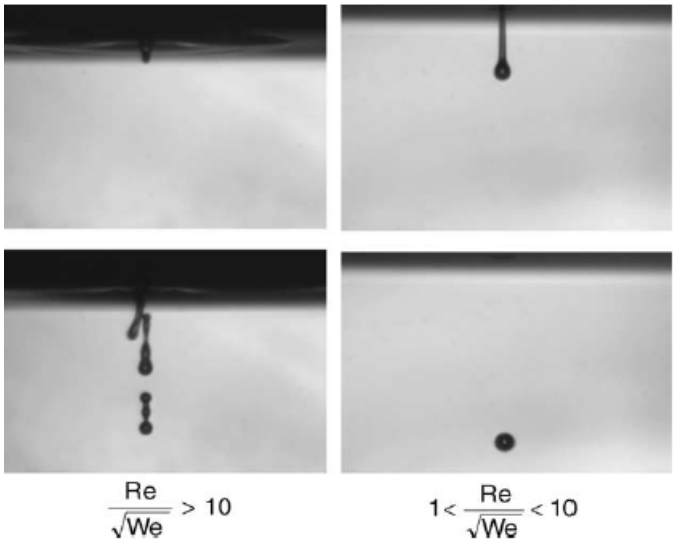

Figure 3.17: Effect of the ratio $\mathrm{Re}/\sqrt{\mathrm{We}}$ on the suspension injection [81].

When the ratio $\mathrm{Re}/\sqrt{\mathrm{We}}$ is too high, bigger than 10, a continuous column of the suspension is injected, what is not the purpose of this thesis.
The properties of the suspension used in the experiment, presented in Table 3.2, have been optimized to obtain the ratio equals:

$$\frac{Re}{\sqrt{We}} = 5.98 \tag{3.6}$$

It is one of the condition to obtain the emission of a single droplet. Figure 3.18 presents the suspension droplets before a) and after b) the optimization of the injection parameters.

To eliminate satellite droplets the voltage driving pulse has been optimized in collaboration with Ceradrop. A voltage trapezoidal pulse, shown in Figure 3.19, has been applied.

The magnitude of the voltage (V_{max}), the pulse times, which include the rise time, duration time and fall time (respectively τ_1, τ_2 and τ_3 in Figure 3.19) and the frequency have been defined and sent to the controller. During the rising time (τ_1) the piezoelectric material (PZT: lead zirconate titanate) moves inward due to shearing stress by applying an electric field in the direction perpendicular to the polarization direction of the piezoelectric material. It results in positive pressure for the liquid in the chamber.

The PZT has no deformation during τ_2. As the voltage drops from V_{max} to 0 during τ_3, the piezoelectric material moves outward, what results in the generation of a negative pressure in the liquid of the chamber. The appropriate optimization of these parameters is important in the injection process since the liquid column is ejected by the positive pressure and then the break-up into droplets by the negative pressure.

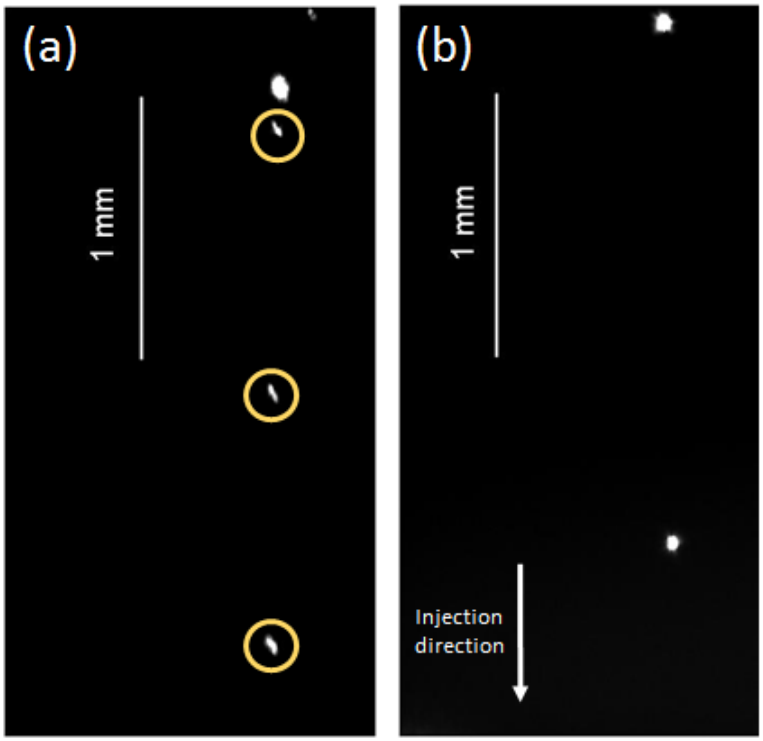

Figure 3.18: Observation of droplets injection by the camera and laser illumination: a) satellite droplets marked by the circles, b) single drops with no satellites as the result of correctly optimized parameters.

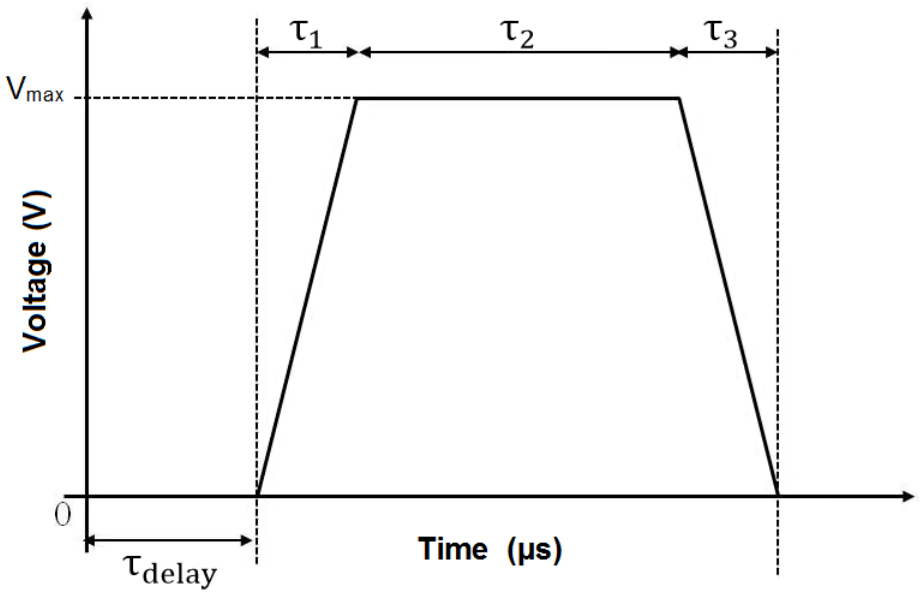

Figure 3.19: Form of the voltage pulse driven piezoelectric actuator.

To observe the suspension injection without producing the plasma but by the synchronized camera and laser with the injector the signal similar to the arc voltage has to be generated. The TTL signal, sent to the Ceradrop console, has been formed by Agilent 33250A

Waveform Generator (Palo Alto, CA, USA). The ramp signal has been generated with the frequency regulated to 1.4 kHz, what has been intended to simulate the arc voltage signal. From produced in this way signal the TTL pulse has been formed by the synchronization box and sent to Ceradrop platform.

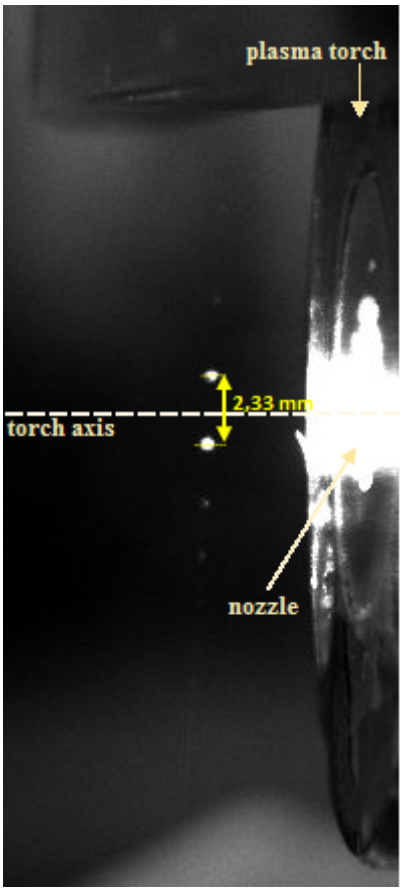

Figure 3.20: Measurement of droplet velocity. The brightness at the nozzle exit is due to the laser reflection. The picture taken by Infinimax objective.

It has allowed to activate the piezoelectric injector, the camera and the laser. The time-resolved imaging system has been used to observe the suspension injection and to make the measurements of the droplet velocity. The suspension injection frequency, f_i, according to Equation 3.2, is equal to 1.4 kHz. Figure 3.20 presents two suspension droplets illuminated by the laser and recorded by the camera. The measured distance, d_d, between them equals 2.33 mm, what gives the droplet velocity, v_d, of 3.26 m.s^{-1}, obtained as follows: $v_d = d_d.f_i$.

II.4 Observation of the suspension droplets inside the plasma

The following section presents the suspension injection inside the pulsed plasma jet. Figure 3.21 demonstrates the use of the suspension injection synchronized with the arc voltage signal. It shows four successive pictures taken by a standard, not synchronized, camera (aperture time 1/6000 s, 24 frames per second). The photos present the individual plasma pulses containing TiO_2 particles resulting from heat treatment of injected droplets. In the first picture the moment of the synchronized suspension injection into the plasma ball is given. Then, in the successive pictures the plasma/droplet interaction is presented, what is characterized by a strong radiation. As can be observed in each photo, the material can be transported by the plasma jet over a long distance, i.e. more than 80 mm.

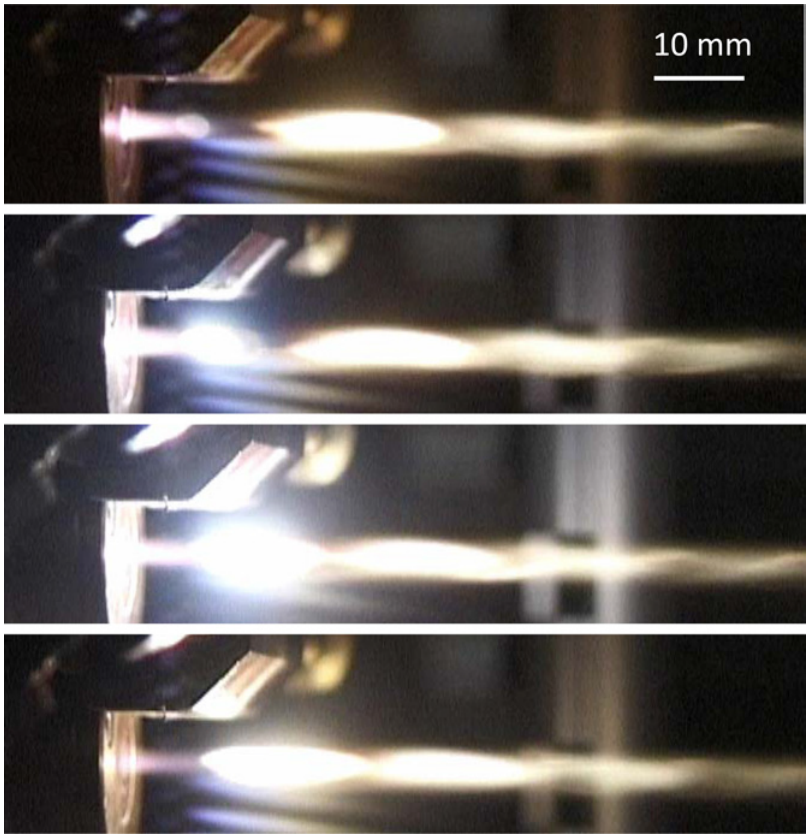

Figure 3.21: Imaging of synchronous suspension injection in the pulsed plasma jet taken by a standard camera: aperture time 1/6000 s, 24 frames per second.

To better analyze the synchronized injection systems and the time-resolved imaging, the timing diagram for droplet emission and imaging is presented in Figure 3.22.

As has been mentioned, the emission of suspension droplet is triggered from sampling of the torch voltage after an adjustable delay, τ_{droplet}, counted after a falling front, as follows:

$$\tau_{droplet} = nT + \tau_j \tag{3.7}$$

where:

T	is the arc voltage period, presented in Figure 3.22,
τ_j	the time at which a droplet penetrates the plasma.

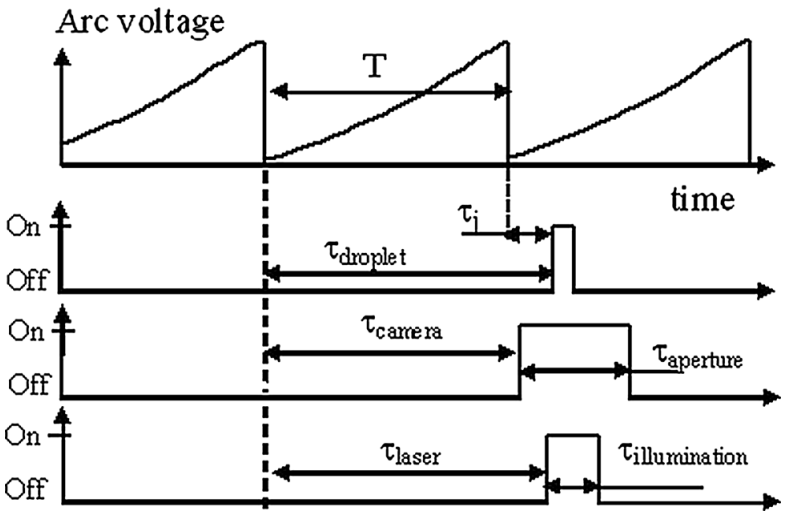

Figure 3.22: Timing for droplet emission and synchronous imaging [79].

The suspension injected to the plasma jet is observed by time-resolved and synchronous imaging system. The delay time of the camera, τ_{camera} in Figure 3.22, and of the laser, τ_{laser}, are adjusted with the emission of suspension droplet. As the obtained results have highlighted, τ_{camera} and τ_{laser} are respectively of 14 μs and 36 ns. τ_{aperture} is an adjustable time in the range of 5 μs and 65 ms, at which camera aperture is opened. $\tau_{\text{illumination}}$ is the laser pulse duration, which can be chosen up to 1 μs. In the following experiments $\tau_{\text{illumination}}$ equals to exact 1 μs.

In Figure 3.23 the time-resolved imaging of the dynamic interactions between the plasma jet and the droplets is presented. The pictures 3.23 a-d are obtained with a low-magnification objective (with the resolution presented in Figure 3.4 c)) for the different time delays over one period with 10 μs camera aperture time and 1 μs laser pulse duration. It has to be noted that the camera aperture of 10 μs is low enough to ensure that the plasma is immobile during the observation. To obtain the reliable results hundreds of pictures related to 3.23 a-d, triggered with the same τ_j, have been recorded. The laser shot has been used to visualize the solid particles left in the jet after solvent vaporization. However, their individual images are strongly oversized by diffraction, scattering, or resolution due to pixel size [79].

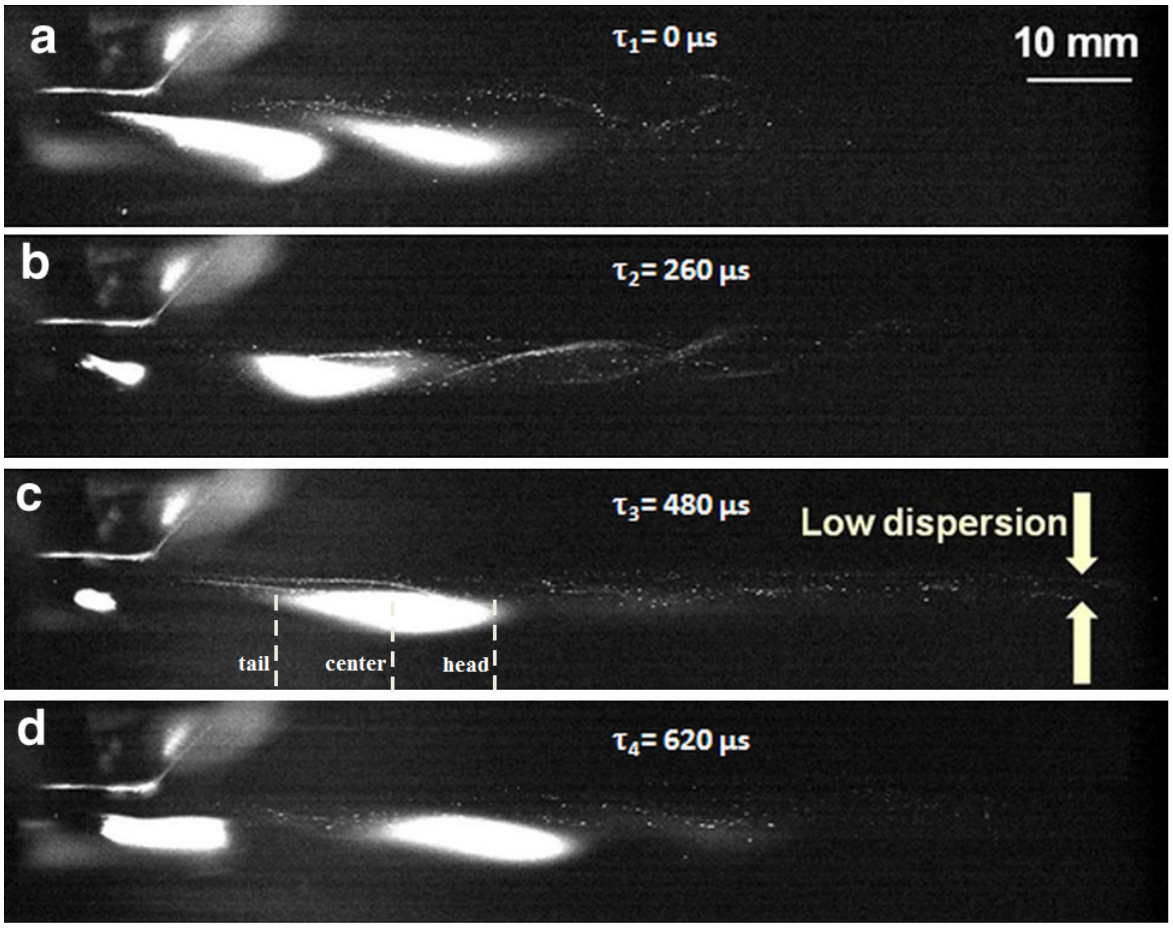

Figure 3.23: Time-resolved imaging of synchronized suspension injection with laser illumination for different injection time delay τ_j.

The image analysis has permitted to estimate the velocities of the center of mass of plasma balls with the vapors coming from the droplet vaporization. The velocities vary between around 30 m.s^{-1} for the case presented in 3.23 a) and 50 m.s^{-1} for 3.23 c). Moreover, it can be observed that each plasma ball is stretched while moving. Therefore, not only velocities of the center of mass of plasma balls should be defined. The velocities concerning the distance between the tails and between the heads of two succeeding balls should be also determined. This gives for Figure 3.23 c), respectively, 35 m.s^{-1} for the end of the balls, calculated above 50 m.s^{-1} for the center and 70 m.s^{-1} for the head. This means also that velocity of this pulsed plasma jet is time- and space-modulated. The obtained results correspond to the order of magnitude of mean plasma velocity evaluated from the following formula [55]:

$$\overline{v} = h_0 \frac{\dot{m}(\gamma - 1)}{P_a.S.\gamma} \tag{3.8}$$

where:

γ	is the nitrogen plasma isentropic coefficient,
P_a	the pressure at the nozzle exit (atmospheric pressure).

Assuming that $\gamma \simeq 1.3$ and $h_0 \simeq 13.3 MJkg^{-1}$ the calculated mean plasma velocity is estimated to around 100 $m.s^{-1}$. Moreover, this expression indicates also that velocity must be modulated because the specific enthalpy changes with time due to the voltage variations.

Table 3.3: Summary of experimental conditions.

Plasma	Time-resolved imaging system	Synchronized injection
N_2: 2 slm	$\tau_{illumination} = 1$ μs	$\tau_1 = 0$ μs
I = 15 A	$\tau_{aperture} = 10$ μs	$\tau_2 = 260$ μs
$d_{nozzle} = 4$ mm	interferential filter = 801 nm	$\tau_3 = 480$ μs
	Frequency of image	$\tau_3 = 620$ μs
f = 1410 Hz	acquisition = 75 Hz	$f_i = 1410$ Hz

Table 3.3 summarizes the conditions of the experiment shown in Figure 3.23 a-d. It demonstrates that the trajectories and related thermal history of injected materials depend on the moment when droplets penetrate into the plasma. In case of $\tau_1 = 0$ μs, the most significant part of materials travels in the plasma fringes giving rise to large dispersion of trajectories ($\sim$ 10 mm) and limited axial distance of material transport ($\sim$ 40-60 mm). In case of $\tau_2 = 260$ μs, the treatment materials in the plasma core is improved with a lower radial dispersion and a slightly increased transport distance. The pulsed plasma jet is trapping particles all along its own axis, what can be observed as alternate and intricate trajectories. This effect seems to be due to the pulsed emission of the plasma balls that alternate their curvatures by interacting between each others. This gives a certain spatial coherence for the plasma jet and also recalls some visual effects such as the Von Karman Street in vortices emission. In Figure 3.23 c) ($\tau_3 = 480$ μs), a low material dispersion is observed corresponding to the longest transport distance. At last, the case of $\tau_4 = 620$ μs, because it is almost the 700 μs period, resembles the first case $\tau_1 = 0$ μs.

Moreover, the influence of the moment at which a droplet penetrates the pulsed arc jet has been investigated using the camera with mounted Infinimax objective (Figure 3.4 b)). The results are presented in Figure 3.24.

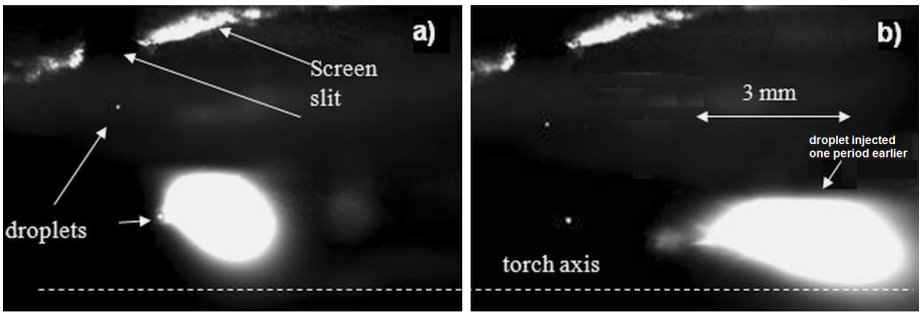

Figure 3.24: Influence of the local instantaneous specific enthalpy on droplet thermal treatment: (a) high level of enthalpy, (b) low level. Camera exposure time: 5 μs, laser illumination: 1 μs [74, 79].

The camera and the laser are delayed by the same time after the droplet emission but the suspension penetrate the plasma earlier in Figure 3.24 a) than in b), what has been obtained by changing τ_j. The droplet, which is possible to observe due to the illumination by the laser, enters the plasma 4 mm downstream of the nozzle exit. The picture a) and b) are observed through a narrow band-pass filter centered on the laser wavelength. As has been mentioned in the previous sections, this configuration permits to eliminate on the image the light coming from the pure nitrogen plasma. Therefore, Figure 3.24 shows merely the seeded plasma balls characterized by a strong increase of the brightness, which resulted from the interaction of the nitrogen plasma with the material contained in the suspension droplet. In Figure 3.24 a) the lower droplet penetrates the plasma at a moment corresponding to a situation presented in Figure 3.10 d). This moment has been chosen due to high level of local specific enthalpy. Therefore, Figure 3.24 b) corresponds to the plasma characterized by a low enthalpy level, shown in Figure 3.10 a). In case presented in Figure 3.24 a) the almost immediate vaporization process of the droplet has been observed, what differs from the situation shown in b). In this case, the vaporization-seeding process does not concern the injected droplet but the one introduced one period earlier, what gives the plasma ball at the right of Figure b).

Figure 3.25 a-d displays four successive pictures taken by the high-speed camera (6000 frame/s) with an exposure time of 100 μs. The time between each picture is about 166 μs. The observation area is shifted by approximately 1 cm downstream of the torch exit, compared to results presented in Figure 3.23. $\tau_{droplet}$ is adjusted so that each droplet reaches the plasma axis $\tau_j = 260$ μs after a voltage falling front. On the left of Figure 3.25 a), the tip of the arc jet is presented that contains no droplet. The spherical shape, which follows immediately on the right, is the result of a droplet injected in the preceding period. The right part of the picture shows the result of the plasma interaction with a droplet injected two periods before. Figure 3.25 b) follows a) by 166 μs.

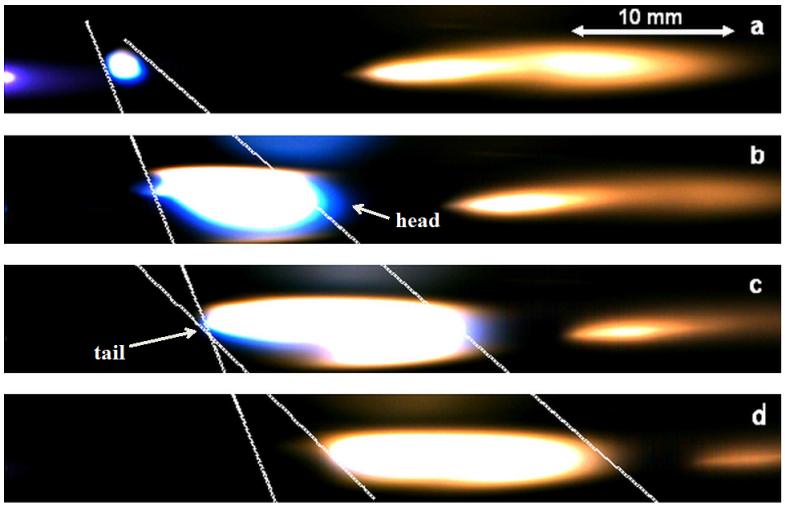

Figure 3.25: Fast imaging (6000 frame/s, time aperture: 100 μs) of synchronized suspension injection in nitrogen pulsed arc plasma jet for the injection time delay τ_j = 260 μs. The white lines indicate that for each plasma bull the tail and the head of a single plasma ball do not travel at the same speed, as previously mentioned.

The spherical shape has been strongly expanded and lengthened due to vaporization process. However, the sharp details at the left of the plasma ball suggest that a certain amount of liquid still remains non-vaporized. The expansion is continued in Figure 3.25 c) and seems to reach a maximum in Figure 3.25 d). The dotted lines drawn on these pictures show that the front part of the plasma ball travels at a speed approximately twice that of the rear part, which is consistent with the expansion process. The rear part lags behind the plasma ball because it still contains a small amount of suspension under acceleration. Once the vaporization is complete, the plasma ball travels as a whole as it can be seen in Figure 3.25 c) and d). A picture taken 166 μs after the situation of Figure 3.25 d) should be similar to a).
The evolution of successive volumes over a sequence of four pictures is measured by the image analysis. Assuming that the resulting plasma balls have an ellipsoidal shape, the volume of the ball is given as follows: $V = \frac{4}{3}\pi \Delta x.\Delta y.\Delta z$, where z is the axial coordinate and the radial expansion is established to be isotropic: $\Delta x \sim \Delta y$. Figure 3.26 presents the measurements of the expansion rates of droplets during plasma treatment for the different injection time delays, τ_j, given in Figure 3.25.

The expansion rate is defined as: $(V_i - V_{i-1})/\Delta t$, with V_i determined as the volume at the instant $t_i = i \times \Delta t$, where Δt = 166 μs, $i \in [0;3]$. t_0 corresponds to the moment presented in Figure 3.25 a). The standard deviation results from the measurements of the volumes for 10 similar sequences of pictures. The expansion rate, Figure 3.26, significantly depends on τ_j, particularly during the first 166 μs.

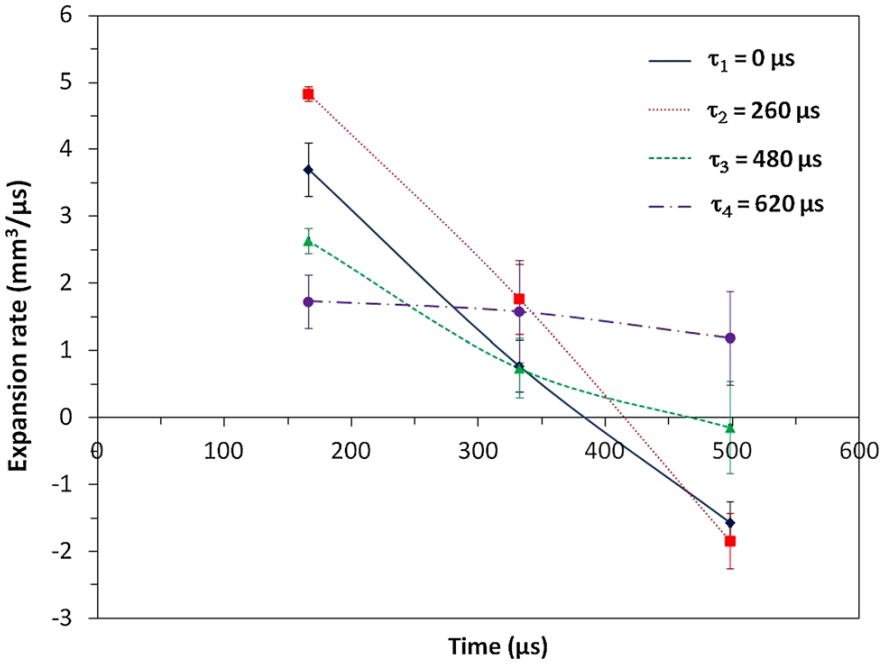

Figure 3.26: Dependence of measured expansion rates of plasma balls on the injection time delay τ_j.

Later, the expansion rate decreases and becomes negative for $\tau_1 = 0$ μs and $\tau_2 = 260$ μs, what is related to the recombination process of plasma. As has been presented, the enthalpy of the plasma is strongly modulated in the proportion: $h_{max}/h_{min} \simeq 18$ with a mean value of 13.3 MJkg^{-1}. Therefore, the heat transfers to droplets and, consequently, the expansion rates are affected by this modulation.
Table 3.4 gives the calculated parameters describing the system of the suspension phased injection in pulsed arc jet.

Table 3.4: Parameters of suspension phased injection system.

Nitrogen mass flow rate	(kg.s^{-1})	4.2×10^{-5}
Nitrogen/one period	(kg)	3×10^{-8}
Energy/one plasma ball	(J)	0.5
Injection velocity	(m.s^{-1})	3.26
Injection frequency	(Hz)	1.4×10^{3}
Droplet diameter	(m)	50×10^{-6}
Suspension density	(g.cm^{-3})	1.204
Droplet mass	(kg)	8×10^{-11}
Suspension flow rate	(ml.min^{-1})	5.6×10^{-3}
Powder mass flow rate	(g.min^{-1})	3.4×10^{-4}

The nitrogen mass flow rate, measured by a Brooks Instrument mass flow controller, is around 4.2 $\times$ 10^{-5} kg.s^{-1}. Therefore, the amount of nitrogen which flows during one period, T = 700 μs, is approximately equal to 3 $\times$ 10^{-8} kg and the energy content in one plasma ball is 0.5 J, which is obtained by the division of the power net by the plasma frequency 1.4 kHz. The mass of a suspension droplet, entering to the plasma jet, is given by the formula: $m = \rho.\frac{4}{3}\pi(\frac{d_d}{2})^3$ and equals approximately 8 $\times$ 10^{-11} kg. The energy needed for water vaporization is determined as follows: $E_{vap} = m_{droplet}.L_v$, where the mass of the droplet, $m_{droplet}$, has been defined above and the water latent heat, L_v, has been given in chapter 1 in table 1.2 and is equal to around 2.26 x 10^6 J.kg^{-1}. Therefore, the energy needed for water vaporization $E_{vap} \simeq 1.8\,10^{-4}$ J, what is much smaller than the energy content in one plasma ball 0.5 J. Consequently, it can be stated that the available energy of pulsed plasma jet is high enough to vaporize completely the solvent and liberate solid particles, what will be presented in the following sections.

II.5 Thermo-physical phenomena of suspension droplets

As has been presented in Chapter 1 the suspension droplets, injected to the plasma jet, undergo the fragmentation and vaporization processes. The fragmentation depends on the dimensionless Weber number which is determined by the following equation:

$$We = \frac{{v_r}^2.d_l.\rho_p}{\sigma_l} \tag{3.9}$$

where:

ρ_p is the plasma density,
v_r the relative velocity between the plasma and the droplet,
d_l the diameter of the liquid droplet,
σ_l the surface tension of the liquid.

The determination of the modulation of the plasma enthalpy has presented that h_{min} = 1.4 MJ/kg and h_{max} = 26 MJ/kg. By using the data found in [17] it is possible to determine the nitrogen plasma density, related to h_{min} and h_{max}, what is presented in Table 3.5.

Table 3.5: Properties of the nitrogen plasma [17].

Temperature	Density	Enthalpy
K	kg/m^3	MJ/kg
1500	2.27 10^{-1}	1.4
7100	3.24 10^{-2}	26

Introducing to Equation (3.9) the plasma density presented in Table 3.5 and suspension properties given in Table 3.2, calculated Weber number ranges between 0.04 and 0.48.

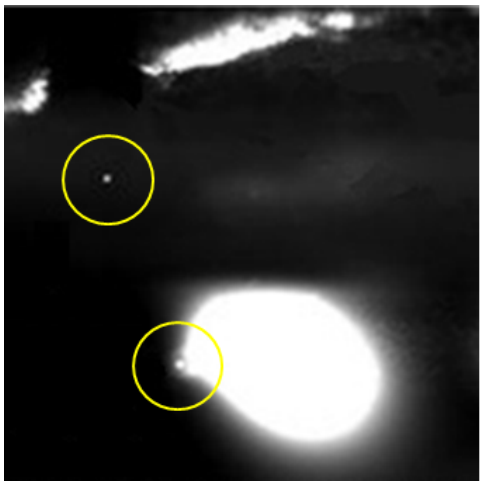

Figure 3.27: Treatment of the suspension droplet in the plasma jet characterized by high local instantaneous specific enthalpy.

As has been presented in Chapter 1, the critical value of We, over which the droplet undergoes the breakup process, equals 14. The obtained results have shown that in the present system the fragmentation process of the suspension droplet does not occur. Figure 3.27 confirms this postulate, where two suspension droplets, marked by yellow circles, seems not to undergo the breakup process.
Under these conditions, the process of solvent reduction from the suspension droplet is governed by the heat transfer and vaporization, which can be represented by the scheme shown in Figure 3.28.

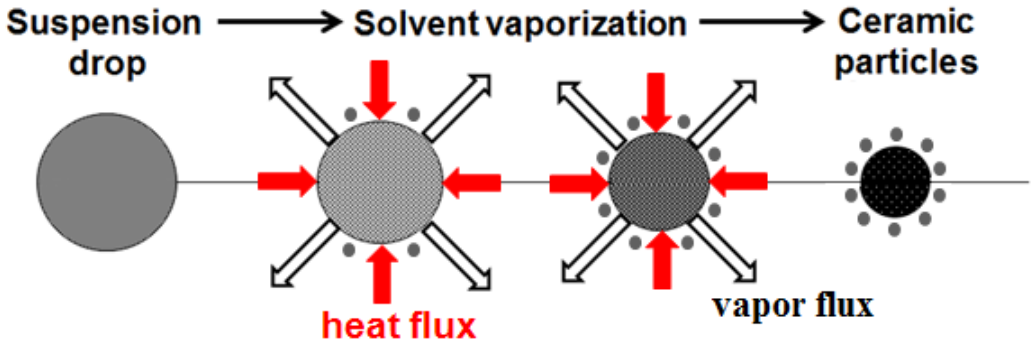

Figure 3.28: Schematic of suspension treatment by modulated plasma jet.

To estimate the vaporization time of the suspension in the plasma jet, certain assumptions have to be made. The diameter of the solid particle is determined as follows:

$$d_s = d_l\Big[1 + \frac{1 - x_m}{x_m}\frac{\rho_s}{\rho_{solvent}}\Big]^{-1/3} \tag{3.10}$$

where:

d_l	is the diameter of the suspension droplet,
x_m	the mass fraction of the ceramic,
ρ_s	the solid density,
$\rho_{solvent}$	the solvent density.

The thermal power transferred to a sphere of radius, r, is evaluated from the heat transfer coefficient by convection, h_c, as follows:

$$\Phi_{th} = h_c(T - T_l).4\pi r^2 \tag{3.11}$$

where:

T	is the plasma temperature,
T_l	the temperature at the surface of the liquid,
h_c	the heat transfer coefficient given by : $h_c = \frac{Nu.\kappa}{d_l}$.

Introducing the enthalpy, h, and the heat capacity, c_p, to Equation 3.11, the thermal power is presented as follows:

$$\Phi_{th} = \frac{(Nu.\kappa)(h - h_l).4\pi r^2}{c_p.d_l} \tag{3.12}$$

where:

h	is the plasma specific enthalpy, which can be determined by torch energy balance measurements or more locally from the temperature measurement by the emission spectroscopy,
h_l	the plasma enthalpy at the temperature of the droplet, which is much lower than h.

κ/c_p is, in fact, the ratio of the conduction potential, $\varphi(T) = \int_{T_{ref}}^{T} \kappa(T)dT$ (defined in chapter 1), to specific enthalpy, $h = \int_{T_{ref}}^{T} c_p(T)dT$. Using the thermodynamic and transport properties of N_2, it can be shown, from a numerical point of view, that it gives: $\varphi(T) \simeq a_\varphi h(T)$, where a_φ is the coefficient determined in the model in chapter 1. For the nitrogen and the enthalpy range of the plasma produced in "Mosquito" mode, $a_\varphi = 2.8\ 10^{-4}$ kg.m^{-1}.s^{-1}.

Knowing that $d_l = 2r$, the heat flux is given by:

$$\Phi_{th} = (Nu.a_\phi)h.2\pi r \tag{3.13}$$

During the vaporization phase of the solvent, the droplet diameter decreases from d_l to d_s. Considering the latent heat of vaporization of the solvent, Lv, and the liquid density, $\rho_{solvent}$, the decrease of the radius, r, due to the vaporization requires the energy as follows:

$$dE = 4\pi r^2 dr.\rho_{solvent}.L_v \tag{3.14}$$

what is given for the period of time dt by the heat flux Φ_{th} so that:

$$4\pi r^2 dr.\rho_{solvent}.L_v = -(Nu.a_\phi)h.2\pi r dt \tag{3.15}$$

Introducing the vaporization time, for which the solvent has disappeared completely ($r=d_s/2$) and knowing that this process starts at $t=0$ with $r=d_l/2$, it gives the following formula:

$$d_l{}^2 - d_s{}^2 = \frac{4Nu.a_\phi.h}{\rho_{solvent}.L_v} t_{vap} \tag{3.16}$$

Taking into account the mass fraction of the ceramic, x_m, the vaporization time is given as follows:

$$t_{vap} = \frac{\rho_{solvent}.L_v}{4Nu.a_\phi}\left[1 - (1 + \frac{1 - x_m}{x_m}\frac{\rho_s}{\rho_{solvent}})^{-2/3}\right]\frac{d_l{}^2}{h_p} \tag{3.17}$$

The factor $\left[1 - (1 + \frac{1-x_m}{x_m}\frac{\rho_s}{\rho_{solvent}})^{-2/3}\right]$ is in the range between 0.73, for the mass fraction, x_m, of 0.4 and $\rho_s/\rho_{solvent}$ of 4, and 0.85 for the mass fraction of 0.2.

Moreover, Equation (3.17) highlights that the vaporization time depends on the square of the diameter of the initial suspension droplet and the plasma specific enthalpy, h. For the specific enthalpy of 1.4 MJ/kg and the diameter, d_g, of 50 μm the vaporization time equals 1.4 ms (for $x_m = 0.4$) or 1.65 ms (for $x_m = 0.2$). For the specific enthalpy of 26 MJ/kg, t_{vap} equals, respectively, 77 μs and 90 μs.

The calculation of t_{vap} highlights that the choice of the injection time delay can have an effect on solvent vaporization, what is verified by Figure 3.24. The obtained results by pulsed laminar plasma jet show the possibility of control of material injection into different zones of modulated plasma. This can allow controlling some of the thermo-physical processes occurring at the droplet scale, such as the evaporation.

III Time-resolved spectroscopy

The following section presents the last part of the experimental setup given in Figure 3.1, described in the introduction to this chapter. The measurements performed by the time-resolved optical emission spectroscopy, presented in Figure 3.29, will be highlighted.

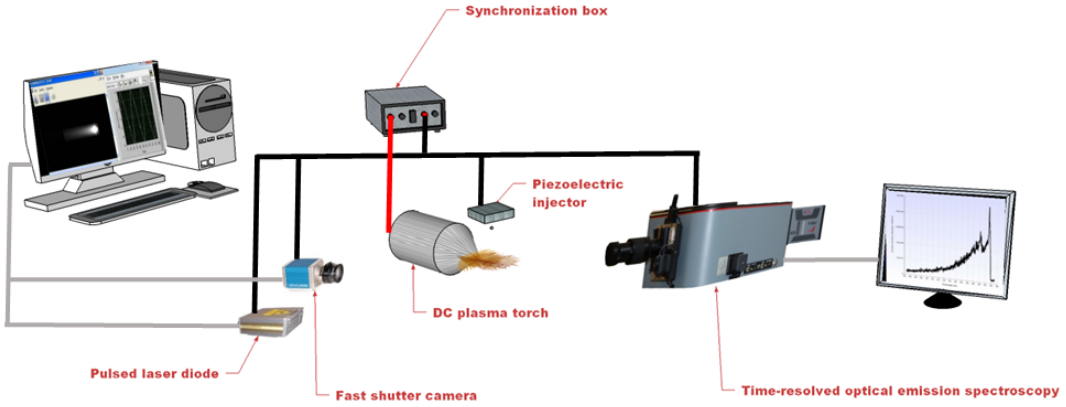

Figure 3.29: Schematic view of the experimental setup with added time-resolved optical emission spectroscopy.

The previous paragraphs have shown that the pulsed plasma jet is characterized by the specific enthalpy strongly modulated, what has been demonstrated by the results obtained from the energy balance measurements. To determine in more precise and local way this modulation the plasma temperature measurements have to be performed. However, in the case of plasma, the direct diagnosis of the temperature, e.g. by the thermometer, are often impossible. Among all available techniques the optical emission spectroscopy has been chosen, what will be presented in the following sections.
Moreover, the diagnosis of modulated plasma, produced by a "Mosquitorch", requires the method which allows to study the plasma in synchronized dynamic way. Therefore, the plasma temperature measurements have been carried out by time-resolved optical emission spectroscopy (TROES).
The following section will give the approach to the optical emission spectroscopy as the measurement technique of the gas temperature. Therefore, firstly, the preparation of the experimental setup to the measurements will be presented. The calibration of the system of the wavelength and intensity axis will be highlighted. Then, to determine the gas temperature the $N_2(C^3\Pi_u - B^3\Pi_g)$ system (the second positive system of nitrogen) or $N_2{}^+(B^2\sum_u^+ - X^2\sum_g^+)$ system (the first negative system of nitrogen) have to be defined. Consequently, the investigation of the species in the pulsed plasma produced by the "Mosquitorch" have been performed. All given above procedures have leaded to the gas temperature measurements. The use of the spectrograph working at medium spatial resolution permits to obtain reliable measurements of the rotational temperatures because

they are performed with a wide spatial range of the excited states, what will be presented in the following paragraphs.

III.1 Fundamentals of TROES

The following section will be focused on a merely part of the broad subject of the optical emission spectroscopy. The essential information about the fundamentals of the spectroscopic measurements, which has been studied for the gas temperature measurements, will be highlighted.
In the emission spectroscopy the light emitted from the plasma is recorded and analyzed. The total energy emitted through the surface of the plasma as the electromagnetic radiation is defined as a radiant flux, Φ (W), presented in Figure 3.30.

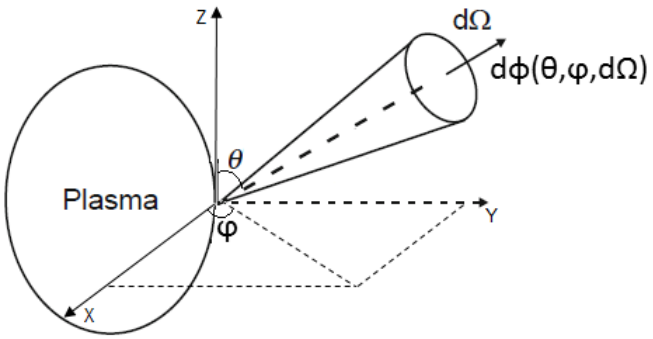

Figure 3.30: Definition of the radiance [84].

The radiant intensity, I ($W.sr^{-1}$), is the flux per solid angle emitted from the plasma:

$$I(\theta,\phi) = \frac{d\Phi(\theta,\phi,d\Omega)}{d\Omega} \tag{3.18}$$

where:

Ω is the solid angle, defined in Figure 3.30.

The radiance, L, at the position $\overrightarrow{r}$, is the intensity radiated per unit area dA ($W.m^{-2}.sr^{-1}$). Therefore, it is the energy flow radiated by an unit area per unit solid angle determined as follows:

$$L(\theta,\phi) = \frac{I(\theta,\phi)}{dA.cos\theta_A} = \frac{d^2\Phi(\theta,\phi,d\Omega_A)}{d\Omega_A\ dA\ cos\theta_A} \tag{3.19}$$

where:

dA is the surface element.

In the spectral measurements the radiance is defined as emitted at the wavelength, dλ, therefore the spectral radiance is determined as follows:

$$L_\lambda(\theta,\phi) = \frac{dL(\theta,\phi)}{d\lambda} \tag{3.20}$$

Moreover, the local emission, $\varepsilon(\theta,\phi)$, has to be defined. It is the intensity emitted by the plasma in a given direction and unit volume ($W.m^{-3}.sr^{-1}$), determined as follows:

$$\varepsilon(\theta,\phi) = \frac{I(\theta,\phi)}{dV} = \frac{d^2\Phi(\theta,\phi,d\Omega)}{d\Omega\, dV} \tag{3.21}$$

In the spectral measurements the emission coefficient, ε, of the line should be defined. The spectral line is emitted when a bound electron undergoes a transition from an upper level (p) of energy E(p) to a lower level (q). With each transition a photon is emitted, and ε of the line thus is given by:

$$\varepsilon_{p\to q} = \frac{hc}{4\pi\lambda_0}\, n(p)\, A_{p\to q} \tag{3.22}$$

where:

$A_{p\to q}$ is the characteristic atomic constant for that specific transition and known as as atomic transition probability (unit s^{-1}) or Einstein coefficient of spontaneous emission,

n (p) the population density of the excited level p.

The quantity that is recorded by the spectrometer is the result of the light emitted all along the line of sight (assuming that the absorption is neglected). The absolute line intensity (unit $(m^3s)^{-1}$) is defined as follows:

$$I^{(y)}{}_{p\to q} = \int_{line\ of\ sight} \varepsilon_{p\to q}\,(x,y)\,dx \tag{3.23}$$

where y is the height of the line of sight above the plasma axis. $I_{p\to q}$ is the intensity of the spectral line, which has the same unit that L. If the dependence of the intensity with the wavelength is needed, it is possible to introduce the spectral profile, $I(\lambda)$, so that:

$$I_{p\to q}(\lambda,y) = I_{p\to q}(y).\Phi(\lambda) \tag{3.24}$$

where: $\int_{\Delta\lambda} \Phi(\lambda)\, d\lambda = 1$

The molecular spectra are characterized by the complex structure: the states due to electronic excitation as well as the ground state, conventionally known as the X state, are split into vibrational levels, and these again into rotational ones. Figure 3.31 highlights the partial energy level diagram for N_2, N_2^+ and N_2^- states versus their internuclear distance (R).

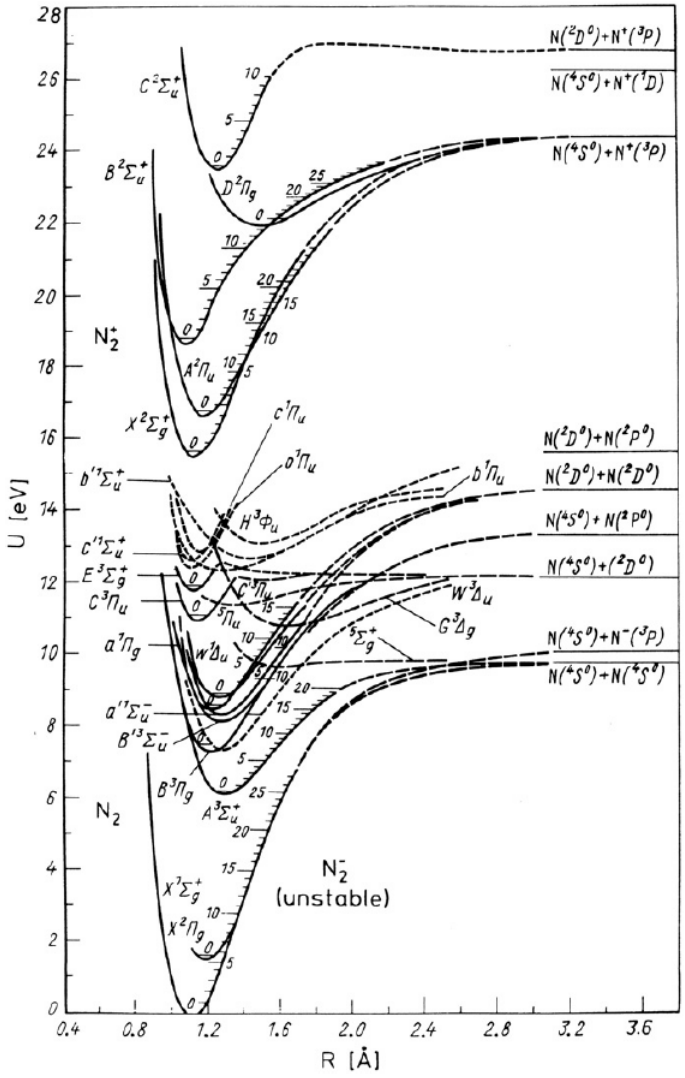

Figure 3.31: Diagram of potential energy curves of N_2 molecular state [85].

As can be seen in Figure 3.31 the electronic energy levels are defined by e.g. $X^2\sum_g^+$, $B^3\Pi_g$, $B^2\sum_u^+$. The electronic energy levels of atoms, 3.25, and diatomic molecules, 3.26, have their spectroscopic notation, as follows:

$$n\ell^{W\,2S+1}L_{L+S} \tag{3.25}$$

$$n\ell^{W\,2S+1}\Lambda_{\Lambda+\sum_{g,u}^{+,-}} \tag{3.26}$$

where:

n	is the main quantum number,
ℓ	the angular momentum,
w	the number of electrons in the shell,
S	the spin,
2S+1	the multiplicity,
L+S = J	the total angular momentum,
+, - and g, u	the symmetry of the electronic wave function.

The optically allowed transitions follow the selection rules for dipole transitions which can be summarized as: ΔL = 0, $\pm$1, ΔJ = 0, $\pm$1, ΔS = 0 for atoms and Δ L = 0, u $\leftrightarrow$ g for molecules.

As has been mentioned above, the molecular electronic levels are divided into vibrational and rotational ones, with the transitions occurring between pairs of these levels. Each level is specified by its electronic state (e), vibrational (v) and rotational quantum number (J). The internal energy of a molecule in this so-called rovibronic level (e,v,J) is given by [86]:

$$T_{evJ} = T_e + G_v + F_J \tag{3.27}$$

Therefore, considering the transition from upper rovibronic level $(\mathrm{e}', \mathrm{v}', \mathrm{J}')$ to lower level $(\mathrm{e}'', \mathrm{v}'', \mathrm{J}'')$ the spectral emission coefficient can be determined, following the equation (3.22), by:

$$\varepsilon(\nu) = n_{e'v'J'}\,\frac{A_{e'v'J'-e''v''J''}}{4\pi}\,(T_{e'v'J'} - T_{e''v''J''})\,\Phi(\nu-\nu_0) \tag{3.28}$$

where:

$n_{e'v'J'}$	is the population of the upper level,
$A_{e'v'J'-e''v''J''}$	the Einstein coefficient for spontaneous emission, defined above,
$T_{e'v'J'} - T_{e''v''J''}$	the energies of the upper and lower levels respectively, defined as follows: $T_{e'v'J'} - T_{e''v''J''} = h\nu_0 \simeq h\nu$,
$\Phi(\nu-\nu_0)$	the lineshape function.

The population $\mathrm{n_{e'v'J'}}$ of the upper state in the further experiments will be assumed as Boltzmann distributed. Therefore, the following relation presents the calculation of $\mathrm{n_{e'v'J'}}$ described by a Boltzmann distribution, as follows:

$$n_{e'v'J'} = n_{total}\frac{g_{e'}\,(2J'+1)\,exp\Big[-\frac{T_{e'}}{kT_{el}}-\frac{G(v')}{kT_{vib}}-\frac{F(J')}{kT_{rot}}\Big]}{\sigma\sum_{e,v,J} g_e\,(2J+1)\,exp\Big[-\frac{T_e}{kT_{el}}-\frac{G(v)}{kT_{vib}}-\frac{F(J)}{kT_{rot}}\Big]}L(J', P'_{ef}, P'_{gu}) \quad (3.29)$$

It assumes that the internal levels follow Boltzmann distribution at T_{el}, T_{vib} and T_{rot}. n_{total} defines the total population of the molecule, $L(J', P'_{ef}, P'_{gu})$ the line alternation factor due to nuclear spin defined in e.g. [87]. σ is a factor equals 2 for homonuclear molecules and 1 for heteronuclear molecules, $g_{e'}$ is the degeneracy of the electronic level defined as follows: $g_{e'} = (2 - \delta_{0,\Lambda'})\,(2S+1)$.

III.2 Experimental setup

The spectroscopic measurements have been carried out by the IsoPlane spectrograph (Princeton Instruments, Trenton, New Jersey), presented in Figure 3.32.

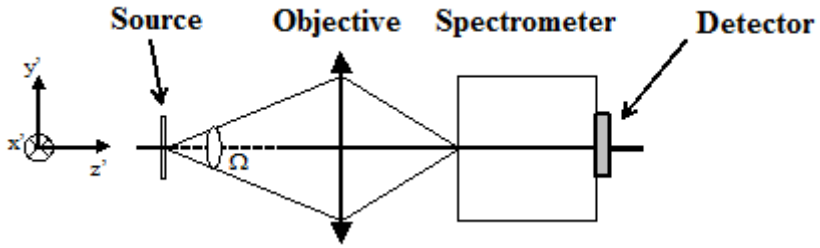

Figure 3.32: Schematic view of the emission spectroscopy system.

The objective consists of the quartz lens, characterized by the transmission > 80% from 200 to 1100 nm. The detector, Figure 3.32, is PI-MAX4 ICCD camera (Princeton Instruments) mounted directly at the image plane of the spectrograph exit. The pixel size influences the spectral resolution of the system. Therefore, the camera characterized by the imaging array of 1024 × 1024 and the pixel size of 13 × 13 μm has been chosen. Moreover, the connection to the computer allows controlling the measurements by LigthField software and recording the spectra. LightField permits to regulate the following acquisition settings which define the response of the ICCD detector:

- Exposure time, τ_{exp}
  The length of time between the beginning and the end of the acquisition sent by LightField to the camera, defining the exposure time of the sensor.

- Number of accumulations, N_{acc}
  The number of times on which the photocathode is gated during the exposure. The charge is accumulated on CCD array when these gates occur during the exposure and then is readout at the end of it.

- Gate width, τ_{width}
  The time during which light is detected by an intensifier, strengthened, and applied to the sensor.

- Gain, G
  The determination of the amount of electron multiplication that is applied to improve the signal.

IsoPlane spectrograph (SCT 320, 320 mm focal length) consists of: the entrance and exit slit, the grating as the dispersive element, the imaging mirrors. The choice of the spectrometer grating, which is determined by the grooves per millimeter (lines/mm) is of importance for the spectral resolution and to determine the wavelength range of the spectral measurement. The fundamental grating equation is defined as follows:

$$m\lambda = d(sin\alpha + sin\beta) \tag{3.30}$$

where:

m	is the diffraction order,
d	the groove spacing,
α	the angle at which the beam of parallel radiation incident on the grating,
β	the angle of the spectral line.

The IsoPlane spectrograph is equipped with 300, 1200 and 2400 g/mm gratings. Figure 3.33 presents the principle of the spectroscopic measurement by the system used in this work. The image of the plasma is formed with a negative magnification (the result of image inversion) on the spectrometer entrance slit, characterized by the width, w_e, which can be changed from 10 μs up to 12 mm to give the possibility to perform imaging with PIMAX camera. Then, the spectrometer forms the monochromatic image, centered around λ_1 with the magnification of 1, in the detector plane. As has been mentioned above, the detector is composed of the imaging array of 1024 $\times$ 1024 with the pixel size of 13 $\times$ 13 μm, what can be grouped into lines of height, Δy_p, by the Lightfield function called binning. The "enlightened" area on the detector, in Figure 3.33, presents the plasma surface of $w'_e.\Delta y'$.

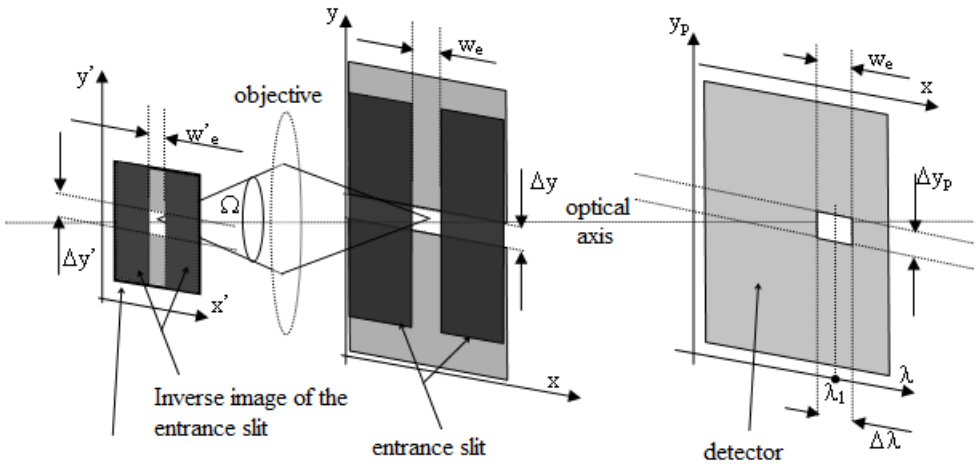

Figure 3.33: Schematic view of the image formation by the spectroscopy system.

III.2.1 Calibration

The important issue of the spectroscopic measurement is the calibration of the system. To obtain precise information about plasma parameters the calibration of the wavelength and intensity axis have been performed. In the case of wavelength axis the calibration has been done by recording spectra of a source with known wavelengths. The USB Light Source (Princeton Instruments, Trenton, New Jersey) has been used which consists of Hg and Ne-Ar lamps with well-defined atomic emission lines presented in Figure 3.34.

The mercury and neon-argon lamps have been used because of their wide wavelength range which covers the lines of nitrogen plasma and the plasma-suspension interaction. In case of the calibration of the intensity axis, a standard radiator of known radiance, L_0, is placed close to the spectrometer entrance slit to fill the solid angle, Ω. Then, the flux, $\Phi_\lambda(\lambda)\Delta\lambda = L_{0\lambda}(\lambda)\Delta\lambda A_s\Omega$, over a spectral interval, $\Delta\lambda$, produces a signal S_0 at the exit of a detector. Keeping all settings constant, the respective flux in the same spectral interval from the plasma gives the signal, S_{plasma}. Therefore, the radiance of plasma is given by:

$$L_{plasma_\lambda}(\lambda) = \frac{S_{plasma}}{S_0} L_{0\lambda} \tag{3.31}$$

In the calibration process the tungsten strip lamp has been applied. It is the most commonly used secondary standard source, in which a strip of tungsten is mounted in a glass envelope with a window of fused silica, characterized by the transmission coefficient, α_T, around 0.9. The parameters of the tungsten lamp are commonly given by the constructor. However, these standard radiators age, therefore, to obtain precise spectrometer calibration it has been calibrated in the laboratory by the pyrometer.

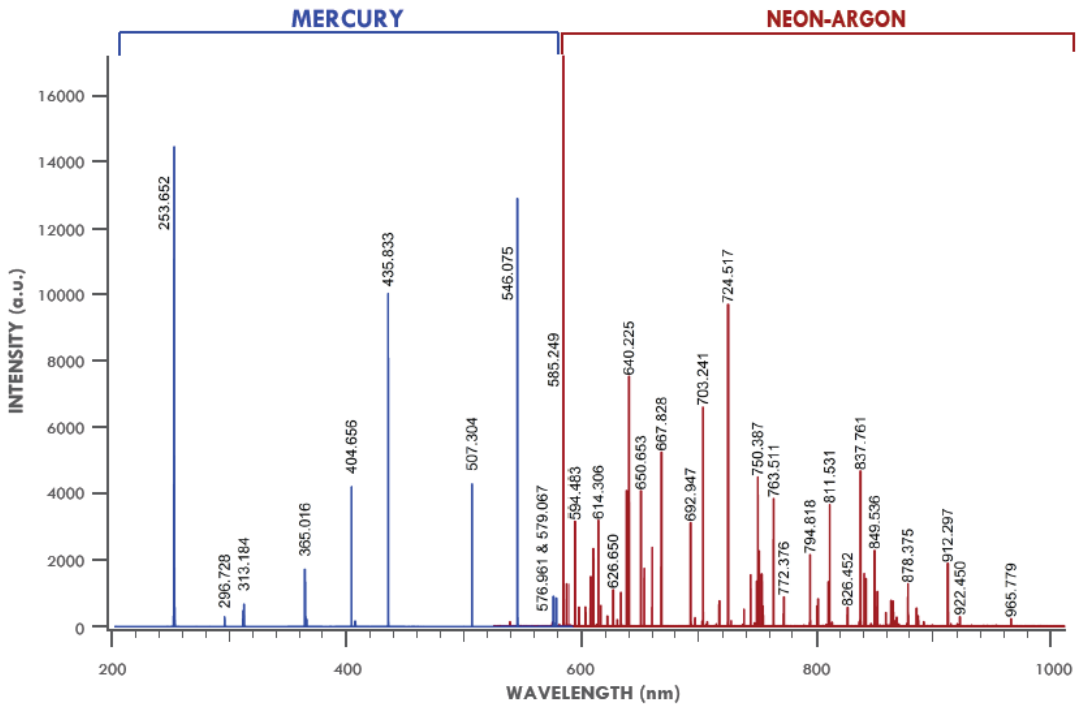

Figure 3.34: Wavelength calibration spectra of mercury and neon-argon lamps.

The lamp has been power supplied by a stabilized source. The current, presented in Figure 3.35, has been measured using a precision shunt.

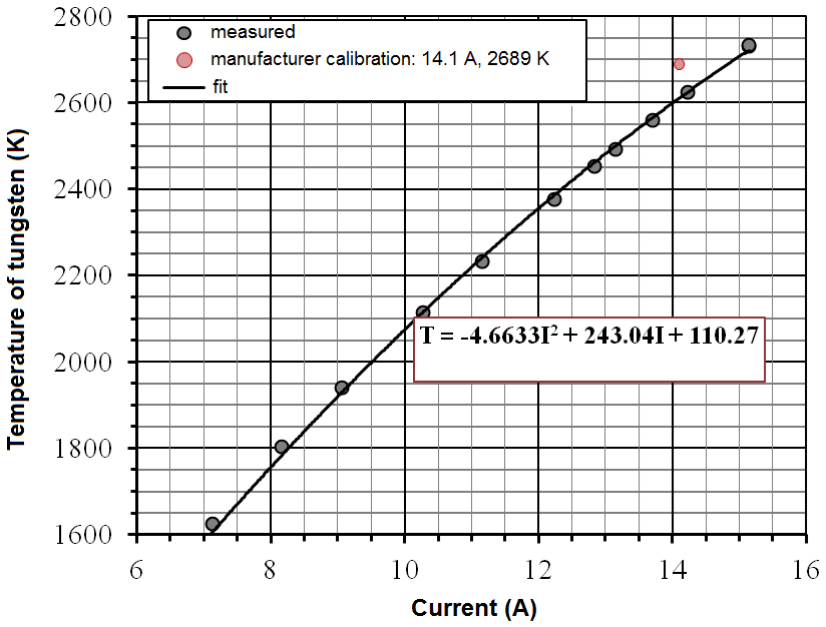

Figure 3.35: Calibration curve of tungsten strip lamp.

Afterwards, the spectral radiance of the tungsten strip lamp, $L_0(\lambda, T)$, has been obtained by multiplying the Planck function with the spectral emissivity of tungsten, $\varepsilon_0(\lambda, T)$, as follows:

$$L_0(\lambda, T) = \varepsilon_0(\lambda, T)\frac{2hc^2}{\lambda^5}\frac{1}{exp(\frac{hc}{\lambda kT}) - 1} \tag{3.32}$$

$\varepsilon_0(\lambda, T)$ has been determined from the data given by De Vos [88]. The calibration procedure have been carried out for the parameters of the spectrometer and detector given in Table 3.6.

Table 3.6: Parameters of the spectroscopy system.

Slit width	w_e	10 μm- 12 mm		
Grating	g/mm	300	1200	2400
Reciprocal dispersion	D_λ(nm/mm)	9.854	2.334	1.017
Central wavelengthl	$\lambda_{central}$ (nm)	378	378	378
Gain	G	1-100		
Effective gain	G_{eff}	f(G) measured experimentally		
Gate width time	τ_{width}	1 μs- a few ms		
Number of accumulations	N_{acc}	1 - hundreds		
Exposure time	τ_{exp}	$\tau_{exp} = \tau_{width}.N_{acc}$		
Line height (in pixels)	Δy_p			
Readout rate		2 or 8 MHz		

The above listed parameters have allowed to determine the coefficient $a(\lambda, T)$ given by the following equation:

$$a(\lambda, T) = \frac{S_0(\lambda, T)}{w_e.G_{eff}.\tau_{exp}.\Delta y_p.\alpha_T.L_0(\lambda, T)} \tag{3.33}$$

It highlights that the sensitivity calibration of a spectrographic system has been done for the complete system, not separately for the individual components. $a(\lambda, T)$ has been obtained by the averaging of 21 spectra in case of the measurements for readout rate of 2 MHz and 15 spectra for 8 MHz. Then, $a(\lambda, T)$ has been estimated by the regression analysis, as follows:

$$E = \sum_{\lambda_i}\left({L_0}^G(\lambda_i) - b\frac{{L_0}^{G_{ref}}(\lambda_i)}{G_{ref}}\right)^2 = 0 \tag{3.34}$$

where:

${L_0}^G(\lambda_i)$	is the spectral radiance of the tungsten strip lamp for given gain, G, and wavelength, λ ,
G_{ref}	the referential gain,
b	the estimated constant.

The presented Equation 3.34 is determined for the measurements obtained for variable gain, G. The same procedure has been applied to the results obtained for the following parameters: τ_{exp}, w_e. Figure 3.36 presents the measured exposure time, τ_{exp}, in a function of the theoretical τ_{exp}. It highlights the linear response of the ICCD detector.

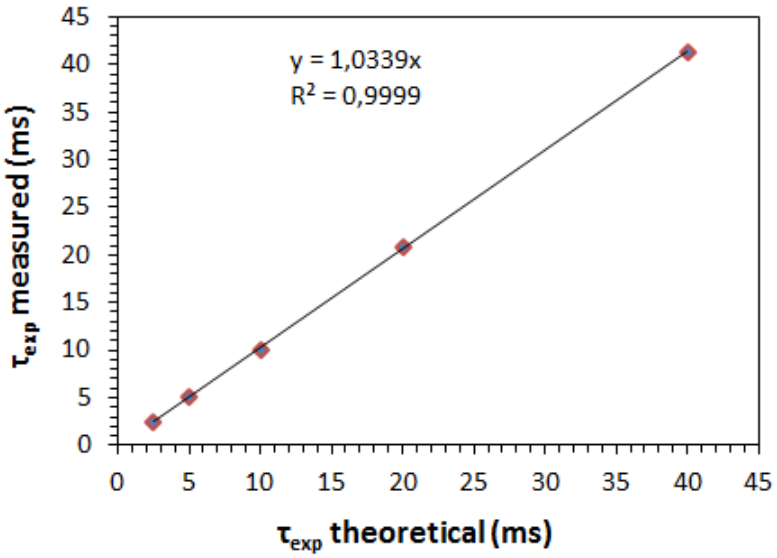

Figure 3.36: Calibration curve measured for variable exposure time τ_{exp}.

The same characteristics have been obtained for the slit width, w_e, and the gain. The calculation of the coefficient $a(\lambda, T)$ has allowed to define the calibrated radiance of plasma given by:

$$L_{plasma}(\lambda, T) = \frac{S_{plasma}(\lambda, T)}{a(\lambda, T)} \frac{1}{w_e{}'.G_{eff}{}'.\tau_{exp}{}'.\Delta y_p{}'} \tag{3.35}$$

where $w_e{}', G_{eff}{}', \tau_{exp}{}', \Delta y_p{}'$ are parameters of the system for the plasma spectroscopic measurement.

III.3 Investigation of the plasma species

To determine the plasma temperature, the optical emission spectroscopy has to be applied to examine the species of the pulsed plasma jet produced by the "Mosquitorch". The pure nitrogen (N_2 2 slm) has been used as plasma forming gas, therefore, the spectroscopic studies have been focused on the identification of N_2 molecular emissions. In the previous paragraphs the partial energy level diagram based on the data of Gilmore *et al.* for N_2, $N_2{}^+$ and $N_2{}^-$ states versus their internuclear distance (R) in Figure 3.31 has been presented.

The use of this diagram allows to determine the following transitions in the nitrogen plasma:

- $N_2(C-B)$
  The $N_2(C^3\Pi_u - B^3\Pi_g)$ system (the second positive system of nitrogen) with the vibrational branches ranged between 280 and 500 nm, where the head of the (0,0) vibrational transition is at 337 nm. The second positive system is often responsible for the dominant emission in air or N_2-containing plasmas.

- $N_2{}^+(B-X)$
  The $N_2{}^+(B^2\sum_u^+ - X^2\sum_g^+)$ system (the first negative system of nitrogen) is often observed in air and nitrogen-containing ionizing plasma. The (0,0) vibrational transition is usually the strongest band, observed at 391.4 nm. The rotational lines of this system are often used to determine the rotational and vibrational temperatures of the plasma, as presented in [89, 90]. Therefore, initially, this system will be chosen to define the plasma temperature in the following experiments.

Figure 3.37 highlights the identification of the emission features in the plasma produced by the "Mosquitorch".

The spectra have been obtained by non-time-resolved acquisition, choosing the gate width time, τ_{width}, of 7 ms which is equal to 10 periods, T, of the pulsed plasma jet (T of 700 μs), what results in the average spectra of the modulated plasma. To determine a broad wavelength range of the spectra 300 g/mm gratings and the slit width of 75 μm have been chosen. Moreover, the function "step and glue" provided by LightField software has been used, what allows to measure large wavelength ranges. By this function the broad measurement range is divided to the series. After the acquisition of the particular spectral sequence, the grating moves to measure the other series and, then, the spectral measurements are glued together to create a single spectrum. It has to be mentioned that the intensity of the spectra has been normalized in order to compare the measurements.

The spectra have been obtained for different distances from the nozzle exit, where 0 mm corresponds to the exit of the torch. The analysis of the species performed by Speciar software and presented in Figure 3.37 highlights that the plasma jet from 0 to 10 mm contains mainly the transitions: $N_2(C-B)$ and $N_2{}^+(B-X)$. It has to be mentioned that the second positive system of N_2 and the first negative system of $N_2{}^+$ are frequently observed simultaneously. Moreover, at the nozzle exit the spectrum contains the atomic lines of nitrogen, what can be explained by the flow of N_2 plasma forming gas. In the spectrum measured in 10 mm CN violet system ($B^2\sum^+ - X^2\sum^+$) at 388 nm has been observed, what demonstrates the mixing of the plasma jet with the surrounding air that contains the trace of CO_2.

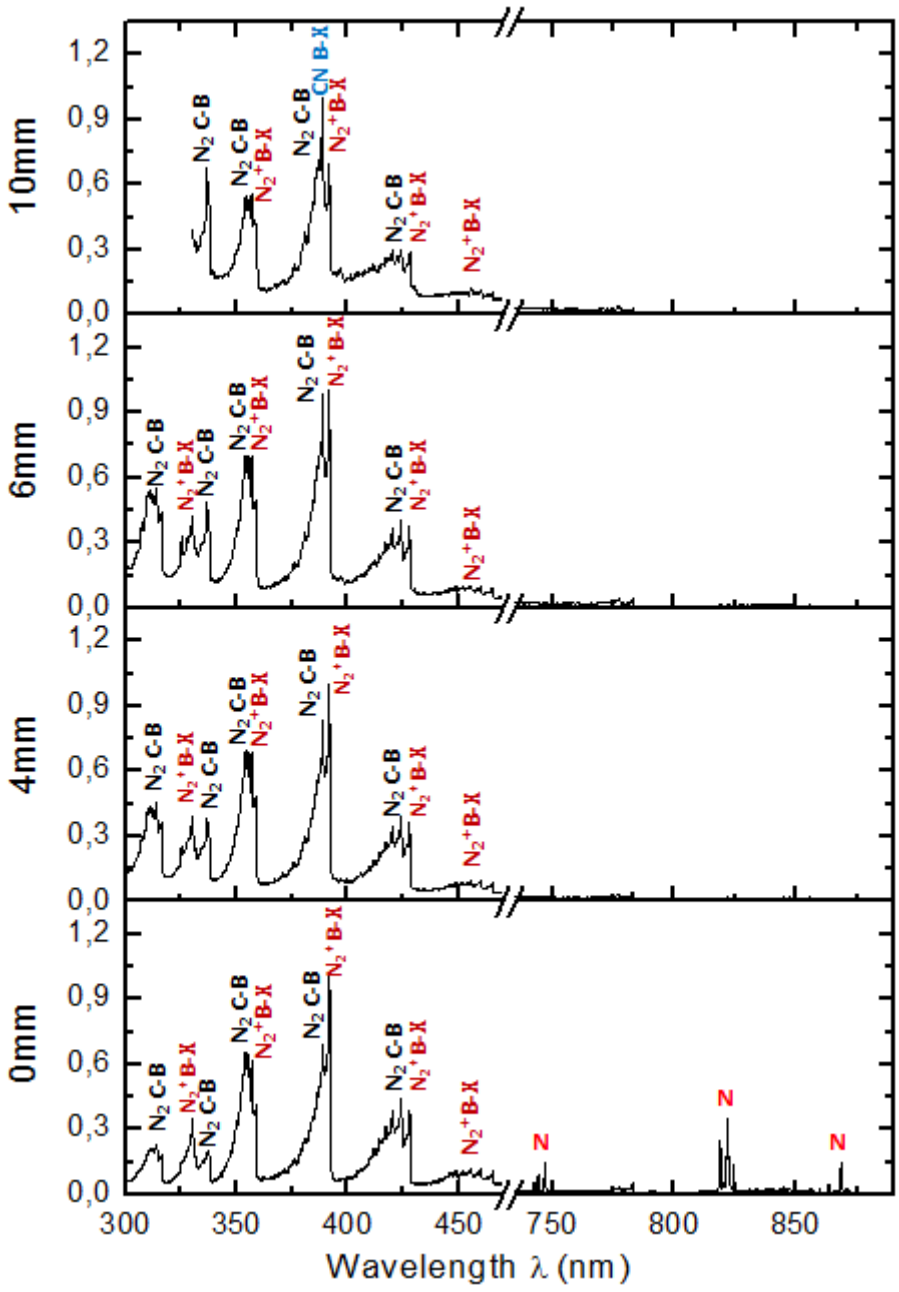

Figure 3.37: Identification of the plasma emission spectra in the range of 300 to 900 nm measured in different distances from the nozzle exit, where 0 mm corresponds to the exit of the torch.

Moreover, at the distance of 10 mm the spectrum range has been reduced due to significant atomic line of Cu at 324 nm.

The obtained results have confirmed the choice of using the nitrogen first negative system to measure temperature of the plasma up to the distance of 6 mm.

III.4 Temperature measurements

As has been highlighted in the previous paragraphs the time-resolved optical emission spectroscopy has been applied in a newly developed system of the suspension phased injection in pulsed arc jet to determine the temperature of the modulated plasma. The gas temperature measurements are mainly obtained by emission spectroscopy from the population distribution in rotational levels, what is generally close to the kinetic gas temperature as presented in [89–92]. The previously highlighted investigation of the plasma species has shown the possibility of the use of the first negative $B^2\sum_u^+ - X^2\sum_g^+$ system of $N_2{}^+$.

Therefore, the spectral measurements have been focused on $N_2{}^+(B^2\sum_u^+ - X^2\sum_g^+)$ system, which is a blue-degraded system with a head band at 391.4 nm. The 1200 g/mm grating has been used with the slit width of 300 μm corresponding to around 0.7 nm spatial resolution. The gate width, τ_{width}, has been regulated to 60 μs. Considering the plasma velocity of $\sim$ 50m.s^{-1}, the plasma moves only by 3 mm during the time of 60 μs. Smaller values of τ_{width} have resulted in the increase of On-CCD accumulation number, N_{acc}, and also on the increase of the signal/noise ratio. Therefore, the compromise has to be found between the exposure time, i.e. the signal/noise ratio and the temporal window during which the plasma is observed for measurement with frozen properties.

III.4.1 Spectral simulations

In the frame of this thesis, the measured spectra have been analysed by Specair. It is a commercial software developed to simulate the radiative, molecular and atomic transitions in air plasma, including N_2 (second positive system), $N_2{}^+$ (first negative system), CN (violet system). Specair assumes that the rotational states are Boltzmann distributed at T_{rot} , defined by the equation (3.29). According to Bruggeman *et al.*, this condition is fulfilled if N_2 effective lifetime of the excited state, τ_{eff}, is longer than N_2 time of thermalization, τ_{therm} [91]. The latter can be evaluated by calculating the elastic collision frequency of $N_2{}^+$ and assuming about 10 collisions to reach the thermalization. In the range of expected temperature, $\tau_{\text{therm}} \simeq 10$ ns. The time τ_{eff} is defined as follows:

$$\tau_{eff} \simeq \frac{1}{\sum_v A_{Xv'}^{Bv'}} \tag{3.36}$$

where $A_{Xv'}^{Bv'}$ is the transition probability between $B^2\sum_u^+$ and $X^2\sum_g^+$ states of $N_2{}^+$ for the $\Delta v = 0$ vibrational bands, which can be found in [93]. It has been found that $\tau_{\text{eff}} \simeq 80$ ns.

Consequently, in the following measurements the Boltzmann distribution will be assumed and also $T_{gas} = T_{rot}$.

To define the rotational temperature, T_{rot}, the theoretical spectrum has to be simulated by Specair and compared to the measured one. This procedure consists of several stages. Firstly, the background subtraction has to be implemented. It is the method which minimizes the noise in the spectral measurements and thus makes small peaks more visible. The noise can be caused by the plasma continuum radiation or the dark current (background current that flows in a CCD camera system). Figure 3.38 presents two spectra of (N_2^+) first negative system: spectrum before the background subtraction (in red) and after that.

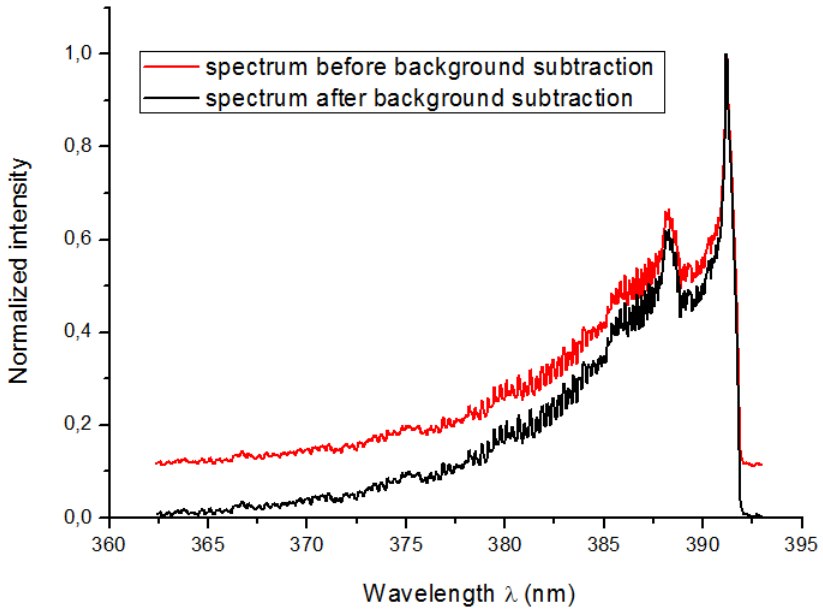

Figure 3.38: Effect of the background subtraction.

It can be noticed that the noise of the background is determined on the level of around 0.1. The background subtraction plays an important role in the intensity calibration procedure, where this noise signal can be magnified and deform spectral measurement, because the calibration function $a(\lambda, T)$ depends on λ. Therefore, during calibration procedure the background has been subtracted from the measurements. Moreover, it can be noticed that the obtained spectra have been normalized to a maximum value of 1 by Specair software due to different intensity levels. This procedure permits to compare the spectra.

The spectra presented in Figure 3.38 have been obtained before the calibration of the system of the wavelength axis. Therefore, they had to be also corrected in x (wavelength) scale. This procedure permits to recalculate the measured data in order to compare with other spectra or to define the unknown transitions in a spectrum by the Specair database.

Moreover, wavelength corrections are necessary to optimize the fitting of experimental spectra.
As has been presented above to obtain precise information about the plasma parameters as the gas temperature the calibration of the wavelength and intensity axis have to be performed.

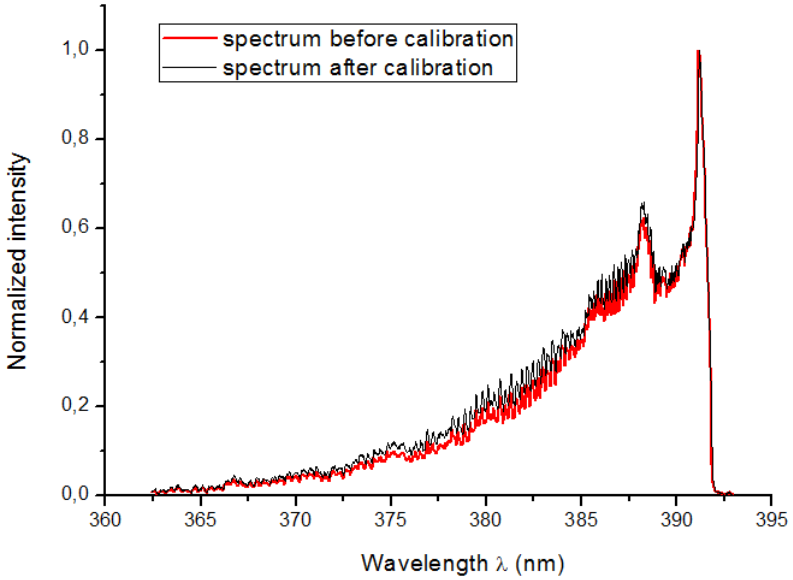

Figure 3.39: Effect of the calibration.

Figure 3.39 presents two measured spectra of (N_2^+) first negative system: spectrum before implying the calibration procedure (in red) and after that. As can be noticed the intensity levels of the rotational lines are lower in the case of non-calibrated spectrum. It has resulted in the difference of the temperature measurements: 7500 K defined for the spectrum obtained by the calibrated system and 6800 K measured in the case of the second spectrum. Therefore, it highlights that the calibration procedure has the importance in the spectral measurements.
The important parameter in the spectral simulation by Specair software is the determination of the instrumental function which defines the resolution of the collected data. The slit function represents the broadening caused by the spectrometer (slit width, pixel width, grating dispersion). The measured spectrum, $I_{measure}$, is the result of the convolution of the real emitted radiance, I_{plasma}, and the slit function SL as presented by the relation: $I_{measure}(\lambda) = \int_0^\infty I_{plasma}(\xi)\ SL\ (\lambda - \xi)\ d\xi$. To ameliorate the accuracy of the spectral measurements, two different slit functions have been chosen: the trapezoidal function, proposed in the literature [84,94] and presented in Figure 3.40, and the function determined by measuring Hg lamp at 404.7 nm.

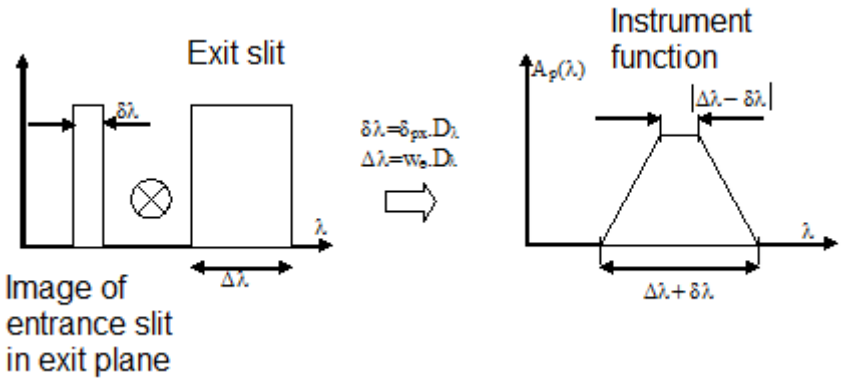

Figure 3.40: Slit function of the spectroscopy system.

Figure 3.40 illustrates the procedure of the determination of the trapezoidal slit function. The spectral width of the exit slit is presented as $\Delta\lambda$ and the width of the image of entrance slit in exit plane as $\delta\lambda$. It should be assumed that the width of the exit slit should be larger than $\delta\lambda$ in order to not lose any flux. While scanning the exit slit across the spectral image a trapezoidal shape of the recorded line is obtained, what represents the slit function for given settings of entrance and exit slits.

To compare the accuracy of spectrum fitting by Specair software, the alternative slit function has been determined by recording the line profile of the emission from a low-pressure Hg lamp at the wavelength of 404.7 nm, presented in Figure 3.41. It allows to obtain the slit function in good approximation due to a small line width of the lamp ($\sim$ 1 pm FWHM).

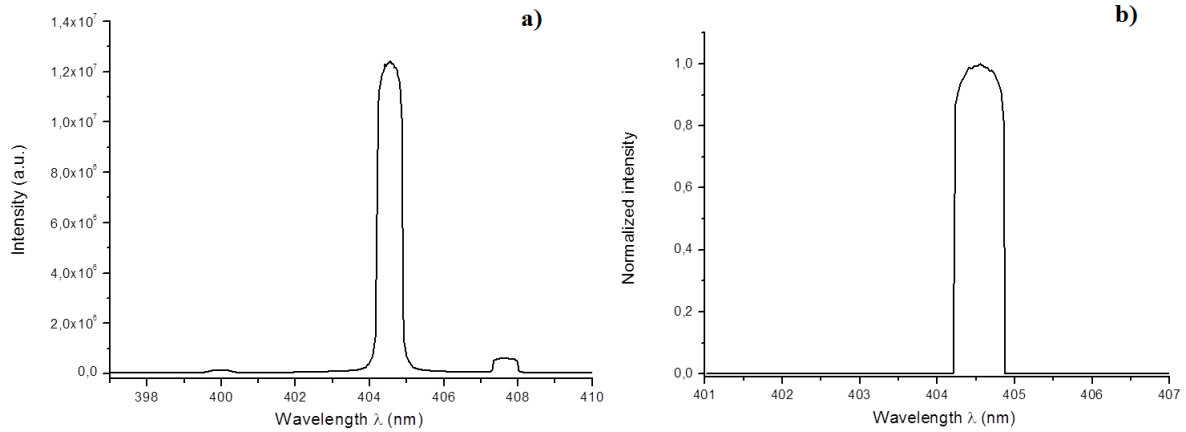

Figure 3.41: Slit function determined by measuring Hg lamp: a) measured spectrum, b) normalized spectrum to avoid the artifacts ($w_e = 300\ \mu$m).

The measured spectrum, 3.41 a), has been normalized to the format given by Specair software, 3.41 b), to avoid the artifacts of the spectrum fitting. To ameliorate the accuracy, recorded line profile has been fitted to the rotational spectrum of the measured (N_2^+) first negative spectrum, presented in Figure 3.42.

Bruggeman *et al.* have shown that for a broad slit opening the trapezoidal instrumental function should be considered and for a small entrance slit the recorded line shape can be approximated by a measured function [91].

As has been mentioned the presented above spectra have been measured with a spectral slit width, w_e, of 300. Therefore, the trapezoidal instrumental function has been applied in the Specair simulations.

The apply of all procedure mentioned above permits to determine the rotational temperature of the plasma by numerical optimization routines provided by Specair software which lead to the adjustment of measured spectrum to that simulated by Specair. Figure 3.42 presents the comparison between the measured and simulated (N_2^+) first negative spectra.

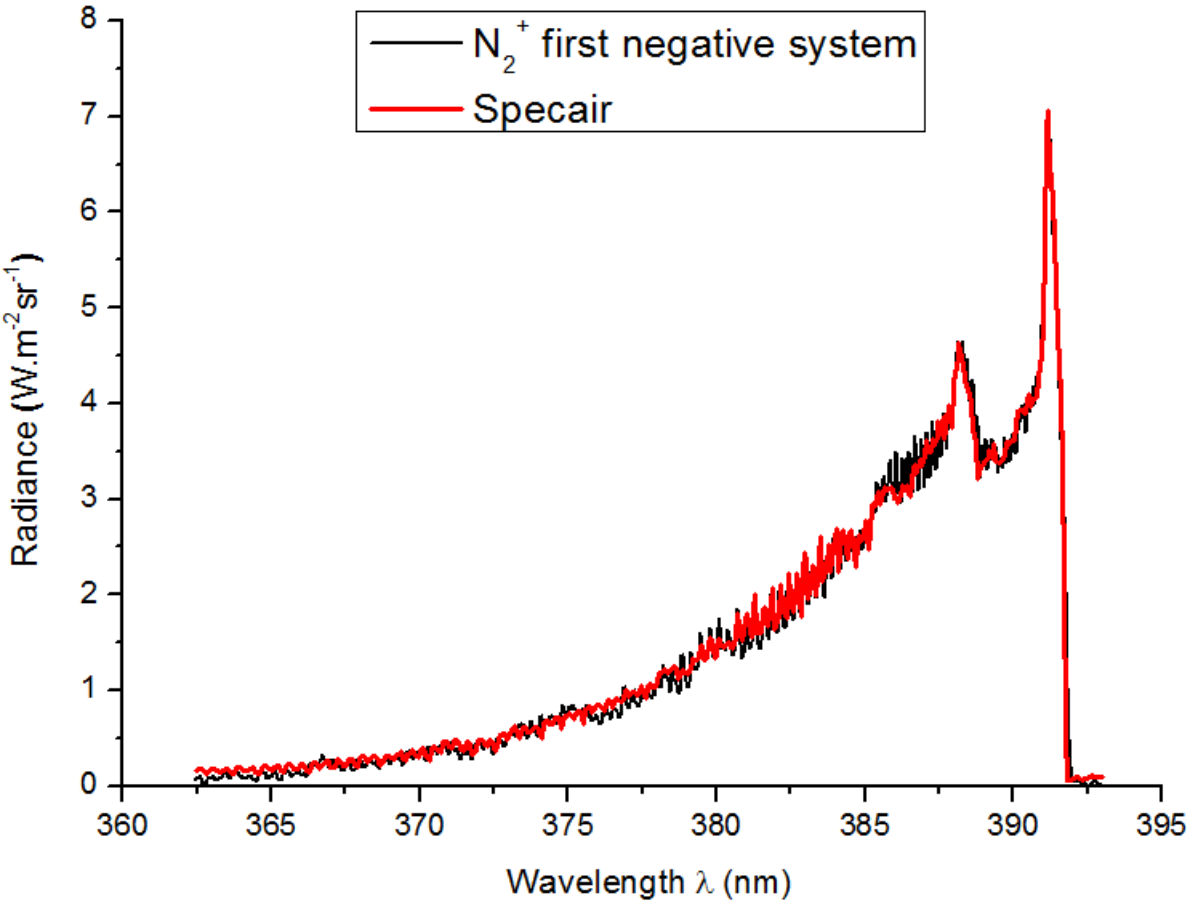

Figure 3.42: Comparison of the measured and simulated by Specair software (N_2^+) first negative spectra.

As can be observed, a good agreement between these two spectra has been obtained. This best correspondence of the simulated spectrum to that experimental provides the rotational temperature. All presented experimental procedures and simulations allow to precisely determine the temperature of the pulsed plasma jet, what will be highlighted in the following section.

III.4.1.1 Determination of the temperature of pulsed plasma jet

As has been shown in the previous paragraphs the time-resolved optical emission spectroscopy is used to determine the temperature of the pulsed plasma jet, characterized by high modulation of the specific enthalpy. To verify the temperatures of different stages of this modulated plasma, the time-resolved spectroscopy measurements have to be synchronized with the arc voltage signal, what is presented in Figure 3.43.

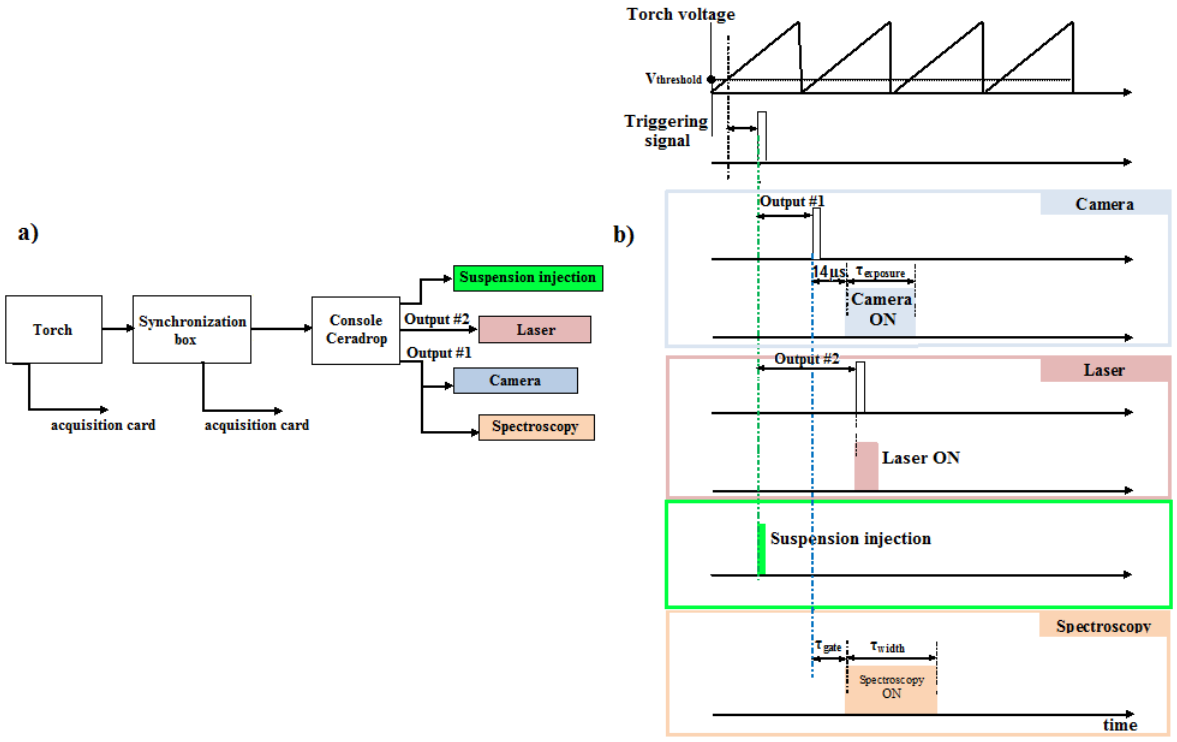

Figure 3.43: Schematic view of the synchronous time-resolved spectroscopy procedure: a) the experimental setup, b) the timing diagram.

The spectrograph has been connected to the output 1 of Ceradrop platform. The synchronization procedure is similar to this one of time-resolved imaging and suspension injection. The TTL signal formed from the arc voltage is sent to Ceradrop console which activates the spectroscopic measurements. The spectrograph is synchronized with the camera by adjusting the delay time, τ_{gate}, to 14 μs.

To verify the temperatures of different stages of the modulated plasma, four moments presented in Figure 3.44 have been chosen. The triggering signals have been formed from the arc voltage and sent to camera and TROES, as presented above, in order to obtain the synchronized measurements.

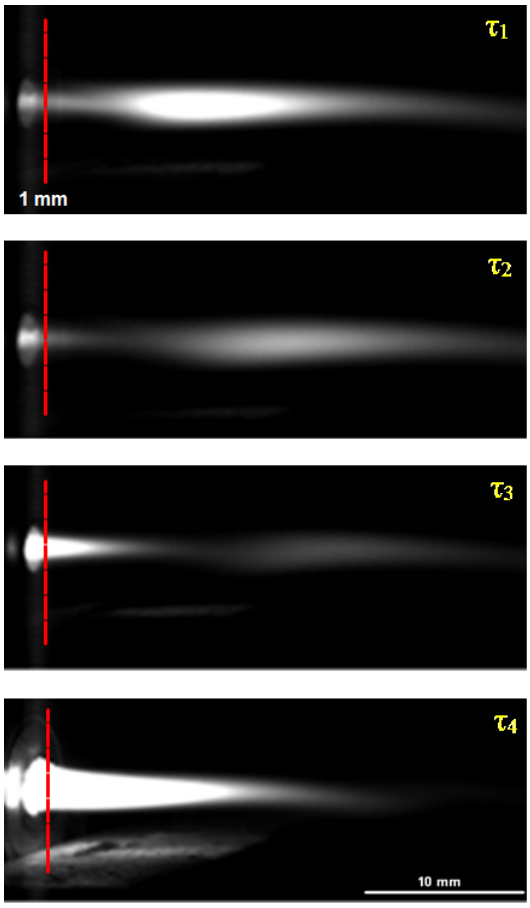

Figure 3.44: Time-resolved imaging of the spectral measured moments of the pulsed plasma jet: τ_1 to τ_4. The spectra obtained 1 mm from the nozzle exit, marked on the photos.

The trigger time delays in one plasma period, τ_1 to τ_4, have been adjusted by the synchronization box. The generated TTL signals have been sent to the camera and the spectrograph. Moreover, they have been recorded by LabView software, what is given in Figure 3.45. These measurements highlight that the moment of the pulsed plasma, τ_4, corresponds to the maximum voltage signal, $U_{max}(t) = 100$ V. In the comparison, τ_1 is obtained at $U(t) \simeq 60$ V.

The measured spectra, presented in Figure 3.46, have been processed by Specair software, by applying the procedures mentioned above, to obtain the plasma temperatures, indicated in Figure 3.46.

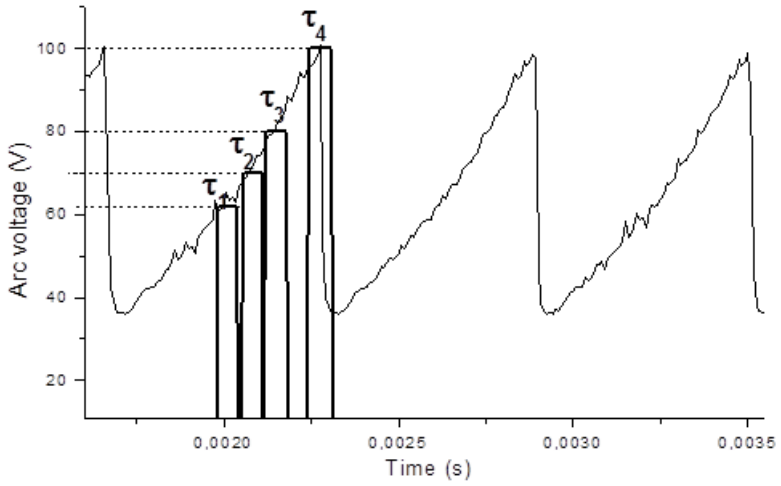

Figure 3.45: The trigger signals, τ_1 to τ_4, of the pulsed plasma moments presented in Figure 3.44, sent to the Time-Resolved Optical Emission Spectroscopy.

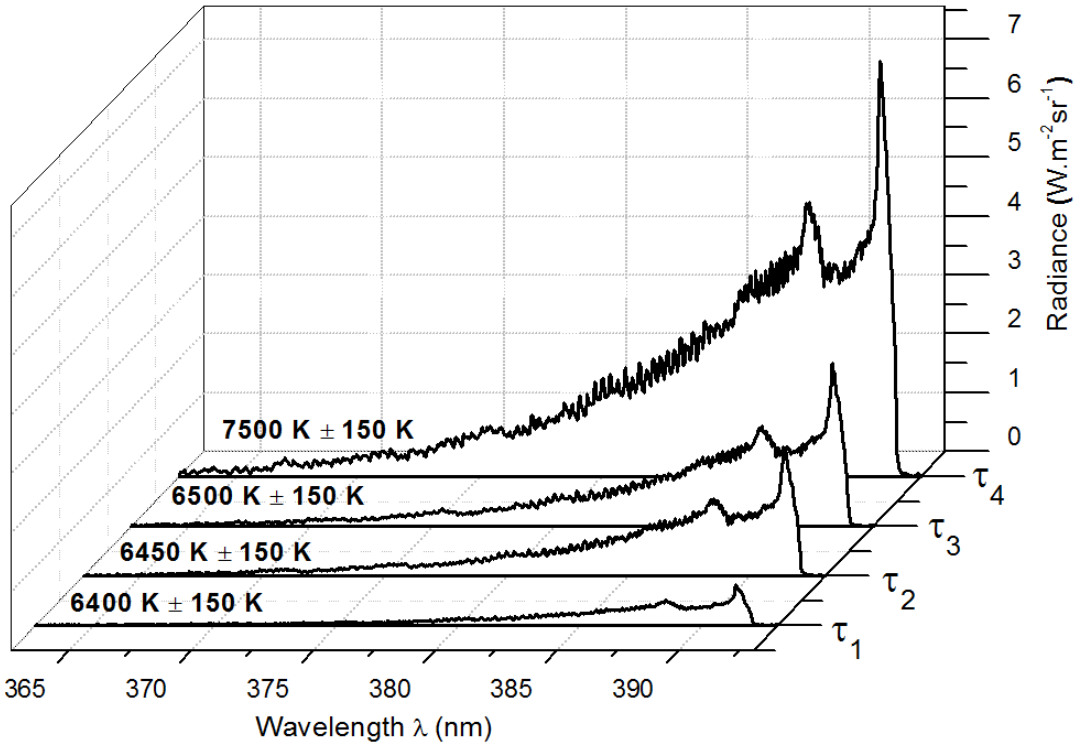

Figure 3.46: (N_2^+) first negative spectra for four different moments, τ_1 to τ_4 of the periodic arc voltage.

Analyzing the N_2^+ first negative system, it can be observed that the spectrum measured in the moment τ_4 is characterized by the highest value of the intensity comparing to the spectra obtained at τ_1 to τ_3.

The spectroscopic estimation of the rotational temperature highlights that the gas temperature increases from 6400 K ± 150 K to 7500 K ± 150 K by changing the moment of a periodic arc voltage, as is presented in Figure 3.46. The obtained results can be compare

with the data of the specific enthalpy of the nitrogen plasma given in [17] and gathered in Figure 3.47. The region distinguished in the figure corresponds to the dissociation of N_2 molecule resulting in a steep change of the enthalpy in a small range of temperature.

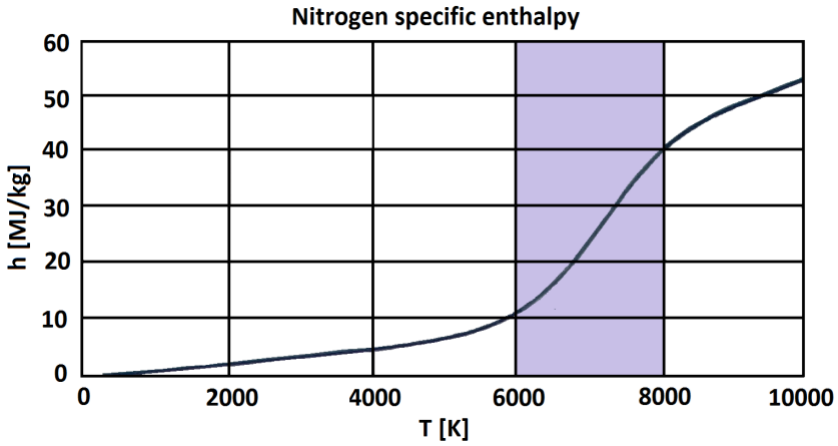

Figure 3.47: The nitrogen specific enthalpy based from the data given in [17].

The comparison of the obtained results with the nitrogen enthalpy data, shown in Figure 3.47, highlights that the plasma jet analyzed at the moment τ_4 is characterized by the enthalpy value of 35 $\pm$ 3 MJ/kg. To compare, at the moment τ_1 the enthalpy is of 15 $\pm$ 2 MJ/kg. It proves experimentally that the pulsed plasma jet is characterized by the enthalpy and the temperature modulated. However, the ratio of the enthalpy modulation $h_{\tau_4}/h_{\tau_1} \simeq 2.3$ obtained in this experiment is much lower than that presented in the previous section, $h_{max}/h_{min} \simeq 18$, determined by the energy balance measurements and the hypothesis about constant thermal voltage (36 V). This significant difference has led to the conclusion that the enthalpy modulation ratio of around 18 is overestimated because the thermal losses are not constant. The assumption of the fluctuating thermal losses has given the estimated ratio h_{max}/h_{min} of around 2.

Moreover, the presented method to determine the plasma temperature has encountered the difficulties in the spectroscopic measurements of the moment of the pulsed plasma jet, which corresponds to $U_{min}(t) \simeq 40$ V. This instant of the jet is characterized by a weak plasma radiation, therefore the precise determination of the rotational temperature, in this case, following N_2^+ negative system is not relevant.

Furthermore, it has to be mentioned that despite the setup calibration and the determination of the instrumental function procedures, the errors in the temperature measurements have occurred, what is indicated in Figure 3.46. To improve the measurements, the researchers apply the Abel inversion technique to obtain radially resolved emission profile, from which the temperature profile can be deduced. However, this method requires the assumptions that the plasma jet is optically thin and it is

characterized by the axial symmetry. The results obtained by the pulsed plasma jet have highlighted that this kind of plasma does not meet these assumptions. As Tanaka and *et al.* have shown in this case the Abel inversion is not useful because can engender the higher error [95]. Moreover, the errors in the temperature measurements, highlighted above, do not influence significantly on the determination of the specific enthalpy.

As has been already mentioned, the purpose of plasma spraying is the production of the coatings. Therefore, the material injected to the plasma torch has to be melted, what requires the heat transfer. The following measurements have been performed to define the level of the enthalpy and the temperature of the plasma at the moment of the suspension injection to the plasma jet. Figure 3.48 indicates the location at which the suspension droplet is inserted, 5 mm. To compare the results the plasma has been also measured in the distance of 1 mm from the nozzle exit.

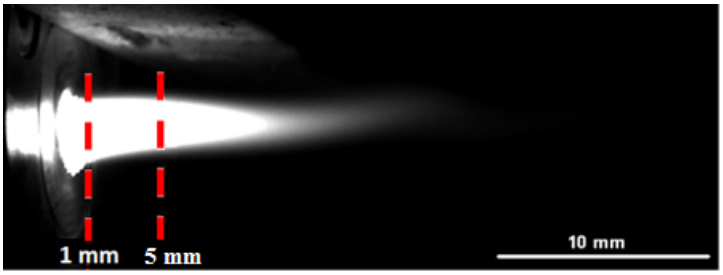

Figure 3.48: Time-resolved imaging of the spectral measured moment of the pulsed plasma jet, τ_4 in Figure 3.45. Two distances, 1 and 5 mm, from the torch exit indicated.

The same synchronization procedure, as mentioned above, has been applied. The moment of the pulsed plasma, which corresponds to the maximum voltage signal, $U_{max}(t)$ = 100 V, has been chosen.

Analyzing the obtained N_2^+ spectra, it can be observed that the spectrum measured in 1 mm is characterized by the higher value of the intensity than the spectrum detected in 5 mm.

It can be explained by analyzing the cross-section of the plasma jet in Figure 3.48. In the distance of 1 mm the radiance of the plasma is higher than in 5 mm. Moreover, the measured temperature decreases from 7500 K ± 150 K to 6900 K ± 150 K , when the distance from the torch nozzle exit increases. It results in the decrease of the enthalpy from 35 ± 3 MJ/kg to 23 ± 2 MJ/kg. However, the obtained enthalpy level is sufficient to obtain the material melted in this region of the plasma jet and to form the coatings, what will be presented in the next paragraph.

The presented sections have highlighted the possibility to use the time-resolved optical emission spectroscopy to measure the temperature of the pulsed plasma jet produced

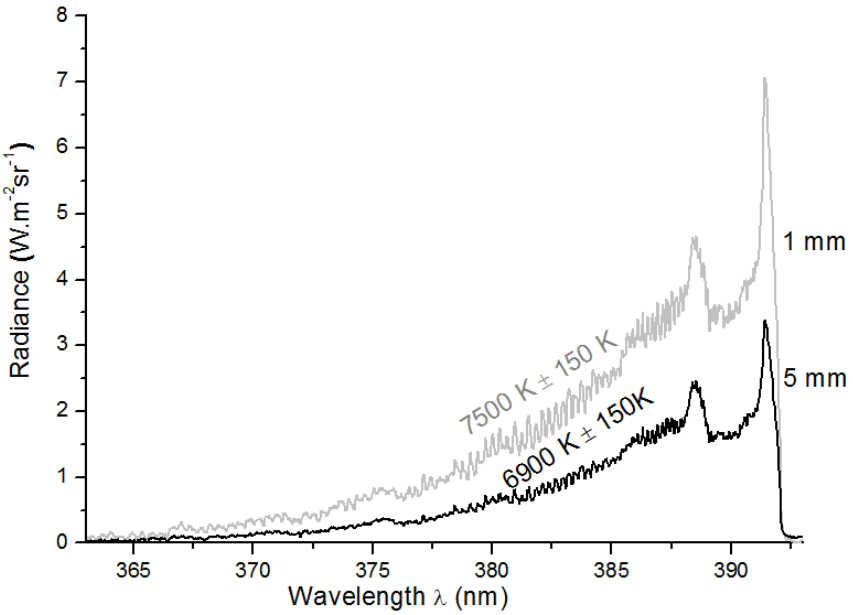

Figure 3.49: (N_2^+) first negative spectra measured at the distance of 1 mm and 5 mm from the nozzle exit.

by the "Mosquitorch". The results have highlighted that the careful choices of the experimental procedure and the spectral simulation process are the important parameters in the spectroscopic measurements. The selection of the system plays also the significant role in this type of the diagnosis. The use of the time-resolved optical emission spectroscopy has allowed synchronizing the system with the pulsed plasma jet what has resulted in the temperature measurements of different moments of this periodic plasma. Moreover, by analyzing the experimental results with the data of the nitrogen plasma it has been possible to obtain the local specific enthalpy of different moments of the plasma jet. The presented measurements have verified the high modulation of the specific enthalpy in the pulsed plasma. The following section will present the use of this periodic plasma to obtain the first coatings by a new system, the suspension phased injection in pulsed arc jet.

IV Material deposition

The following paragraph describes the first attempts to deposit the material by a new system, the suspension phased injection in pulsed arc jet.

In the conventional SPS method the spray parameters, as the plasma and suspension characteristics but also the spray distance, the substrate preparation and the substrate cooling, determine the properties of the obtained coatings. For several years, the researchers have been developing these parameters, what can be found in the large

number of works [3, 13, 14, 54, 96–98]. To obtain the first coatings by a new method it has been decided to follow the experimental conditions for the suspension plasma spraying. However, it can be noticed that the synchronized SPS with pulsed arc jet method differs from the conventional SPS process, what is presented in Table 3.7.

Table 3.7: Comparison of injection features for conventional SPS with the mechanical injection and the high power plasma torch ($\sim$ 35 kW) and for suspension phased injection with mosquitorch ($\sim$ 1 kW).

	Droplets diameter (μm)	Injection velocity (m.s^{-1})	Suspension flow rate ml.min^{-1})	Powder mass flow rate (g.min^{-1})
Conventional SPS	$\sim$ 300	$\sim$ 25	$\sim$ 20	$\sim$ 3
Synchronized SPS	50	3.26	5.6×10^{-3}	3.4×10^{-4}

The suspension is injected with lower velocity. Moreover, the suspension and powder mass flow rates are much smaller than in the conventional system using the mechanical injection. On the other hand, the Mosquitorch is supplied by much lower power than the conventional torch. It has to be mentioned that this low power plasma torch, combined with the pure nitrogen characterized by good properties in thermal transfers, is sufficient to treat the materials, as the previous results have highlighted. Therefore, the following spray parameters have been chosen:

- the spray distance of 32 mm from the torch exit
  The spray distance in the conventional plasma spraying using the powder is of around 100 mm. However, as Darut *et al.* have highlighted in the SPS method this parameter has to be drastically lowered to about 30 mm due to the significantly lower momentum and thermal inertia of the material particles [99].

- the substrate cooling
  The rotating sample holder has been chosen, what allows to avoid the overheating of the substrate. The linear speed of the holder has been regulated to 1 ms^{-1}, by analyzing the studies presented in [100, 101].

- the substrate preparation
  To collect the splats produced by SPS method the mirror-polished substrate is commonly used due to its low roughness. Therefore, the stainless steel substrates have been polished using water-cooled silicon carbide (SiC) papers with the grit sizes of 600, 1200, 2400 and 4000 μm. Than, the final mirror-like surface has been obtained by using the velvet polishing pad and colloidal silica. The substrates before the spraying process have been cleaned in the ethanol and dried with the argon stream.

To obtain the deposition of the material the aqueous suspension of TiO_2, described in

Table 3.2, has been used. In the experiments presented in the previous paragraphs the exact moment of the suspension emission synchronized with the periodic arc voltage signal has been studied. However, to obtain the coatings using the suspension phased injection in pulsed arc jet the moment of the suspension-plasma interaction has to be determined.

To protect the injector from the plasma heat flux it has been supported by a water-cooled screen and mounted in the distance of 5 mm from the plasma jet axis. Therefore, the time of the flight of suspension droplet from the injector to the plasma has to be defined. Knowing that the distance is 5 mm and taking into consideration the experimental result of the suspension droplet velocity equal to 3.26 $m.s^{-1}$, the material flight time, t_{flight}, is around 2 T, where T is the arc voltage period. The obtained results highlight that the suspension is treated by the plasma two periods after the suspension droplet emission.
The characterization of the deposited material is an important step in plasma spraying method to e.g. select the parameters of the process, improve the method. Therefore, to study these first obtained coatings the basic measurements of the structural characteristics have been performed. To observe the structure of the coating and the particles of the diameters $d > 1$ μm the optical microscopy has been used. To obtain the microctructure of the coating with better precision the Scanning Electron Microscopy (SEM) has been applied combined with Energy Dispersive Spectroscopy (EDS) which gives a spatially resolved compositional analysis of the coating. The following sections give the description of these methods and highlight the microstructure of the obtained splats.

IV.1 Optical microscopy

The optical microscopy examination allows for basic observations of the coatings structures. It should be a first instrument to be used for metallographic observations since it is faster and much less expensive than e.g. Scanning Electron Microscopy (SEM). Moreover, the optical microscopy compared to other techniques allows to observe large area of the sample. It is a type of microscope which uses visible light and a system of lenses to magnify images of small samples. In the frame of the thesis the coatings have been observed by polarizing microscope Eclipse LV 100 POL (Nikon, Japan) which permits to observe the samples with objective magnifications: 5x, 10x, 20x, 50x and 100x. One of the key parameters of the optical microscopy measurement is image contrast, which depends on the quality of the optics, coatings on lenses and reduction of flare and glare. The microscope Eclipse is equipped with a high intensity 50W halogen light source and a fly-eye lens design what gives brighter, clearer and higher contrast images.
The important parameter of optical microscopy is the image resolution which corresponds to the ability to see fine details, presented in Figure 3.50.

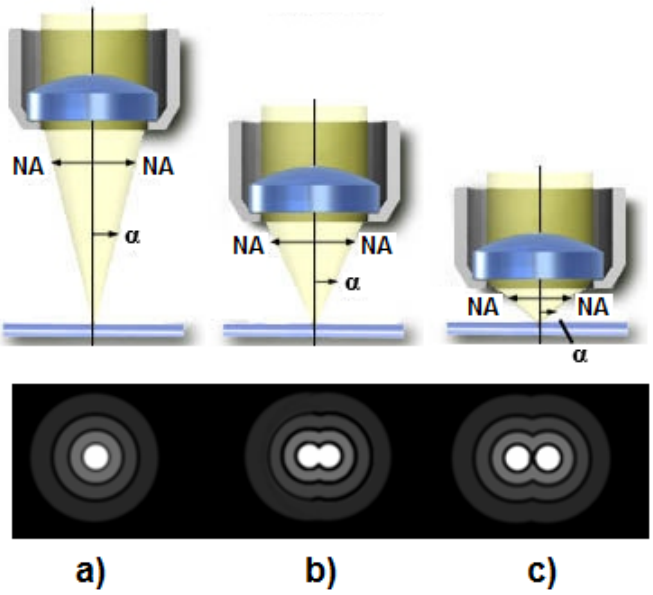

Figure 3.50: Resolving two adjacent points: a) $\alpha = 7°$, NA = 0.12, b) $\alpha = 20°$, NA = 0.34, c) $\alpha = 60°$, NA = 0.87.

It is defined by the smallest distance, r, between two points which can be resolved, as follows:

$$r = 1.22\frac{\lambda}{2NA_{obj}} \tag{3.37}$$

where:

λ	is the wavelength of the light,
NA_{obj}	the objective numerical aperture defined by equation:

$$NA_{obj} = n.sin\alpha \tag{3.38}$$

where:

α	is a half-cone angle of light half captured by the objective lens,
n	the lens refractive index.

The other important characteristic of optical microscopy is the depth of field, D, area in front of and behind the specimen that will be in acceptable focus. The depth of field is related to the wavelength of the light and to the numerical aperture (NA), as follows: $D = \lambda/NA^2$.

IV.2 Scanning electron microscope (SEM)

The Scanning Electron Microscopy is a method which uses electrons instead of light to form an image. The electron beam with an energy ranging from 0.5 to 40 keV is thermionically emitted from an electron gun, what is schematically presented in Figure 3.51. Then, the electron beam is focused by condenser lenses. In the final lens, the beam passes through pairs of scanning coils or deflector plates which deflect the beam in the x and y axes, what results in scanning over a rectangular area of the sample surface.

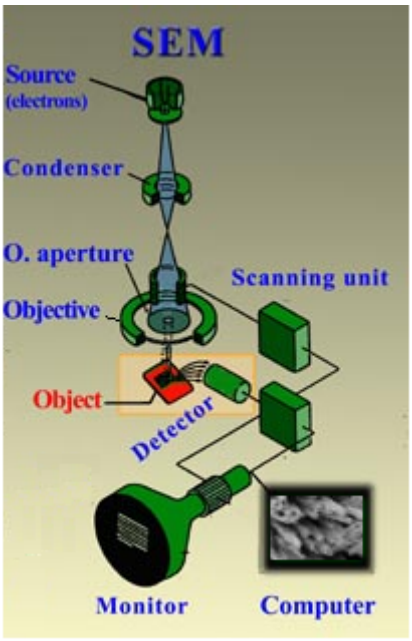

Figure 3.51: Schematic view of a Scanning Electron Microscope.

This electron beam carries significant amount of kinetic energy, what is dissipated as a variety of signals produced by electron-sample interactions. These signals include secondary electrons (which give SEM images), backscattered electrons (BSE), photons (X-rays which are used for elemental analysis, can be detected in SEM equipped with energy-dispersive X-ray spectroscopy), visible light (cathodoluminescence-CL)and heat. Secondary and backscattered electrons are commonly used for imaging the sample. Secondary electrons are most valuable for showing morphology and topography of the sample. Backscattered electrons are used for illustrating contrasts in composition in multiphase sample.

To characterize coatings produced in the frame of this thesis JEOL 7400F microscope has been used (JEOL, Tokyo, Japan). It is a scanning electron microscope equipped with a Cold Field Emission Gun (FEG). It is designed for the analysis of the physical and chemical microstructure of solid state materials at nanometer resolution (max. resolution: 1 nm). It additionally allows for spatially resolved compositional analysis by using the

PGT Energy Dispersive Spectroscopy (EDS).
As a consequence of the use of the vacuum conditions and electrons to form an image in SEM method, the samples have to be specially prepared. The metals as the conductive materials require no preparation before the measurement. All non-metal samples have to been covered by a thin layer of conductive material. The automatic sputter coater (Agar Scientific, Stansted, UK) has been used in the experiments to cover TiO_2 coatings with platinum.

IV.3 Microstructure of deposited material

The following section presents the first basic characterizations of the obtained coatings microstructures. The purpose of these studies is to verify the spraying parameters and develop the coatings deposition process.

The spray distance of 32 mm has been chosen by analyzing the results obtained by SPS method. Therefore, to verify this choice for synchronized SPS process this parameter has been increased to 42 mm.
Figure 3.52 shows the examination of the influence of the spray distance on the coatings microstructure. It has to be highlighted that it presents the basic study by the optical microscope.

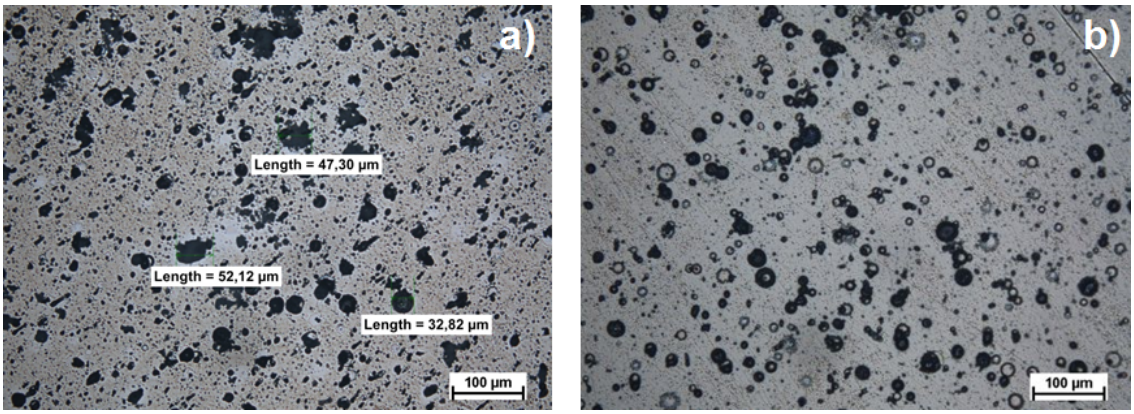

Figure 3.52: Microstructure of the coating obtained at the distance: a)32 mm, b)42 mm. The measurements performed by the optical microscope, using the objective magnification 20x.

The first photo, 3.52 a), gives the microstructure of the coating obtained at the distance of 32 mm. Figure 3.52 b) shows the results of increasing this spraying parameter to 42 mm. It has to be mentioned that both coatings have been produced by the injection of the suspension droplets at the moment of the pulsed plasma corresponding to maximum voltage signal. Figure 3.52 a) highlights that the coating is composed of two different zones: uniform light area which gives the impression of being fine and nanometric, the

dark elements of large sizes up to around 50 μm. The increase of the spraying distance to 42 mm, presented in Figure 3.52 b), mainly results in dark elements which have different structures than these ones presented in Figure 3.52 a). Moreover, the characteristic feature of the substrate surface can be observed, what means that the distance between the torch and the substrate is too long and the resolidified particles can be mainly observed. The obtained results highlight the importance of the choice of the spraying distance, which will be regulated to 32 mm in the following experiment.

In the previous experiment the suspension droplet has been emitted at the maximum level of the arc voltage signal. To determine the influence on the coatings formation of the different moments of the pulsed plasma jet, two cases have been chosen related to the spectroscopic measurements of the plasma: the suspension emission at the maximum level of the arc voltage signal, presented in Figure 3.44 as τ_4 and the medium level, indicated in Figure 3.44 as τ_1. Figure 3.53 presents the coatings characterizations performed by the optical microscope.

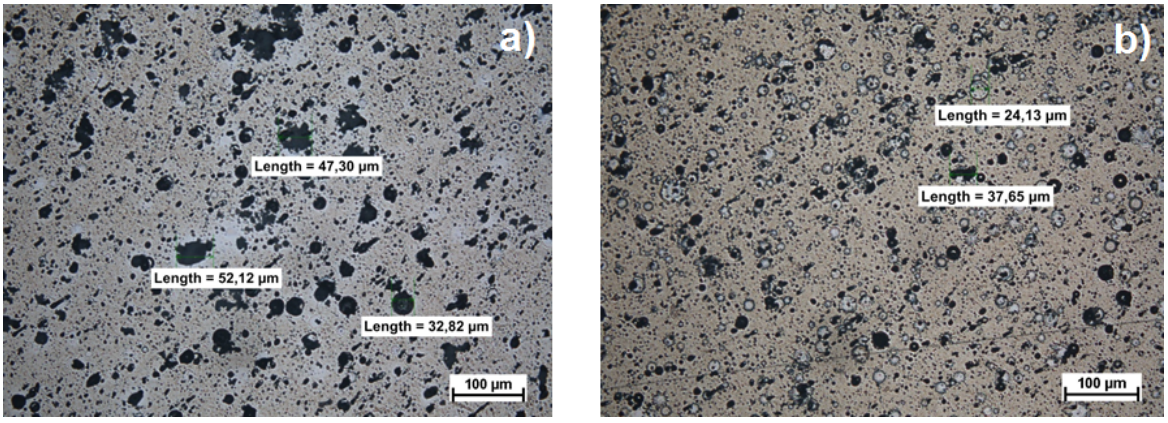

Figure 3.53: Microstructure of the coating obtained at the moment corresponding to: a) maximum voltage signal, b) medium level of arc voltage. The measurements performed by the optical microscope, using the objective magnification 20x.

It has to be mentioned that the injected suspension droplet at e.g. maximum voltage enters the plasma jet at maximum level of the signal as well but two periods later. Figure 3.53 a) presents the microstructure of the coating obtained at the maximum level of arc voltage and b) at the medium level. In the picture 3.53 a) and in smaller amount in b) it is possible to observe the dark structures with the diameters up to around 50 μm, what corresponds to the diameter of the injected droplet. Moreover, as the analysis of the particle size distribution has highlighted, the suspension used in the experiments has the peak of the particle size distribution curve centered on 66 nm (d_{50}) and the dispersion size ($d_{90} - d_{10}$) equal to 48 nm. Therefore, the obtained large micro-metric structures can be the result of the agglomeration of the particles and they have been examined by SEM microscopy. In both coatings microstructures the uniform light area which seems

to be nanometric can be found. Therefore, it has been measured by SEM microscopy as indicated in Figure 3.54.

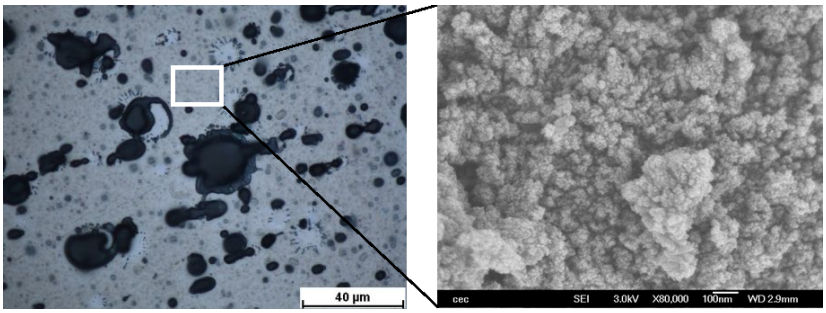

Figure 3.54: Coating obtained at the moment of maximum arc voltage, shown in Figure 3.53, measured by the optical microscope, using the objective magnification 100x, with the marked region measured by SEM and presented on the right.

The result obtained by the scanning electron microscopy measurement highlights that by using the suspension formulated of nano-sized powder particles it is possible to obtain the nano-sized layers of the coatings. However, the diameter of the particles composing this layer is much smaller than the size of TiO_2 powder in the suspension, what might be the result of the material vaporization. Moreover, the obtained layer is very thin. The energy dispersive spectroscopy (EDS) analysis presented the dominant quantity of nickel and chromium from the substrate than titanium from the coating.
In addition to this light zone in the coatings microstructures the dark elements have been found, what is indicated in Figure 3.55. Figure 3.55 presents the distinction of different features appeared in the coating produced at the maximum level of the arc voltage signal.

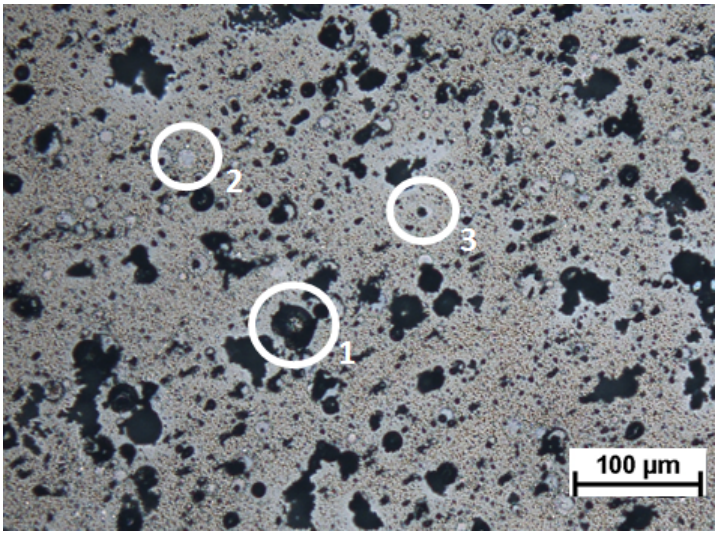

Figure 3.55: Coating obtained at the moment of maximal voltage signal, shown in Figure 3.53, measured by the optical microscope, using the objective magnification 100x, with the indicated features 1), 2), 3) and 4) measured by SEM.

Figure 3.56 shows the main structure appearing in the microstructure given in Figure 3.55. It has been highlighted in Figure 3.53 a) and b) that the diameters of these features are up to around 50 μm.

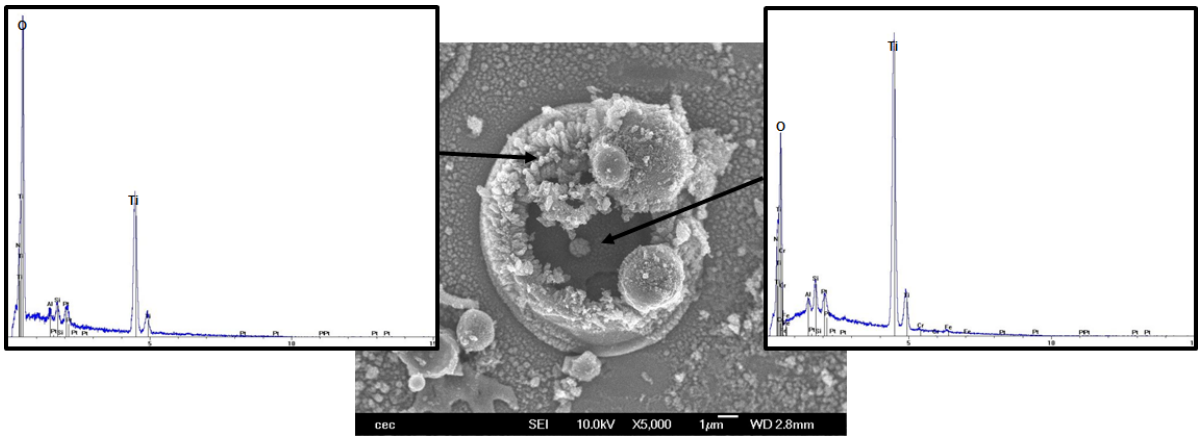

Figure 3.56: Feature 1) from Figure 3.55 measured by the scanning electron microscope and analyzed by EDS.

The measurement by SEM highlights that this structure contains the resoldified and agglomerated particles. The energy dispersive spectroscopy (EDS) analysis shows the interesting characteristic of this splat. The proportion of Ti and O detected in the external part corresponds to stoichiometric TiO_2, what has been used as the powder to formulate the suspension. However, the measurement of the region inside this structure shows the dominant quantity of Ti.

Figure 3.57 highlights the structure occurring only in the case of the coating obtained at the moment of the maximal level of the arc voltage signal.

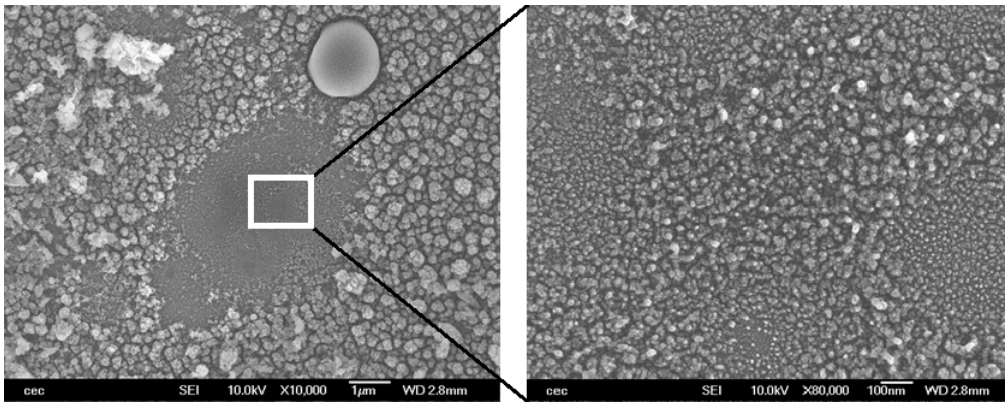

Figure 3.57: Feature 2) from Figure 3.55 measured by the scanning electron microscope.

Under high magnification (right sight of Figure 3.57), nanosized particles, incorporated into this structure, are revealed. The morphology of this feature is non-homogeneous compared to the result shown in Figure 3.58. The shape and the morphology of this

feature resembles the strongly melted or vaporized structure. It may be produced also by the impact of the molten particle on the substrate but the adhesion forces could be too weak to produce the bonding between this particle and the substrate.

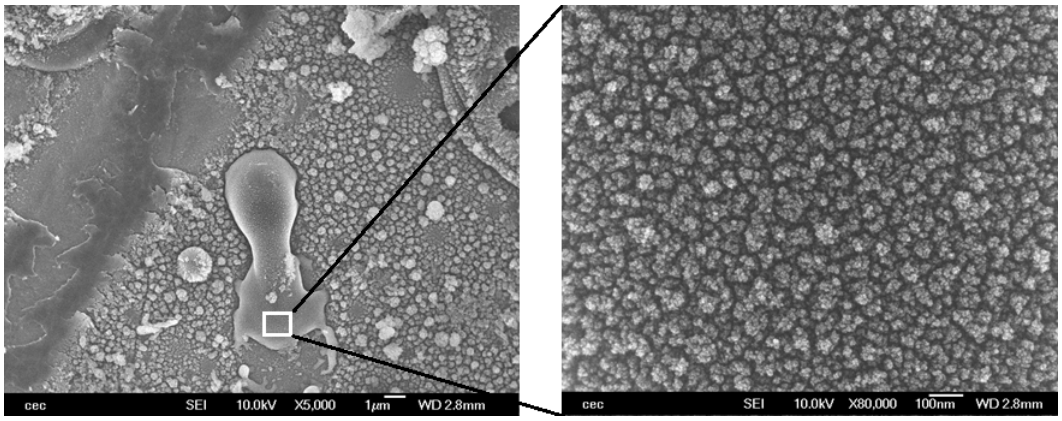

Figure 3.58: Feature 3) from Figure 3.55 measured by the scanning electron microscope.

Figure 3.58 presents the structure of molten particles, what has been found in all obtained coatings, in lower quantities in the case of 3.52 b). The high magnification of this structure has highlighted that it is characterized by homogeneous nano-sized particles.

In the case of the coating produced at the moment of the pulsed plasma corresponding to medium level of the voltage signal, Figure 3.53 b), the features indicated in Figure 3.59, in addition to the structures described above, have been found. They have been analyzed by the scanning electron microscope, what is presented in Figure 3.60.

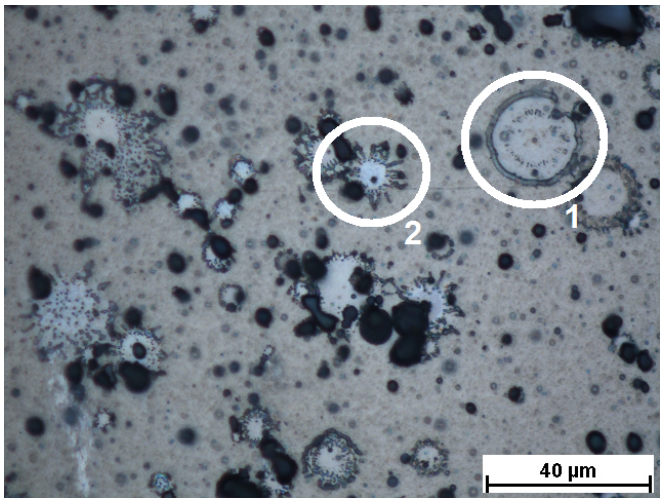

Figure 3.59: Coating obtained at the moment of the medium level of the arc voltage signal, shown in Figure 3.53, measured by the optical microscope, using the objective magnification 100x, with the indicated features 1) and 2) measured by SEM presented in Figure 3.60.

Figure 3.60 1) presents a ring structure with a distinct rim at the periphery. This increase of the material thickness in the external part of this structure may result from recoiling

process of the spread and flattened droplet, what is related to the wetting properties and surface tension of the liquid ceramics.

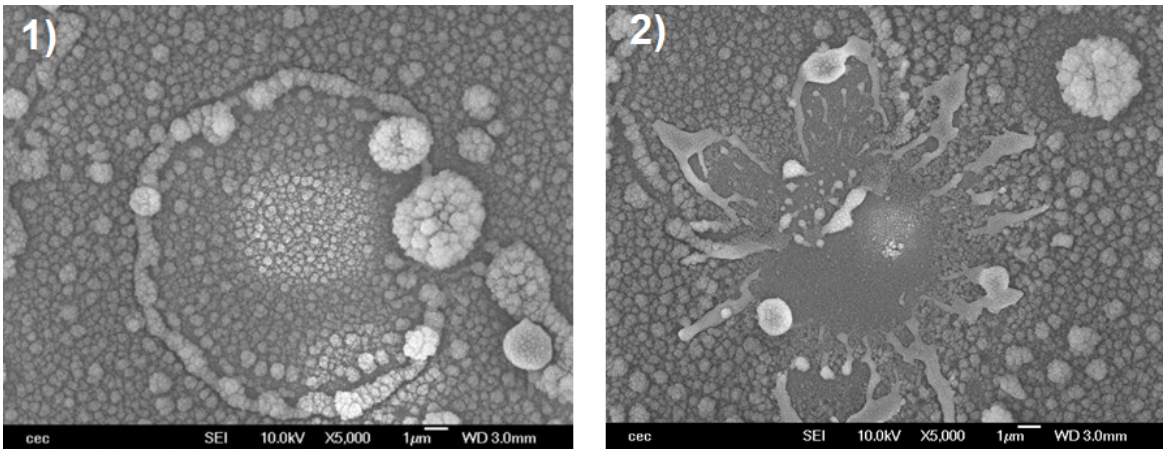

Figure 3.60: Features 1) and 2) from Figure 3.59 measured by the scanning electron microscope.

Figure 3.60 2) exhibits the structure characterized by the finger-like perturbations. The same feature has been observed in all obtained coatings. The studies presented in [102,103] have highlighted the dependence of the splats on the substrate temperature. The splats collected on the low temperature sample are distorted with the shape of the splashed fingers, what exhibits the splashing during droplet impact and spreading. Blazdell *et al.* have shown that preheating the substrate results in much more regular splats, what is presented in Figure 3.61 [46].

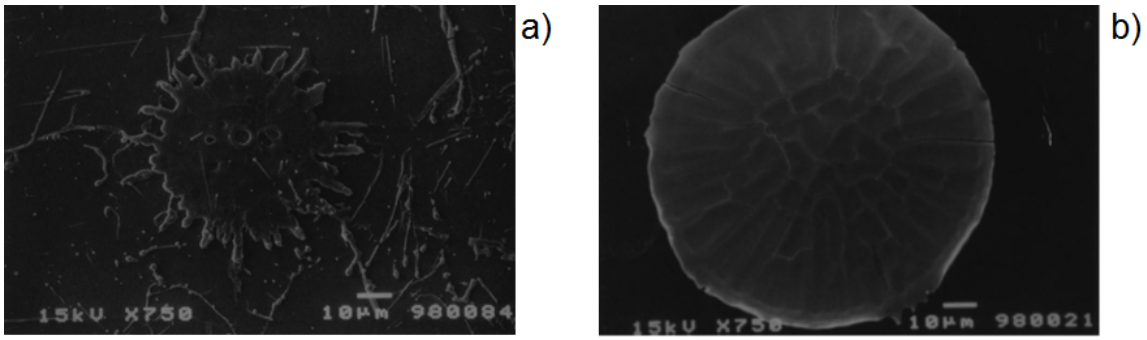

Figure 3.61: Zirconium suspension plasma spraying on a) cold substrate, b) hot substrate [46].

A more regular splat due to the preheating of the substrate might be obtained due to the increase of the solidification rate of the particle.

Moreover, in Figure 3.60 1) and 2) the spherical agglomerated structures with the diameter of around 3 μm can be observed. They highlight that in the case of using the plasma with low level of the enthalpy the thermal energy is sufficient to remove the solvent from the suspension droplets but is too low to ensure that they are still molten when they hit

the substrate. Consequently, the drops solidify and agglomerate in flight and land as the balls on the substrate.

The first attempts to produce the coatings by a new system have been highlighted. The results have shown that the choice of the spraying parameters plays the important role in the coatings formation. The spray distance influences on the microstructure of the coating, what has been presented in Figure 3.52. Too long distance has resulted in the observation of the resolidified particles collected on the substrate surface. Moreover, the coatings at the different levels of the pulsed plasma jet have been obtained. The measurements by the optical and scanning electron microscopes have highlighted the occurrence of different features depending on the level of this periodic plasma, thus, the specific enthalpy and temperature levels. The coating obtained at the medium level of the voltage signal has presented the necessity of the preheating of the substrate before the splats collection. However, the microstructure of the coating obtained at the maximal voltage level has not exhibited the structures characterized by the finger-like perturbations, what has to be studied in the future work. In addition, the synchronized suspension with the pulsed plasma has jet has allowed obtaining the coatings features which have not been observed in the conventional suspension plasma spraying. Therefore, the coatings production by a new method requires further investigation.

V Conclusions

The studies of the instabilities of the plasma produced by the conventional dc torch, presented in Chapter 2, have determined the parameters influencing the fluctuations modes, Helmholtz and restrike. It has leaded to a new approach to plasma fluctuations, the possibility of coupling these two modes together. This is achieved e.g. by the particular design of the plasma torch characterized by large cathode cavity and by using the nitrogen as plasma forming gas. This new resonant mode has been called "mosquito" mode, due to the sharp monotonic sound emitted by the torch, what resembles the noise produced by the mosquito. Therefore, the term "Mosquitorch" has been used to describe a newly designed torch. The plasma, produced in this "mosquito" mode, is a pulsed laminar plasma jet, characterized by the local specific enthalpy modulated with a ratio $h_{max}/h_{min} \simeq 18$, what has been presented by the obtained results. Moreover, this pulsed plasma has the modulated velocity and the local temperature, which has been measured by the time-resolved optical emission spectroscopy. This periodic structure of the plasma jet has been used to synchronize the plasma with the suspension injection. The droplets have been ejected using a piezoelectric device, ink-jet printer, triggered by

the voltage signal sampled at the torch connections. To synchronize the plasma jet with the suspension a new synchronization system has been developed. The time-resolved imaging system and time-resolved optical emission spectroscopy have been implemented to observe the moments of this modulated plasma and the interaction between the plasma and the suspension. The results have shown that the trajectories and thermal treatment of the material depend on the moment at which the droplets penetrate the plasma jet. Therefore, the method shows a great possibility of the control of dynamic and thermal interaction between the plasma pulses and the injected material. Moreover, the analysis of thermo-physical phenomena of the inserted material has shown that thermal treatment of the suspension in the plasma jet is governed by the heat transfer and vaporization. The fragmentation process does not occur compared to the conventional methods. Moreover, the first attempts of the coatings production have highlighted the interesting features which have not been observed in the microstructure of the conventional SPS coatings. However, it requires further investigation. First of all, instead of rotating sample holder, the water-cooled support has to be used. Furthermore, the measurement method of the substrate temperature should be applied, e.g. by using the pyrometer. In addition, the obtained coatings presented in this dissertation have highlighted the necessity of the preheating the substrates to obtain regular splats.

Part III

Résumé du chapitre 3

Ce chapitre présente l'application d'oscillations régulières de plasma produites en mode "mosquito" pour le traitement de la suspension et la synthèse de dépôts. Comme cela a été mis en évidence dans les chapitres précédents, la méthode conventionnelle SPS démontre des difficultés dues à l'absence de contrôle des trajectoires des particules et des transferts de chaleur, ce qui rend la maîtrise des propriétés des revêtements. Le but de ce travail est de développer un nouveau système qui peut permettre d'augmenter la reproductibilité et la fiabilité du procédé par l'utilisation des oscillations régulières de plasma synchronisées avec l'injection de la suspension. L'activation de l'émission de la gouttelette de suspension au moment choisi dans le cylcle périodique d'oscillation du plasma, suivant les conditions pour le traitement thermique du matériau particulier, peut être capable d'améliorer le contrôle des transferts de chaleur et de quantité de mouvement entre le plasma et les matériaux. Par conséquent, il est important d'optimiser le système qui va permettre de synchroniser l'injection de la suspension avec le signal de tension d'arc. En outre, les différents types de méthodes de diagnostic, résolues en temps et synchronisées, sont nécessaires pour étudier les traitements thermiques et dynamiques de la matière dans le plasma oscillant. Par conséquent, un nouveau système a été développé dans le cadre de cette thèse. Il se compose de trois parties importantes:

I Le système d'imagerie résolue en temps
Il se compose d'une caméra et d'une diode laser pulsée. Cette partie du système nécessite de définir le choix des dispositifs appropriés pour observer et enregistrer le plasma oscillant de période de l'ordre de 700 μs. En outre, des expériences doivent être réalisées pour obtenir la synchronisation de la caméra avec le laser.

II L'injection de suspension synchronisée
Les oscillations périodiques du plasma permettent d'obtenir une nouvelle approche de l'injection d'un matériau dans le jet de plasma d'arc. La goutte de suspension peut être injectée au moment choisi, ce qui peut conduire à la régulation de l'interaction dynamique et thermique entre le plasma et le matériau. Cependant, il nécessite un système d'injection capable de contrôler le moment de l'introduction de la matière dans le plasma. Cette condition a été trouvée dans une imprimante à jet d'encre piézoélectrique fournies par la Société Ceradrop (Limoges, France).

III La spectroscopie résolue en temps
Le chapitre 2 a mis en évidence que le plasma produit dans le mode "Mosquito" est caractérisé par une enthalpie modulée. Pour déterminer expérimentalement cette estimation la spectroscopie d'émission optique résolue en temps a été mise en œuvre. Cette méthode a été utilisée pour prendre les mesures de la température de rotation du plasma et de déterminer les espèces de plasma. Cependant, cette technique nécessite des méthodes d'étalonnage minutieuses, qui sont présentés avec les premières

mesures spectroscopiques du plasma périodique.

Pour observer les oscillations périodiques de plasma obtenues en mode "mosqutio", le système d'imagerie résolue en temps et synchrone a été mis en œuvre. Il se compose d'une caméra rapide, une diode laser de forte puissance et un filtre interférentiel (801 nm). Le laser et le filtre ont été combinés avec la caméra afin de permettre l'observation du traitement de la suspension dans le jet de plasma. Le principe est d'observer la pénétration de la suspension dans le jet de plasma par l'illumination des gouttelettes à l'aide du laser. Le filtre interférentiel (801 nm) centré sur la longueur d'onde de laser permet d'éliminer la lumière du plasma d'azote pur sur l'image. Pour observer les différents moments des oscillations de plasma, l'imagerie résolue en temps doit être synchronisée avec le signal de tension d'arc. De plus, les gouttelettes de suspension doivent être illuminées par le tir du laser lors de l'enregistrement par la caméra. Par conséquent, le laser et la caméra doivent être également synchronisés, ce qui signifie que le temps de réponse, t_d, de chaque dispositif doit être déterminé. Le temps de retard du laser a été déterminé par le fournisseur et égal à 36 ns. Le délai de réponse t_d de la caméra a été défini par l'expérience en utilisant deux générateurs, et est égal à 14 μs.
Le système d'imagerie résolue en temps doit être synchronisé avec la tension d'arc. Pour obtenir cette synchronisation, le signal TTL est formé à partir de la tension d'arc, qui est mesurée par le pont diviseur connecté entre la cathode de la torche et la masse. Pour générer le signal TTL initial le dispositif de synchronisation est conçu et composé de:

- l'unité d'amplification-filtrage pour isoler la composante de mode de Helmholtz à partir du signal brut, V_{arc},
- l'unité de réglage de seuil qui se compose du comparateur pour régler le niveau de déclenchement, $V_{threshold}$,
- la génération de l'impulsion à la fréquence fondamentale, f_H, unité qui produit une impulsion TTL V_s (5 V, 10 μs). Il permet de générer le signal avec un retard réglable, τ, par rapport au seuil.

Le signal TTL, généré par ce boîtier de synchronisation, par l'ajustement du niveau de seuil et le temps de retard, est ensuite envoyé au panneau de commande Ceradrop. Il génère deux signaux de déclenchement pour activer la caméra et le laser.
Le plasma pulsé a été observé par la caméra déclenché à un moment donné de ce jet périodique. Une période de cycle de tension est d'environ 700 μs. Le temps d'ouverture de la caméra est réglé à 60 μs et 75 images sont enregistrées dans chaque situation: à partir de a) à e) de la figure 3.10. L'image a) correspond à un déclencheur de 70 μs après un front descendant de la tension. Les moments de b) à e) ont été prises avec des retards respectifs: 210, 310, 520 et 770 μs, ce qui correspond à 70 μs dans la prochaine

période. La Figure 3.10 a) présente le moment après le réamorçage. L'arc est très court et situé dans la partie arrière de la tuyère. Les photos b) - d) montrent le développement progressif de l'arc et la figure 3.10 e) représente une situation similaire à a), mais pour le cycle suivant. Cette séquence témoigne de la forte modulation du plasma. L'examen de la série des 75 images a montré une évolution très reproductible du plasma dans chaque cycle.

La Figure 3.11 est obtenue avec une caméra standard pour un temps d'exposition de 10^{-2} s, ce qui se traduit par la superposition de 13 cycles présentés dans la figure 3.10. Elle montre la caractéristique laminaire de l'écoulement plasma, ce qui peut être vérifié expérimentalement par le nombre de Reynolds, défini par l'equation (3.4). Le nombre de Reynolds permet de définir différents régimes d'écoulement, tels que l'écoulement laminaire ou turbulent. L'écoulement laminaire se produit à faibles nombres de Reynolds. La transition de l'écoulement laminaire à turbulent commence à propos de $\mathrm{Re} > 2100$ et l'écoulement est considéré comme pleinement turbulent à $\mathrm{Re} > 4000$. Pour les paramètres du plasma, donnés dans le tableau 2.12, le nombre de Reynolds est estimé à environ 70, ce qui définit l'écoulement laminaire du plasma.

Les oscillations périodiques de plasma nécessitent une méthode d'injection appropriée, capable de contrôler le moment de l'introduction de la matière dans le jet de plasma. L'analyse des différentes techniques d'injection, présentée dans la revue de la littérature dans le chapitre 1, a abouti à la sélection de l'imprimante à jet d'encre piézo-électrique, fourni par Ceradrop (Limoges, France), en raison de la possibilité de l'émission de chaque gouttelette déclenchée à la fréquence du plasma pulsé, c'est à dire 1.4 kHz. L'injecteur de type piézo-électrique avec une éjection de gouttes à la demande (Drop On Demand) a été utilisé. Le liquide est éjecté par de petits orifices (buses de 50 μm de diamètre) grâce à des impulsions de pression appliquées sur le liquide et générées par un matériau piézo-électrique. La déformation de celui-ci est contrôlée par l'application d'une impulsion de tension de l'ordre de 120 volts. La tête d'impression contient 128 buses indépendantes espacés de 0.5 mm et sont commandées par Labview. Les gouttes ont une vitesse variant de 2 à 10 $\mathrm{m.s^{-1}}$. La fréquence d'éjection peut être ajustée jusqu'à 20 kHz. La formulation de la suspension doit être optimisée en fonction de la nature et la quantité des différent composants (par exemple solvant, dispersant, liant, surfactant) et de la charge massique de matériau céramique afin d'éviter d'une part la sédimentation et le colmatage des buses, et d'autre part d'ajuster les propriétés rhéologiques de la suspension (viscosité, tension de surface).

Le principe de l'injection synchrone de la suspension consiste à injecter des gouttelettes de la matière au bon moment des oscillations périodiques de jet de plasma. Ce processus de synchronisation est possible lorsque la fréquence du mode de résonance de Helmholtz (égale à la fréquence de plasma) est égal à la fréquence de l'injection de la suspension:

$f_H = f_i$. L'émission de la gouttelette est déclenchée par le signal TTL formé à partir de la tension d'arc, en utilisant la boîte de synchronisation.
La suspension utilisée dans les expériences, préparée par Ceradrop (Limoges, France), est composée d'une poudrede dioxyde de titane (90% TiO_2 phases de rutile) et est constituée de 5 wt% de poudre et 95 wt% d'eau. La distribution de taille de particules a été déterminée en utilisant le Mastersizer 2000 (Malvern Instruments Ltd, Royaume-Uni), qui est basé sur la technique de diffraction laser. Le pic de la courbe de distribution de taille de particules de la suspension utilisée dans l'expérience est centré sur 66 nm (d_{50}). La taille de dispersion ($d_{90} - d_{10}$) est égale à 48 nm.
Dans les imprimantes à jet d'encre, la formulation de la suspension doit être optimisée afin d'éviter la sédimentation le bouchage des buses et être compatible avec la tête d'impression. De plus, l'injection d'une seule goutte calibrée est le paramètre important dans ce genre de procédé.
Pour obtenir l'émission d'une seule goutte deux conditions doivent être remplies:

- les propriétés rhéologiques de la suspension (par exemple, la viscosité, la tension de surface) doivent être ajustés pour obtenir le rapport $\mathrm{Re}/\sqrt{\mathrm{We}}$ variait entre 1 et 10
- le signal de tension envoyé à l'injecteur piézo-électrique doit être optimisé

La première condition nécessite la définition du rapport $\mathrm{Re}/\sqrt{\mathrm{We}}$. C'est le coefficient adimensionnel qui permet d'analyser le fluide. Il se compose de respectivement un nombre de Reynolds et Weber, définies par les équations (3.4) et (3.5). Ce rapport calculé pour la suspension utilisés dans les expériences est égale à $\mathrm{Re}/\sqrt{\mathrm{We}} = 5.98$. De plus, pour éliminer les gouttelettes satellites l'impulsion de tension envoyée à l'injecteur a été optimisée en collaboration avec Ceradrop. Une impulsion de tension de forme trapézoidale, représentée sur la Figure 3.19, a été appliquée.
Ce système, présenté ci-dessus, contenant de l'injecteur, la caméra et le laser synchronisés avec le signal de la tension d'arc a permis d'observer l'injection de la suspension dans les différents moments du jet de plasma pulsé.
Sur la figure 3.23, l'imagerie résolue en temps des interactions dynamiques entre le jet de plasma et les gouttelettes est présentée. Les photos 3.23 a-d sont obtenues avec un objectif à faible grossissement (avec la résolution présentée dans la figure 3.4 c)) pour les différents retards sur une période. Pour obtenir les résultats fiables des centaines de photos liées à 3.23 a-d, déclenchées avec le même temps τ_j, ont été enregistrées. Le laser a été utilisé pour visualiser les particules solides restantes dans le jet après évaporation du solvant. L'analyse d'image a permis d'estimer les vitesses du centre de masse des "boules" de plasma, qui varient entre environ 30 m/s pour le cas présenté dans 3.23 a) et 50 m/s pour 3.23 c). L'expérience a montré sur les figures 3.23 a-d que les trajectoires et l'histoire thermique associée aux matériaux injectés dépend du moment où les gouttelettes

pénètrent dans le plasma. Dans le cas $\tau_1 = 0$ μs, la partie la plus importante de matériau voyagent en périphérie de plasma donnant lieu à grande dispersion des trajectoires (∼10 mm) et la distance axiale de transport des matériaux est limitée (∼40-60 mm). Dans le cas $\tau_2 = 260$ μs, le traitement des matériaux dans le cœur du plasma est amélioré avec une dispersion radiale inférieure et une distance de transport légèrement augmentée. Sur la figure 3.23 c) ($\tau_3 = 480$ μs), une faible dispersion de la matière est observée correspondant à la distance de transport plus longue. Enfin, le cas de $\tau_4 = 620$ μs ressemble le premier cas $\tau_1 = 0$ μs, car il est presque 700 μs de période.

Par ailleurs, l'influence du moment où une gouttelette pénètre le jet d'arc pulsé a été étudiée en utilisant la caméra avec l'objectif Infinimax (Figure 3.4 b). Les résultats sont présentés sur la figure 3.24. La caméra et le laser sont retardés par le même temps, après l'émission de gouttelettes mais la suspension pénètrent dans le plasma précédemment sur la figure 3.24 a) que sur b), ce qui a été obtenu en changeant τ_j. La goutte, observée par l'illumination du laser, pénètre dans le plasma 4 mm en aval de la sortie de tuyère. Les images a) et b) sont observées à travers le filtre interférentiel passe-bande centré sur la longueur d'onde du laser. Cette configuration permet d'éliminer la lumière provenant du plasma d'azote pur sur l'image. Par conséquent, la figure 3.24 montre simplement les boules de plasma, caractérisées par une forte augmentation de luminosité résultant de l'interaction du plasma avec le matériau contenu dans la goutte de suspension. Sur la figure 3.24 a) la gouttelette inférieure pénètre dans le plasma à un moment correspondant à une situation présentée sur la figure 3.10 d). Ce moment a été choisi en raison du niveau élevé de l'enthalpie spécifique locale. Par conséquent, la figure 3.24 b) correspond au plasma caractérisé par un faible niveau d'enthalpie, représentée sur la figure 3.10 a). Dans le cas présenté sur la figure 3.24 a), le processus de vaporisation instantanée de la goutte a été observé, ce qui diffère de la situation illustrée en b). Dans ce cas, le processus de vaporisation ne concerne pas la goutte injectée mais celle introduite une période antérieure générant la boule de plasma à droite dans la figure b).

L'effet de modulation de l'enthalpie sur les phénomènes de thermo-physiques des gouttelettes de suspension a été étudié. Le nombre de Weber calculé, dont le processus de fragmentation dépend, est compris entre 0.04 et 0.48. Il s'avère que le procédé de fragmentation n'apparaît pas dans le cas de l'injection de la suspension dans le jet de plasma pulsé. Le calcul du temps de vaporisation a mis en évidence que le choix de la temporisation d'injection peut avoir un effet sur la vaporisation du solvant, ce qui est vérifié par la figure 3.24. Les résultats obtenus par jet de plasma laminaire pulsé montrent la possibilité du contrôle du matériau injecté dans les différentes zones du plasma modulé. Ceci peut permettre de contrôler certains des procédés thermo-physiques se produisant à l'échelle de gouttelette, telles que l'évaporation.

Les paragraphes précédents ont montré que le jet de plasma pulsé est caractérisé par

l'enthalpie spécifique fortement modulée. Pour déterminer cette modulation de façon plus précise et locale, les mesures de température de plasma doivent être effectuées. Parmi toutes les techniques disponibles, la spectroscopie d'émission optique a été choisie. Le spectrographe Isoplane (Princeton Instruments, Trenton, New Jersey) équipé d'une tourelle de 3 réseaux de diffraction (300, 1200 et 2400 tr/mm) a été utilisé. L'acquisition des spectres a été réalisée en utilisant une caméra PI-MAX4 ICCD (Princeton Instruments) connectée à l'ordinateur et commandée par un logiciel LigthField. Pour obtenir des informations précises sur les paramètres du plasma, l'étalonnage du spectromètre a été effectué en longueur d'onde et en intensité.
Pour déterminer la température du plasma, la spectroscopie d'émission optique doit être appliquée pour examiner les espèces du plasma pulsé produit par la "Mosquitorch". L'azote pur (N_2 2 slm) a été utilisé comme le gaz plasmagène, par conséquent, les études spectroscopiques ont mis l'accent sur l'identification des émissions moléculaires de l'azote. L'analyse des espèces, montré sur la figure 3.37, présente que le jet de plasma de 0 à 10 mm contient principalement les transitions du second système positif de $N_2(C-B)$ et du premier système négatif de $N_2{}^+(B-X)$. Le premier système négatif $B^2\sum_u^+ - X^2\sum_g^+$ de l'ion moléculaire azote $N_2{}^+$ a été choisi pour mesurer la température de rotation du plasma jusqu'à une distance de 6 mm. Dans le cadre de cette thèse, les spectres mesurés ont été analysés par Specair. Il s'agit d'un logiciel commercial développé pour simuler le rayonnement, les transitions moléculaires et atomiques d'un plasma d'air, y compris les transitions N_2 (C-B) (second système positif), $N_2{}^+$ (B-X) (premier système négatif), et le système violet CN. Specair suppose que les états de rotation sont Boltzmann distribués à Trot, définie par l'équation (3.29). Selon Bruggeman *et al.*, cette condition est remplie si la durée de vie effective de l'état excité de N_2, τ_{eff}, est plus long que le temps de thermalisation de N_2, τ_{therm} [91], ce qui a été confirmé dans le jet de plasma pulsé par les calculs lorsque les mécanismes de quenching ne sont pas pris en compte. Les résultats ont donné que : $\tau_{\text{therm}} \simeq 10$ ns et $\tau_{\text{eff}} \simeq 80$ ns. Pour définir la température de rotation, T_{rot}, le spectre théorique doit être simulée par Specair et comparé à celui mesuré. Ce procédé comporte plusieurs étapes. Tout d'abord, la soustraction du bruit de fond continu doit être mise en œuvre. En outre, pour obtenir des informations précises sur la température du plasma, l'étalonnage en longueur d'onde et en intensité doivent être effectuées.
Le paramètre important dans la simulation spectrale par le logiciel Specair est la détermination de la fonction d'appareil qui définit la résolution des données obtenues. La fonction de fente d'entrée représente l'élargissement causé par le spectromètre (largeur de la fente, la largeur en pixels, la dispersion réseau). Pour améliorer la précision des mesures spectrales, deux fonctions de fente différentes ont été choisies: la fonction trapézoidale, proposée dans la [84,94] et présenté dans la figure 3.40, et la fonction déterminée par la mesure d'une lampe au mercure à 404.7 nm.

Pour vérifier les températures des différents pulses de ce plasma modulé, les mesures de spectroscopie résolue en temps doivent être synchronisées avec le signal de tension d'arc. Les délais de déclenchement dans une période de plasma, τ_1 à τ_4, ont été ajustés par la boîte de synchronisation, comme τ_4 correspond au signal de tension maximale, $U_{max}(t)$ = 100 V, τ_1 a été obtenu à U(t) $\simeq$ 60 V. Les signaux TTL générés ont été envoyés à la caméra et au spectrographe. En analysant le premier système négatif de N_2^+, on peut observer que le spectre mesuré dans l'instant τ_4 est caractérisé par la plus haute valeur de l'intensité en comparant les spectres obtenus à τ_1 de τ_3. L'estimation spectroscopique de la température de rotation met en évidence que la température du gaz augmente de 6400 K $\pm$ 150 K à 7500 K $\pm$ 150 K en changeant le moment de déclenchement dans la tension d'arc périodique, comme cela est présenté sur la figure 3.46. Les résultats obtenus ont été comparés avec les données de l'enthalpie spécifique du plasma d'azote donné dans [17], ce qui montre que le jet de plasma analysés à l'instant τ_4 est caractérisé par la valeur enthalpie de 35 $\pm$ 3 MJ/kg. Pour comparer, au moment τ_1 l'enthalpie est de 15 $\pm$ 2 MJ/kg. Il s'avère expérimentalement que le jet de plasma pulsé est caractérisé par l'enthalpie et la température modulée. Cependant, le rapport de la modulation de l'enthalpie, $h_{\tau_4}/h_{\tau_1} \simeq 2.3$, obtenue dans cette expérience est beaucoup plus faible que celle présentée dans la section précédente, $h_{max}/h_{min} \simeq 18$, déterminée par les mesures du bilan d'énergie et l'hypothèse sur la tension thermique (36 V) constante. Cette différence significative a conduit à la conclusion que le rapport de la modulation de l'enthalpie de 18 est surestimé parce que les pertes thermiques ne sont pas constantes. L'hypothèse sur les pertes thermiques fluctuantes a donné le ratio h_{max}/h_{min} estimé d'environ 2.

Les premiers essais pour produire des revêtements par un nouveau système ont été présentés. Les paramètres de projection ont été choisis comme les paramètres de la méthode SPS conventionnelle:

- La distance de projection de 32 mm de la sortie de la torche
  La distance de projection dans APS est de l'ordre de 100 mm. Cependant, Darut *et al.* ont mis en évidence dans la méthode SPS que ce paramètre doit être considérablement réduit à environ 30 mm en raison de l'inertie dynamique et thermique significativement plus faible des particules matérielles [99].

- Le refroidissement du substrat
  Un porte-échantillon rotatif a été choisi, ce qui permet d'éviter la surchauffe du substrat. La vitesse linéaire de la porte a été régulée à 1 ms^{-1}, en analysant les études présentées dans [100, 101].

- La préparation du substrat
  Pour recueillir les lamelles produites par la méthode SPS, le substrat poli-miroir est

couramment utilisé en raison de sa faible rugosité. Par conséquent, les substrats d'acier inoxydable ont été polis à l'aide du carbure de silicium (SiC) papiers avec les tailles de grain de 600, 1200, 2400 et 4000 μm refroidis à l'eau. Ensuite, la surface du miroir en forme finale a été obtenue en utilisant le pad de polissage en velours et la silice colloidale. Les substrats avant projection ont été nettoyés à l'éthanol et séché avec le courant d'argon.

Pour produire les revêtements, la suspension aqueuse de TiO_2, décrit dans le tableau 3.2, a été utilisée. Les caractérisations des revêtements ont été effectuées par la microscopie optique et la microscopie électronique à balayage (SEM en anglais) en combinaison avec la spectroscopie à dispersion d'énergie (EDS), qui donne une analyse de la composition résolue spatialement du revêtement.
La distance de projection de 32 mm a été choisie par l'analyse des résultats obtenus par la méthode SPS. Par conséquent, pour vérifier ce choix, ce paramètre a été augmenté à 42 mm. Les résultats ont montré que la distance de projection influence la microstructure du revêtement, ce qui a été présenté sur la figure 3.52. La distance trop longue a conduit à l'observation des particules resolidifié recueillies sur la surface du substrat. Pour déterminer l'influence des différents moments du jet de plasma pulsé sur la formation des revêtements, deux cas ont été choisis liés à des mesures spectroscopiques du plasma: l'émission de la suspension au niveau maximum du signal de tension d'arc, présenté sur la figure 3.44 comme τ_4 et le niveau moyen, indiqué sur la figure 3.44 comme τ_1. Les mesures effectuées par les microscopes optique et électronique à balayage ont mis en évidence la présence des caractéristiques différentes en fonction du niveau de ce plasma périodique, donc, les niveaux d'enthalpie et de température spécifiques. Le revêtement obtenu au niveau moyen du signal de tension a présenté la nécessité du préchauffage du substrat avant la collection des splats. Cependant, la microstructure du revêtement obtenu au niveau de tension maximal n'a pas présenté les structures caractérisées par des perturbations en forme de doigts, qui se trouvent dans le revêtement produit au niveau moyen. En outre, la suspension synchronisée avec le plasma pulsé a permis d'obtenir les caractéristiques des couches qui n'ont pas été observés dans la méthode SPS classique. Par conséquent, la production de revêtements par une nouvelle méthode nécessite l'examen plus approfondi.

General conclusions

This thesis presented the studies of the plasma spraying method with the emphasis on the use of the suspension as the feedstock material.

The literature review has highlighted the advantages of the plasma spraying technique deposition, i.e. a wide range of the materials which can be used to produce coatings, a relatively low cost, that is commonly the goal of technological development. Moreover, the development of this method, i.e. the use of the suspension of fine particles as material injected has allowed obtaining the finely structured nano-sized coatings. This amelioration has resulted in the extension of the coatings application area to more complex integrated devices, such as solid oxide fuel cells, photocatalytic coatings. However, as has been highlighted by the examples of the coatings microstructures or the studies of the suspension fragmentation according to the arc voltage fluctuations, the researchers face still many problems in this method. The large discrepancies in the particles trajectories and the heat transfers, the plasma instabilities result in the insufficient reproducibility and reliability of the suspension plasma spraying process. By analyzing the current results obtained in the field of SPS, e.g. the techniques leading to the reduction of the plasma fluctuations, the developments of the dc plasma torches, the following thesis has presented the alternative method resulting in a new approach to the arc instabilities and to the injection of reactive material in an arc jet.

Firstly, a new approach to the plasma fluctuations has been highlighted. In the literature the processes to reduce the plasma oscillations can be found. This thesis shows the method to increase the arc instabilities in a controlled way to obtain a new resonant mode characterized by very periodic arc voltage signal. This process has required the understanding of the origins of the arc instabilities. Initially, the time-resolved measurements and data processing methods applied to the arc voltage signal have leaded to determine a mode due to Helmholtz resonance in the torch. The arc voltage power spectrum has highlighted the presence of a sharp peak at $\sim$4.3 kHz, which could not been attributed the acoustic longitudinal stationary waves in the nozzle channel or the restrike fluctuations, the repetition of the elongation-re-arcing sequences characterized by non-reproducible spectral components. Therefore, following the works in the field of combustion systems where it has been discovered that the burners behave like Helmholtz resonators, these periodic oscillations in the plasma produced by dc plasma torch have been considered as the coupling between the arc and pressure variations in the cathode cavity. The presented results obtained by the time-resolved measurements of the arc voltage signal and the pressure in the torch have confirmed this assumption. The use of the external resonator mounted on the torch has shown the significant reduction of the arc voltage due to the modification of the pressure inside the cathode cavity. Moreover, the model of the frequency of Helmholtz oscillations, defined in the framework of vibration

theory, given by the equation: $f_H = 1/2\pi\sqrt{\gamma_g P_g/\rho_p}\sqrt{S/L_p V_g}$, has been confirmed by the obtained results. The increase of the cathode cavity volume has noticeably influenced the Helmholtz mode by reducing its frequency. The use of the nitrogen as plasma forming gas has reinforced the Helmholtz mode and dominated the acoustic modes. Moreover, the obtained have shown a good matching between the arc voltage and pressure variations. In addition, the presented results have allowed to assume the model for the acoustic resonances by combination of the axial modes and those of radial and azimuthal modes in the cathode cavity, presumed to be an annular tube closed at the injection ring and opened at the cathode tip. The model has shown a good agreement with the experiments. However, to define the changes of the acoustic oscillations with the increase of the cathode cavity more advanced modelling has to be implemented. Moreover, the arc voltage signal has highlighted that to Helmholtz oscillations are superimposed more randomly distributed short events with sharp peaks and sudden falls. The filtering method has underlined that these features, with a mean characteristic time of a few tens of μs, correspond to the restrike mode. The studies of this mode of the instabilities have been found in the literature. However, the model for restrike fluctuations has been evaluated for pure restrike mode (without the influence of Helmholtz or acoustic modes). Therefore, the necessity to verify this model for the restrike fluctuations superimposed to Helmholtz mode has leaded to the statistical studies of the filtered restrike from the arc voltage fluctuating component signal. The presented results have verified that the restrike fluctuations follow the model given in the literature, what highlights that restrike and Helmholtz modes are relatively separated. It can be confirmed by the calculation of the times at which these modes appear: a few hundreds of μs of Helmholtz mode and a few tens of μs of restrike. Moreover, Helmholtz oscillations strongly depend on the volume of cathode cavity, the restrike fluctuations depend on the properties of the cold boundary layer around the arc column. Therefore, it highlights that both modes, Helmholtz and restrike, are relatively decoupled. However, the understanding of Helmholtz and restrike phenomena has leaded to a new mode of the arc instabilities. By changing the parameters influencing the Helmholtz and restrike fluctuations, the possibility to couple them together has been presented. To obtain this coupling a new dc plasma torch has been designed. The arc voltage signal obtained in this new mode is very repeatable saw-tooth shaped. Moreover, the energy balance measurements have highlighted that the plasma produced in this new mode is characterized by the enthalpy highly modulated. This new approach to the plasma fluctuations by increasing the arc instabilities in a controlled way to obtain very periodic plasma has leaded to the second part of this thesis, to the injection of reactive material synchronized with the regular oscillations of the plasma jet.

The principle of a new system is to inject the suspension droplet at the right moment of the periodic plasma jet. The obtained regular plasma oscillations have been applied to the suspension treatment and coatings deposition process. First of all, the further examination of the periodic plasma jet has highlighted that this newly obtained resonant mode results in a pulsed and laminar plasma jet. The observation of this periodic plasma jet with the frequency of 1.4 kHz was possible by the design of time-resolved imaging system which contains of the fast shutter camera with the laser, both synchronized with the arc voltage signal. This pulsed plasma jet allows obtaining a new approach to the injection of reactive material. First of all, the system capable to control the moment of material introduction to the plasma has been chosen. The use of the piezoelectric ink-jet printer has provided the possibility to insert the suspension droplet at the selected moment of the regular plasma oscillations. The obtained results have highlighted that this periodic plasma is not only characterized by the high modulation of the enthalpy but also of the velocity. Moreover, the suspension droplet injection synchronized with the pulses of the plasma jet has highlighted the choice of the injection moment has an effect on the thermo-physical processes occurring at the droplet scale. Therefore, a new system may provide the control of dynamic and thermal interaction between the plasma and the material. Moreover, this new method is based on the synchronization of all devices with the arc voltage signal. Therefore, the synchronization system has been implemented in the framework of this thesis. To verify the modulation of the enthalpy the plasma temperature measurements have been performed by time-resolved optical emission spectroscopy. The obtained results have shown the species in the nitrogen modulated plasma in the function of the distance. Moreover, the synchronization of the spectrograph with the arc voltage signal has allowed to perform the temperature measurements of different moments of the pulsed plasma jet. The have verified the high modulation of the temperature and, thus, of the specific enthalpy in the pulsed plasma. In the future work, the use of this spectroscopic system to define the suspension-plasma interaction should be studied. It could verify the process of the thermal treatment of the material in the plasma jet by the measurement of the temperature and investigation of the species. This thesis has presented also first attempts to produce the coatings by a new system. The examination of the coatings microstructures have highlighted that they seem to be dependent on the enthalpy modulation. Moreover, the obtained results have shown the necessity to develop the system of the splat collection and apply the water-cooled support. The spraying parameters should be changed, e.g. the preheating of the substrates. In addition, the increase of the coatings thickness by for example the use of more than one injector nozzles, should be verified.

Bibliography

[1] M. Gell. Application opportunities for nanostructured materials and coatings. *Materials Science Engineering*, 204:246–251, 1995.

[2] C. Monterrubio-Badillo, H. Ageorges, T. Chartier, J. F. Coudert, and P. Fauchais. Preparation of $LaMnO_3$ perovskite thin films by suspension plasma spraying for SOFC cathodes. *Surf. Coat. Technol.*, 200:3743–3756, 2006.

[3] F.-L. Toma, L.M. Berger, D. Jacquet, D. Wicky, I. Villaluenga, Y.R. de Miguel, and Lindelov J.S. Comparative study on the photocatalytic behaviour of titanium oxide thermal sprayed coatings from powders and suspensions. *Surf. Coat. Technol.*, 203:2150–2156, 2009.

[4] K.E. Schneider, V. Belaschenko, M. Dratwinski, S. Siegmann, and A. Zagorski. *Thermal Spraying for Power Generation Components*. Wiley, Chichester, UK, 2006.

[5] C. K. Muoto, E. H. Jordan, M. Gell, and M. Aindow. Identification of desirable precursor properties for solution precursor plasma spray. *J. Therm. Spray Techn.*, 20:802–816, 2011.

[6] D. Chen, E. H. Jordan, and M. Gell. The solution precursor plasma spray coatings: Influence of solvent type. *Plasma Chem. Plasma Process*, 30:111–119, 2010.

[7] R. Vassen, H. Kassner, G. Mauer, and D. Stoever. Suspension plasma spraying: Process characteristics and applications. *J. Therm. Spray Techn.*, 19:219–225, 2010.

[8] J. Karthikeyan, C. C. Berndt, J. Tikkanen, J. Y. Wang, A. H. King, and H. Herman. Preparation of nanophase materials by thermal spray processing of liquid precursors. *Nanostruct. Mater.*, 9:137–140, 1997.

[9] F. Gitzhofer, E. Bouyer, and M.I. Boulos. Atomized into droplets, injection into plasma discharge, vaporization and agglomeration into partially melted drops, March 11 1997. US Patent 5,609,921.

[10] R. Vassen, A. Stuke, and D. Stoever. Recent developments in the field of thermal barrier coatings. *J. Therm. Spray. Technol.*, 18:181–186, 2009.

[11] M. Saremi, A. Afrasiabi, and A. Kobayashi. Microstructural analysis of YSZ and YSZ/Al_2O_3 plasma sprayed thermal barrier coatings after high temperature oxidation. *Surf. Coat. Technol.*, 202:3233–3238, 2008.

[12] A. Kulkarni, A. Vaidya, A. Goland, S. Sampath, and H. Herman. Processing effects on porosity-property correlations in plasma sprayed yttria-stabilized zirconia coatings. *Mater. Sci. Eng., A*, 359:100–111, 2003.

[13] K. Nakata and A. Fujishima. TiO_2 photocatalysis: Design and applications. *J. Photochem. Photobiol., C: Photochemistry Reviews*, 13:169–189, 2012.

[14] R. Henne. Solid oxide fuel cells: A challenge for plasma deposition processes. *J. Therm. Spray Technol.*, 16:381–403, 2007.

[15] P. Fauchais. Understanding Plasma Spraying. *J. Phys. D: Appl. Phys.*, 37:R86–R108, 2004.

[16] M.A. Lieberman and A.J. Lichtenberg. *Principles of plasma discharges and materials processing.* Wiley, New York, USA, 1994.

[17] M.I. Boulos, P. Fauchais, and E. Pfender. *Thermal plasmas: fundamentals and applications, Volume 1.* Plenum Press, New York, USA, 1994.

[18] P.M. Bellan. *Fundamentals of Plasma Physics.* Cambridge University Press, Cambridge, UK, 2006.

[19] M.F. Zhukov, I.M. Zasypkin, A.N. Timoshevskii, B.I. Mikhailov, and G.A. Desyatkov. *Thermal plasma torches: Desing, Characteristics, Applications.* Cambridge International Science Publishing Ltd, Cambridge, UK, 2007.

[20] P. Fauchais and A. Vardelle. Pending problems in thermal plasmas and actual development. *Plasma Phys. Control. Fusion*, 42:B365–B383, 2000.

[21] J. Heberlein. Electrode Phenomena in Plasma Torches. *Ann. N.Y. Acad. Sci.*, 891, Heat and mass transfer under plasma conditions:14–27, 1999.

[22] A. A. Sadek, U. Masao, and Fukuhisa M. Effect of rare earth metal oxide additions to tungsten electrodes. *Metall. Trans. A*, 21A:3221–3236, 1990.

[23] P. Fauchais, J.F. Coudert, and B. Pateyron. La production des plasmas thermiques. *Rev. Gen. Therm.*, 35:543–560, 1996.

[24] J.F. Coudert, M.P. Planche, and P. Fauchais. Velocity measurement of DC plasma jets based on arc root fluctuations. *Plasma Chem Plasma Process*, 15:47–70, 1995.

[25] A. Fridman and Y.I. Cho. *Advances in Heat Transfer: Transport Phenomena in Plasma, Volume 40.* Elsevier Inc., 2007.

[26] P. Roumilhac. *Contribution to the metrology and understanding of the DC plasma spray torches and transferred arcs for reclamation at atmospheric pressure (in french).* PhD thesis, Université de Limoges, 1990.

[27] Z. Duan and J. Heberlein. Arc instabilities in a plasma spray torch. *J. Therm. Spray Technol.*, 11:44–51, 2002.

[28] S.A. Wutzke, E. Pfender, and E.R.G. Eckert. Study of electric arc behavior with superimposed flow. *AIAA Journal*, 5:707–713, 1967.

[29] M.N. Hirsh and Oskam H.J. *Gaseous Electronics. Volume 1: Electrical Discharges.* Academic Press, New York, USA, 1978.

[30] O. Anciello and Flamm D.I. *Plasma Diagnostics vol.1.* Academic Press, New York, USA, 1989.

[31] M.I. Boulos. *Advanced course on thermal plasmas technology and applications, Volume 1, Lecture Notes.* Eindhoven University of Technology, 1985.

[32] M. Leylavergne, B. Dussoubs, A. Vardelle, and Goubot N. Comparison of plasma-sprayed coatings produced in argon or nitrogen atmosphere. *J. Therm. Spray Techn.*, 7:527–536, 1998.

[33] P. Fauchais, V. Rat, J.-F. Coudert, R. Etchart-Salas, and G. Montavon. Operating parameters for suspension and solution plasma-spray coatings. *Surf. Coat. Technol.*, 202:4309–4317, 2008.

[34] A. Killinger. Thermokinetische beschichtungsverfahren zur verarbeitung submikron- und nanoskaliger werkstoffe. *Proceedings of Fertigungstechnisches Kolloquium Stuttgart*, ISBN 978-3-00-025623-3, 2010.

[35] J. Fazilleau. *Contribution à la compréhension des phénomènes impliqués dans la réalisation de dépôts finement structurés d'oxydes par projection de suspensions par plasma.* PhD thesis, Université de Limoges, 2003.

[36] O. Marchand, L. Girardot, M. P. Planche, P. Bertrand, Y. Bailly, and G. Bertrand. An insight into suspension plasma spray: Injection of the suspension and its interaction with the plasma flow. *J. Therm. Spray Techn.*, 20(6):1310–1320, 2011.

[37] P. Fauchais, A. Joulia, S. Goutier, C. Chazelas, M. Vardelle, A. Vardelle, and S. Rossignol. Suspension and solution plasma spraying. *J. Phys. D: Appl. Phys.*, 46:224015 (14pp), 2013.

[38] H.S. Jazi. *Advanced Plasma Spray Applications.* InTech, 2012.

[39] N. Ashgriz. *Handbook of Atomiztion and Sprays, Theory and Applications.* Springer, New York, USA, 2011.

[40] L. Wang, Y. Wang, X.G. Sun, J.Q. He, Z.Y. Pan, and C.H. Wang. Thermal shock behavior of 8YSZ and double-ceramic-layer $La_2Zr_2O_7$/8YSZ thermal barrier coatings fabricated by atmospheric plasma spraying. *Ceram. Int.*, 38:3595–3606, 2012.

[41] S.W.K. Kweh, K.A. Khor, and P. Cheang. The production and characterization of hydroxyapatite (HA) powders. *J. Mater. Process. Technol.*, 89-90:373–377, 1999.

[42] L. Pawlowski. Suspension and solution thermal spray coatings. *Surf. Coat. Technol.*, 203:2807–2829, 2009.

[43] J. Fazilleau, C. Delbos, V. Rat, J.F. Coudert, P. Fauchais, and B. Pateyron. Phenomena Involved in Suspension Plasma Spraying. Part 1: Suspension Injection and Behavior. *Plasma Chem. Plasma Process*, 26:371–391, 2006.

[44] R. Etchart-Salas, V. Rat, J.-F. Coudert, P. Fauchais, N. Caron, K. Wittman, and S. Alexandre. Influence of Plasma Instabilities in Ceramic Suspension Plasma Spraying. *J. Therm. Spray Techn.*, 16:857–865, 2007.

[45] R. Etchart-Salas. *Approche expérimentale et analytique des phénomènes impliqués dans la reproductibilité et la qualité des dépôts.* PhD thesis, Université de Limoges, 2007.

[46] P. Blazdell and S. Kuroda. Plasma spraying of submicron ceramic suspensions using a continuous ink jet printer. *Surf. Coat. Technol.*, 123:239–246, 2000.

[47] J. Oberste-Berghaus, S. Bouaricha, J.-G. Legoux, and C. Moreau. Injection conditions and in-flight particle states in suspension plasma spraying of alumina and zirconia nano-ceramics. *Proceedings of the International Thermal Spray Conference and Exposition (ITSC)*, pages 512–518, 2005.

[48] M. Pilch and C.A. Erdman. Use of breakup time data and velocity history data to predict the maximum size of stable fragments for acceleration-induced breakup of a liquid drop. *Int. J. Multiphase Flow*, 13:741–757, 1987.

[49] S. Basu, E.H. Jordan, and B.M. Cetegen. Heat transfer of liquid precursor droplets injected into high-temperature plasmas. *Therm. Spray Technol.*, 17:60–72, 2008.

[50] S. Saha, B. Seal, S. Cetegen, E. Jordan, A. Ozturk, and S. Basu. Thermo-physical processes in cerium nitrate precursor droplets injected into high temperature plasma. *Surf. Coat. Technol.*, 203:2081–2091, 2009.

[51] P. Fauchais, J.V.R. Heberlein, and Boulos M.I. *Thermal Spray Fundamentals, From Powder to Part.* Springer, New York, USA, 2014.

[52] O. Tingaud, G. Montavon, A. Denoirjean, J.-F. Coudert, V. Rat, and P. Fauchais. Al_2O_3-ZrO_2 Finely Structured Multilayer Architectures from Suspension Plasma Spraying. *J. Therm. Spray Technol.*, 19:207–218, 2010.

[53] O. Tingaud, A. Grimaud, A. Denoirjean, G. Montavon, V. Rat, J. F. Coudert, P. Fuachais, and T. Chartier. Suspension plasma-sprayed alumina coating structures: Operating parameters versus coating architecture. *J. Therm. Spray Technol.*, 17, 2008.

[54] H. Kassner, R. Siegert, D. Hathiramani, R. Vassen, and D. Stoever. Application of suspension plasma spraying (sps) for manufacture of ceramic coatings. *J. Therm. Spray Technol.*, 17:115–123, 2008.

[55] V. Rat and J. F. Coudert. A simplified analytical model for dc plasma spray torch: influence of gas properties and experimental conditions. *J. Phys. D: Appl. Phys.*, 39:4799–4807, 2006.

[56] J. P. Trelles. *Finite Element Modeling of Flow Instabilities in Arc Plasma Torches.* PhD thesis, University of Minnesota, 2007.

[57] J.P. Trelles, E. Pfender, and J. Heberlein. Multiscale Finite Element Modeling of Arc Dynamics in a DC Plasma Torch. *Plasma Chem. Plasma Process.*, 26:557–575, 2006.

[58] J.P. Trelles, E. Pfender, and J.V.R. Heberlein. Modelling of the arc reattachment process in plasma torches. *J. Phys. D: Appl. Phys.*, 40:5635–5648, 2007.

[59] X. Tu, B.G. Chéron, J.H. Yan, and K.F. Cen. Electrical and spectroscopic diagnostic of an atmospheric double arc argon plasma jet. *Plasma Sources Sci. Technol.*, 16:803–812, 2007.

[60] L. Leblanc and C. Moreau. Study on the Long-term Stability of Plasma Spraying. *Proceedings of the 1st International Thermal Spray Conference*, pages 306–317, 2000.

[61] J. F. Coudert, M.P. Planche, and P. Fuachais. Characterization of d.c. plasma torch voltage fluctuations. *Plasma Chem. Plasma Proc.*, 16, 1996.

[62] O.P. Solonenko. *Thermal Plasma Torches and Technologies, Volume 1: Plasma Torches, Basic Studies and Design.* Cambridge International Science Publishing, Cambridge, UK, 2003.

[63] J. Schein, J. Zierhut, M. Dzulko, G. Forster, and K. D. Landes. Improved plasma spray torch stability through multi-electrode design. *Contrib. Plasma Phys.*, 7:498–504, 2007.

[64] Fr.W. Bach, A. Laarmann, and T. Wenz. *Modern Surface Technology.* Viley VCH, Weinheim, Germany, 2006.

[65] J.-L. Marques, G. Forster, and J. Schein. Multi-Electrode Plasma Torches: Motivation for Development and Current State-of-the-Art. *The Open Plasma Physics Journal*, 2:89–98, 2009.

[66] H. Nishiyama. Magnetic control of homogeneous and dust-laden plasma jets. *Pure Appl. Chem.*, 71:1899–1907, 1999.

[67] H. Nishiyama, H. Tsukada, Y. Matsushima, and S. Kamiyama. The effect of an applied magnetic field on non-equilibrium plasma flow along a biased flat plate. *J. Phys. D: Appl. Phys.*, 30:2804–2811, 1997.

[68] F. Younis, S.A. Zaabi, M. Nader, W. Yousif, and A.R. Beig. Design and challenges of current sensing and harmonic extraction for active power filtering for an industrial drive in oil and gas industry. *IEEE proceeding*, pages 1–6, 2012.

[69] L. Delair, X. Tu, A. Bultel, and B. G. Cheron. Helmholtz behavior of a nitrogen plasma arc chamber. *High Temp. Mater. Processes*, 9:583–597, 2005.

[70] Y.H. Kweon, T. Aoki, Y. Miyazato, H.D. Kim, and T. Setoguchi. Computational study of an incident shock wave into a Helmholtz resonator. *Comput. Fluids*, 35:1252–1263, 2006.

[71] E.C. Fernandes and R.E. Leandro. Modeling and experimental validation of unsteady impinging flames. *Comput. Fluids*, 146:674–686, 2006.

[72] V. Rat and J. F. Coudert. Pressure and arc voltage coupling in dc plasma torches: Identification and extraction of oscillation modes. *J. Appl. Phys.*, 108:043304–8, 2010.

[73] V. Rat and J. F. Coudert. Acoustic stabilization of electric arc instabilities in nontransferred plasma torches. *Appl. Phys. Lett.*, 96:101503–3, 2010.

[74] J. Krowka, V. Rat, and J.F. Coudert. Resonant mode for a dc plasma spray torch by means of pressure-voltage coupling: application to synchronized liquid injection. *J. Phys. D: Appl. Phys.*, 22, 2013.

[75] J. Krowka, V. Rat, and J.F. Coudert. Investigation and control of dc arc jet instabilities to obtain a self-sustained pulsed laminar arc jet. *J. Phys. D: Appl. Phys.*, 46, 2013.

[76] B. Pateyron. TTWinner free download from www.unilim.fr/spcts or http://ttwinner.free.fr.

[77] A. Vardelle, P. Fauchais, B. Dussoubs, and N.J. Themelis. Heat generation and particle injection in a thermal plasma torch. *Plasma Chem. Plasma Process*, 18:551–574, 1998.

[78] J. F. Coudert, V. Rat, and D. Rigot. Influence of helmholtz oscillations on arc voltage fluctuations in a dc plasma spraying torch. *J. Phys. D: Appl. Phys.*, 40:7357–7366, 2007.

[79] J. Krowka, V. Rat, S. Goutier, and J.F. Coudert. Synchronization of suspension plasma spray injection with the arc fluctuations. *J. Therm. Spray Technol.*, 23, 2014.

[80] R. Ye, P. Proulx, and M. I. Boulos. Turbulence phenomena in the radio frequency induction plasma torch. *Int. J. Heat Mass Transfer*, 42:1585–1595, 1999.

[81] R. Noguera, M. Lejeune, and T. Chartier. 3D fine scale ceramic components formed by ink-jet prototyping process. *J. Eur. Ceram. Soc.*, 25:2055–2059, 2005.

[82] B.-J. De Gans and U. S. Schubert. Inkjet printing of polymer micro-arrays and libraries: Instrumentation, requirements, and perspectives. *Macromol. Rapid Commun.*, 24:659–666, 2003.

[83] C. Kullmann, N.C. Schirmer, M.-T. Lee, S.H. Ko, N. Hotz, C.P. Grigoropoulos, and D. Poulikakos. 3D micro-structures by piezoelectric inkjet printing of gold nanofluids. *J. Micromech. Microeng.*, 22:055022(11pp), 2012.

[84] H.-J. Kunze. *Introduction to Plasma Spectroscopy*. Springer, Heidelberg, Germany, 2009.

[85] F.R. Gilmore, R.R. Laher, and P.J Espy. Franck-Condon Factors, r-Centroids, Electronic Transition Moments, and Einstein Coefficients for Many Nitrogen and Oxygen Band Systems. *J. Phys. Chem. Ref. Data*, 21:1005, 1992.

[86] C.O. Laux. *Optical Diagnostics and Collisional-Radiative Models*. VKI Course on Hypersonic Entry and Cruise Vehicles, Stanford University, June 30-July 3, 2008.

[87] G. Herzberg. *Molecular Spectra and Molecular Structure I. Spectra of Diatomic Molecules*. NY: Van Nostrand Reinhold, New York, 1950.

[88] J.C. De Vos. A new determination of the emissivity of tungsten ribbon. *Physica*, XX:690–714, 1954.

[89] C. Parigger, D.H. Plemmons, J.O. Hornkohl, and J.W.L. Lewis. Temperature measurements from first-negative N_2^+ spectra produced by laser-induced

multiphoton ionization and optical breakdown of nitrogen. *Appl. Opt.*, 34:3331–3336, 1995.

[90] C.O. Laux, R.J. Gessman, C.H. Kruger, F. Roux, F. Michaud, and S.P. Davis. Rotational temperature measurements in air and nitrogen plasmas using the first negative system of N_2^+. *J. Phys. D: Appl. Phys.*, 43:265201 (12pp), 2010.

[91] P.J. Bruggeman, N. Sadeghi, D.C. Schram, and V. Linss. Gas temperature determination from rotational lines in non-equilibrium plasmas: a review. *Plasma Sources Sci. Technol.*, 23:023001 (32pp), 2014.

[92] D.M. Phillips. Determination of gas temperature from unresolved bands in the spectrum from a nitrogen discharge. *J. Phys. D: Appl. Phys.*, 8:507–521, 1975.

[93] C.O. Laux and C.H. Kruger. Arrays of radiative transition probabilities for the N_2 first and second positive, and O_2 Schumann-Runge ban systems. *J. Quant. Spectrosc. Radiat. Transfer*, 48:9–24, 1992.

[94] S. Florek and H. Becker-Ross. High-resolution spectrometer for atomic spectrometry. *J. Anal. At. Spectrom.*, 10:145–147, 1995.

[95] Y. Tanaka, T. Nagumo, H. Sakai, Y. Uesugi, Y. Sakai, and K. Nakamura. Nanoparticle synthesis using high-powered pulse-modulated induction thermal plasma. *J. Phys. D: Appl. Phys.*, 43:265201 (12pp), 2010.

[96] R. Vassen, Z. Yi, H. Kassner, and D. Stoever. Suspension plasma spraying of TiO_2 for the manufacture of photovoltaic cells. *Surf. Coat. Technol.*, 203:2146–2149, 2009.

[97] G. Mauer, A. Guignard, and R. Vassen. Plasma spraying of efficient photoactive TiO_2 coatings. *Surf. Coat. Technol.*, 220:40–43, 2013.

[98] P. Michaux, G. Montavon, A. Grimaud, A. Denoirjean, and P. Fauchais. Elaboration of porous NiO/8YSZ layers by several SPS and SPPS routes. *J. Therm. Spray. Technol.*, 19:317–327, 2010.

[99] G. Darut, H. Ageorges, A. Denoirjean, and P. Fauchais. Tribological performances of YSZ composite coatings manufactured by suspension plasma spraying. *Surf. Coat. Technol.*, 217:172–180, 2013.

[100] G. Di Girolamo, F. Marra, L. Pilloni, G. Pulci, J. Tirillo, and T. Valente. Microstructure and wear behavior of plasma-sprayed nanostructured WC-Co coatings. *International Journal of Applied Ceramic Technology*, 10:60–71, 2013.

[101] N. Curry, K. Van Every, T. Snyder, and N. Markocsan. Thermal conductivity analysis and lifetime testing of suspension plasma-sprayed thermal barrier coatings. *Coatings*, 4:630–650, 2014.

[102] L. Bianchi, A.C. Leger, M. Vardelle, A. Vardelle, and P. Fauchais. Splat formation and cooling of plasma-sprayed zirconia. *Thin Solid Films*, 305:35–47, 1997.

[103] P. Fauchais, M. Fukumoto, A. Vardelle, and M. Vardelle. Knowledge concerning splat formation: An invited review. *J. Therm. Spray Techn.*, 13:337–360, 2004.

[104] R.B. Heimann. *Plasma-Spray Coating: Principles and Applications*. VCH, New York, USA, 1996.

[105] P. Fauchais, A. Vardelle, and B. Dussoubs. Quo vadis thermal spraying? *J. Therm. Spray Techn.*, 10:44–66, 2001.

[106] A. Vardelle, C. Chazelas, C. Marchand, and G. Mariaux. Modelling time-dependent phenomena in plasma spraying of liquid precursors. *Pure Appl. Chem.*, 80:1981–1991, 2008.

[107] L. Leblanc and C. Moreau. The long-term stability of plasma spraying. *J. Therm. Spray Techn.*, 3:380–386, 2002.

[108] R. M. Young and E. Pfender. A novel approach for introducing particulate matter into thermal plasmas: The triple-cathode arc. *Plasma Chem. Plasma Process*, 9:465–481, 1989.

[109] S.W. Rienstra and A. Hirschberg. *An Introduction to Acoustics*. Eindhoven University of Technology, 2014.

[110] V. Kopecky and M. Hrabovsky. Resonant Excitation of Boundary Layer Instability of DC Arc Plasma Jet by Current Modulation. *Plasma Chem. Plasma Process.*, 31:827–838, 2011.

[111] E. Moreau, C. Chazelas, G. Mariaux, and A. Vardelle. Modeling the restrike mode operation of a DC plasma spray torch. *J. Therm. Spray Technol.*, 15:524–530, 2006.

[112] J.P. Trelles, C. Chazelas, A. Vardelle, and J.V.R. Heberlein. Arc plasma torch modeling. *J. Therm. Spray Technol.*, 18:728–752, 2009.

[113] R. Benocci, R. Florio, A. Galassi, M. Paolicchio, M. Piselli, C. Sala, M. Sciascia, and E. Sindoni. Experimental study for the optimization of plasma torch operations. *Eur. Phys. J. D*, 6:269–279, 1999.

[114] S. Paik, P.C. Huang, J. Heberlein, and E. Pfender. Determination of the Arc-Root Position in a DC Plasma Torch. *Plasma Chem. Plasma Proces.*, 3:379–397, 1993.

[115] Th. Peters. Uber den zusammenhang des steenbeckschen minimumprinzips mit dem thermodynamischen prinzip der minimalen entropieerzeugung. *Zeitschrift fur Physik*, 144:612–631, 1956.

[116] V. Rat and J.F. Coudert. Torche à plasma et procédé de stabilisation d'une torche à plasma. Plasma torch and method for stabilizing a plasma torch, November 12 2011. EP 2 502 468 B1, Patent CNRS.

[117] J. F. Coudert and V. Rat. Influence of configuration and operating conditions on the electric arc instabilities of a plasma spray torch: role of acoustic resonance. *J. Phys. D: Appl. Phys.*, 41:205208 (10pp), 2008.

[118] J. F. Coudert and P. Fuachais. Transient Phenomena in d.c. Plasma-Spray Torches. *Annals of the New York Academy of Sciences: Heat and mass transfer under plasma conditions*, 891:382–390, 1999.

[119] Y. Wang, J.-G. Legoux, R. Neagu, S. Hui, and B.R. Marple. Suspension plasma spray and performance characterization of half cells with NiO/YSZ anode and YSZ electrolyte. *J. Therm. Spray. Technol.*, 21:7–15, 2012.

[120] X.Q. Cau, R. Vassen, and D. Stoever. Ceramic materials for thermal barrier coatings. *J. Eur. Ceram. Soc.*, 24:1–10, 2004.

[121] E.P. Busso, J. Lin, S. Sakurai, and M. Nakayama. A mechanistic study of oxidation-induced degradation in a plasma-sprayed thermal barrier coating system.: Part i: model formulation. *Acta Mater.*, 49:1515–1528, 2001.

[122] M. Gell, J. Eric, V. Krishnakumar, K. McCarron, B. Barber, Y.-H. Sohn, and Tolpygo V.K. Bond strength, bond stress and spallation mechanisms of thermal barrier coatings. *Surf. Coat. Technol.*, 120-121:53–60, 1999.

[123] W.J. Quadakkers, V. Shemet, D. Sebold, R. Anton, E. Wessel, and L. Singheiser. Oxidation characteristics of a platinized MCrAlY bond coat for TBC systems during cyclic oxidation at 1000 C. *Surf. Coat. Technol.*, 199:77–82, 2005.

[124] U. Fantz. Basics of plasma spectroscopy. *Plasma Sources Sci. Technol.*, 15:S137–S147, 2006.

[125] Ch. de Izarra. Calibration d'une lampe à filament de tungstène. *7eme Colloque Capteur, Bourges*, 2009.

[126] A. Fierro, G. Laity, and A. Neuber. Optical emission spectroscopy study in the VUV-VIS regimes of a developing low-temperature plasma in nitrogen gas. *J. Phys. D: Appl. Phys.*, 45:495202 (11pp), 2012.

[127] A. Lofthus and P. Krupenie. The spectrum of molecular nitrogen. *J. Phys. Chem. Ref. Data*, 6:113–307, 1977.